Multifunctional hybrid nanomaterials for cancer theranostics

Thesis Submitted to AcSIR For the Award of the

Degree of

DOCTOR OF PHILOSOPHY

In

Chemical Sciences

By
Rajendra Prasad Meena
Registration Number: 10CC11A26001

Under the guidance of
Dr. Kaliaperumal Selvaraj

CSIR-National Chemical Laboratory
Dr. Homi Bhabha Road, Pune 411008

CERTIFICATE

This is to certify that the work incorporated in this Ph.D. thesis entitled "**Multifunctional hybrid nanomaterials for cancer theranostics**" submitted by **Mr. Rajendra Prasad Meena** to Academy of Scientific and Innovative Research (AcSIR) in fulfillment of the requirements for the award of the **Degree of *Doctor of Philosophy,* in *Chemical Sciences***, embodies original research work under my supervision. I further certify that this work has not been submitted to any other University or Institution in part or full for the award of any degree or diploma. Research material obtained from other sources has been duly acknowledged in the thesis. Any text, illustration, table etc., used in the thesis from other sources, have been duly cited and acknowledged.

Rajendra Prasad Meena

(Student)

Dr. Kaliaperumal Selvaraj

(Supervisor)

DECLARATION

I, **Rajendra Prasad Meena**, hereby declare that the work described in this thesis entitled **"Multifunctional hybrid nanomaterials for cancer theranostics"** was carried out by me for the degree of *Doctor of Philosophy in Chemical Sciences* under the guidance and supervision of Dr. Kaliaperumal Selvaraj, Catalysis and Inorganic Chemistry Division, CSIR-National Chemical Laboratory, Pune, India. I confirm that this work was done by me while in candidature for a research degree at this institute. This work is original and no part of this thesis has been submitted for a degree or any other diploma at this institution or in any other institution. The interpretation put forth are based on my literature survey of the original articles and all sources have been duly acknowledged in this thesis.

Date: 24/3/17

Place: Pune

Rajendra Prasad Meena

(Student)

Dedicated to my
Family

ACKNOWLEDGEMENTS

I am short of words to express my deep sense of gratitude to all those people whom I have come across. I take this opportunity to acknowledge and extend my sincere gratitude towards all those people who have been involved, directly or indirectly, to make the research work possible.

First, I would like to express my deepest gratitude to my research supervisor Dr. K. Selvaraj, for giving me an opportunity to pursue my Ph.D. research with him. It has been a great privilege to work under his guidance for the past five years. His innovative thinking and highly spirited attitude have inspired me to conduct and complete my doctoral research efficiently. His constant encouragement helped me to push beyond my limits. His guidance always challenged me intellectually and provided a perfect ambience. I am grateful to him for his critical comments and great efforts in preparing this thesis. I thank him for his endless support filled with patience and enthusiasm during my whole tenure of Ph.D.

I would also like to thank my doctoral advisory committee members, Dr. D. Srinivas, Dr. A. Prabhune and Dr. M. V. Badiger for their constructive and innovative suggestion. I owe a great deal of appreciation and gratitude to my collaborators Prof. Rohit Srivistava and his team, IIT-B, Mumbai and Dr. Gopal Kundu and his group, NCCS, Pune. I warmly thank them for their support, precious advice, analysis and discussions on my work.

I extend my sincere thanks to the present (Dr. Ashwini Kumar Nangia) and former director (Dr. Sourav Pal) for their kind help during the course of this work. I am grateful to UGC, New Delhi for fellowship support. I thank all the non-teaching staff of CSIR-NCL for their assistance on various occasions.

I take this opportunity to thank Dr. Sailaja Krishnamurthy (CSIR-CECRI) for her constant support and encouragement. Further, I would like to thank my fellow labmates Suman, Meghna, Krati, Zinoy, Parul, Deena, Pallavi, Chithi, Dr. Pragya, Dr. T. Govindraja and all alumini. Although many have moved away from NCL (Dr. Vashab Da, Prof. Dheeraj, Dr. Rana, Dr. Asheesh, Dr. Omkar, Dr. Jugal, Dr. Bhanu, Dr. Puneet), I will never forget the experiences we've shared and hope to stay in touch. I thank Krati and Suman for interesting scientific discussions for making GMS nanohybrid at

late night in lab and NCML group on a cup of tea. These friends have been there for me when the challenges of Ph.D. seemed too great to overcome. I also thank all project trainees and Niya Kayalvizhi for learning from them.

A special thank to my roommates Puneet, Jugal, Bhanu and Omkar for the stimulating discussions, sleepless nights, discussions on Sunday morning tea, best food, many trips and for all the support at various critical time points and fun we had in the last five years. I also thank to my friends, Vikas, Ashish, Kavita, Yachi, Chechi, Kundan, Manoj (NCL), Manoj (IIT-B), Deepak (IIT-B), Mukesh (IIT-B), Piyush Sir (IIT-B), Luve (IIT-B), Sumit (IIT-B), Janhavi and RK, Mahadeo (NCCS), Amit, Prabhu, Pravin for their help and support at the time of PhD. I extend my thanks to Ramhari, Ramkesh, Roopsingh, Kaushal, Sonu, Pawan, Prem, Guddi, Vinod, Dr. Narendra, Ajay, Balram, Chinga for their help and support at several time points during my PhD and with them I have enjoyed a lot.

I would like to express the deepest gratitude to my family (Late. Sri Khana Ram, Prem Devi, Bajrang Lal, Durga Lal, Satyanarayan, Shanti Devi, Virma Devi, Kauslya, Vinod, Meena, Pinki, Kavita, Pooja, Deshrath, Jeetu, Chota and Bada Lala) who always supported me. Thank you for believing in me and allowing me to pursue my ambition. Thanks Selvaraj, Sailaja, Niya (sometimes), Suman, Zinoy for listening to my problems and providing perspective.

Rajendra……

Table of contents

List of Figures

List of Schemes

List of Tables

List of Abbreviations

GNPs	Gold nanoparticles
GNRs	Gold nanorods
NPs	Nanoparticles
FDA	Food and Drug Administration
PET	Positron-emission tomography
CT	Computed tomography
OCT	Optical coherence tomography
MRI	Magnetic resonance imaging
US	Ultrasound
NIR	Near-infrared
PTT	Photothermal therapy
PDT	Photodynamic therapy
MS	Mesoporous silica
QDs	Quantum dots
GO	Graphene oxide
GQDs	Graphene quantum dots
CQDs	Carbon quantum dots
DDS	Drug delivery system
DB24C8	Dibenzo[24]crown-8
CD	Cyclodextin
CB6	Cucurbit [6] uril
PEI	Polyethylenimine
DOX	Doxorubicin
CdS	Cadmium sulfide
GSH	Glutathione
DTT	Dithiothreitol
ME	Mercaptoethanol
DNP	1, 5-dioxynaphthalene
PEM	Polyelectrolyte multilayers
AB	Azobenzene
TSUA	4-(3-triethoxylsilyl propylureido) azobenzene
PNIPAM	Poly-N-isopropylacrylamide
PI	Propidium iodide
XRD	X-ray diffraction
TEM	Transmission electron microscope
SEM	Scanning electron microscopy
AFM	Atomic force microscopy
DLS	Dynamic light scattering
XPS	X-ray photoelectron spectroscopy
FTIR	Fourier transform infrared spectroscopy
CTAB	Cetyltrimethyl ammonium bromide
AR	Aspect ratio
SPR	surface plasmon resonance

EDAX	Energy-dispersive X-ray
DPPC	Dipalmitoylphosphatidylcholine
MPW	Millipore water
EDC	N, N-(3-Dimethylaminopropyl)-N′ ethylcarbodiimide
NHS	N-hydroxysuccinimide
FA	Folic acid
DMEM	Dulbecco’s modified Eagle’s medium
FBS	Fetal bovine serum
AA	Ascorbic acid
HU	Hounsfield unit
IAEC	Institutional Animal Ethical Committee
HC	High cargo
MC	Moderate cargo
GMS	Gold nanorods encapsulated mesoporous silica
MFT	Multifunctional theranostics
TEOS	Tetraethylorthosilicate
APTS	3-aminopropyltrimethoxysilane
BET	Brunauer-Emmett-Teller
PBS	Phosphate-buffered saline
BJH	Barrett-Joyner-Halenda
GOF	Graphene oxide nanoflakes
DMSO	Dimethylsulphoxide
UV-Vis	Ultraviolet visible spectroscopy
PL	Photoluminescence
RT	Room temperature
IVIS	In vivo imaging system
RBCs	Red blood cells
IV	Intravenous
TG	Thermogravimetric
MCF-7	Michigan Cancer Foundation-7

Chapter I

Introduction

This chapter provides an introduction to the remarkable impact of nanotechnology in the area of medicine especially cancer theranostics. A brief review on the evolution of nano sized hybrids materials (nanohybrids) for multifunctional cancer theranostics applications is introduced here. In this context, basic requirements and challenges for designing multifunctional nanohybrids for cancer theranostics (diagnostics and therapeutics by single system is called theranostics) is highlighted. Major hurdles experienced in the synthesis routes and limitations of the designed product such as poor biocompatibility, low photostability, non-specific targeting, low cargo capacity, poor biodegradation and lower theranostics efficiency are discussed in-depth. The current scenario of theranostics systems and their multifunctional applications have been presented in this chapter along with the significance of the thesis.

1.1 Material science in cancer nanomedicine

Manipulation of matter at atomic, molecular and supramolecular scale to create materials with remarkably new properties is a rapidly expanding area of research.[1-4] Materials science involves an understanding of interconnect between synthesis routes, structural design and properties of the materials.[3] Depending upon the property, a well designed multi functional material could have promising applications in the areas spanning chemistry, physics, biology and engineering.[3, 5, 6] To date, functional hybrid nanomaterials are applied extensively in the areas such as catalysis, energy storage, sensors, clean energy and health care, etc.[7-13] One of the most significant and impactful application of nanomaterials is in the area of nanomedicine. So far, several nano sized hybrid/composite materials (nanohybrids/nano-composites) are being applied as diagnostic or therapeutic probes with their tremendous impact on human health.[14, 15] Further, a single hybrid nanostructure capable of multi-model diagnostics and combined therapies (chemo-photothermal therapy, chemo-photodynamic, photothermal-photodynamic therapy etc.) is an area of recent development with possible significant outcome on health care.[15-24] Integration of multiple components with multiple function at nano level produces hybrid nanostructures that allows the above interest of application.[18, 22, 24]

In the context of human health care, imbalances in genetic and recently evolving environmental factors increase the possibilities of multifactorial complex diseases such as cancer, a leading cause of mortality in the modern world.[2] Cancer is understood in a better way from the genetic, molecular and cellular biology viewpoints requiring new strategies of diagnosis and treatment. In cancer, nanotechnology based medicine has great potential in the area of new drug delivery systems, multifunctional diagnostics and as therapeutic agents.[7, 16]

Comprehensively used various nanoparticles (NPs) for this have overall dimensions less than several hundred nanometers and are comparable to large biomolecules, such as enzymes, receptors and antibodies.[16-20] On account of this specific physical property, these NPs exhibit excellent interactions with biomolecules present on the exterior and interior environment of cancer cells. However, generally, nonspecific targeting nature, multiple heavy dose requirements of contrast agents and drugs, poor water solubility, rapid clearance and time consuming planning are limiting their applications in today's diagnosis and therapies.[25] In addition, traditionally used chemotherapy and radiation therapy treatments are less effective for cancer patients due to side effects from heavily used radiations and drug molecules.[26-29]

As solution to above, nanoparticles designed with combined diagnostic and therapeutic abilities is a recently developing concept for cancer detection and targeted therapies.[26, 28] Performing high efficiency of both imaging and therapeutic functions by a single hybrid material is the major advantage of nanosized multifunctional systems and consequently various research efforts have been devoted towards this.

1.2 Theranostics concept and its advantages

In 2008, the major challenges and opportunities within newly designed medical products are reported by U.S. Food and Drug Administration (FDA).[30] On the other hand, John Funkhouser, the Chief Executive Officer of PharmaNetics, has introduced the term "Theranostics" (meaning diagnostics and therapuitics by a single system) for the first time in 1998 as a concept. Furthermore, the primary objective of theranostics is to be able to monitor the response of treatment, effect of drug efficacy and safety for healthcare systems. Recent advances in nano biomedicine have expanded the ability to design and fabricate multifunctional nanoparticles that combine targeting, therapeutic and diagnostic functions in

a single nanoplatform,[22-24, 31, 32] in the specific that integrates, the combination of contrast/diagnostics (molecular imaging) and therapeutics agent (molecular targeted treatment "all-in one" Scheme 1.1).[32] Imaging and therapeutic modality have their unique strengths for medical diagnosis and treatment. Imaging has advantages for diagnosis from two or more imaging modalities in a single platform that provides overall structural and molecular information.[33, 34] Similarly, the multimodality in therapy also show their significant advantage on cancer cell/tumor elimination.[23] Combined modalities of diagnostic and therapeutic agent in a single system at nanoscopic level is newly emerging as "nano-theranostics" an urgent need for nanomedicine.

Their major and visible advantages are high water solubility, specific optical properties, good biocompatibility, high theranostics efficiency, easy to functionalize with biomolecules (capping agent/targeting ligands), high cargo capacity, smooth circulation, localized binding ability and high tumor accumulation.[29, 31-34] Image guided stimuli triggered targeted cancer therapy could be a new rapid advance for theranostics. The distinct advantage of these theranostics is to provide localized and detailed information and therapy in specific sites of diseases.[35-39] However, challenges such as optimal circulation, biocompatibility, biodegradation and excretion remain as major concern and are currently being addressed.[40-50]

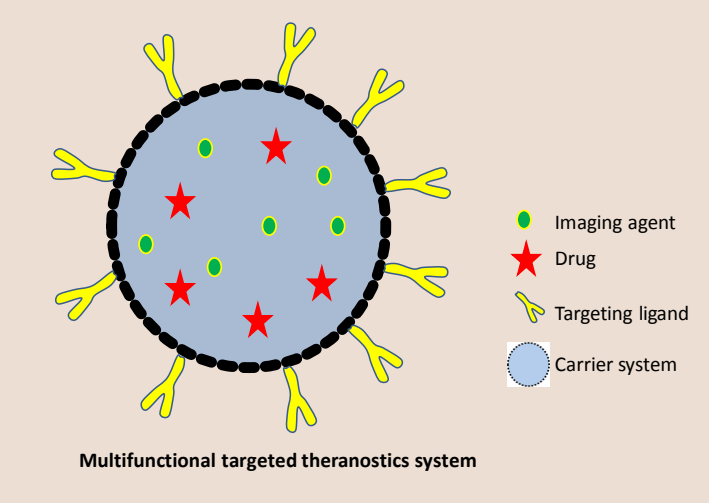

Scheme 1.1. *Integration of contrast agent (imaging), drug molecule (therapy) and targeting ligand in a single platform as a multifunctional targeted theranostics system.*

1.3 Components of theranostic system

A successful design of a theranostics system essentially needs understanding of various functions and the components that perform them. Nanosized imaging (contrast/emissive media) and therapeutic agent in a single system is a recent development in nanomedicine. [20-24, 32, 35, 39] Today, several diagnostic techniques such as positron-emission tomography (PET), X-ray computed tomography (X-ray CT), optical coherence tomography (OCT), magnetic resonance imaging (MRI) etc. are routine procedures in hospitals due to the unparalleled and complementary details that they can provide about the interior body.[35, 36] These techniques are becoming progressively a significant piece of the diagnostic portfolio available to physicians that helps in the understanding the specific location of tumor in animal or human body. In order to facilitate the understanding of healthcare practitioners on the abnormalities of a diagnostic image, contrast agents are often employed to create visible changes in the resulting image after interacting with the incident radiation.[35] The above imaging modalities

are heavily dependent on the choice of contrast agents and thus this makes one important function/component of theranostics system. The development of nanosized novel and improved contrast agents has significant impact to this field further improvement on their contrast ability, biocompatibility, targeting ability and specific bio-distribution etc are intensively being investigated.[35]

Among all, the X-ray computed tomography (X-ray CT) technique provides detailed three-dimensional (3D) anatomic information with high resolution and good brightness.[51] X-ray CT is one of the commonly used imaging techniques due to its wide availability, high efficiency and quick response. This technique is characteristically accomplished by stimulating multiple X-rays from different angles to

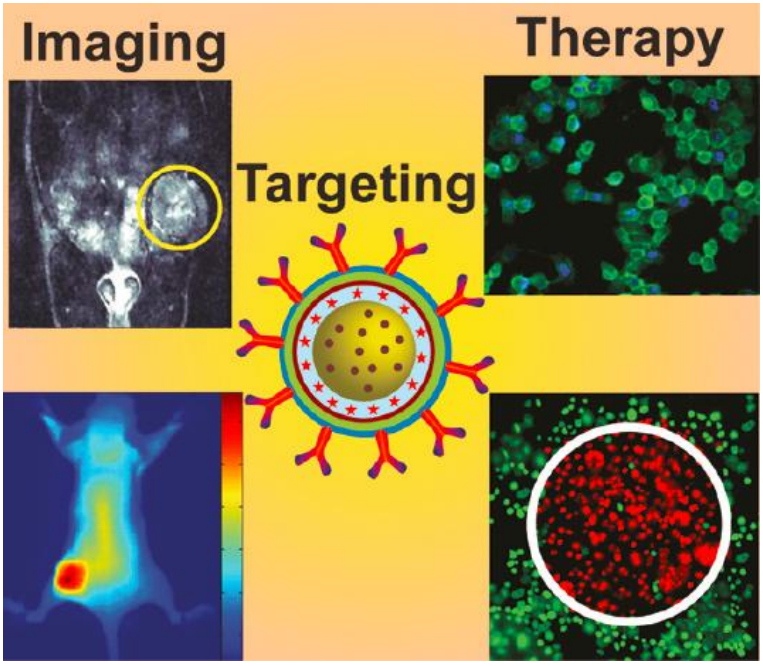

Figure 1.1. *Probe design multifunctional theranostics. Imaging and therapy by a single system. Adapted from Acc. Chem. Res., 2011, 44, 936.*

form slices which can further be composited collectively to form a detailed set of cross-sectional image.[52] In this context, iodine and gadolinium based contrast agents are commonly used due to high atomic number and X-ray attenuation.[35] However, these contrast agents suffer from many problems including short circulation half time (<10 min. for conventional iodinated contrast), nonspecific bio-distribution, rapid excretion and renal toxicity, poor contrast ability, high dose requirement (~ 100-400 mg/mL concentration).[35, 51, 52] Hence, in recent years, various nanosized contrast agents have been developed which are able to overcome many of these shortcomings. Nano-formulations of bismuth, barium, gadolinium, dysprosium, ytterbium, tantalum, gold nanoparticles, etc. with high atomic number and X-ray absorption coefficient have been investigated for multimodal diagnosis.[35] Various fluorescent contrast agents such as organic dyes, NIR responsive quantum dots (metal and graphene/carbon dots) for emissive diagnosis are also designed in recent years.[53, 54]

Another major component of theranostics system is a carrier system that transports the contrast agent and/or therapeutic agent to the interested specific site with the help of a targeting ligand (Scheme 1.1 and Figure 1.1). A number of carrier systems are designed with their high cargo loading capacity such as inorganic porous hollow spheres, mesoporous silica nanoparticles, magneto-plasmonic nanocapsules, gold nano shells, liposomal, polymeric and graphene oxide nanoparticles, etc.[35, 55-61] Combination of both imaging agent and carrier in one system fulfill the fundamental criteria of a nano-theranostics. These hybrids facilitate easy functionalization of targeting ligands on its surface to have longer circulation (at least 24 h), specific targeting and bio-distribution.[23, 40]

External stimuli responsive combined therapeutics viz., chemo-photothermal therapy, chemo-photodynamic therapy, photothermal-photodynamic therapy are other important capabilities

of theranostics systems. Combining above mentioned multiple therapies into a single system are more effective and significant for cancer treatment. Various nanohybrids/nano-composites such as gold nanorods embedded porous silica, dye loaded mesoporous silica, MoS_2 nanohybrids, NIR light responsive and thermal responsive graphene-gold nanohybrids/ nano-composites etc. have been explored for combined therapeutic applications due to their high rate of light-to-heat conversion, drug loading capacity, a large amount of reactive oxygen species generation, etc.[8, 12, 17, 18, 22] Next generation of combined therapy will help in following: (i) reduced side effects, (ii) enhanced efficacy of therapeutic outcomes, (iii) improved survival and quality of life of cancer patients.

1.4 Current scenario of nanotheranostics

Theranostics with additional functions are progressively getting popular especially with combined therapeutic abilities.[18, 22] From molecular understanding to clinical trials, few of them have been translated. Some are on in vivo studies.[22-25] Fabrication of nano sized theranostics systems are highly interesting for medical scientist. However, large scale production through rapid process, aqueous solubility, high cargo capacity, localized controlled release, biocompatibility, circulation and specific targeting ability are the major concerns and also current demands for any types of theranostics.[61-63] Designing of bio-responsive, degradable and targeted nanotheranostic systems are though of current demand for nanomedicine yet remain as major challenges. The designed theranostics systems should be able to show their best performance at specific site in cancer cell or at tumor environment. Thus, real time monitoring of delivered nanotheranostics in cancer mimicked environment can be made possible to provide critical information about specific diagnostics and therapeutic efficiency. So far, various nanoparticles such as metal (Au, Ag, Fe, WS_2),

liposome, polymers, mesoporous silica, silica coated gold nanorods, graphene quantum dots, nano-gated porous silica, up-conversion luminescent materials and many more have been used for multifunctional theranostics applications.[34, 64] A number of studies have confirmed their potential usage for theranostics and various formulations of these nanoparticles are already in the preclinical and clinical stages of development. For example, Polyethylene glycol (PEG), PEGlated silica-gold nanoshell (AuroShell) as a photothermal agent, silica-quantum dots (C dots-silica composite) for molecular imaging, PEGlated liposomal doxorubicin for ovarian cancer treatment, etc., are used for human trials for the first time.[65-69] Several other nano sized formulations are under clinical trials and many more are currently being evaluated at the preclinical level for cancer diagnosis and treatment.[69] However, several properties of these theranostics systems need to be understood such as surface chemistry, dispersibility/solubility, stability, doses/concentration, biocompatibility, circulation time, pharmacokinetics, specific bio-distribution and specific site binding ability prior to clinical applications. This enable them to become an important clinical weapon for cancer cure in the near future.

On other hand, traditionally used chemotherapeutic drugs and radiation therapy show heavy side effects on health.[70] These conventional therapeutics require further improvements for better and fast treatment without any side effects. Photothermal therapy (PTT, photothermal agents which exhibit strong absorption in the near-infrared region (600-1100 nm), photodynamic therapy (PDT, oxidize targeted site via singlet oxygen which causes cell damage and death), thermal and magnetic hyperthermia have recently gained popularity as compared to the conventional radiotherapy and chemotherapy.[22-24, 34]

1.5 Design of nanohybrids as nanotheranostic

Sufficient chemical and physical protection of biological cargo molecules or payloads should be provided by carrier system during their delivery to the desired target site. Several organic and inorganic based carrier systems have been designed at nanoscopic level. Surface modifiers are attached to these systems and estimated to provide theranostics nanomaterials with additional properties such as long circulation time, barrier-penetrating ability and specific binding ability (Scheme 1.2).[28] Further, several organic-inorganic combinations are tried especially after 2005 and experienced a considered a rapid progress in nanomaterials design bringing about new opportunities for cancer diagnosis and treatment.[71, 72,73]

Several cancer theranostics strategies are based on non-metallic, metallic and composite nanohybrids.[73] Fluorescent diagnosis and drug delivery are the major part of non-metallic systems. These systems are generally designed by carbon (top-down and bottom-up approaches) nanoparticles, organic dyes, soft materials (polymeric, micelles, surfactants etc.) and silica based (sol-gel methods) framework, etc.[35] Due to aqueous solubility, good photoluminescence and stability, various formulations of carbon nanoparticles such as carbon quantum dots, graphene quantum dots, graphene oxide nano sheets, etc. are used as fluorescent diagnostics probe.[74] In addition, various classes of mesoporous silica such as MCM-41, MCM-48, SBA-15, hollow silica spheres etc. highly explored for drug delivery applications.[75] High surface area (700-1200 m^2/g), highly ordered pores (2-50 nm in range), high cargo capacity (10-27 % of doxorubicin anticancer drug) and easy surface functionalization are the main features of these materials for biomedical applications.[22-26, 75]

On the other side, various metal nanoparticles like gold nanoparticles (many faces of gold, such as spheres, nanorods, nanocage, cubes, shell, nanoclusters, hollow), iron nanoparticles,

silver nanoparticles are widely used for biomedical applications due to their unique characteristics such as highly tunable optical properties, contrast ability (high atomic number), specific surface plasmonic nature, good hyperthermia and photothermal efficiency.[76, 77] Moreover, these nanoparticles can efficiently convert incident light/radiofrequencies into heat.[18, 22] However, lack of chemotherapeutic efficiency of these nanoparticles limits their theranostics conditions.[19] Further, the combination of non-metallic and metallic components in a single system is the better way to overcome the theranostics problems. The theranostics design depends on interest of application. For example, gold nanorods-mesoporous silica nanohybrid[18] is suitable for CT based diagnosis and NIR responsive multifunctional cancer theranostics while nano-gated mesoporous silica nanohybrid[75] is fit for stimuli responsive triggered drug delivery with multimodal bio-imaging and iron oxide-silica composites are commonly used for MRI and magnetic hyperthermia for cancer theranostics etc.

1.6 Limitations and recent developments of nanotheranostic systems

Nano sized metallic and non-metallic theranostics systems are limited due high cost of precursors, sophisticated and time consuming synthesis process, poor control on premature cargo release, low product yield, poor stability, uncontrolled growth and particle size, low biocompatibility, non specific targeting ability and bio-distribution, poor image resolution, low cargo capacity, etc.[34, 35, 38, 47, 63] In addition, several organic dyes and quantum dots have been studied for molecular imaging but due to poor photo blinking, photostability and biocompatibility, these are not recommended for *in vivo* or clinical applications but limited only for *in vitro* level.[78] As a consequence, extensive efforts have been made to design new theranostics systems which can prevail over the above mentioned limitations. Recent studies

demonstrate that the mesoporous silica (MS, explored and declared as a safe material for human trials by US FDA) is recognized as a good cargo carrier due to its

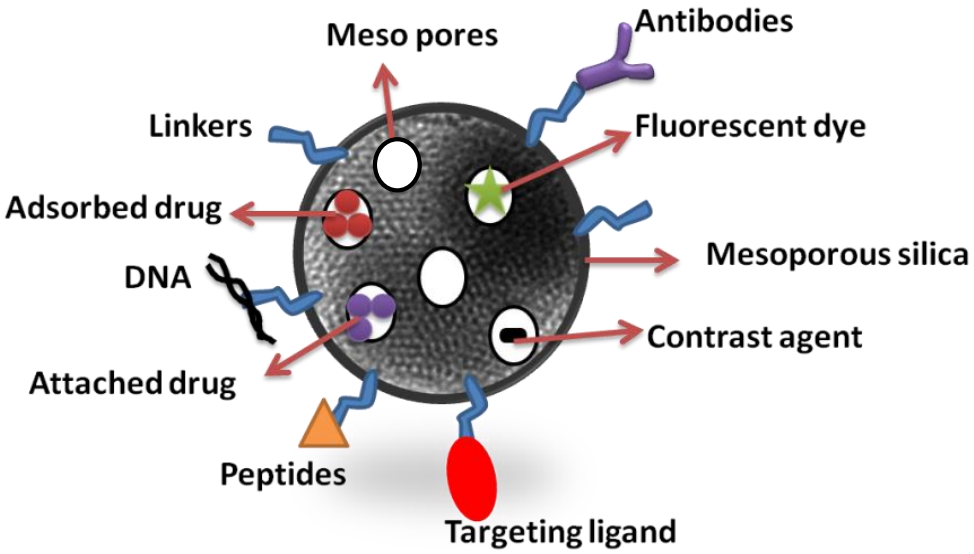

Scheme 1.2. *Design of multifunctional mesoporous porous nanotheranostic system. Various contrast and therapeutic agents are loaded in the porous system and its surface of is functionalized with several biomolecules such as proteins, enzymes, antibodies, peptides, targeting ligands and nucleic acids.*

high surface area, pore size tunability, high cargo capacity, easily functionalizable surfaces (both exterior and interior) with biomolecules and targeting ligands, chemical and physical inertness, good biocompatibility etc.[79] Mesoporous silica based nanohybrids are highly recommended as a drug delivery system (DDS) due to high surface area and cargo capacity. Architectural control and surface decoration of these porous cargo carriers have brought new possibilities for controlled drug delivery in nanomedicine.[75]

1.7 Nano-gated theranostics systems

A recent concept of nano-gated systems has evolved in the area of nanomedicine, where stimuli responsive controlled drug release can be triggered for improved and safe cancer therapies through zero or negligible premature release.[75] Nano-gates seal the pore opening of nanohybrid/theranostics to prevent the premature release of drug.[75, 80] Surface modifications with various functionalities is used for controlled the drug release (Scheme 1.3).[75,80,81] Pore are gated using bulky groups like supramolecules (nanovalve of cyclodextrin, aromatic amine, polymers, proteins, support of lipid layers) or nanoparticles, such as, carbon quantum dots, gold nanoparticles, iron oxide nanoparticles, etc.[75, 81] These sealed gates either degrade or get detached on exposure of specific stimuli or to the cancer mimicked environment.[81] To date, various structures based nanohybrids such as light responsive plasmonic nanoparticles, superparamagnetic nanoparticles with responsiveness to magnetic fields, polymeric and liposomal based nanohybrids which are high-frequency ultrasound responsive, etc., have been thoroughly studied for remotely triggered drug release.[75,81]

Another recent development in theranostics viz., a nanovalve gated mesoporous silica (MS) with stimuli responsive controlled drug delivery has acquired great attention. The exterior surface of MS is functionalized with other pore covering agents such as metal nanoparticles, graphene quantum dots, carbon nanodots etc. for preventing the premature drug leakage and for various stimuli responsive controlled drug delivery.[75, 81] In that context, Sir F. Stoddart

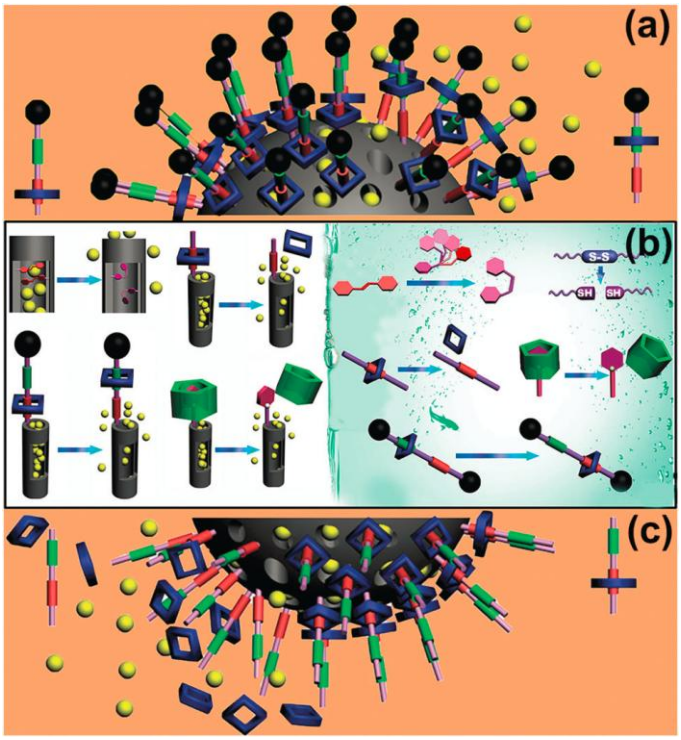

Scheme 1.3. *Schematic illustration of nano-gated multifunctional theranostics systems and nanovalves switch mechanisms (a) Molecular switches, (b) evolution and (c) supramolecular switches. Adapted from Chem. Soc. Rev.,* ***2015****, 44, 3474.*

and J. Zink have conceptualized stimuli responsive supramolecular gatekeepers on mesoporous silica nanoparticles that respond to various stimuli such as light, temperature, pH and enzyme (Scheme 1.4),[81, 82] among which individual stimuli, pH and redox-responsive release mechanisms have been recognized as effective ones.[81]

1.8 MS based stimuli responsive controlled drug delivery system

In this section, the decoration of nano gates/switches onto the surfaces of MS based nanohybrids and their gated mechanism toward pH, light, temperature enzyme, (Scheme 1.4) will be discussed.[75, 81, 82] The importance of MS as a drug carrier has been discussed earlier.[81]

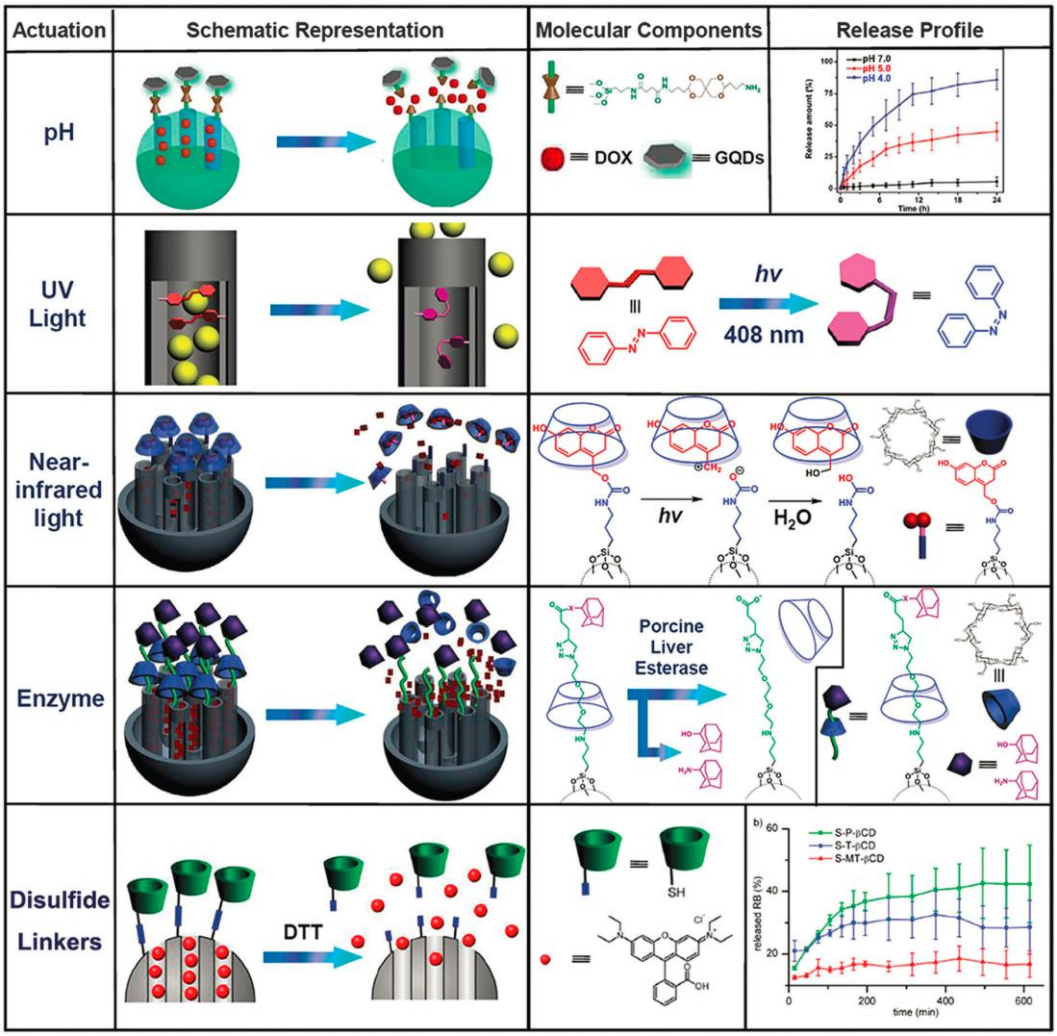

Scheme 1.4. *Schematic illustration of stimuli responsive (pH, UV NIR light, enzyme and disulphide linkers) nano-gated multifunctional theranostics systems and their controlled cargo release profile. Adapted from Chem. Soc. Rev.,* ***2015****, 44, 3474.*

1.8.1 pH-responsive nano-gates

Various MS gated nanohybrids have been exploited for pH-responsive controlled drug delivery in cancer mimicked environment (pH ~ 2-4).[82, 83] MS as a cargo carrier is reported by Vallet-Regi et al. in 2001 for the first time.[84] Stimuli responsive release of guest molecules from MS is reported by Mal et al. in 2003.[85] The MS nanoparticles are prepared by sol-gel process and N-(3-triethoxysilylpropyl-2-aminoethyl)-ethylenediamine is grafted on its exterior surface to obtain amine functionalized mesoporous nanohybrid.[75] In detail, anchored amine groups are deprotonated at high pH values and the delivery system goes to an "open gate" state.[75, 82] However, at low pH conditions, amine groups repel to each other due to coulombic repulsion effect and cover the pore openings brining the delivery system to a "close gate" state (Scheme 1.5).[86]

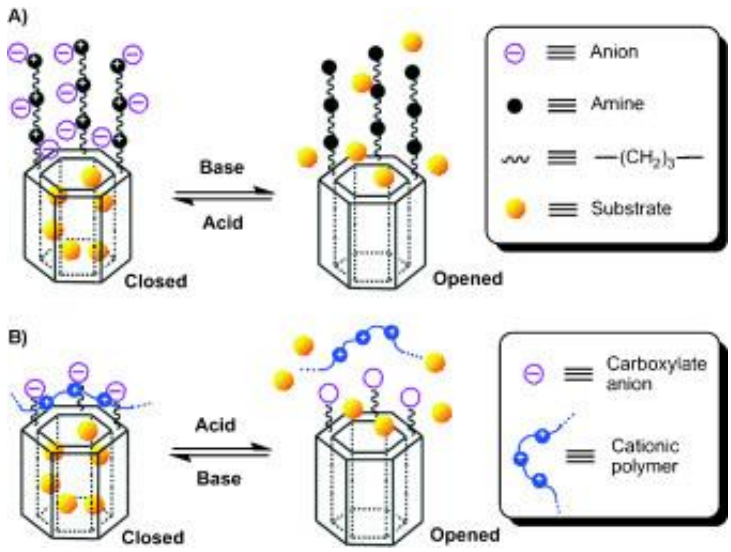

Scheme 1.5. *Schematic illustration of pH responsive nano-gated multifunctional theranostics systems and their controlled cargo release profile. Adapted from J. Am. Chem. Soc. 2004,* ***126****, 8612.*

In 2004, Sir F. Stoddart, J. Zink and coworkers have designed nano-gated mesoporous silica utilizing the recognition between surface-tethered naphthalene-containing secondary

dialkylammonium ions and supramolecular gates (dibenzo[24]crown-8 (DB24C8)).[86] The loaded drug molecules from the pores of MS are released at various pH levels and the rate of cargo release is determined by the effect of electrostatic interactions and steric hindrance of the added salts. Similar concept is described by Kim and coworkers in 2007, where the pores are blocked by grafting a biocompatible version of pH-responsive polyethylene amine (PEI)/ cyclodextin (CD) polypseudorotaxanes.[87] In 2008, Sir Stoddart and Zink's groups have reported the first cucurbituril based supramolecular nanovalves on MS nanoparticles (bisammonium stalks and cucurbit [6] uril (CB6) rings).[88] The successful operation of these nanovalves on mesoporous nanohybrids is observed under pH variation. The nanovalves operation depends on the ion-dipole interaction between CB6 and the bisammonium stalks as a function of pH values of an external environment. When pH values are neutral and acidic, CB6 rings close the bisammonium stalks tightly and results in the pore sealing of nanohybrid. However, the deprotonation of bisammonium stalks is noticed in basic environment (pH ~ 9-10). Hence, the pH-responsive supramolecular nano-valves play a significant role in cancer therapy due to the variation in pH values in cancer and normal cells in living systems.

Zink and coworkers have contributed significantly to studies on the pH-responsive cargo uptake and release in cancer mimicked environment using cyclodextin (CD) threaded phenylaminomethyl stalk based nano-valves as reported in 2011.[89] It is shown that, the CDs encircle the stalks on the nanohybrid surface through hydrophobic interactions. On protonation in the stalks, CD gates/caps detach from the stalks and result in the pore

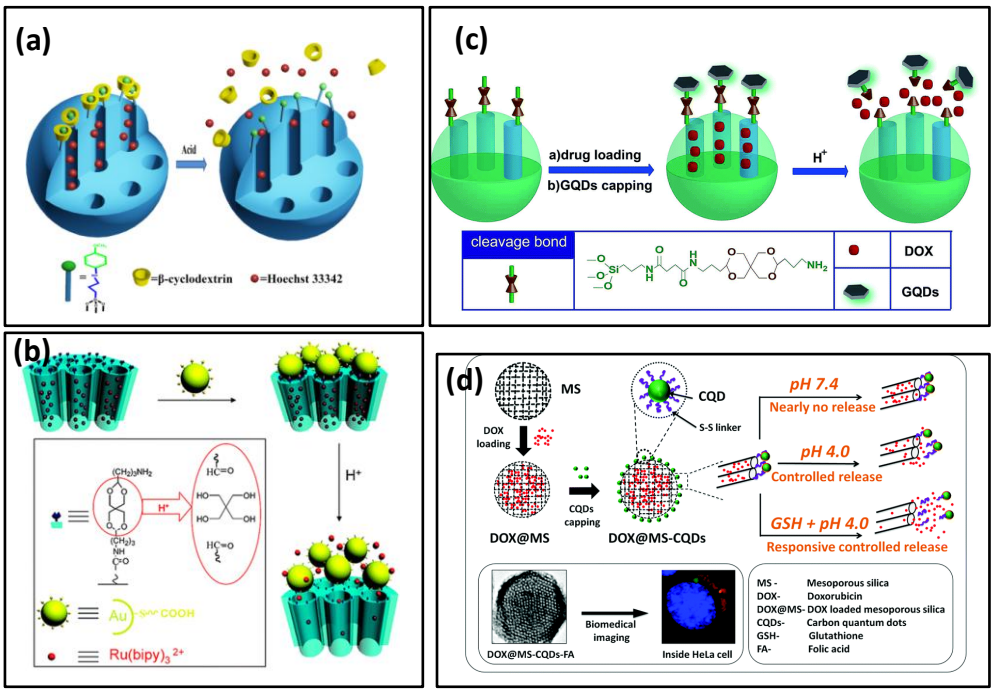

Scheme 1.6. *Schematic illustration of various pH responsive nano-gates on mesoporous silica (a) cyclodextrin gated MS surface, adapted from adapted from J. Am. Chem. Soc.* ***2010****, 132, 13016, (b) pH-responsive nano-gated ensemble based on gold-capped mesoporous silica through an acid-labile acetal linker, adapted from J. Am. Chem. Soc.* ***2010****, 132, 1500, (c) GQDs gated MS through acid-cleavable acetal bond, adapted from J. Mater. Chem. B,* ***2014****, 2, 4979 and (d) tightly sealed bioresponsive carbon nano-gates on MS surface its drug release concept, adapted from Nanoscale,* ***2016****, 8, 4537.*

opening in acidic condition (pH ~ 3-5). Similarly, other types of pore covering agents such as poly (methacrylic acid) (PMAA), lipid bilayer, metal complexes etc. are incorporated on the exterior surface of MS nanohybrids.[86, 90] However, their poor aqueous solubility is a major concern for nanomedicine with the exception of few molecules such as lipid bilayer, CB (6) etc.[90]

Alternatively, more soluble, biocompatible and stable systems such as gold nanoparticles, graphene quantum dots/carbon quantum dots (GQDs/CQDs) are being recently explored as gate keepers (2013, 2014 and 2016, Scheme 1.6).[75, 91] In a first such report in 2013, Qu and coworkers have attempted to cap the exterior surface of MS by CQDs and significant

premature release (about 15 %) of anticancer drug, doxorubicin (DOX) is observed.[92] The issue of premature release of cargo molecules from MS has been later addressed to a larger extent by Fu and coworkers in 2014 using graphene quantum dots (GQDs) as caps.[93] No other literature is available on the design and testing of GQDs/CQDs as capping agents. Thus, there appears to be a huge scope for further improvements in pore sealing, prevent premature drug release and aqueous solubility of MS based systems capped by the above agents. These limited reports further suggest that the inconsistency between pore diameter of MS and size of CQDs/GQDs results in loosely sealed pores attributing to the premature drug release. A part of the present thesis attempts to discuss a successful design of a MS based bioresponsive multifunctional theranostics system with tightly sealed pores by fluorescent CQDs/GQDs.[91] The concept of fluorescent nano-gate on mesoporous silica and its controlled drug delivery response in cancer mimicked environment is reported (2016) as a consequence that solves the solubility problem and sophisticated stimuli responsive mechanism of macromolecular nanovalve for drug delivery.[91] This is believed to provide a new direction for stimuli responsive nanomedicine for cancer theranostics.

1.8.2 Redox responsive nano-gates

Many diseases are related to redox homeostasis in the human body and cancer being the deadliest one.[88] Importantly, the redox homeostasis is also responsible for atherosclerosis, heart diseases and chronic diseases of major internal organs. Thus, it is significantly important to design a redox-responsive cancer theranostics system for the intracellular transport of drugs. Further, the continuous progress and successful therapeutic out comes in redox responsive nanohybrids are reported. In 2003, Lin and coworkers have designed cadmium sulfide (CdS) decorated MS nanoparticles as a first redox-responsive drug

delivery system.[94] In detail, the pores of drug loaded MS are covalently capped by mercaptoacetic acid functionalized CdS nanocrystals through 2-(propyldisulfanyl) ethylamine linker. Prevention of premature drug release from this system for a long time has been observed under normal physiological conditions. However, the disulfide linkages between the MS surface and CdS nanoparticles could be cleaved in the presence of various disulfide-reducing agents, such as glutathione (GSH, 2-20 mM), dithiothreitol (DTT) and mercaptoethanol (ME).[82, 91, 94] Along the same lines, Lin and coworkers have also designed superparamagnetic iron oxide nanoparticles (Fe_3O_4) gated MS nanohybrid as a stimuli-responsive controlled drug delivery system.[95] The disulfide linkages between the MS surface and Fe_3O_4 nanoparticles could be cleaved with above mentioned disulfide-reducing agents to implement successful redox-responsive controlled drug release. The above mentioned site-specific magnetic nanohybrids can also be attractive for the development of targeted and controlled drug delivery in intracellular environment opening a new direction for site-selective controlled drug delivery devices and nano biosensors.

Zink's group developed macromolecule based redox responsive gatekeepers in 2004.[86] These gates are related to tethered 1, 5-dioxynaphthalene (DNP)-containing derivative (DNPD) that is decorated on the MS surface and cyclobis-(paraquat-p-phenylene) ($CBPQT4^+$) which identify the DNP units through non-covalent interactions. The specific signal for pore opening is from an external reducing reagent (NaCNBH3) which operates the nanovalve and permits the control release of cargo molecules. Subsequently, the pseudorotaxane based gatekeepers are developed by same group through a fabrication of a bistable, reversible redox-responsive nano-switch on MS exterior surface.[96] The nano-

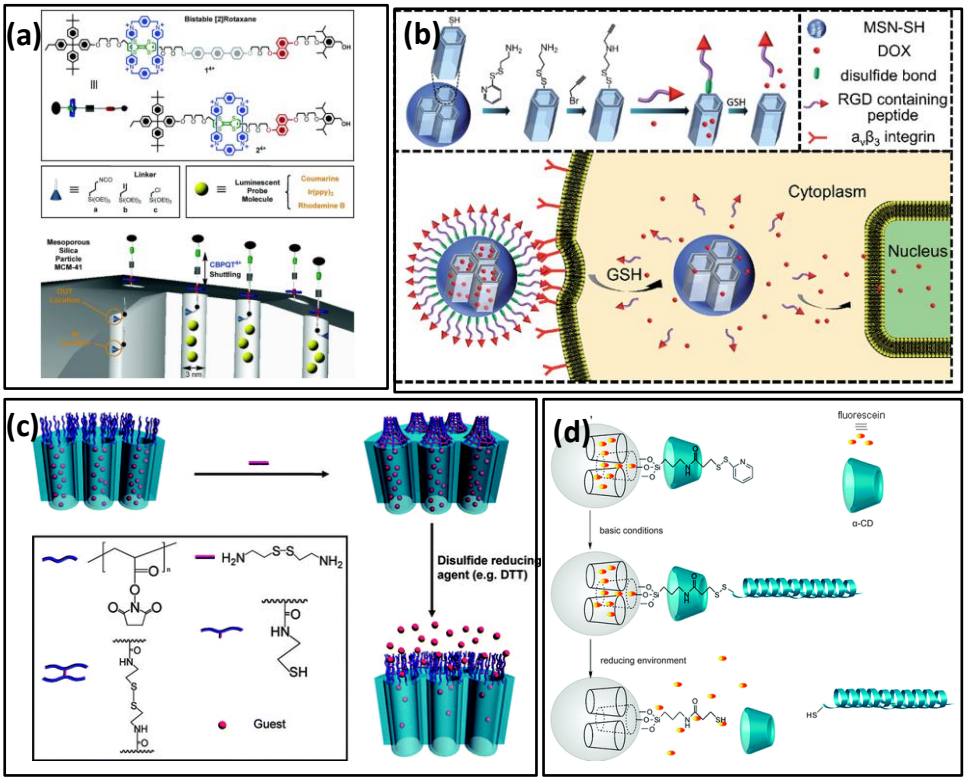

Scheme 1.7. *Schematic illustration of redox responsive nano-gates on mesoporous silica (a and b) nano-gates with the structural formulas of the bistable rotaxanes, adapted from J. Am. Chem. Soc.* ***2007****, 129, 626 and J. Mater. Chem. B,* ***2015****, 3, 39, (c) Redox-responsive nano-gated ensemble based mesoporous silica capped with redox-active cross-linked polymeric networks, adapted from J. Am. Chem. Soc.,* ***2008****, 130, 14418, Nanoscale,* ***2016****, 8, 4537 and (d) redox-triggered release systems based on peptide modified mesoporous silica. The release of the drugs takes place when the disulfide bridge linking the mesopore outlet and the peptide is cleaved in the presence of dithiothreitol, adapted from Phys. Chem. Chem. Phys.,* ***2011****, 13, 9982.*

switch is controlled with mild redox reagents and relied on the sliding of gated rings on the bistable thread. A polymeric gated MS based redox system is reported by Feng et al. in 2008 for the first time.[97] The cross-linked polymeric network on MS surface is worked as a redox responsive nano-switch where poly (N-acryloxysuccinimide) are attached on the exterior of MS pore through cystamine linking a disulfide-based bifunctional primary amine that could respond in GSH, DTT, ME, environment (Scheme 1.7). In 2009, Wang et al. has reported aptamer functionalized polyelectrolyte multilayers (PEM)-coated MS nanohybrids

as a targeted controlled drug delivery system.[98] These layers cover the MS pore opening and deliver the drug in cytosolic space. Cyclodextrins are also preferred to modify the exterior surface of MS with the various disulfide linkers that could prevent the premature release of the loaded drugs but leading to controlled drug delivery performance in the cytosolic space.[98] In 2012, Li et al.[99] has introduced GSH responsive disulfide bond containing PEG modified MS nanohybrid as controlled drug release system. In summary, the redox-responsive gates on the surface of MS based nanohybrids are widely explored in controlled drug delivery applications.

1.8.3 Light responsive nano-gates

The above two discussed stimuli responsive systems are basically designed for controlled drug delivery in intracellular environment. A nano-gate operation on MS surface could also be controlled through external stimuli viz., light exposure and these systems are in high demand as controlled drug delivery devices. Light irradiation can control the distribution and release of drug molecules from cargo carrier in cancer mimicked environment. The generated heat by photothermal agent during light exposure operates the nano-gates on MS surface (Scheme 1.8). Tanaka and coworkers reported the light responsive coumarin modified MS nanohybrid for the first time.[100] Designed system reveals the controlled release of drug via light responsive reversible intermolecular dimerization of coumarin derivatives on MS surface. Photosensitive coumarin blocks the MS pores through photodimerization of cyclobutane dimers under 310 nm light exposure. The cleavage of cyclobutane rings are observed during 250 nm UV light exposure that lead to the pore opening of MS nanohybrid.

Interestingly, various stalk and ring components (pseudorotaxanes approach) are also applied to understand the control drug delivery with light. In 2009, for the first time, Sir Stoddart and

coworkers fabricated a controlled drug delivery vehicle that is based on photoresponsive pseudorotaxane of azobenzene (AB) derivative and *β*-cyclodextrin (*β*-CD).[101] The exterior surface of MS is grafted with pseudorotaxane stalks viz., 4-(3-triethoxylsilyl propylureido) azobenzene (TSUA) groups or more water-soluble (E)-4-((4-(benzylcarbamoyl) phenyl)diazenyl) benzoic acid groups. Under the irradiation of 351 nm light, both azobenzene derivatives isomerize from the more stable *trans* form to a less stable *cis* form and then *β*-CD or fluorescently labeled pyrene-*β*-cyclodextrin (Py-*β*-CD) are introduced. The strong binding ability between *trans*-AB and *β*-CD locks the *β*-CD rings of MS surface. On the other hand, owing to the weak binding affinity between *cis*-AB and *β*-CD, the isomerization of *trans*- to *cis*-AB stalks leads to the dissociation of pseudorotaxanes and thus allowing the release of cargo molecules from carrier system. These CD based gates are applied by several groups after the demonstration by Zink and Sir Stoddart.[88, 90, 96]

Photosensitive cleavable thymine based nano-gates are conceptualized in 2012 where 365 nm UV light irradiation results in the formation of cyclobutane dimer and then block the pores whereas on a 240 nm light irradiation, the pores are opened due to photocleavage of cyclobutane dimer and entrapped drug is released from the carrier system.[102] Similarly, a continuous progress has been reported on light mediated controlled drug delivery by various nanohybrids such as, up-conversion nanohybrid, silica coated gold nanorods, NIR dye loaded lipid, silica, polymeric nanoparticles, etc.

The NIR responsive metal nanoparticles (800-900 nm wavelength) encapsulated MS nanohybrids for near-infrared (NIR) light mediated controlled drug delivery is a recent development in nanomedicine and these studies are reported from 2010 onwards.[16-18, 103] A noteworthy report in this context demonstrate an azobenzene gated mechanism by using MS

coated NaYF4:Tm, YbNaYF4 nanohybrids under 980 nm light exposure.[104] The released drug amount could be controlled through varying the intensity or exposure duration of NIR light.[103]

Several other NIR active systems with internal photothermal heating by plasmonic nanoparticles, photodimerizations (*cis-trans* conversion) have been reported for controlled release of drugs or dyes.[106] Focus has been on designing nano-gated light mediated systems for site specific localized treatment avoiding the irradiation of surrounding healthy tissues.[75, 82] In 2014, MS coated gold nanorods gated with sulfonatocalix[4]arene (SC[4]A)/quaternary ammonium supramolecular switches have been designed as a novel cancer theranostics platform.[103]

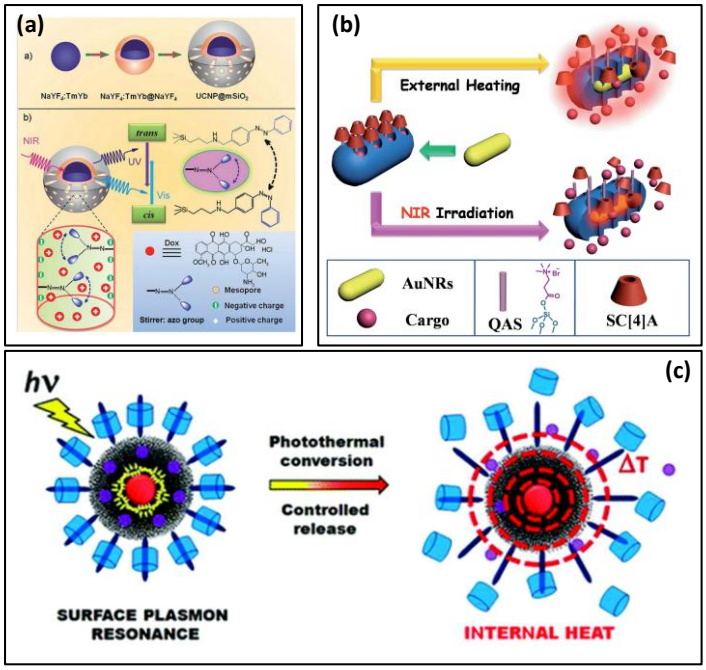

Scheme 1.8. *Schematic illustration represents the light responsive nano-gates on various nanohybrid (a) cis-trans* based *nano-gate operation with the structural formulas of gated system, adapted from Angew. Chem. Int. Ed.* ***2013****, 52, 4375, (b) near-infrared light-responsive supramolecular nanovalve based system, adapted from Chem. Sci.,* ***2014****, 5, 2804 and (c) near-infrared light-responsive supramolecular nanovalve, adapted from J. Am. Chem. Soc. 2012, 134, 7628.*

Through a supramolecular host-guest interaction these nano-valves close the pore opening of the nanohybrid. The internal heating generated by gold nanorods under NIR light exposure decreases the host-guest binding affinity so that SC[4]A rings dissociate from the stalks on the exterior surfaces thereby allowing the pore opening for release of trapped cargo molecules.

Among the light responsive techniques, UV light responsive method shows various side effects on healthy tissues due to its poor penetration ability.[107] NIR light responsive controlled drug delivery systems have several advantages over the above as well as the other stimuli responsive approaches. Controlled switching gated operation for controlled delivery, low side effects, specific distribution of drug molecules in site location, etc are few of the advantages.[34, 64] Additionally, these find significant importance in nanomedicine due to its ability to deeply penetrate without tissue damage and its good photothermal response for controlled delivery of drugs through open and close gated mechanism.[105, 108]

1.8.4 Temperature responsive nano-gates

In living body the presence of tumors, inflammation and any type of infection can cause an increase in the temperature of the whole body by up to 4-5 °C. Hence, it is advantageous to design a temperature responsive drug delivery system that only releases drugs at temperatures above 37 °C.[109] The modification of MS surface with temperature responsive nano-switch makes it to be a stimuli responsive controlled drug/dye delivery system. So far, poly-N-isopropylacrylamide (PNIPAM) and its derivatives are widely used temperature sensitive gatekeepers on MS surface.[109] More recently, Yang's group has designed the thermo responsive core–shell magnetic MS nanohybrid where Fe_3O_4 nanoparticles are in cores and the exterior MS surface is functionalized with cross-linked thermosensitive (PNIPAM, PNIPAM-co-NHMA) copolymer.[110] A controlled drug release is noticed below the lower

critical solution temperature (LCST) of these polymers where they exhibit a hydrophilic extended state. PNIPAM is functionalized on the internal surface of the MS through atom transfer radical polymerization (ATRP) as reported by Lopez and coworkers, who claimed that the PNIPAM-functionalized MS can release the drug molecules at a high temperature (50 °C) and hinder the drug release at low temperature (25 °C).[109] A thiol-functionalized polymeric gated MS surface with pyridyl disulfide-terminated poly (N-isopropylacrylamide) (PNIPAM-S-S-Py) is examined by Oupický et al.[111] The polymer gate is in the random coil formation at room temperature (below the LCST of the polymer) which results in the release of loaded cargo molecules at the same temperature.

Interestingly, Wang, Cui and coworkers have reported dual stimuli responsive (pH and thermal) copolymer-lipid bilayer-coated MS drug delivery system in 2013.[112] The designed system contains natural phospholipids (soyphosphatidylcholine, SPC) and poly(N-isopropylacrylamide-methacrylic acid-octadecyl acrylate) copolymer (p(NIPAM-MAAODA)) with a phase transition temperature of 42 °C and maximum DOX release (54 %) is observed at 42 °C that is five times larger with compared release at 25 °C temperature. Similarly, many more temperature responsive nano-gated systems have been designed and their successful controlled drug release performances are reported by several research groups.[113]

1.8.5 Conclusion

In summary, the recent developments of cancer theranostics systems and their clinical translations with current demand have been discussed. In addition, the key requirements to design a multifunctional theranostics and its limitations also have been highlighted in above sections. Further, the various designs of stimuli (viz., redox, light, pH, thermal, etc.) responsive nano-gated systems with various supramolecular and molecular switches are

reviewed in detail. Whole a significantly remarkable progress and contribution towards biocompatible design of multifunctional nanohybrids for cancer theranostics is visible, several issues on their successful parameters along with minimal cytotoxicity are yet to be understood and resolved.

1.9 State of art in the research area

1.9.1 What is known?

Various nano sized formulations for biomedical applications are known. Several multimodal imaging agents and therapeutic probes are well studied for molecular imaging and therapies. These imaging and therapeutic systems for medical applications are well explored individually and some of them are in clinical trials. Further, numerous synthesis methods such as top-down, sol-gel, solvothermal, hydrothermal, surfactants assisted, seed mediated growth, post-graft, etc have been reported to fabricate the multifunctional theranostics system with various contrast agents and drug carriers of various sizes and shapes. Role of various characteristics such as, size, shape, surface chemistry, framework, composition, physicochemical property, etc. of these systems on the theranostics performance have been understood by using modern techniques.

1.9.2 What needs to be understood?

Although the chemistry and biomedical applications of various nano sized systems are known since past few decades, there are several major concerns that need to be answered/addressed such as:

1. Knowledge on how to control the size and shape of nano sized imaging and therapeutic agents is not fully understood. Their surface chemistry and boundary between inorganic core and stabilizing agents/capping agents at nanoscopic level are poorly understood so far. For

example, the organic soft moieties on metal surface and their architecture is not visualizable through microscopic techniques (TEM, SEM, AFM, STEM etc.).

2. The formation of specific size distributed metal nanoparticles such as gold nanorods, their mechanism and surface chemistry are less understood.

3. Similarly, the various modes and details on the interaction between two (inorganic or organic) components are not known fully.

4. The specific targeting and communication of various nanohybrids with cancer cell membrane are less understood.

5. Rapid and scalable production of imaging and therapeutic systems with high product yield is highly challenging.

6. The design of multifunctional biodegradable theranostics system where diagnostics and therapeutics agents are integrated in a single system with maintained optical property is a major challenge.

7. Understanding on the theranostics performance (specific site location, high cargo capacity, photothermal conversion efficiency, etc.) of multifunctional systems is inadequate but important.

8. Finally, the optimal circulation and efficient clearance through excretion of theranostics systems from the body are to be studied well.

1.9.3 Objectives and scope of the thesis

The research work presented in the thesis focuses on the following objectives

- To design the biocompatible plasmonic nanorods for cancer theranostics
- To fabricate the biocompatible NIR responsive multifunctional hybrid for cancer theranostics

- ❖ To design the nano-gated bioresponsive mesoporous nanohybrid for stimuli responsive drug delivery and imaging
- ❖ To design a biodegradable red emissive and NIR responsive multifunctional nanotheranostic

The thesis presents (i) various recipes developed and optimized for the production of materials as mentioned above, (ii) characterization of all of them to understand the correlation between their structural design and their performances and (iii) demonstrate their promising candidature in biomedical applications using *in vitro* and *in vivo* experiments along with other associated tests. The present thesis presents few attempts made towards design of advanced multifunctional theranostics systems for cancer diagnosis and therapies. Focus has been on key bottlenecks such as achieving rapid and scalable design of nanohybrids, enhancing their critical properties such as biodegradation ability, enhanced biocompatibility, high surface area, high cargo capacity, enhanced theranostics performance, good water solubility, specific targeting ability as well as bio-distribution. This includes attempts for a simple designs of multifunctional nanohybrids by integrating multimodal diagnostics agents (X-ray CT and fluorescence), chemotherapeutic anti-cancer drug) and photothermal agents in a single system. Identifying and addressing various issues that limits factors such as surface modification, enhanced theranostics performance and combined chemo-photothermal therapeutic efficiency is a general objective in various part of the work presented.

There is ample scope of further research and development in fabrication of the nanotheranostic systems. To name a few, maximizing the biodegradability in a given time frame, simplifying the synthesis of more complex theranostics systems and molecular level understanding of their performances at in vivo condition.

1.10 Thesis organization

The thesis is entitled "**Multifunctional hybrid nanomaterials for cancer theranostics**" and is organized into five chapters.

Remarkable impact, basic requirements and challenges of functional nanohybrid for cancer theranostics applications are discussed in **Chapter 1**. Gated nanohybrids for stimuli responsive controlled drug delivery and their significant role in cancer mimicked environment are explained in this **Chapter**.

A positive attempt to design biocompatible multifunctional plasmonic gold nanorods (GNRs) for cancer diagnosis and photothermal therapy has been described in **Chapter 2**. The cetyltrimethyl ammonium bromide (CTAB) is a popular surfactant for stabilizing the shape of GNRs however the CTAB stabilized GNRs face serious concerns for biomedical application due to toxicity of CTAB. Through a careful replacement of CTAB with biocompatible lipid bilayer without losing the optical property of GNRs this concern is addressed in this chapter. Improved contrast ability, good biocompatibility and targeted photothermal therapy are being demonstrated with the lipid bilayer covered GNRs.

To further add a significant cargo capacity and to maintain their aspect ratio and in turn to their sustain optical property, a systematic attempt has been made to directly deposit mesoporous silica (MS) over them. Various studies to understand structure and property of the silica-gold nanohybrid make the description of **Chapter 3.** In this chapter, the understanding about the tunability in silica thickness over GNRs and their large scale production with high cargo capacity has been presented. Much improved biocompatibility (*in vitro* and *in vivo* studies), targeted safe contrast ability (*in vitro* and *in vivo* studies), stimuli (pH, temperature and NIR light) responsive controlled drug release performance and effective

photothermal performance of the new design have been described in this chapter along with details of targeted *in vitro* chemo and photothermal therapy.

Chapter 4 describes a successful design of a multifunctional (gatekeeping, contrasting and targeting) bioresponsive fluorescent carbon nano-gated mesoporous silica nanohybrid for cancer theranostics. Apart from a complete understanding of their physicochemical details, intracellular tracking through fluorescence emission and its multi stimuli responsive (GSH and pH) drug release in cancer mimicked environment are demonstrated. An attempt to synthesis a biodegradable theranostics design with the multifunctionalities of NIR responsive red fluorescent graphene oxide flakes (GOF) and liposome for targeted cancer theranostics is presented in **Chapter 5**.

Finally, **Chapter 6** is a brief conclusion of this thesis, summarizing overall accomplishments and potential future scopes of the research area. A list of publications made out and that under consideration during the research is also attached in the thesis.

1.11 References

1. Maltzahn, G.; Park, J. H.; Agrawal, A.; Bandaru, N. K.; Das, S. K.; Sailor, M. J.; Bhatia, S.N., *Cancer Res.*, 2009, **69**, 3892.

2. Cheng, Y.; Samia, A. C.; Meyers, J. D.; Panagopoulos, I.; Burda, C.F.B., *J. Am. Chem. Soc.*, 2008, **130**, 10643.

3. Nam, J.; Won, N.; Jin, H.; Chung, H.; Kim, S., *J. Am. Chem. Soc*., 2009, **131**, 13639.

4. Croissant, J.; Zink, J.I., *J. Am. Chem. Soc*., 2012, **134**, 7628.

5. Farokhzad, O. C.; Langer, R., *ACS Nano*, 2009, **3**, 16.

6. Shi, J.; Votruba, A. R.; Farokhzad, O. C.; Langer, R., *Nano Lett*. 2010, **10**, 3223.

7. Chen, Y. S.; Frey, W.; Kim, S.; Kruizinga, P.; Homan, K.; Emelianov, S., *Nano Lett*., 2011, **11**, 348.

8. Zhang, Z.; Wang, L.; Wang, J.; Jiang, X.; Li, X.; Hu, Z.; Ji, Y.; Wu, X.; Chen. C., *Adv. Mater*., 2012, **24**, 1418.

9. Wu, S. H.; Hung, Y.; Mou, C.Y., *Chem. Commun*., 2011, **47**, 9972.

10. Zhao, Y.; Trewyn, B. G.; Slowing, I. I.; Lin, V. S.Y., *J. Am. Chem. Soc.*, 2009, **131**, 8398.

11. Zhu, Y.; Fang, Y.; Kaskel, S., *J. Phys. Chem. C*, 2010, **114**, 16382.

12. Li, L.; Tang, F.; Liu, H.; Liu, T.; Hao, N.; Chen, D.; Teng, X.; He, J., *ACS Nano*, 2010, **4**, 6874.

13. Slowing, I.; Trewyn, B. G.; Lin, V. S., *J. Am. Chem. Soc*., **128**, 14792.

14. Han, Y. F.; Chen, F.; Zhong, Z.; Ramesh, K.; Chen, L.; Widjaja, E., *J. Phys. Chem. B*, 2006, **110**, 24450.

15. Lin, Y. S.; Tsai, C. P.; Huang, H. Y.; Kuo, C.T.; Hung, Y.; Huang, D.M.; Chen, Y.C.; Mou, C.Y., *Chem. Mater*., 2007, **17**, 4570.

16. Huang, P.; Bao, L.; Zhang, C.; Lin, J.; Luo, T.; Yang, D.; He, M.; Li, Z.; Gao, G.; Gao, B.; Fu, S.; Cui, D., *Biomaterials*, 2011, **32**, 9796.

17. Yang, X.; Liu, X.; Liu, Z.; Pu, F.; Ren J.; Qu, X. *Adv. Mater*. 2012, **24**, 2890.

18. Chang, Y. T.; Liao, P. Y.; Sheu, H. S.; Tseng, Y. J.; Cheng, F. Y.; Yeh, C. S. *Adv. Mater*. 2012, **24**, 3309.

19. Murphy, C. J.; Gole, A. M.; Stone, J. W.; Sisco, P. N.; Alkilany, A. M.; Goldsmith, E. C.; Baxter, S. C. *Acc. Chem. Res*. 2008, **41**, 1721.

20. Cong, H.; Toftegaard, R.; Arnbjerg, J.; Ogilby, P. *Langmuir*, 2010, **26**, 4188.

21. Liu, W.; Zhu, Z.; Deng, K.; Li, Z.; Zhou, Y.; Qiu, H.; Gao, Y.; Che, S.; Tang, Z. *J. Am. Chem. Soc.*, 2013, **135**, 9659.

22. Shen, S.; Tang, H.; Zhang, X.; Ren, J.; Pang, Z.; Wang, D.; Gao, H.; Qian, Y.; Jiang, X.; Yang, W. *Biomaterials*, 2013, **34**, 3150.

23. Huang, X.; El-Sayed, I.H.; Qian, W.; El-Sayed, M. A. *J. Am. Chem. Soc.* 2006, **128**, 2115.

24. Huff, T. B.; Tong, L.; Zhao, Y.; Hansen, M.N.; Cheng, J.X.; Wei, A. *Nanomedicine*, 2007, **2**, 125.

25. Lee, J. E.; Lee, N.; Kim, T.; Kim, J.; Hyeon, T., *Acc. Chem. Res*, 2011, **44**, 893.

26. Bentzen, S. M., *Nat. Rev. Cancer*, 2006, **6**, 702.

27. Cairns, R.; Papandreou, I.; Denko, N., *Mol Cancer Res*, 2006, **4**, 61.

28. Lammers, T., Kiessling, F., Hennink, W.E. and Storm, G., *Mol. Pharm*., 2010, **7**, 1899.

29. Loeffler, J. S.; Durante, M., *Nat. Rev. Clin. Oncol*., 2013, **10**, 411.

30. Woodcock, J.; Woosley, R., *Annu. Rev. Med*., 2008, **59**, 1.

31. Kobler, J.; Moller, K.; Bain, T., *ACS Nano*, 2008, **2**, 791.

32. Torney, F.; Trewyn, B. G.; Lin, V. S.; Wang, K., *Nat. Nanotechnol*., 2007, **2**, 295.

33. Lee, S.; Chen, X., *Molecular imaging*, 2009, **8**, 7290.

34. Xie, J.; Liu, G.; Eden, H. S.; Ai, H.; Chen, X., *Acc. Chem. Res*, 2011, **44**, 883.

35. Lee, N.; Choi, S. H.; Hyeon, T., *Adv. Mater*., 2013, **25**, 2641.

36. Kobayashi, H.; Brechbiel, M. W., *Adv. Drug Deliv. Rev*., 2005, **57**, 2271.

37. Slowing, I.I.; Vivero-Escoto, J.L.; Wu, C.W.; Lin, V.S., *Adv. Drug. Deliv. Rev.*, 2008, **60**, 1278.

38. Vivero-Escoto, J.L.; Slowing, I.I.; Trewyn, B. G.; Lin, V.S, *small*, 2010, **6**, 1952.

39. Torney, F.; Trewyn, B. G.; Lin, V.S.; Wang, K., *Nat. Nanotechnol*., 2007, **2**, 295.

40. Rosenholm, J. M.; Sahlgren, C.; Lind, M., *Nanoscale*, 2010, **2**, 1870.

41. Radu, D.R.; Lai, C.Y.; Jeftinija, K.; Rowe, E.W.; Jeftinija, S.; Lin, V.S., *J. Am. Chem. Soc*., 2004, **126**, 13216.

42. Munoz, B.; Ramila, A.; Perez-Pariente, J.; Diaz, I.; Regi, M. V., *Chem. Mater.*, 2003, **15**, 500.

43. Nayak, S.; Lee, H.; Chmielewski, J.; Lyon, L.A., *J. Am. Chem. Soc.*,2004, **126**, 10258.

44. Rosenholm, J.M.; Meinander, A.; Peuhu, E.; Niemi, R.; Eriksson, J.E.; Sahlgren, C.; Linden, M., *ACS Nano*, 2009, **3**, 197.

45. Brandon-Peppas, L.; Blanchette, J.O., *Adv. Drug. Deliv. Rev*., 2004, **56**, 1649.

46. Ward, C. M.; Acheson, N.; Seymour, L. W., *J. Drug Target*, 2000, **8**, 119.

47. Low, P. S.; Henne, W. A.; Doorneweerd, D. D., *Acc. Chem. Res*., 2008, **41**, 120.

48. Lu, Y.; Low, P.S., *Adv. Drug. Deliv. Rev.*, 2002, **54**, 675.

49. Sudimack, J.; Lee, R. J., *Adv. Drug. Deliv. Rev*., 2000, **41**, 147.

50. Zhang, X.; Meng, L.; Lu, Q.; Fei, Z.; Dyson, P.J., *Biomaterials*, 2009, **30**, 6041.

51. Liaw, J.; Taylor, J.; Goh, V., *Radiotherapy in Practice-Imaging*, 2010, **4**, 5.

52. Shen, G.; Mao, H.K., *Reports on Progress in Physics*, 2016, **80**, 16.

53. Zhao, W.; Li, Y.; Yang, S.; Chen, Y.; Zheng, J.; Liu, C.; Qing, Z.; Li, J.; Yang, R., *Anal. Chem.*, 2016, **88**, 4833.

54. Padmanabhan, P.; Kumar, A.; Kumar, S.; Chaudhary, R.K.; Gulyás, B., *Acta Biomater*., 2016, **41**, 1.

55. Gu, J.; Fan, W.; Shimojima, A.; Okubo, T., *Small*, 2007, **3**, 1740.

56. Pasqua, L.; Testa, F.; Aiello, R.; Cundari, S.; Nagy, J.B., *Micropoprous Mesoporous Mater.*2007, **103**, 166.

57. Schwartzberg, A. M.; Olson, T.Y.; Talley, C.E.; Zhang, J.Z., *J. Phys. Chem. B*, 2006, **110**, 19935.

58. El-Sayed, I.H.; Huang, X.; El-Sayed, M.A., *Nano Lett.* 2005, **5**, 829.

59. Huang, X.; El-Sayed, I.H.; Qian, W.; El-Sayed, M.A., *J. Am. Chem. Soc.*, 2006, **128**, 2115.

60. Diagaradjane, P.; Shetty, A.; Wang, J.C.; Elliott, A.M.; Schwartz, J.; Shentu, S.; Park, H.C.; Deorukhkar, A.; Stafford, R.J.; Cho, S.H.; Tunnell, J.W.; Hazle, J.D.; Krishnan, S. *Nano Lett.*,2008, **8**,1492.

61. Jiang, Y.; Fei, W.; Cen, X.; Tang, Y.; Liang, X., *Curr. Cancer Drug Ta.*, 2015, **15**, 406.

62. Athar, M.; Das, A.J., *Adv. Mater. Rev*, 2014, **1**, 25.

63. Sardan, M.; Ozkan, A.D.; Zengin, A.; Tekinay, A.B.; Guler, M.O., *Therapeutic Nanomaterials*, 2016, **6**, 197.

64. Chen, N.T.; Tang, K.C.; Chung, M.F.; Cheng, S.H.; Huang, C.M.; Chu, C.H.; Chou, P.T.; Souris, J.S.; Chen, C.T.; Mou, C.Y.; Lo, L.W., *Theranostics*, 2014, **4**, 798.

65. Lal, S.; Clare, S. E.; Halas, N. J., *Acc. Chem. Res.* 2008, **41**, 1842.

66. Gad, S.C.; Sharp, K.L.; Montgomery, C.; Payne, J.D.; Goodrich, G.P., *Int. J. Toxicol*., 2012, **31**, 584.

67. Cole, J.R.; Mirin, N.A.; Knight, M.W.; Goodrich, G.P.; Halas, N.J., *J. Phys. Chem. C*, 2009, **113**, 12090.

68. Barenholz, Y.C., *J. Control. Release*, 2012, **160**, 117.

69. (a) Rosenholm, J.M.; Mamaeva, V.; Sahlgren, C.; Lindén, M., *Nanomedicine*, 2012, **7**, 111, (b) Bobo, D.; Robinson, K. J.; Islam, J.; Thurecht, K. J.; Corrie, S. R.; *Pharm Res*, 2016, **33**, 2373-2387.

70. Meirow, D.; Nugent, D., *Human reproduction update*, 2001, **7**, 535.

71. Kawasaki, E.S.; Player, A., *Nanomedicine, Nanotechnology, Biology and Medicine*, 2005, **1**, 101.

72. Moghimi, S.M.; Hunter, A.C.; Murray, J.C., *The FASEB journal*, 2005, **19**, 311.

73. Liu, T.M.; Conde, J.; Lipiński, T.; Bednarkiewicz, A.; Huang, C.C., *NPG Asia Materials*, 2016, **8**, 295.

74. Yang, K.; Feng, L.; Shi, X.; Liu, Z., *Chem. Soc. Rev*., 2013, **42**, 530.

75. Sun, R.; Wang, W.; Wen, Y.; Zhang, X., *Nanomaterials*, 2015, **5**, 2019.

76. Dreaden, E.C.; Alkilany, A.M.; Huang, X.; Murphy, C.J.; El-Sayed, M.A., *Chem. Soc. Rev*., 2012, **41**, 2740.

77. Chen, M.; Kim, Y.N.; Lee, H.M.; Li, C.; Cho, S.O., *J. Phys. Chem. C*, 2008, **112**, 8870.

78. Resch-Genger, U.; Grabolle, M.; Cavaliere-Jaricot, S.; Nitschke, R.; Nann, T., *Nature methods*, 2008, **5**, 763.

79. Chen, Y.; Chen, H.; Shi, J., *Adv. Mater*., 2013, **25**, 3144.

80. Chen, T.; Yang, N.; Fu, J. *Chem. Commun*. 2013, **49**, 6555.

81. Song, N.; Yang, Y.W., *Chem. Soc. Rev*., 2015, **44**, 3474.

82. Du, L.; Liao, S.; Khatib, H.A.; Stoddart, J.F.; Zink, J.I., *J. Am. Chem. Soc*. 2009, **131**, 15136.

83. Zhao, Y.L.; Li, Z.; Kabehie, S.; Botros, Y.Y.; Stoddart, J.F.; Zink, J.I., *J. Am. Chem. Soc.* 2010, **132**, 13016.

84. Vallet-Regi, M; Rámila, A.; del Real, R. P.; Pérez-Pariente, J., *Chem Mater*, 2001, **13**, 308.

85. Mal, N. K.; Fujiwara, M.; Tanaka, Y., *Nature*, 2003, **421**, 350.

86. Hernandez, R.; Tseng, H.R.; Wong, J.W.; Stoddart, J.F.; Zink, J.I., *J. Am. Chem. Soc.* 2004, **126**, 3370.

87. Park, C.; Oh, K.; Lee, S.C.; Kim, C., *Angew. Chem. Int. Ed.*, 2007, **46**, 1455.

88. Angelos, S.; Yang, Y.-W.; Patel, K.; Stoddart, J. F.; Zink, J. I., *Angew. Chem., Int. Ed*., 2008, **47**, 2222.

89. Li, Z.; Nyalosaso, J. L.; Hwang, A. A.; Ferris, D. P.; Yang, S.; Derrien, G.; Charnay, C.; Durand, J.-O.; Zink, J. I., *J. Phys. Chem. C*, 2011, **115**, 19496.

90. (a) Ambrogio, M. W.; Thomas, C. R.; Zhao, Y.-L.; Zink, J. I.; Stoddart, J. F., *Acc. Chem. Res.*, 2011, **44**, 903, (b) Xu, Z.; Liu, S.; Kang, Y.; Wang, M., *Nanoscale*, 2015, **7**, 5859.

91. Prasad, R.; Aiyer, S.; Chauhan, D. S.; Srivastava, R.; Selvaraj, K., *Nanoscale*, 2016, **8**, 4537.

92. Zhou, L.; Li, Z. H.; Liu, Z. ; Ren, J. S.; Qu, X. G., *Langmuir*, 2013, **29**, 6396.

93. Chen, T.; Yu, H.; Yang, N.; Wang, M.; Dinga C.; Fu, J., *J. Mater. Chem. B*, 2014, **2**, 4979.

94. Lai, C.Y.; Trewyn, B.G.; Jeftinija, D.M.; Jeftinija, K.; Xu, S.; Jeftinija, S.; Lin, V.S.Y. A, *J. Am. Chem. Soc*,. 2003, **125**, 4451.

95. Giri, S.; Trewyn, B.G.; Stellmaker, M.P.; Lin, V.S. *Angew. Chem. Int. Ed*., 2005, **44**, 5038.

96. Nguyen, T. D.; Tseng, H.-R.; Celestre, P. C.; Flood, A. H.; Liu, Y., Stoddart, J. F.; Zink, J. I., *Proc. Natl. Acad. Sci. USA.*, 2005, **102**, 10029.

97. Liu, R.; Zhao, X.; Wu, T.; Feng, P., *J. Am. Chem. Soc*,. 2008, **130**, 14418.

98. Zhu, C.L.; Song, X.Y.; Zhou, W.H.; Yang, H.H.; Wen, Y.H.; Wang, X.R. *J. Mater. Chem.* 2009, **19**, 7765.

99. Cui, Y.; Dong, H.; Cai, X.; Wang, D.; Li, Y. *ACS Appl. Mater. Interface*, 2012, **4**, 3177.

100. Mal, N.K.; Fujiwara, M.; Tanaka, Y., *Nature*, 2003, **421**, 350.

101. Ferris, D.P.; Zhao, Y.L.; Khashab, N.M.; Khatib, H.A.; Stoddart, J.F.; Zink, J.I., *J. Am. Chem. Soc.* 2009, **131**, 1686.

102. Mei, X.; Yang, S.; Chen, D.; Li, N.; Li, H.; Xu, Q.; Ge, J.; Lu, J., *Chem. Commun*., 2012, **48**, 10010.

103. Li, H.; Tan, L.-L.; Jia, P.; Li, Q.-L.; Sun, Y.-L.; Zhang, J.; Ning, Y.-Q.; Yu, J.; Yang, Y.-W., *Chem. Sci*., 2014, **5**, 2804.

104. Liu, J.; Bu, W.; Pan, L.; Shi, J., *Angew. Chem., Int. Ed.*, 2013, **52**, 4375.

105. Croissant, J.; Zink, J. I., *J. Am. Chem. Soc*., 2012, **134**, 7628.

106. Li, Q.-L.; Wang, L.; Qiu, X.-L.; Sun, Y.-L.; Wang, P.-X.; Liu, Y.; Li, F.; Qi, A.-D.; Gao, H.; Yang, Y.-W., *Polym. Chem*., 2014, **5**, 3389.

107. Katiyar, S.K.; Matsui, M.S.; Mukhtar, H., *Photochemistry and Photobiology*, 2000, **72**, 788.

108. Cui, S.; Yin, D.; Chen, Y.; Di, Y.; Chen, H.; Ma, Y.; Achilefu, S.; Gu, Y., *ACS nano*, 2012, 7, 676.

109. Fu, Q.; Rao, G.R.; Ista, L.K.; Wu, Y.; Andrzejewski, B.P.; Sklar, L.A.; Ward, TL.; López, G.P. *Adv. Mater*. 2003, **15**, 1262.

110. Liu, C.; Guo, J.; Yang, W.; Hu, J.; Wang, C.; Fu, S., *J. Mater. Chem*., 2009, **19**, 4764.

111. You, Y.Z.; Kalebaila, K.K.; Brock, S.L. *Chem. Mater*. 2008, **20**, 3354.

112. Hu, X.; Hao, X.; Wu, Y.; Zhang, J.; Zhang, X.; Wang, P.C.; Zou, G.; Liang, X.J., *J. Mater. Chem. B.*, 2013, **1**, 1109.

113. Baeza, A.; Ruiz-Molina, D.; Vallet-Regí, M., *Expert Opin. Drug Deliv*, 2016, 14.

Chapter II

Biocompatible plasmonic gold nanorods (GNRs) for cancer theranostics

Various shapes of gold nanoparticles (GNPs) especially gold nanorods (GNRs) are widely used for biomedical applications such as contrast imaging, bio-sensing, photothermal therapy etc. on account of high atomic number of gold, tunable surface plasmon property and photothermal efficiency these rods. They also exhibit superior optical and physical properties making them efficient in both diagnostics and therapeutics for cancer theranostics. However, cetyltrimethyl ammonium bromide (CTAB, a structure directing agent for GNRs) stabilized GNRs are not recommended for biomedical applications due to the toxicity of CTAB. Hence, there is a demand to enhance the biocompatibility of these GNRs through CTAB substitution with biocompatible molecules. The replacement of CTAB layer with biocompatible lipid bilayer on GNRs surfaces is reported in this chapter. The designed biocompatible gold nanorods are studied for multifunctional cancer theranostics (diagnostics and therapeutics) such as contrast agent for X-ray computed tomography imaging (X-ray CT) and NIR responsive *in vitro* plasmonic photothermal therapy especially for cancer.

A part of the work presented in this chapter is communicated for publication.

2.1 Introduction

Since last few years, various shapes of Gold NanoParticles (GNPs) are used as contrast agents for tumor diagnosis that is because of their high atomic number and X-ray absorption coefficient.[1,2] GNPs are known for varying chemical, optical and electronic properties as a function of their aspect ratio (AR).[1-5] Particularly, Gold Nano Rods (GNRs) are of interest for cancer theranostics applications (imaging and therapeutic) due to their localized surface plasmon resonance (LSPR), X-ray absorption coefficient and stability in physiological environment. To fine-tune the aspect ratio of GNRs, several synthesis routes have been used in recent years.[1] Widely used method, viz., seed-mediated growth process using cetyltrimethylammonium bromide (CTAB) surfactant and silver nitrate is known to produce high yield of gold nano rods.[1,6, 7] Addition of silver nitrate ($AgNO_3$) helps the growth of gold particles from seeds and control their aspect ratio.[7] On the other hand, the aspect ratio range from 1.5 to 5 of GNRs are routinely obtained by varying the amount of $AgNO_3$. The aspect ratio of the nanorods can also be controlled consistently by keeping the silver nitrate concentration constant and varying the amount of seed.[4] An important contribution towards understanding the role of both Ag^+ ions and the crystalline structure of the seeds was again provided by Li. The cationic trimethylammonium head moiety of CTAB bilayer tightly adsorbs on the gold surface via Br anions and thus these GNRs are able to maintain their aspect ratio due to the presence of silver ions and structure directing agent (CTAB surfactant).[1, 6-8] However, on account of CTAB toxicity these nanorods pose serious concern for medical diagnostics and therapeutic applications.[1, 9-11]

In order to enhance the biocompatibility of CTAB stabilized GNRs for medical applications, the surface modification of these GNRs is currently under exploration.[12]

Accordingly, several attempts to CTAB replace with various stabilizing agents viz. polyethylene glycol (PEG), thiolated-PEGs (PEG-SH), alkanethiols, phenylphosphine, various polymeric chains etc have been reported.[1, 11, 13-19] However, partial removal of CTAB, poor control on aspect ratio, low dispersion ability, stability, easy aggregation with low biocompatibility is noticed in such attempts.[13] Complete removal of CTAB from nanorods surface without losing their aspect ratio and leaching of silver ion during surface modification with various biomolecules is still challenging though remaining as a key bottleneck for theranostics applications.[1, 13, 20-23] This requires a deep understanding of the surface chemistry of GNRs at nanoscopic level.[1, 23-31]

The primary aim of this chapter is to achieve a complete replacement of CTAB bilayer with DPPC lipid bilayer on GNRs surface without losing its aspect ratio and prevent leaching of silver ions. The main task to follow this is to understand the biocompatibility, photothermal efficiency and stability of GNRs after surface modification and to verify its ability usage for tumor diagnosis (imaging) and NIR responsive laser therapy. Previously, the surface modification of GNRs with phospholipid bilayers has been attempted by few groups.[13, 32-35] However with issues such as the poor stability in aspect ratio, poor biocompatibility and high aggregation which are attributed to long reaction time, lack of enough lipid concentration and uncontrolled equilibrium rate between CTAB and lipid bilayer during the course of CTAB replacement.[1, 13, 32] Moreover, the cancer theranostics applications and NIR photothermal performance of lipid modified GNRs are not attempted so far.

This chapter deals with the details of how to achieve a complete replacement of CTAB with a closer understanding of the surface chemistry of GNRs during such modification.

Further, high biocompatibility, *in vivo* tumor diagnosis, specific bio-distribution of lipid modified GNRs in animal body and *in vitro* NIR responsive plasmonic photothermal therapy for cancer cell lines are also presented here. It may be noted that these studies using lipid modified GNRs are being reported for the first time.

Interestingly our studies indicated that a single and minimum dose of such lipid modified GNRs exhibits promising specific tumor targeting ability with good radiodensity and a better photothermal performance. To the best of our knowledge, this is a first report where (1) the complete CTAB replacement by dipalmitoylphosphatidylcholine (DPPC) lipid bilayer has been achieved without leaching silver ions and losing GNRs aspect ratio, (2) high biocompatibility and radiodensity of surface modified GNRs is observed, (3) specific *in vivo* tumor targeting and diagnosis of the same and (4) *in vitro* NIR photothermal therapy with good thermal efficiency are achieved. Scheme 2.1 and 2.2. demonstrate the replacement of CTAB bilayer by lipid bilayer and its surface chemistry.

2.2 Experimental Details

2.2.1 Materials

Millipore/Milli-Q water (MPW) is used in all experiments and to prepare all buffer solutions. All the chemicals are of analytical grade and used as-received without any further purification, unless otherwise described. N-cetyltrimethylammonium bromides (CTAB, 99 %), sodium borohydride ($NaBH_4$, 99 %), ascorbic acid (AA, 99.5 %), silver nitrate ($AgNO_3$, 99.9 %) are purchased from Merck. Tetrachloroauric acid ($HAuCl_4.3H_2O$, 99.9 %), Propidium iodide (PI), N, N-(3-Dimethylaminopropyl)-N′ ethylcarbodiimide hydrochloride (EDC, 98 %), N-hydroxysuccinimide (NHS, 99.8 %), polyethylene glycol (PEG, 98 %), folic acid (FA, 97 %) and (3-(4, 5-dimethylthiazol-2-yl)-2, 5-

diphenyltetrazolium bromide-MTT) are purchased from Sigma-Aldrich. Dipalmitoylphosphatidylcholine phospholipids are purchased from Avanti Polar Lipids (Alabaster, AL). Dulbecco's modified Eagle's medium (DMEM), antibiotic-antimycotic solution and fetal bovine serum (FBS) are procured from HiMedia Laboratories Pvt. Ltd, India. It may be noted that the abbreviation of each chemical is provided in parenthesis after each name and these abbreviated forms will be used in remaining text. All glasswares are rinsed with double distilled water before using them for synthesis and applications.

2.2.2 Characterization techniques

The size and morphology of different nanoparticles are examined using transmission electron microscopy (TEM instrument FEI Tecnai T-20, operated at 200 kV). Elemental analysis and mapping are done by energy-dispersive X-ray analysis (EDAX) as performed on TEM system (TEM instrument FEI Tecnai T-20, operated at 200 kV). CTAB and lipid stabilized gold nanorods in an aqueous medium are characterized by UV-Vis-NIR spectrophotometer dual beam spectrometer (Jasco-V570) operated at a wavelength resolution of 2 nm. Absorption spectra are recorded by using quartz cell of 1 mm path length. Fourier transform infrared (FT-IR) spectra are recorded by using Perkin-Elmer FT-IR spectrum GX instrument. All photothermal transduction experiments and photothermal performance of nanohybrids are carried out using 750 nm continuous wave NIR laser source (SDL-750-LM-1000T) with power density of 1 W. Fluorescence microscopic images during i*n vitro* studies are examined by fluorescence microscope (Axio observer. Z1). All CT scans are performed on a clinical CT scanner (Toshiba 64 slice, 0.5 mm slice per rotation) operated at 120 kV, 50 mA. The radiodensity in Hounsfield unit (HU) is measured by using RadiAnt DICOM Viewer software (V3.10ER009).[19]

2.2.3 Synthesis of gold nanorods (GNRs)

Gold nanorods (GNRs) are prepared according to seed-mediated growth procedure.[7] The preparation of Au seed solution is carried out by adding 2.5 mL of 0.2 M CTAB solution with 1.5 mL of 1.0 mM $HAuCl_4$ solution. 0.6 mL of ice cold 0.01 M $NaBH_4$ is added to the seed solution which results in the formation of brownish-yellow solution. Vigorous stirring of the solution is continued for 2 min. After 2 minutes the stirred solution is kept at 25 °C. The growth solution for nanorods is prepared by adding additional 50 mL of 0.2 M CTAB solution to 2.8 mL of 0.004 M $AgNO_3$ solution. To the above solution, 5 mL of 15 mM $HAuCl_4$ solution and 1.25 mL of 0.08 M ascorbic acid are added and mixed gently. After that 1 mL of seed solution is added to the whole growth solution at 27-30 °C. The color of solution gradually changed to dark blue within 10-15 min. The temperature of the growth medium is kept with a temperature range of 27-30 °C throughout the procedure. The GNRs are collected after three cycles of centrifugation.

2.2.4 Replacement of CTAB bilayer with DPPC lipid bilayer (GNRs-Lipid)

Alongside, a DPPC lipid bilayer solution is prepared by following procedure. In a round bottom flask, 100 mg DPPC lipid is dissolved in chloroform (6 mL) and the organic solvent is evaporated using a rotary evaporator at 40 °C temperature. The resulting lipid film is hydrated in PBS solution (10 mL, 7.4 pH) overnight. The unilamellar lipid assemblies are obtained by sonicating the hydrated lipid solution. To replace the CTAB surfactant from GNRs surface, 5-15 mM concentration range of DPPC lipid (1 mL) solution is mixed with 1 mL of CTAB stabilized GNRs for a period of 3-12 h under gentle stirring (100 rpm) at room temperature. A 10 mM concentration of lipid bilayer and 3 h of reaction time are optimal to complete replacement of the CTAB bilayer by DPPC bilayer.

Such surface modified GNRs are collected via centrifugation and stored at 20 °C temperature for further studies.

2.2.5 Functionalization with folic acid as a targeting ligand

Folic acid (FA) is used as a targeting ligand for testing the cancer cells/tumor.[19] To attach the FA on exterior surface of GNRs-Lipid, the EDC/NHS (1 : 1 molar ratio)[33-37] activated folic acid (100 mg in 20 mL PBS) is anchored with Poly(ethylene glycol) 2-aminoethyl ether acetic acid (1 mg/mL) using 6 h coupling reacting reaction in dark condition at room temperature (37 °C). 1 mL of PEG-FA[38] (1 mg/mL) is mixed with same volume of lipid modified GNRs (1 mL) under gentle stirring (100 rpm) at room temperature. The PEG-FA functionalized GNRs-Lipid is collected via centrifugation and use for further applications.

2.2.6 Photothermal performance of surface modified GNRs

Various concentrations (50-1000 µg/mL) of designed plasmonic GNRs in PBS (pH 7.4) are made. Aliquots (200 µL) are deposited into 96 well plates. The initial temperature is stabilized at 37 °C in water bath. Wells are illuminated with 750 nm continuous wave NIR laser source with power density 1 W for 5 minutes and the temperature variation with respect to time is recorded.

2.2.7 Contrast performance (radiodensity/Hounsfield unit measurement)

To evaluate the contrast ability, the CT scans of surface modified GNRs (GNRs-Lipid) samples and FA functionalized GNRs-Lipid samples injected into mice are carried out on a CT scanner operated at 120 kV and at 50 mA. All prepared solutions in plastic eppendrof are placed in CT scanning holder and then scans (materials as well as animals) are performed. The radiodensity is calculated in Hounsfield unit (HU) using following equation as measured by RadiAnt DICOM Viewer software[19] and following equation.

$$\text{Radiodensity (HU)} = \frac{\text{HU value of suspended nanohybrid- HU value of water}}{\text{HU value of water-HU value of air}} \quad \text{(eq. 2.1)}$$

2.3 Applications

2.3.1 Cell culture and *in vitro* biocompatibility study

To understand the biocompatibility and therapeutic efficiency of plasmonic nanorods before and after surface modification following procedure is followed L929 and 4T1 cell lines are earlier cultured in DMEM media supplemented with 10% FBS, 1 % penicillin and 1 % streptomycin, under 5 % CO_2 atmosphere at 37 ºC.

To check the biocompatibility of designed nanorods, L929 normal cells are seeded at density of 1×10^4 cells per well in 96 well plates and incubated for 24 h in 5 % CO_2 atmosphere at 37 ºC. After 24 h incubation, 200 µl of different concentration (10-1000 µg/mL dispersed in media) of CTAB stabilized GNRs, GNRs-Lipid and GNRs-Lipid-FA are added into the wells. Following 24 h, incubation wells are washed off with PBS and 20 µl of MTT dye is added. Formazan crystals formed after 4 h are dissolved by 200 µL of DMSO. Optical absorbance is recorded at 570 nm and 690 nm using microplate reader (Tecan Infinite 200 PRO). Percentage cell viability is calculated in reference to untreated cells (control).

2.3.2 Animals models and tumor growth

Animal protocols are approved by the Institutional Animal Ethical Committee (IAEC, SSBS/IAEC/05/2016 project). ~ 20 g female Balb/c mice are used in the current study. PBS suspended 1×10^4 4T1 breast cancer cells are injected subcutaneously into the flank of Balb/c mice.

2.3.3 *In vitro* targeted plasmonic photothermal therapeutic study

To understand the therapeutic efficiency of nanorods, 4T1 cancer cells are seeded into 96 well plates with a density of 2×10^4 cells/well and incubated for 24 h in 5 % CO_2 atmosphere at 37 ºC. After being rinsed with PBS, the cells are incubated with 200 µg/mL of designed nanorods for 4 h. After incubation the cells are washed with PBS for three times to get rid of all the unbound nanorods. This therapy test is divided into eight groups: (i) Group 1 is only cancer cells, (ii) group 2 is NIR light exposure on cells, (iii) group 3 is only GNRs-Lipid treated cells, (iv) group 4 is GNRs-Lipid treated cells under NIR exposure, (v) group 5 is GNRs-Lipid-FA treated cells and (vi) group 6 is GNRs-Lipid-FA treated cells under continuous NIR exposure (5 min. 750 nm) for targeted plasmonic photothermal therapy. (vii and viii) Group 7 and 8 indicate the therapeutic efficiency of pre-saturated folate receptor (FR) with free FA on cell membrane in the presence and absence of NIR light. Cell viability is determined by the addition of MTT (20 µL, 1 mg/mL dye in sterile PBS). The plate is incubated for an additional 4 h at 37 °C and 5 % CO_2, allowing viable cells to convert the blue solution into pink dye. Formazan crystals are dissolved by adding 100 µL DMSO to each well. Optical absorbance is recorded at 570 nm using microplate reader (Tecan Infinite 200 PRO). Percentage cell viabilities are calculated by following equation.

$$\% \text{ Cell viability} = \frac{\text{OD (treated)-OD (blank)}}{\text{OD (negative control)-OD (blank)}} \times 100 \qquad \text{(eq. 2.2)}$$

In addition, to check the impact of targeted plasmonic photothermal therapy on 4T1 breast cancer cells, the LIVE-DEAD Kit is used to visualize the dead cells (propidium iodide, PI

staining). Breast cancer cells are cultured for 24 h in 96 well plates at a density of 2×10^4 cells per well. After 24 h of incubation, 100 µl of nanorods are added into each wells and cultured for further 4 h. Moreover, the corresponding wells are exposed with 750 NIR laser (1 W) for 5 min. Following that, the media is replaced with fresh media and cultured further for 24 h. After washing, cells are stained with propidium iodide and the dead cells are observed in red color (propidium iodide, PI) as seen in the fluorescence microscopic images.

2.3.4 Lipid modified GNRs as a biocompatible contrast agent for *in vivo* tumor diagnosis

A clinical voltage of 120 kV at 50 mA has been used to understand the contrast ability of surface modified GNRs (FA functionalized GNRs-Lipid, GNRs-Lipid-FA) using CT scanner. For *in vivo* tumor diagnosis and specific bio-distribution, a minimum single dose (10 mg/kg) of FA attached GNRs-Lipid as a contrast agent is subcutaneously injected in 4T1 tumor bearing female Balb/c mice. After the injection, the CT scans are performed on anaesthetized mice at various time points (0.25-24 h) and compared with pre-contrast injected mice (control mice without injection of FA attached GNRs-Lipid).

2.4 Results and Discussion

2.4.1 Lipid modified GNRs as a biocompatible multifunctional cancer theranostics

Replacement of toxic cetyltrimethylammonium bromide (CTAB) bilayer[23-31, 39-41] from GNRs surface is critical (Scheme 2.1). The exchange of CTAB bilayer with lipid bilayer is one of the most effective ways to enhance the biocompatibility and yet maintain the optical property of GNRs in cellular environment. A simple recipe for lipid bilayer decoration on GNRs surface (Scheme 2.2) and its usages for multifunctional cancer theranostics are

discussed in this chapter. The localized *in vivo* tumor diagnosis and *in vitro* NIR laser therapy by minimal dose of theranostic agent, viz., GNRs-Lipid-FA is studied and reported for the first time.

TEM images of CTAB stabilized GNRs with average length of ~33 nm and average width of ~10 nm (histogram is in inset) are shown in Figure 2.1 (TEM images a, a1).

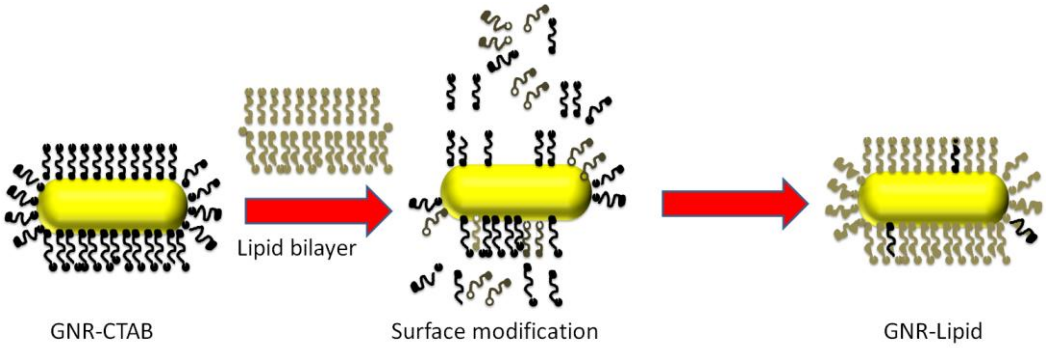

Scheme 2.1. *CTAB replacement with lipid bilayer on GNR surface.*

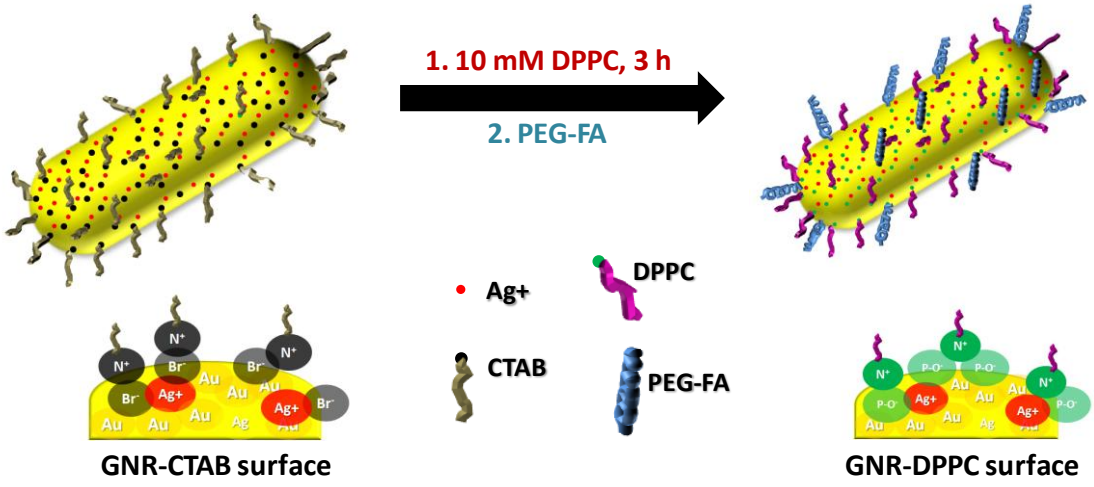

Scheme 2.2. *Surface chemistry of GNR before and after surface modification with DPPC lipid bilayer.*

Surface modified GNRs are obtained with maintained aspect ratio (AR) and comparable with CTAB stabilized GNRs (AR, histogram is in inset). Such surface modified GNRs show average length of ~ 41 nm and average width of ~12 nm (Figure 2.1 b, b1) which are slightly higher than the CTAB stabilized GNRs. It may be noted that the slight enhancement in AR after surface modification is due to the thickness of lipid bilayer. The lattice fringe gap on the GNRs surface is clearly seen from high resolution TEM images. 0.237 nm fringe gap is observed before CTAB replacement from the GNRs surface whereas diminished fringes with reduced gap (0.213 nm) are noticed after surface modification with DPPC lipid bilayer confirming the covering of GNRs surface with thick lipid bilayer (Figure 2.2).

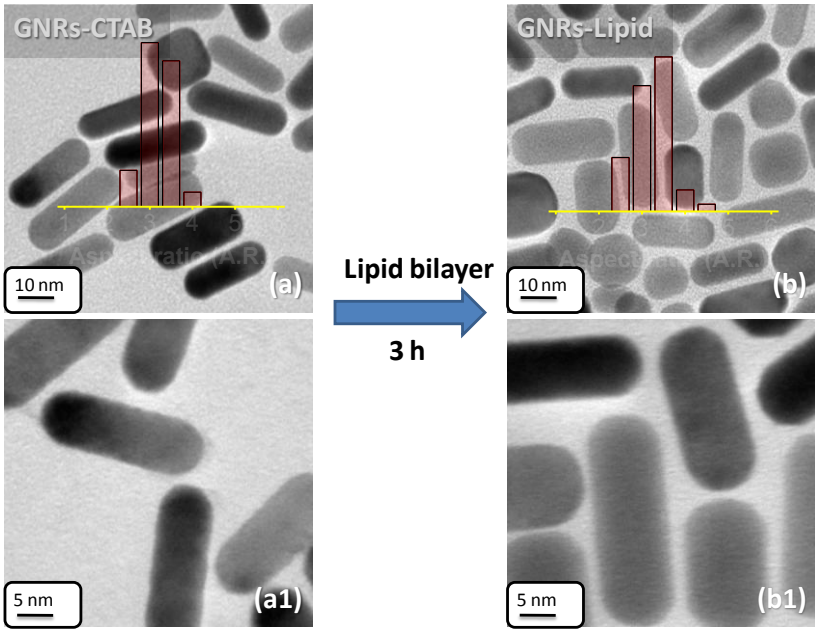

Figure 2.1. *TEM images of as prepared GNRs using CTAB surfactant (a, a1) and surface modified GNRs with DPPC lipid bilayer (b, b1). Their aspect ratio (AR) histograms are in inset.*

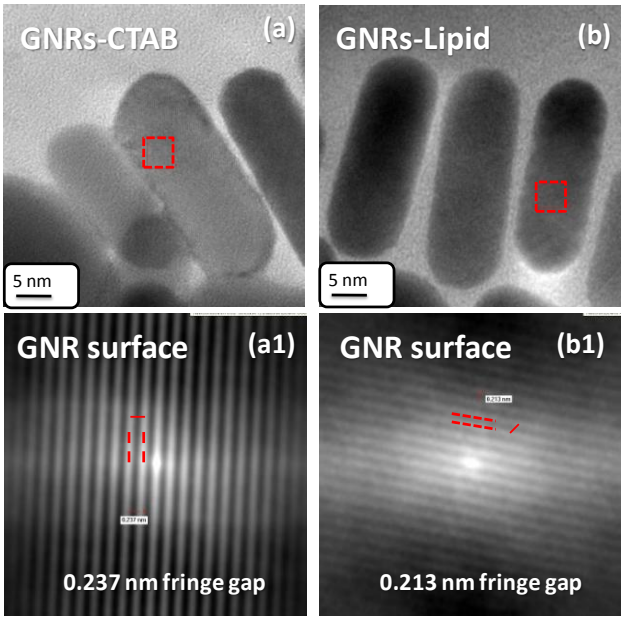

Figure 2.2. *TEM images of (a, a1) GNRs-CTAB and (b, b1) after GNRs-DPPC lipid bilayer (GNR-Lipid) with their lattice fringe gap observation.*

In order to get the above discussed biocompatible plasmonic nanorods, two significant parameters play crucial role viz., (i) concentration of DPPC lipid and (ii) reaction time as discussed below.

2.4.2 Effect of lipid concentration on the CTAB replacement

DPPC lipid concentration is observed to be the first parameter to obtain the biocompatible nanorods (Figure 2.3 a-d). Firstly, the UV-Vis-NIR absorbance spectrum of CTAB stabilized GNRs shows two clear absorption bands viz., 520 nm (transverse) and 690 nm (longitudinal). While replacing the CTAB bilayer from GNRs surface, a lipid concentration range of 5-15 mM (Figure 2.3 b-d) is experimented. Based on our observation it is understood lower concentration (5 mM) of lipid is not enough to replace the CTAB from GNRs surface due to strong binding between CTAB bilayer and gold atoms on GNRs surface. We believe that the red shift and peak broadening[42] (520 to 521

nm for transverse and 690 to 732 nm for longitudinal) in absorption bands at lower lipid concentrations is due to aggregated nanorods (TEM image in Figure 2.3).

On the other hand, at high lipid concentrations (15 mM), GNRs mostly lose their AR due to fast and uncontrolled equilibration[13] between the CTAB and lipid bilayer. Faster equilibration between both CTAB and lipid bilayer on GNRs surface during surfactant exchange process, reshapes the GNRs promoting the aggregation of nanoparticles and thereby affecting their local surface plasmon resonance (LSPR) and optical properties as demonstrated in Figure 2.3. Accordingly, the absorbance spectrum of nanorods at 15 mM lipid concentration shows blue shift in transverse band (520 to 511 nm) and red shift with peak broadening in longitudinal band (690 to 735 nm).

At moderate concentrations of DPPC lipid (10 mM) the surface modified GNRs maintain the AR and optical property. The obtained GNRs are observed to have uniform dispersion and slight enhancement in AR, ~ 3.2 to 3.5 due to the presence of thick lipid bilayer on GNRs surface (TEM image Figure 2.3) indicating the successful replacement of CTAB bilayer by lipid bilayer. The UV-Vis-NIR absorbance spectrum of these nanorods show two clear absorption bands viz., 522 nm (transverse) and 750 nm (longitudinal) with red shift. Thus, 10 mM concentration of lipid is found to be an optimal concentration for CTAB replacement from GNRs surface.

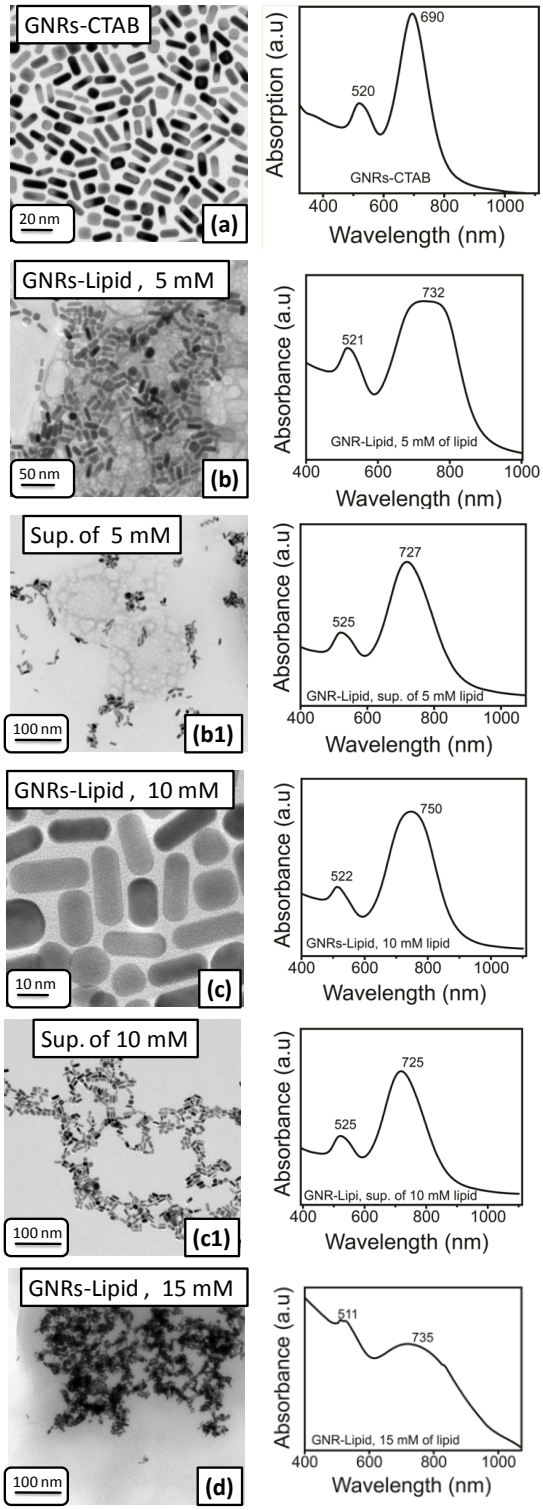

Figure 2.3. *TEM images and respective absorbance spectrum of gold nanorods (a) before CTAB replacement and (b-d) after surface modification with DPPC lipid at various concentrations (5-15 mM).*

2.4.3 Effect of reaction time on CTAB replacement

The equilibrium time between CTAB and DPPC lipid bilayer is another important parameter which determines the maintenance of GNRs AR (Figure 2.4 a-d). To replace the CTAB bilayer while maintaining the shape and size of GNRs, the reaction time of between 3 to 12 h is tested using 10 mM concentration of DPPC lipid under gentle stirring (100 rpm). The size and shape of GNRs after CTAB replacement is verified from electron microscopic images and their absorbance spectra at various reaction times. Results revealed that a longer reaction time of 6 and 12 h is not favorable for maintaining the AR due to fast equilibrium between CTAB and DPPC bilayer. We have understood that the longer reaction times result in aggregated nanorods with excess lipid mixture (TEM image in Figure 2.4 a-d). As a consequence, the optical property of GNRs is modified and following observations are made: (1) For a 6 h reaction time of lipid modification, nanorods show two absorption bands with red shift and peak broadening[42] (520 to 540 nm for transverse and 690 to 720 nm for longitudinal), (2) for 12 h reaction time the nanorods show two absorption bands with red shift and peak broadening (520 to 530 nm for transverse and 690 to 709 nm for longitudinal with peak diminishing).

In the case of a moderate 3 h reaction time, nanorods sustained their original uniform size and shape (Figure 2.4). This is attributed the possibly moderate reaction period that help to control exchange rate between CTAB and lipid bilayer on GNRs surface. Accordingly, UV-Vis absorbance spectrum of these nanorods shows two clear absorption bands with red shift in transverse band (520 to 522 nm) and longitudinal band (690 to 750 nm).

In conclusion, 10 mM concentration of DPPC lipid and 3 h of reaction time at ambient conditions are observed to be optimal reaction parameters for CTAB replacement from GNRs surface while maintaining their aspect ratio.

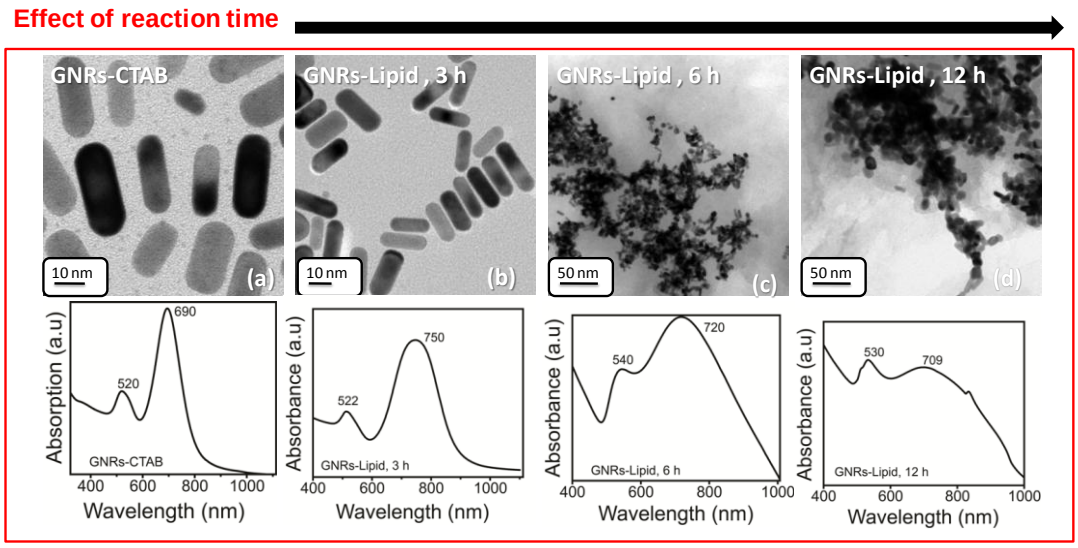

Figure 2.4. *TEM images of gold nanorods (a) before CTAB replacement and (b-d) after surface modification with DPPC lipid at various reaction time (3 to 12 h) and their respective absorbance spectrums.*

2.4.4 Characterization of lipid modified GNRs

The structural aspect of surface modified GNRs (Figure 2.5) is evaluated using various characterization techniques. The presence of DPPC lipid on GNRs surface is confirmed by spectroscopic and elemental analysis tests. The elemental analysis of gold nanorods before and after surface modification confirms the components of structure directing agents viz., CTAB and DPPC lipid (Figure 2.6 and 2.7).

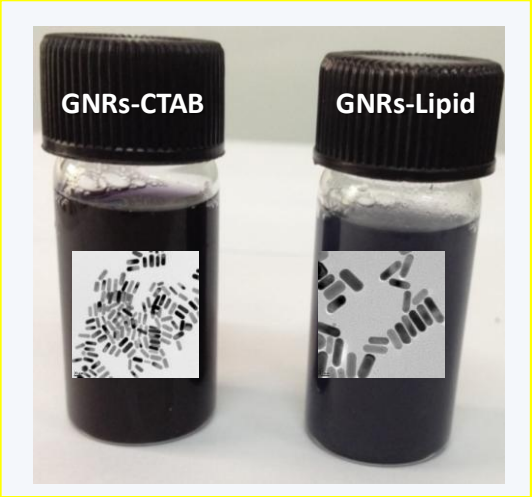

Figure 2.5. *Digital photographs of GNRs before (GNRs-CTAB) and after surface modification (GNRs-Lipid) with their corresponding TEM images (inset).*

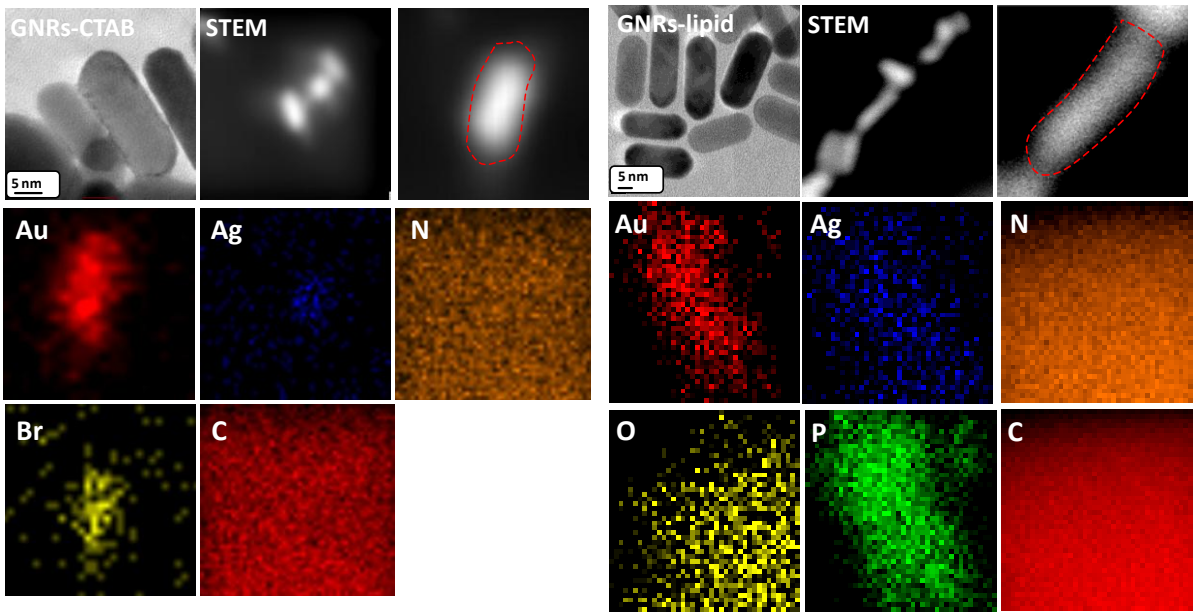

Figure 2.6. *Elemental analysis of gold nanorods before and after surface modification (GNRs-CTAB and GNRs-Lipid) and their TEM images.*

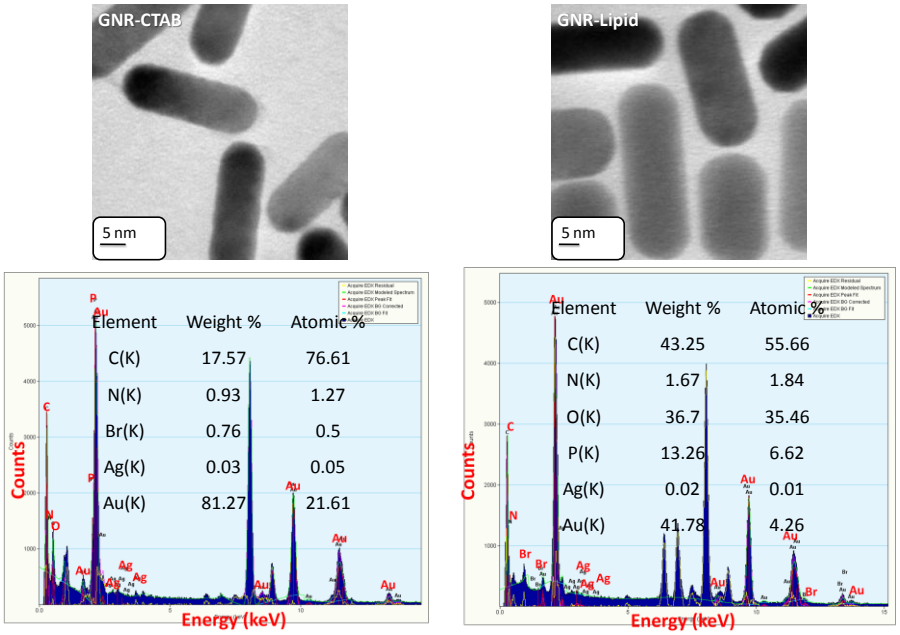

Figure 2.7. *Energy-dispersive X-ray analysis (EDAX) elemental analysis of gold nanorods before and after surface modification (GNRs-CTAB and GNRs-Lipid) and their TEM images.*

The elemental analysis of GNRs before and after surface modification is confirmed by elemental mapping (Figure 2.6) and EDAX analysis (Figure 2.7). CTAB stabilized GNRs indicates the presence of Au, Ag, C, N, Br whereas the surface modified GNRs show the existence of Au, Ag, C, N, O, P indicating the presence of DPPC lipid on GNRs surface. We have understood that diminished fringe gap of surface modified GNRs (see Figure 2.2) can corroborate the replacement of CTAB by lipid bilayer.

In addition, the surface modification of GNRs with DPPC and folic acid attachment is corroborated by FTIR (Figure 2.8 a). The O-H stretching vibrations (3430 cm^{-1}) and the C=O stretching vibrations (1690 cm^{-1}) confirm carboxyl groups of lipid molecules. Further, stretching vibrations of O-P-O is observed between 800-1200 cm^{-1} in FT-IR

spectra. Peak between 1500-1620 cm^{-1} corresponding to $-NH_2$ bending of the DPPC moiety that reveals the successful functionalization of GNRs. Peaks at 2830 and

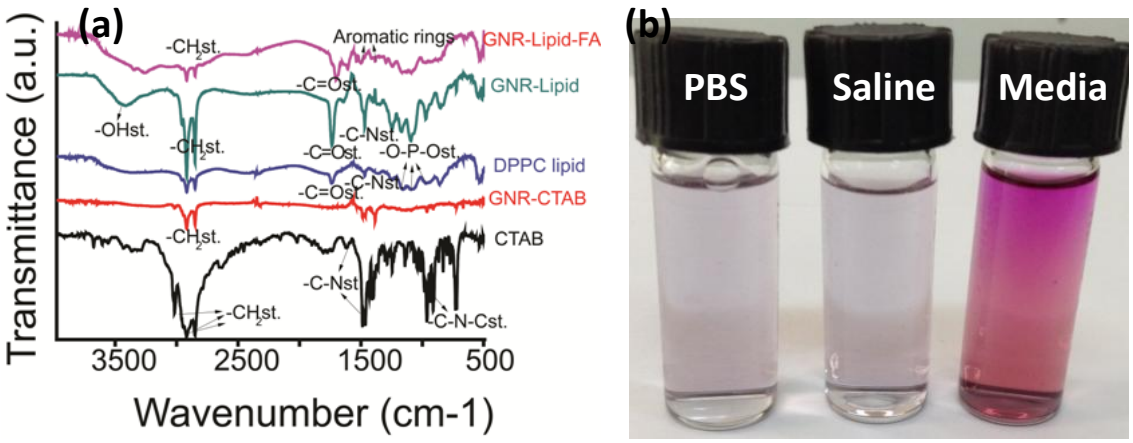

Figure 2.8. *(a) FTIR spectra of gold nanorods before and after surface modification and folic acid attachment, (b) dispersion ability of designed nanorods in various solvents viz., PBS, saline and culture media.*

2925 cm^{-1} corresponding to $-C-H_2$ stretching vibrations. In addition, the IR bands between 1400-1500 cm^{-1} indicate stretching vibrations of the aromatic rings of folic acid moieties.[19] Thus, the successful CTAB replacement is confirmed by elemental mapping, EDAX analysis and FTIR spectroscopy without losing AR and silver ions. Further the lipid modified GNRs show good dispersion ability in various aqueous solvents viz., PBS, saline and cell culture media (Figure 2.8 b).

2.4.5 Photothermal and contrast ability of GNRs

The photothermal transduction efficiency of designed nanorods is understood prior to its radiodensity and cytotoxicity tests. To check the photothermal performance of plasmonic nanorods, the photothermal heating experiments are carried out using 750 nm NIR laser source. The photothermal behavior of nanorods at different concentrations (50-1000

µg/mL) is evaluated by continuous exposure of NIR radiation (750 nm with 1 W power) for a period of 5 minutes. Prior to this, the initial temperature is stabilized at 37 °C in the water bath. The photothermal response constantly increases with the concentration of nanorods (Figure 2.9 a). A hyperthermia temperature (43 °C) is recorded on a NIR exposure for 5 minutes at lower concentration (50 µg/mL) of surface modified GNRs. On the other hand, the same temperature is recorded within 2 minutes of NIR exposure at a higher concentration of 1000 µg/mL. The temperature increases up to 46 °C for 1000 µg/mL concentration on 5 minutes of NIR irradiation. The results revealed that the designed nanorods are highly suitable for photothermal therapy.

These nanorods show good contrast ability (due to high atomic number of Au and its X-ray attenuation) which help to extract the 3D structure of tumor at high resolution. The contrast ability/radiodensity (Hounsfield unit, HU value) of nanorods is measured using RadiAnt DICOM Viewer. The radiodensity of gold (HU 60) is higher than that of Iodine (HU 23) and is shown in Figure 2.9 b.

2.4.6 *In vitro* biocompatibility and photothermal therapeutic study

In vitro biocompatibility study (MTT assay) of GNRs before and after CTAB replacement by lipid bilayer is carried out on normal cells (L929). The biocompatibility is also studied for folic acid attached GNRs-Lipid (Figure 2.9 c). In contrast, a drastic reduction in cell viability (~ 5 %) is observed for CTAB stabilized GNRs. More than 95 % cell viability is observed for GNRs-Lipid and GNRs-Lipid-FA even at maximum concentration (1000 µg/mL) demonstrating their significant biocompatibility. The enhanced biocompatibility of surface modified GNRs (GNRs-Lipid) attributed to the successful

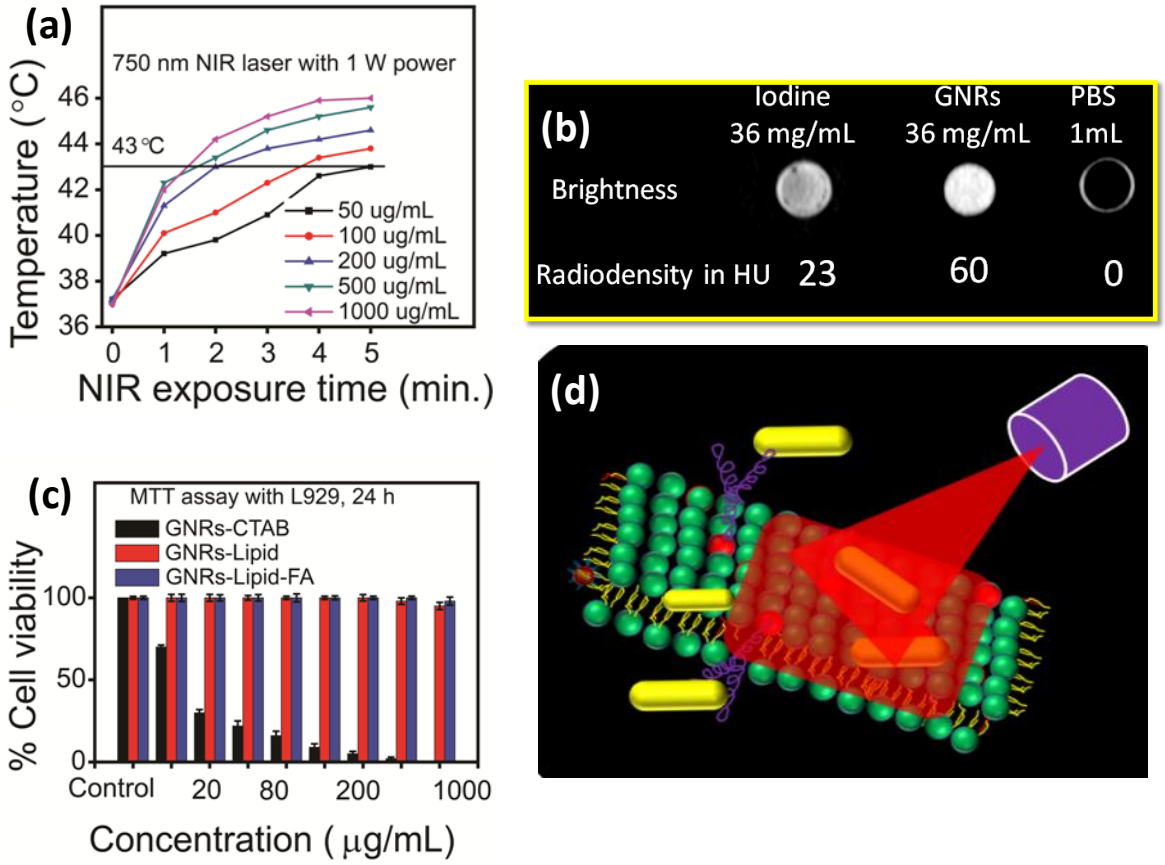

Figure 2.9. *(a) Concentration dependent photothetrmal transduction efficiency of designed nanorods, (b) contrast ability of nanorods and Iodine (today's contrast agent) with its TEM image and tumor location in mice body (inset), (c) MTT assay for CTAB stabilized GNRs (GNRs-CTAB), lipid modified GNRs (GNRs-Lipid) and folic acid attached GNRs-Lipid (GNRs-Lipid-FA) and (d) cartoon shows the plasmonic photothermal therapy on cancer cell under NIR exposure.*

replacement of CTAB of the GNRs surface in addition to the validations by spectroscopic and microscopic analysis (as presented earlier in the discussion about elemental analysis and mapping).

The plasmonic photothermal therapy of biocompatible nanorods is studied by testing them on cancer cell lines (4T1, Figure 2.9 d) under the exposure of NIR laser irradiation. It is observed that merely treating the 4T1 cancer cell lines with GNR-Lipid or GNR-Lipid-FA

does not cause cell death as almost 100 % cell viability is observed (Figure 2.10 a). This proves a phenomenal biocompatibility of GNRs due to surface modification by lipid and these by removing the cytotoxic CTAB as reported earlier.

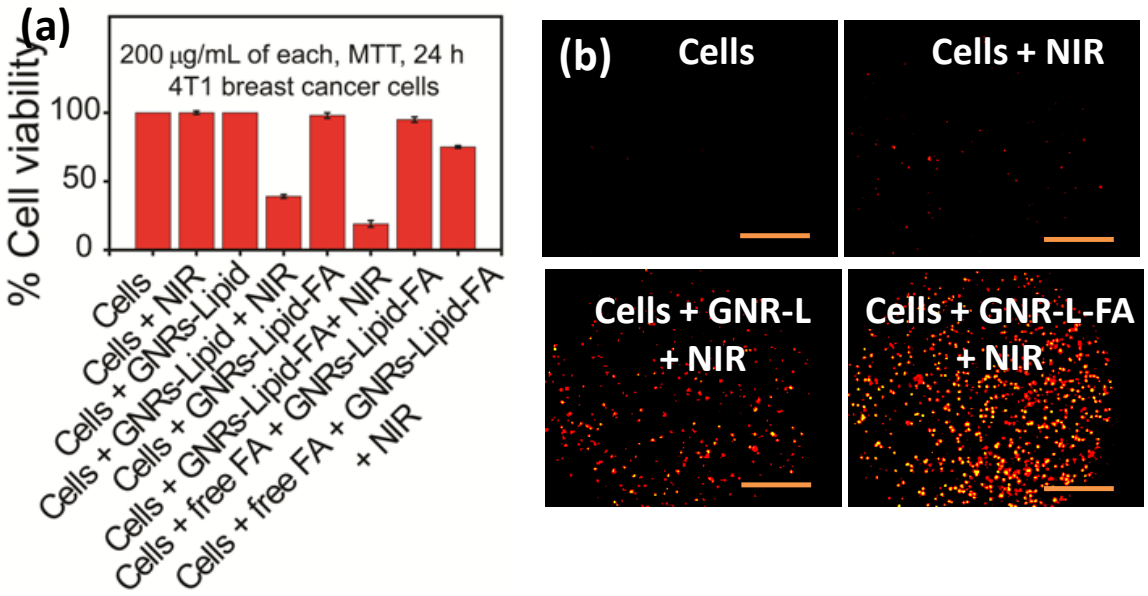

Figure 2.10. *Therapeutic efficiency of designed nanorods (a) % cell viability of breast cancer cells (4T1) that are treated with various formulations of designed nanorods and pre saturated folate receptors (FR) on cell membrane by free FA with and without NIR light exposure, (b) dead cells can be seen in fluorescence microscopy images of breast cancer cells (red, PI staining) scale bar is 150 µm.*

In case of cell treated GNR-Lipid and GNR-Lipid-FA (FA attached GNR-Lipid) under NIR exposure (photothermal therapy), the observed cell viabilities are 42 % and 15 %, respectively (Figure 2.10 a). These results demonstrate the damaging ability of the photothermal surface modified GNRs and that functionalized with targeting ligand, FA. The significant difference in between these viabilities clearly proves the added targeting ability to the system by functionalizing with FA. On the other hand, pre-saturated folate receptors (FR) with free FA show more than 80 % cell viability. This is attributed to the

fact that cancer cells are successfully pre-saturated with free FA and that this prevents the cellular uptake of FA attached nanorods. To observe the presence of dead cells, (4T1, Figure 2.10 b) after photothermal therapy, the nanorods treated cancer cells are stained with propidium iodide (PI red for dead cells). It is important to note that major cell death can be inflicted upon cancer cells just by successfully targeting them with a highly powerful photo responsive nano system such as GNRs. Secondly their earlier biocompatibility issues can be successfully addressed by modifying its toxic surface chemistry.

2.4.7 *In vivo* tumor diagnosis by computed tomography using lipid modified nanorods as targeted contrast agent

To check the targeting ability of FA functionalized nanorods and its ability to accumulate on cancer cells/tumor for better contrast, a minimum and single dose (10 mg/kg body weight) as a targeted contrast agent is subcutaneously injected in 4T1 tumor bearing female Balb/c mice and the CT scans are taken at various time point (0.25 to 24 h, Figure 2.11). Specific breast tumor location is observed through coronal and axial CT slices of mice body with a decent radiodensity (HU 27) within 0.25 hour post-injection of nanorods as contrast agent. The radiodensity on tumor site increases gradually from 27 to 117 HU with higher brightness and contrast with respect to time (0.25 h to 24 h) after post-injection of GNRs-Lipid-FA. However, the tumor location is difficult to identify in pre-injected mice (before injection of GNRs-Lipid-FA in mice).

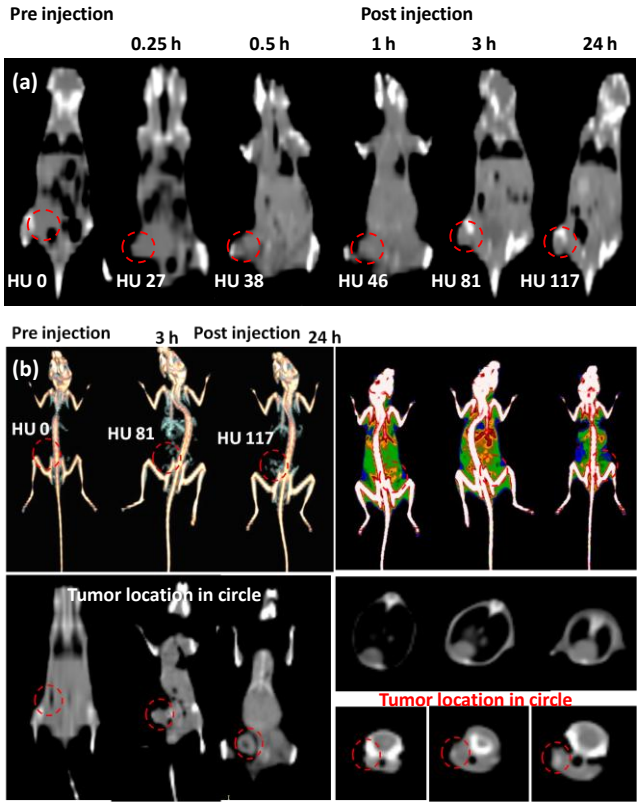

Figure 2.11. *Computed tomography images show (a) tumor location with radiodensity in mice body at various time point (0.25 to 24 h) after nanorods injection with compared to pre-injected mice, (b) radiodensity observation (3 and 24 h) at tumor site which is compared to pre-injected mice as a control and their coronal and axial images through DICOM viewer and K packs show the deep visualization of tumor in mice with enhanced radiodensity and brightness at tumor site.*

2.4.8 Influence of NIR on the morphology of designed nanorods

In the present study, the surface modified GNRs demonstrate their significant photothermal therapeutic effect on cancer cell lines due to their unique optical property. However, sustenance of their AR and thereby their plasmonic property during photothermal therapy course is another challenge for cancer theranostics. Hence, a set of photothermal transduction experiments are carried out in the present work. This is done at 200 µg/mL concentration of designed nanorods exposed for 5 minutes to NIR. After NIR

exposure, the morphological changes and optical property of these nanorods are understood using microscopic and spectroscopic techniques. Figure 2.12 a shows the TEM images of lipid modified GNRs before NIR exposure. The TEM images demonstrate a uniform distribution of AR maintained nanorods before NIR. Aggregated nanorods are noticed in the post NIR treated sample (Figure 2.12 b). These observations are corroborated by absorbance spectra. Two clear absorbance bands viz., 522 nm for transverse and 750 nm for longitudinal are noted for GNRs before NIR exposure (Figure 2.12 a1).

However, after NIR exposure, with a significant lose of intensity peak broadening and a red shift in both bands (transverse, 532 nm and longitudinal, 700 nm) is observed (Figure 2.12 b1). The AR loss and aggregation of nanorods is attributed to the instability of lipid bilayer (destabilized lipid bilayer assembly) on GNRs surface and the temperature raise under NIR exposure. This indirectly proves that CTAB replacement with lipid has not impacted its inherent plasmonic properties in turn their photothermal performance, which greatly improving its biocompatibility by suppressing the cytotoxicity due to CTAB.

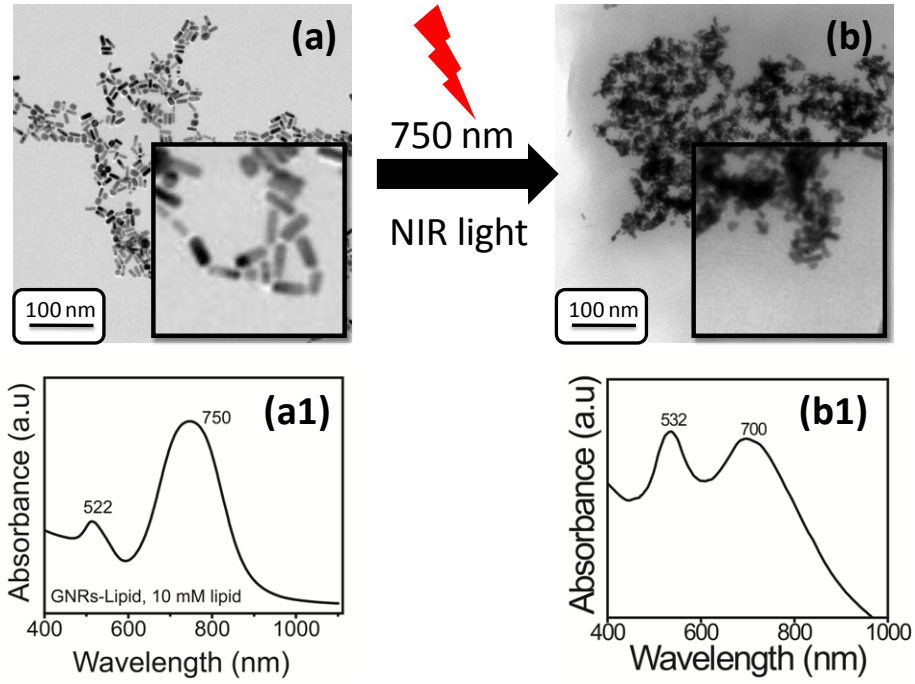

Figure 2.12. *The effect of NIR light on morphology and optical property of lipid modified nanorods (a, a1) show the TEM images and absorbance spectrum of uniform distributed nanorods before NIR exposure and (b, b1) show the TEM images and absorbance spectrum after NIR exposure and resulted in aggregated nanorods.*

2.5 Conclusion

In summary, this chapter systematically explains the procedure developed to replace the CTAB surfactant from GNRs surface successfully with DPPC lipid bilayer at ambient conditions. Various reaction parameters are optimized to get the surface modified GNRs which show good control in aspect ratio and optical property are also discussed. The simple recipe produces monodispersed nanorods with maintained size and shape. The surface modification of GNRs with lipid bilayer is confirmed by microscopic and spectroscopic techniques (TEM, STEM, EDAX, UV-Vis absorbance and FTIR). The surface modified nanorods show good biocompatibility (>95 % cell viability), dispersion

ability in various solvents viz., PBS, saline and culture media, superior and quicker photothermal response (<2 min) at 1 W NIR power density and (f) higher radio density (HU 60) in CT imaging compared to that of the widely practiced iodine (HU 23). *In vitro* plasmonic photothermal therapy on cancer cell lines demonstrates its outstanding multifunctional design and performance. Further, the fabricated nanorods show successful *in vivo* tumor targeting ability by using single and minimal dose (10 mg/kg body weight).

As a consequence, it is envisaged that due to good biocompatibility, radiodensity, optical property and *in vivo* tumor targeting ability of surface modified GNRs, the new design of contrast agent may replace the existing iodinated contrast agents. These nanorods are highly responsive to NIR light and lose their aspect ratio and optical property.

As mentioned in the earlier chapter one of the major objectives of the research adapted in this thesis is to design successful nanotheranostic that can perform multiple functions for diagnosis and therapy synergistically. In this context due to non-porosity or low cargo capacity, the surface modified nanorods are limited to only photothermal therapy and diagnosis not capable of use as cargo carrier to perform various roles for example chemotherapy, combined chemo-photothermal therapy etc. The low theranostics efficiency and poor physiochemical stability of these nanorods has significant scope for further improvements for their efficiency and stability. Coating or covering the unstable surface of nanorods with chemically inert materials is a logical way to improve the above issues which we have studied further and presented in the following chapter. The major objective remains to be new designs of novel materials with improved therapeutic efficiency.

2.6 References

(1) Nathan D. B.; Wayne L.; Joshua G. H.; Jordan M. D.; Ariane M. V.; Nardine S. A.; Elissa M. G.; Lisa M. J.; Ji L.; Catherine J. M., *Langmuir* **2016**, 32, 9905-9921.

(2) Durr, N. J.; Larson, T.; Smith, D. K.; Korgel, B. A.; Sokolov, K.; Ben-Yakar, *Nano Lett*. **2007**, 7, 941-945.

(3) Han, X.; Liu, Y.; Yin, Y., *Nano Lett*. **2014**, 14, 2466-2470.

(4) Mayer, K. M.; Lee, S.; Liao, H.; Rostro, B. C.; Fuentes, A.; Scully, P. T.; Nehl, C. L.; Hafner, J. H., *ACS Nano* **2008**, 2, 687-692.

(5) Grzincic, E. M.; Yang, J. A.; Drnevich, J.; Falagan-Lotsch, P.; Murphy, C. J., *Nanoscale* **2015**, 7, 1349-1362.

(6) Garg, N.; Scholl, C.; Mohanty, A.; Jin, R., *Langmuir* **2010**, 26, 10271-10276.

(7) Nikoobakht, B.; El-Sayed, M. A., *Chem. Mater*. **2003**, 15, 1957-1962., Jana, N. R.; Gearheart, L.; Murphy, C.J., *Chem. Commun*. **2001**, 617-618., Jana, N. R.; Gearheart, L.; Murphy, C.J., *J. Phys. Chem. B*. **2001**, 105, 4065-4067.

(8) Pérez-Juste, J.; Pastoriza-Santos, I.; Liz-Marzán, L. M.; P. Mulvaney, Coord. Chem. Rev., 2005, 249, 1870.

(9) Alkilany, A. M.; Murphy, C. J., *J. Nanopart. Res*. **2010**, 12, 2313-2333.

(10) Wu, B.; Liu, D.; Mubeen, S.; Chuong, T. T.; Moskovits, M.; Stucky, G. D., *J. Am. Chem. Soc*. **2016**, 138, 1114-1117.

(11) Zhang, Z.; Wang, L.; Wang, J.; Jiang, X.; Li, X.; Hu, Z.; Ji, Y.; Wu, X.; Chen, C. *Adv. Mater*. **2012**, *24*, 1418-1423.

(12) Grzelczak, M.; Pérez-Juste, J.; Mulvaney, P.; Liz-Marzán, L. M. *Chem. Soc. Rev*. **2008**, 37, 1783-10.

(13) Orendorff, C. J., Alam, T. M., Sasaki, D. Y., Bunker, B. C., Voigt, J. A., *Acs Nano*, **2009**, 4, 971-983.

(14) Zhenglin, L.; Jing, L.; Ying, H.; Kenneth, A. H.; Zhuo, L.; Xuelei, F.; Manli, C.; Ye, S.; Flemming, B.; Chunying, C.; Miao, Y.; *ACS Nano* **2016**, 10, 9646−9658.

(15) Sungsook, A.; Sung, Y. J.; Sang, J. L.; *Molecules* **2013**, 18, 5858-5890.

(16) Kim, D.; Park, S.; Lee, J. H.; Jeong, Y. Y.; Jon, S.; *J. Am. Chem. Soc.* **2007**, 129, 7661–7665.

(17) Lisa, E. C.; Tracy, Vargo-G.; Ryan, K. R.; *ACS Nano* **2014**, 8, 7486–7496.

(18) Yanlan, L.; Kelong, A.; Lehui, L.; *Acc. Chem. Res.*, **2012**, 45, 1817–1827.

(19) Shen, S.; Tang, H.; Zhang, X.; Ren, J.; Pang, Z.; Wang, D.; Gao, H.; Qian, Y.; Jiang, X.; Yang, W.; *Biomaterials*, **2013**, 34, 3150-3158.

(20) Castellana, E. T., Gamez, R. C., & Russell, D. H., *J. Am. Chem. Soc.***2011**, 133, 4182-4185.

(21) Alkilany, A. M., Nagaria, P. K., Wyatt, M. D., & Murphy, C. J., *Langmuir*, **2010**, 26, 9328-9333.

(22) Vigderman, L., Khanal, B. P., & Zubarev, E. R., *Adv. Mater*, **2012**, 24, 4811-4841.

(23) Jackson, S. R., McBride, J. R., Rosenthal, S. J., Wright, D. W., *J. Am. Chem. Soc.* **2014**, 136, 5261-5263.

(24) Wang, J.; Tan, X.; Pang, X.; Liu, L.; Tan, F., Li, N.; *ACS Applied Materials & Interfaces*, **2016**, 8, 24331-24338.

(25) Hrvoje L; Mark W. G.; *Chem. Rev.* **2013**, 113, 1641−1666.

(26) Aspelin, P.; *Eur. Radiol.* **2006**, 16 (Suppl.), D22.

(27) Berrington de Gonzalez, A.; Mahesh, M.; Kim, K.-P.; Bhargavan, M.; Lewis, R.; Mettler, F.; Land, C. *Arch. Intern. Med.* **2009**, 169, 2071.

(28) Grainger, R. G.; *Br. J. Radiol.* **1980**, 53, 739.

(29) Christiansen, C.; *Toxicology* **2005**, 209, 185.

(30) Li, C. A.; *Nat. Mater.* **2014**, 13, 110–115.

(31) Judith W.; Paul C. B.; Sarah E B.; *Nature Methods*, **2016**, 13, 639–650.

(32) Takahashi, H., Niidome, Y., Niidome, T., Kaneko, K., Kawasaki, H., Yamada, S., *Langmuir*, **2006**, 22, 2-5.

(33) Niidome, Y., Honda, K., Higashimoto, K., Kawazumi, H., Yamada, S., Nakashima, N., Kikuchi, J. I., *Chem. Comm*. **2007**, 36, 3777-3779.

(34) Nakashima, H., Furukawa, K., Kashimura, Y., & Torimitsu, K., *Langmuir*, **2008**, 24, 5654-5658.

(35) Alkilany, A. M., Thompson, L. B., Boulos, S. P., Sisco, P. N., & Murphy, C. J., *Advanced drug delivery reviews*, **2012**, 64, 190-199.

(36) Prasad, R; Aiyer, S; Chauhan, D. S; Srivastava, R; Selvaraj, K, *Nanoscale* **2016**, 8, 4537-4546.

(37) Cauda, V.; Engelke, H.; Sauer, A.; Arcizet, D.; Brauchle, C.; Radler, J.; Bein, T. *Nano Lett.* **2010**, 10, 2484−2492.

(38) Singh, N.; Karambelkar, A.; Gu, L.; Lin, K.; Miller, J. S. ; Chen, C. S.; Sailor M. J.; Bhatia, S. N. *J. Am. Chem. Soc.* **2011**, *133*, 19582-19585.

(39) Murphy, C. J.; Gole, A. M.; Stone, J. W.; Sisco, P. N.; Alkilany, A. M.; Goldsmith, E. C.; Baxter, S. C. *Acc. Chem. Res.* **2008**, *41*, 1721−1730.

(40) Nikoobakht, B.; El-Sayed, M. A. *Chem. Mater*. **2003**, 15, 1957-1962.

(41) Hauck, T. S., Ghazani, A. A., Chan, W. C., *Small* **2008**, 4, 153-159.

(42) Sudeep, P. K.; Joseph, S. T.; Thomas, K. G., *J. Am. Chem. Soc.* **2005**, 127, 6516-6517.

Chapter III

Mesoporous silica coated gold nanorods as a NIR responsive multifunctional cancer theranostics

Mesoporous silica (MS) and gold nanoparticles (GNPs) are being individually widely used material for various applications such as drug delivery, imaging, catalysis, sensing etc. Due to high surface area, high pay load, plasmonic ability and easy surface modification, encapsulation of GNPs in deep MS shell is a current thrust area in material science. In the present chapter, issues such as precise encapsulation of gold nanoparticles (especially gold nanorods, GNRs) in single MS and its cancer theranostics application are addressed. To enhance the cargo capacity and to maintain the optical property of gold nanorods (GNRs), mesoporous silica (MS) is directly deposited over them. MS thickness tunability over GNRs with its precise embedding in single silica shell via rapid and scalable synthesis recipe is described here. The designed biocompatible mesoporous silica coated gold nanorods (GMS also called as GNR-MS) nanohybrid is used for multifunctional cancer theranostics (diagnostics and therapeutics) such as contrast agent for X-ray computed tomography imaging (X-ray CT) of cancer cells/tumor, stimuli responsive (pH, temperature and NIR light) controlled drug delivery, specific targeted agent for cancer cells/tumor, NIR responsive photothermal therapy and combined chemo-photothermal therapy for various cancer cell lines.

A part of the work presented in this chapter is communicated for publication.

3.1 Introduction

Due to the radical impact of sol-gel chemistry on the fabrication of silica and its framework on metal nanoparticles (MNPs) [1-3], a rapid and scalable synthesis of silica based nanohybrids at near ambient temperature would be an interesting and promising approach for advanced nanomedicine. Further, integration of multiple functions in single system (diagnostics and therapeutics agents in one system) is a current challenge which we address in this chapter.[2-6]

Due to unique optical properties, various metal nanoparticles (MNPs) especially gold nanorods (GNRs) are widely used for diagnosis.[7] On the other hand, as mentioned, mesoporous silica (MS) is a well-studied material for drug delivery and recently recognized as safe material for human trials by US FDA[8, 9] on account of its chemical versatility, availability of ordered uniform pores with high surface area and pore volume, biocompatibility etc.[10,11] Silica is also an attractive and promising coating material on gold nanoparticles known for their high contrast abilities in diagnostics.[12-14] In GNRs, the silica coating is significant to maintain their aspect ratio (AR), optical property, chemical and thermal stability.[14] The AR decides the retention of their extraordinary photothermal abilities due to localized surface plasmon resonance (LSPR).[12-17] Free GNRs are reported as good heat sources in photothermal therapy using near infrared (NIR) light source. However, these nanorods are highly instable due to easy reshaping.[12, 18, 19]

Rapidly emerging advanced systems in nanomedicine, namely MultiFunctional Theranostic (MFT) agents are designed to support multiple roles in diagnosis and therapy. Developing one for the combined therapeutic approaches of cancer viz., chemo, photothermal and ablation etc. along with diagnosis is a challenge.[14] Due to high atomic

number, X-ray absorption coefficient and highly spatial control ability, several inorganic nano-contrast agents (Ba, Gd, Dy, Lu, Yb, Pb, Ta, Bi, U and Au) are investigated for multimodal bio-imaging.[7] Among these contrast agents, gold nanoparticles (specifically GNRs) are well understood for tumor diagnosis.[7, 19] GNRs though play roles in: (a) diagnostics and (b) photothermal therapy, they fail to fulfill the requirements of a good cargo carrier in an MFT agent.[19] It is mainly due to: (a) poor drug carrying capacity, (b) instability leading to aggregation and reshaping of GNRs and (c) toxicity of cetyltrimethyl ammonium bromide (CTAB) bilayer that stabilizes them.[12-19] Hence, embedding them into the core of MS, a good cargo carrier via sol-gel route could lead to a perfect and ideal MFT system.[18-33] However, achieving an uniform silica growth with optimal silica layer thickness with high surface area and large product yield via rapid and scalable process are challenging and current demands for material science.[29, 32]

The present chapter addresses the rapid and scalable design of GNRs encapsulated MS (GMS) nanohybrid at ambient conditions. The fabricated nanohybrid is obtained through candid demonstrations with optimized controls on various influencing factors such as concentrations of CTAB surfactant, silica precursor, tetraethylorthosilicate (TEOS), temperature, pH, stirring speed and addition mode of precursors. Argued cytotoxicity due to CTAB is also fixed through post synthesis removal resulting in a highly biocompatible GMS as a MFT agent. Further, several other bottlenecks in exploiting this viable synthesis route as seen below are additionally addressed in this chapter. (1) A recent report clearly authenticates the challenge in scaling the synthesis of GMS with ~ 190 mg per batch[30] of production is a record producible scale in contrast to an earlier work reporting a meager 10 mg per batch.[27] Whereas in our study, a scalability test is performed which demonstrate an

easily achievable product yield ~ 400 to 1000 mg per batch. (2) Another major hurdle is the overall synthesis time. Reports so far provide a large window of 10 h to 3 days (for 13 nm to 30 nm of silica thickness respectively).[13, 14, 18-33] In the present case, the design of GMS is achieved in mere 2 h. (3) To the best of our knowledge, the reported largest surface area of GMS based nanohybrid is 641 m^2/g with a silica thickness of 16 nm.[30,31] Till now, a maximum reported silica thickness around the GNR core is ~ 25-35 nm.[14,24,25] This limits the maximum obtainable cargo capacity to about 25 ±1.5 %.[18] We have achieved a specific surface area of 1100 m^2/g with a doubled cargo capacity. In general, good control on (a) embedding a photothermally stable GNR core, (b) high drug loading efficiency, (c) rapid and easy synthesis and (d) scalability of the route are recognized as the key objectives in designing a viable synthesis route for GMS based MFT agent. There are attempts in this context with limited success.[14, 24, 25, 18-33]

Herein this chapter, we report a scalable, rapid and simple one-step direct deposition of silica over gold nanorods with highly porous and sufficiently thick silica shell as discussed above at near ambient temperature that takes care of above issues. The synthesis recipe demonstrates an easy control on two examples of GMS based MFT agents for different therapeutic requirements (a) High Cargo (GMS-HC/MFT-HC) application for a synergistic near infra red (NIR) responsive chemo-photothermal therapy and (b) Moderate Cargo (GMS-MC/MFT-MC) application for advanced photothermal therapy. The following two perspectives helped us to understand the framework and therapeutic performance of designed nanohybrid (a) achieving precise core-shell structure for the MFT system where in each MS shell is embedded with a GNR core and (b) ensuring the architectural features that enhance their synergistic multifunctional performance. Thus, the objectives are to have

an optimal porous shell-wall thickness for augmented cargo capacity, retention of the aspect ratio (AR) of the core for better photothermal response. In addition the designed nanohybrid shows good aqueous solubility, photothermal efficiency, high biocompatibility and radiodensity, successful synergistic chemo-photothermal therapy and localized tumor diagnosis using single dose of nanohybrid.

3.2 Experimental Details

3.2.1 Materials

Millipore/Milli-Q water (MPW) is used in all experiments and to prepare all buffer solutions. All the chemicals are of analytical grade and used as-received without any further purification, unless otherwise described. N-cetyltrimethylammonium bromides (CTAB, 99 %), tetraethylorthosilicate (TEOS, 99.9 %), sodium borohydride ($NaBH_4$, 99 %), ascorbic acid (AA, 99.5 %), silver nitrate ($AgNO_3$, 99.9 %), sodium hydroxide (NaOH), dimethylsulphoxide (DMSO, 95 %) are purchased from Merck. Tetrachloroauric acid ($HAuCl_4.3H_2O$, 99.9 %), 3-aminopropyltrimethoxysilane (APTS, 99 %), N, N'-dicyclohexylcarbodiimide (DCC, 99.5 %), 1-Ethyl-3-(3-dimethylaminopropyl) carbodiimide (EDC, 98 %), N-hydroxysuccinimide (NHS, 99.8 %), folic acid (FA, 97 %), anhydrous toluene (99.8 %), doxorubicin hydrochloride (DOX, 98 %), rhodamine B (RhB, 95 %), Propidium iodide (PI), calcin AM and (3-(4,5-dimethylthiazol-2-yl)-2,5-diphenyltetrazolium bromide-MTT) are purchased from Sigma-Aldrich. Dulbecco's modified Eagle's medium (DMEM), antibiotic-antimycotic solution and fetal bovine serum (FBS) are procured from HiMedia Laboratories Pvt. Ltd, India. All glasswares are rinsed with double distilled water before using them for synthesis and applications.

3.2.2 Characterization techniques

The size and morphology of different nanoparticles are examined by using transmission electron microscopy (TEM instrument FEI Tecnai T-20, operated at 200 kV). Powder XRD (PXRD) patterns are recorded using a PANalytical X'pert pro dual goniometer diffractometer. The data are collected with a step size of 0.008° and scan rate of 0.5° min^{-1} by using Cu Kα ((λ = 1.54 Å) radiation source. XPS data is recorded in ultra high vacuum (1×10^{-10} millibar) condition in a lab based ambient pressure photoelectron spectrometer (APPES). Elemental analysis is done by energy-dispersive X-ray analysis (EDAX) and measurements are performed on an SEM system (FEI, Model Quanta 200 3D). Gold nanorods and GMS in an aqueous medium are characterized by UV-Vis-NIR spectrophotometer (Jasco-V570) dual beam spectrometer operated at a resolution of 2 nm. Absorption spectra are recorded by using quartz cell of 1 mm path length. Fourier transform infrared (FT-IR) spectra are recorded by using Perkin-Elmer FT-IR spectrum GX instrument. The N_2 adsorption-desorption isotherms are recorded using Quanta chrome Quadra Win instrument Version 5.02. The specific surface area is calculated using the multiple-point Brunauer-Emmett-Teller (BET) theory. Pore volume is estimated at a relative pressure of P/P_0. = 0.99. All photothermal transduction experiments and photothermal performance of nanohybrids have been done by using 808 ± 5 nm continuous wave NIR laser source with power density 0.5 W/cm^2 (SDL-808-LM-1000T). Cell targeting and intracellular localization of nanohybrids have checked by using fluorescence microscope (Axio observer. Z1). All CT scans are performed on a clinical CT scanner (Toshiba 64 slice, 0.5 mm slice per rotation) with 120 kV, 50 mA. The Hounsfield unit (HU) is measured by using RadiAnt DICOM Viewer software (V3.10ER009).

3.2.3 Synthesis of gold nanorods (GNRs)

Gold nanorods (GNRs) are prepared according to seed-mediated growth procedure. The preparation of Au seed solution is carried out by adding 2.5 mL of 0.2 M CTAB solution with 1.5 mL of 1.0 mM $HAuCl_4$ solution. To the stirred solution 0.6 mL of ice cold 0.01 M $NaBH_4$ is added which resulted in the formation of brownish-yellow solution. Vigorous stirring of the solution is continued for 2 min. The solution is stirred and kept at 25 °C. The growth solution for nanorods is prepared by adding 50 mL of 0.2 M CTAB solution to 2.8 mL of 0.004 M $AgNO_3$ solution. To the above solution 5 mL of 15 mM $HAuCl_4$ solution and 1.25 mL of 0.08 M ascorbic acid added and mixed gently. After that 1 mL of seed solution is added to the whole growth solution at 27-30 °C. The color of solution gradually changed in to dark blue within 10-15 min. The temperature of the growth medium is kept constant at 27-30 °C throughout the procedure. The GNRs are collected by three cycles of centrifugation.

3.2.4 Direct deposition of thick mesoporous silica over GNRs (GMS)

A solution of CTAB surfactant (5.7 mM) in 120 mL of Milli-Q water is prepared (pH 10-11 adjusted by adding 2 M aqueous NaOH) and continuously stirred at 50 °C (here excess CTAB promoted the formation of uniform, thick and highly porous coating of MS over the GNRs). Subsequently, freshly prepared 1 mL of GNRs in 12 mL of Milli-Q water and 1.25 mL (43.9 mM) TEOS are added in CTAB solution. They are added simultaneously and the rates of their addition are adjusted to ensure that both solutions finish at the same time (4 min.). The reaction mixture is further stirred for 2 h and the product is collected by centrifugation. The product is thoroughly washed with copious amount of Milli-Q water and methanol and dried under a vacuum at 70 °C temperature. Porous silica coated GNRs

are obtained via surfactant removal process in a methanol solution of HCl (11.2 M) through acid leaching at 60 °C for 6 h. After that, the mixture is cooled to room temperature and then it is collected via centrifugation and thoroughly washed with Milli-Q water and methanol. The resulting surfactant removed product is dried under a vacuum. About 400 mg/batch product yield is obtained from this recipe. To target the cancer cell/tumor, the exterior surface of designed nanohybrid is functionalized by folic acid as a targeting ligand. The preliminary screening of loading efficiencies is done with DOX and RhB dye.

3.2.5 Rapid and large-scale synthesis of GMS nanohybrid

The rapid recipe of GMS nanohybrid is scaled up at 541 mL of total volume which result 1000 mg/batch of product yield within 2 h of reaction time. 56 mL of freshly prepared diluted GNRs in Milli-Q water and 5 mL (43.9 mM) TEOS are added into 480 mL of CTAB surfactant solution (5.7 mM) where all reaction conditions such as pH, temperature, stirring speed, addition rate of GNR and TEOS and reaction time are same as for standard scale (see 3.2.4 section). The final product is collected by centrifugation and thoroughly washed with Milli-Q water and methanol and dried under a vacuum. Here it is important to note that the silica layer deposition over GNRs is direct without any intermediate coating of polymer layer/silane linkers or interval injections of TEOS. To remove CTAB surfactant form as synthesized GMS nanohybrid, the product is refluxed at 60 °C for 6 h in a solution of 0.5 mL of HCl (11.2 M) and 50 mL of methanol. After reflux, temperature is cooled down to room temperature and product is collected via centrifugation at 10,000 rpm for 10 min. The resulting surfactant removed product is washed with Milli-Q water and methanol

further placed under high vacuum at 70 °C temperature to remove the remaining solvent from the pores.

3.2.6 Thin silica shell deposition over GNRs

Prepared GNRs are dispersed in 10 mL of Milli-Q water. The pH of the solution is adjusted in between 10-11 by adding NaOH solution. To the above solution three slots of 20 % TEOS in aqueous media is added with 1 h interval under gentle stirring at room temperature. The reaction mixture is allowed to react for 7 h at room temperature. The final product is collected by centrifugation and then thoroughly washed with Milli-Q water and methanol. The product is dried at 70 °C under vacuum and following steps are for CTAB removal. After removing moisture form as synthesized nanohybrid, the product is refluxed at 60 °C for 6 h in a solution of 0.5 mL of HCl (11.2 M) and 50 mL of methanol, stirring. After completion of the reflux, reaction temperature is cooled down to room temperature and then collects the product via centrifugation at 10,000 rpm for 10 min. The resulting surfactant removed product is placed at 70 °C temperature under high vacuum to remove the remaining solvent from the pores.

3.2.7 Surface functionalization of designed nanohybrid with folic acid targeting ligand

The exterior surface functionalization of designed GMS nanohybrid is carried out by two steps. In the first step, exterior surface is modified to have terminal amino functional groups by a grafting method. For this, the particles of nanohybrid are dried in oven at 100 °C for 6 h. The dried 0.24 g particles are refluxed for 12 h in 30 mL of methanol with 0.24 mL of 3-aminopropyltrimethoxysilane (APTS) to yield the amine-functionalized nanoparticles. Surfactant removal has been done via reflux reaction as mentioned earlier.

In the second step, folic acid (FA) is anchored on the amino functionalized nanohybrid by using standard EDC-NHS reaction. Carboxyl group of FA is activated by 1-Ethyl-3-(3-dimethylaminopropyl) carbodiimide (EDC) and N-hydroxysuccinimide (NHS). Folic acid (180 mg) is activated by 1-Ethyl-3-(3-dimethylaminopropyl) carbodiimide (56 mg) and N-hydroxysuccinimide (46 mg) dissolved in 16 mL of Milli-Q water with stirring for 24 h at room temperature. After that, 15 mL of surfactant free amine-functionalized nanohybrid (150 mg) in Milli-Q water is added to the activated folic acid solution and allowed to react at room temperature for 24 h. The activation and anchoring reaction of folic acid should be protected from light. The product is collected by centrifugation and thoroughly washed with Milli-Q water and methanol which is dried under vacuum.

3.2.8 Anti-cancer drug loading efficiency

DOX is dissolved in PBS buffer (pH 7.4) with 1 mg/mL concentration. Surfactant free GNRs encapsulated mesoporous silica nanoparticles (5 mg) are dispersed in 1.5 mL of drug solution (1 mg/mL). The mixture is stirred at room temperature for 24 h. Then the dispersion is centrifuged to collect the drug loaded nanoparticles. In order to remove drug from the exterior surface of nanoparticles, the drug loaded nanoparticles are thoroughly washed with Milli-Q water and collected by centrifugation. The obtained supernatant from the washing process is combined with the previous supernatant solution. The mass of drug loaded into nanoparticles are calculated by using following equations. The amount of drug adsorbed is analyzed with UV-vis spectrophotometer.

$$\% \text{ loading} = \frac{\text{Mass of drug in nanohybrid}}{\text{Mass of drug-Mass of drug loaded nanohybrid}} \times 100 \qquad \text{(eq. 3.1)}$$

$$\% \text{ Entrapment} = \frac{\text{Mass of drug in nanohybrid}}{\text{Initial mass of drug}} \times 100 \qquad \text{(eq. 3.2)}$$

3.2.9 Preliminary testing of loading efficiency

For this purpose we choose Rhodamine B (RhB) dye which is popular probe molecule for testing of cargo capacity. RhB is dissolved in PBS buffer (pH 7.4) with 1 mg/mL concentration. Surfactant free GNRs encapsulated mesoporous silica nanoparticles (5 mg) were dispersed in 1.5 mL of dye solution (1 mg/mL). The mixture is stirred at room temperature for 24 h. Then the dispersion is centrifuged to collect the dye loaded nanoparticles. In order to remove dye from the exterior surface of nanoparticles, the dye loaded nanoparticles is thoroughly washed with MPW and collected by centrifugation. The obtained supernatant from the washing process is combined with the previous supernatant solution. The mass of dye loaded into nanoparticles are calculated by subtracting the mass of drug in the supernatant from the total mass of the drug in initial solution. The amount of drug adsorbed is analyzed with UV-vis spectrophotometer.

3.2.10 Stimuli responsive (pH, temperature and NIR light mediated) drug release kinetics

For the stimuli responsive drug release kinetics, 1 mL of DOX loaded nanohybrid and FA functionalized nanohybrid in dialysis bag immersed into 100 mL of PBS at various pH (2, 4, 5, 6 and 7.4), temperature (37, 43 and 45 °C) and under NIR light exposure (5 min. 808

nm NIR light exposure). At different time intervals, 2 mL solution is collected and replaced with same volume of fresh PBS solution to keep the volume constant. The amount of DOX in the release medium is measured by UV-Vis spectroscopy at the wavelength of 480 nm and following equation.

$$\% \text{ Release } = \frac{\text{Mass of drug at time}}{\text{Initial mass of drug}} \qquad (\text{eq. } 3.3)$$

3.2.11 Photothermal performance and conversion efficiency test

To evaluate the photothermal performance of nanohybrid, various concentrations (0.2-3.5 mg/mL) of nanohybrid in PBS (pH 7.4, 0.15 M) are made. Aliquots (200 µL) are deposited into 96 well plate. The initial temperature is stabilized at 37 °C in water bath. Wells are illuminated with an 808 ± 5 nm continuous wave NIR laser source with power density 0.5 W/cm^2 for 5 min. Further, time dependent photothermal performance has been done at 0.2 mg/mL concentration of nanohybrid before and after drug loading and surface functionalization with FA. The photothermal conversion efficiency and capacity test have been done by NIR laser "ON-OFF" cycles for 5 min. The nanohybrid is continuously exposed with 808 nm NIR light until reaching a steady-state temperature. After steady-state temperature the laser exposure is OFF and the cooling temperature is recorded by IR digital thermometer. Based on steady-state and cooling temperature the rate of heat transfer from the system is determined. The photothermal conversion efficiency (ηT) is calculated using the following eq.

$$\eta T = \frac{hA\ (Tmax. - Tamb.) - \text{QDis}}{I\ (1 - 10 - A800)} \quad \text{(eq. 3.4)}$$

Where

h = heat transfer coefficient

A = surface area of the container

Tmax = the maximum steady temperature of the GMS solution which is 45.6 oC

Tamb = the ambient temperature of the GMS solution which is 37 oC

I = laser power of NIR source which is 0.5 W

A800 = the absorbance of the nanohybrid at 800 nm.

QDis = expresses heat dissipated from the light absorbed by the water and container or heat input (in mW).

hA is calculated by measuring the rate of temperature drop after switching OFF the NIR source. The value of hA is derived according to following eq.

$$\tau s = \frac{mDcD}{hA} \quad \text{(eq. 3.5)}$$

Where

τs = time constant

mD = mass of water (0.3 g)

cD = heat capacity of water (4.2 J/g)

3.2.12 Radiodensity measurement

To evaluate the contrast ability, the CT scans of nanohybrid, GNRs, Iodine and nanohybrid injected mice are performed on a CT scanner with 120 kV, 50 mA. Aqueous solutions of each component with different concentrations are prepared in plastic eppendrof and placed in scanning holder. All scans (materials as well as animals) are performed with 64

simultaneous 0.5 mm slices per rotation. The radiodensity is measured in Hounsfield unit (HU) for each by using RadiAnt DICOM Viewer software and following equation.

$$\text{Radiodensity (HU)} = \frac{\text{HU value of suspended nanohybrid- HU value of water}}{\text{HU value of water-HU value of air}} \qquad \text{(eq. 3.6)}$$

3.3 Applications

3.3.1 Cell culture and *in vitro* biocompatibility study

To understand the biocompatibility and therapeutic efficiency of nanohybrid, L929 and NIH-3T3 normal cells, HeLa cancer cells, breast cancer cell lines (MCF-7, MDA-MB-231 and 4T1) are cultured in DMEM media supplemented with 10% FBS, 1 % penicillin and 1 % streptomycin, under 5 % CO_2 atmosphere at 37 ºC.

To check the biocompatibility of designed nanohybrid, L929 normal cells are seeded at density of 1×10^4 cells per well in 96 well plates and incubated for 24 h in 5 % CO_2 atmosphere at 37 ºC. After 24 h incubation, 200 µl of different concentration (5-200 µg/mL dispersed in media) of as synthesized GMS, surfactant free GMS and GMS-FA nanoparticles are added into wells. Following 24 h incubation wells are washed off with PBS and 20 µl of MTT dye is added. Formazan crystals formed after 4 h are dissolved by 200 µL of DMSO. Optical absorbance is recorded at 570 nm and 690 nm using microplate reader (Tecan Infinite 200 PRO). Percentage cell viability is calculated in reference to untreated cells (control). In addition, the time dependent short and long term in vitro biocompatibility studies are performed using 12-48 h MTT assay over same normal cell lines. Cells are cultured for 24 h in 96 well plates at density of 1×10^4 cells per well. After

24 h incubation at 5 % CO_2 and 37 ºC, 100 µl of different concentrations (5-500 µg/mL) of nanohybrids are added into wells. Following 12-48 h incubation wells are washed off with PBS and 20 µl of MTT dye is added and incubated for 4 h in addition. Formazan crystals are dissolved by 200 µL of DMSO. Optical absorbance is recorded at 570 nm and 690 nm using microplate reader (Tecan Infinite 200 PRO). Percentage cell viabilities are calculated in reference to untreated cells (control). Similarly, the 24 h MTT assay is also done with NIH-3T3 normal cells.

3.3.2 Blood collection, handling and hemolysis assay

5 mL of blood is taken from healthy mice (ethylenediaminetetraacetic acid stabilized blood). To remove plasma, the collected blood is centrifuged at 3000 rpm for 5 min. (three times) and the remaining red blood cells (RBCs) are washed with PBS. For hemolysis assay, 2 mL of healthy RBCs is diluted to 50 mL with PBS. 0.2 mL of isolated RBCs is mixed with each set of different concentration range (50-1500 µg/mL) of nanohybrids (before and after drug loading and surface functionalization). 0.8 mL of nanohybrid in PBS from desired concentrations is mixed with 0.2 mL of isolated RBCs and further incubated for a period of 12 h at room temperature (RT). Similarly, the positive and negative controls are prepared by mixing 0.8 mL of water and PBS, respectively to RBCs. Then the mixtures are centrifuged at 3000 rpm for 5 min. and supernatant is collected into a cuvette. Hemolytic activity of nanohybrids is calculated by UV-Vis absorption of hemoglobin at 540 nm, which is released in to the solution from hemolyzed RBCs. The percent hemolysis of RBCs is calculated using the following equation:

$$\% \text{ Hemolysis} = \frac{\text{Sample absorbance-Negative control absorbance}}{\text{Positive control absorbance-Negative control absorbance}} \times 100 \quad \text{(eq. 3.7)}$$

3.3.3 Animals models and tumor growth

Animal protocols are approved by the Institutional Animal Ethical Committee (IAEC, SSBS/IAEC/05/2016 project). ~ 20 g female Balb/c mice are used for current study. PBS suspended 1×10^4 4T1 breast cancer cells are injected subcutaneously into the flank of Balb/c mice.

3.3.4 *In vitro* targeting ability and intracellular localization of nanohybrid

The targeting ability of nanohybrids is understood on various cancer cells such as HeLa, MCF-7, MDA-MB-231 and 4T1. To check the targeting ability of designed nanohybrid, HeLa cancer cells are seeded into 96 well plates with a density of 1×10^4 cells/well and incubated for 24 h in 5 % CO_2 atmosphere at 37 ºC. After being rinsed with PBS, the cells are incubated with 100 µg/mL of DOX loaded nanohybrids for 4 h. After incubation the cells are washed with PBS three times to get rid of all the unbound particles i.e. nanohybrid. Then 4 % paraformaldehyde solution is added to the cells and incubated for 10 min and nuclei are stained with 4, 6-diamidino-2-phenylindole (DAPI, 1 µg/mL in PBS). At the end of the incubation period, the staining solution is removed by washing with PBS once. The cover slip is then mounted on a drop of 70 % glycerol on glass slide to fix the phase of the cell. The fluorescence images are taken using fluorescence microscope (Axio observer. Z1). Similar study is also carried out on 4T1 breast cancer cells.

To understand the intracellular localization of nanohybrid, cancer cells (MCF-7 and MDA-MB-231) are cultured for 24 h in 96 well plates at density of 1×10^4 cells per well. After 24

h incubation, 100 µl (200 µg/mL) of FA functionalized DOX loaded nanohybrid is added into wells and cultured for various incubation times (4, 12 and 24 h). In addition, the drug loaded nanohybrid is also incubated with pre FR saturated (with free FA) cell membrane of these cancer cells. The wells are washed three times with PBS after incubation. The cell imaging procedure is same as mentioned earlier.

3.3.5 *In vitro* targeted therapeutic study, targeted synergistic chemo-photothermal therapy and LIVE-DEAD staining

To understand the therapeutic efficiency of nanohybrid, *in vitro* therapies and synergistic chemo-photothermal therapy are tested on MCF-7 and MDA-MB-231 breast cancer cell lines. Cancer cells are seeded into 96 well plates with a density of 2×10^4 cells/well and incubated for 24 h in 5 % CO_2 atmosphere at 37 ºC. After being rinsed with PBS, the cells are incubated with 200 µg/mL of DOX loaded FA attached nanohybrid for 4 h. After incubation the cells are washed with PBS three times to get rid of all the unbound particles. Then *in vitro* therapy test is divided in six groups. Group 1 is only cancer cells, group 2 is NIR light exposure on cells, group 3 is only nanohybrid treated cells, group 4 is cells are treated with DOX loaded nanohybrid without targeting ligand as controls, group 5 is cells treated with DOX loaded nanohybrid-FA for chemotherapy and group 6 is DOX loaded nanohybrid-FA treated cells under continuous 5 min. 808 nm NIR exposure for synergistic chemo-photothermal therapy. Cell viability is determined by the addition of MTT (20 µL, 1 mg/mL dye in sterile PBS). The plate is incubated for an additional 4 h at 37 °C and 5 % CO_2, allowing viable cells to convert the blue solution into pink dye. Formazan crystals are dissolved by adding 100 µL DMSO to each well. Optical absorbance is recorded at 570 nm

using microplate reader (Tecan Infinite 200 PRO). Percentage cell viabilities are calculated in reference to untreated cells (control).

$$\% \text{ Cell viability} = \frac{\text{OD (treated)-OD (blank)}}{\text{OD (negative control)-OD (blank)}} \text{ x } 100 \qquad \text{(eq. 3.8)}$$

In addition, to check the impact of individual targeted chemotherapy, photothermal therapy and synergistic combined chemo-photothermal therapy on breast cancer cells, the LIVE-DEAD Kits are applied to visualize the live and dead cells. Breast cancer cells (MCF-7 and MDA-MB-231) are cultured for 24 h in 96 well plates at density of 2×10^4 cells per well. After 24 h incubation, 100 µl (200 µg/mL) of different set (before and after drug loading and functionalization with FA) of nanohybrids are added into wells and cultured for further 4 h. Moreover, the corresponding wells are exposed with 808 NIR laser (0.5 W/cm^2) for 5 min. After that the media is replaced with fresh media and cultured further for 18 h. After careful washing, cells are stained with LIVE-DEAD Kits. Through fluorescence microscope we have observed green color, for live cells (calcin AM) and red color, for dead cells (propidium iodide, PI).

3.3.6 Nanohybrid as a safe contrast agent for *in vivo* tumor diagnosis through X-ray CT imaging

Clinical voltage of CT scanner (120 kVp) has been used to understand the contrast ability of nanohybrid at various doses. For *in vivo* tumor diagnosis and specific bio-distribution, a minimum single dose (10 mg/kg) of nanohybrid, viz. GMS-FA as a contrast agent is subcutaneously injected in 4T1 tumor bearing female Balb/c mice. After injecting

nanohybrid, the CT scans are performed on anaesthetized mice at 1 and 24 h time points and compared with pre-contrast injected mice. The bio-distribution of contrast agent in major organs (heart, lung, liver, spleen, intestine and kidney) and tumor site are analyzed CT images.

3.3.7 *In vivo* biocompatibility and bio-distribution of nanohybrid

Healthy female Balb/c mice are used to understand the bio-distribution and long time *in vivo* toxicity of nanohybrid at various concentrations/doses (1 to 50 mg/kg body weight). Single dose of PBS dispersed nanohybrid from each concentration set is injected in normal Balb/c mice and CT scans are carried out. The notable contrast in major organs viz. heart, lung, liver, spleen, intestine and kidney are analyzed through CT imaging. To understand the long term *in vivo* toxicity, a high dose (50 mg/kg) of nanohybrid is subcutaneously injected to healthy female Balb/c mice (weight: ~20 g, n = 3). The variations of mice body weight and normal behavior are observed every day for over 14 days. At various time point (1 h, 24 h and 14th day) mice are sacrificed (n = 3) for H&E staining of tissues from heat, lung, liver, spleen and kidney to further investigate the tissue injury.

3.4 Results and Discussion

3.4.1 Rapid and scalable "One-Step Direct Deposition'' of mesoporous silica over plasmonic nanoparticles

Material design which is associated with synthesis innovative is a major hurdle in nano-theranostics research. Precision embedding of plasmonic nanoparticles (especially GNRs) inside each mesoporous silica shell is a challenging task and objective of this work. A simple, facile and one-pot sol-gel route for large scale harvesting of gold nanorods encapsulated mesoporous silica (GMS) is reported herewith. Firstly, a choice of GNR and

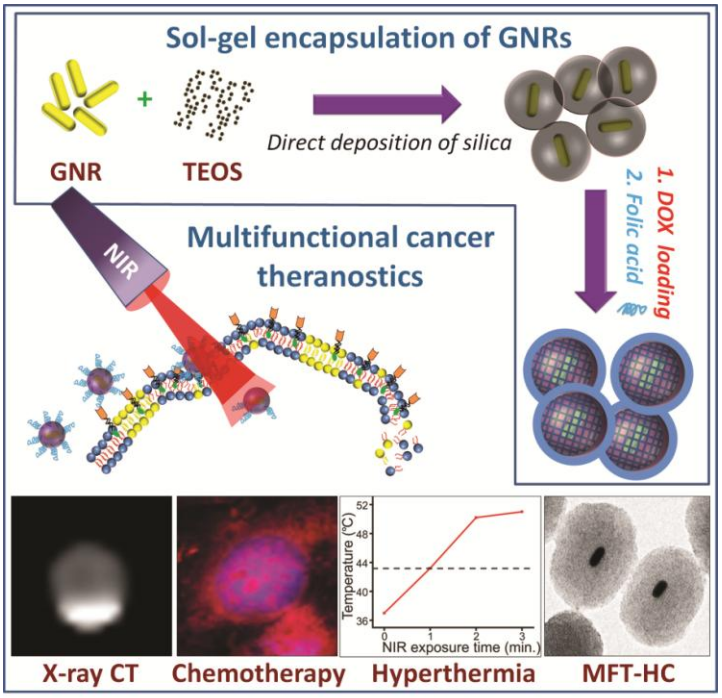

Scheme 3.1. *Schematic showing effective distribution of GNRs in MS shell and cancer theranostics ability of designed nanohybrid.*

its effective embedding in MS shell and their good distribution is addressed for cancer theranostics application (Scheme 3.1).

GNRs (Figure 3.1) with average length of ~33 nm and average width of ~11 nm (histogram is in inset) are prepared in aqueous media using CTAB as surfactant. GNRs and TEOS are added simultaneously but with control into the excess CTAB containing solution at pH 10-11 under gentle stirring at near ambient temperature of 45-50 °C followed by 2 h of stirring. The designed nanohybrid is monodispersed with an average particle size of ~100 nm and uniform thickness providing a rich cargo capacity. A surface area of 1100 m^2/g is obtained and is the largest reported ever for MS based nanohybrids with an unreported silica shell thickness of 51 nm so far. From this we understand that the

availability of free GNRs in the reaction mixture at any given time predominantly regulates the GNR core distribution

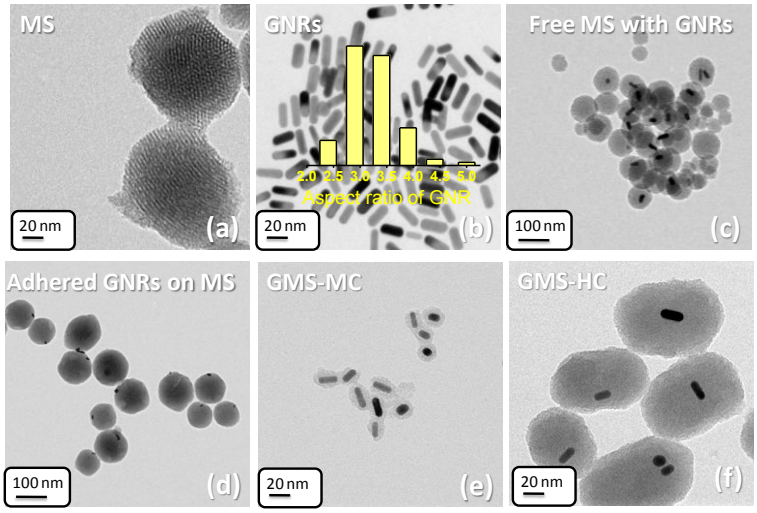

Figure 3.1. *TEM images of (a) mesoporous silica (MS), (b) gold nanorods (GNRs) with histogram (inset), (c) free silica with GNRs, (d) adhered GNRs on silica surface, effective distribution of GNRs in MS shell (e) with 11 nm MS thickness (GMS-MC) and (f) with 51 nm MS thickness (GMS-HC).*

as described below. Two significant observations made during a rigorous optimization helped in arriving at these conclusions. (i) Addition of TEOS and GNRs must be simultaneous into the reaction mixture and (ii) the addition speed of GNRs must be optimal to ensure their distribution on to the MS particles. The individual components of GMS nanohybrid, plain MS ~ 90 nm size and GNRs are shown in Figure 3.1 a, b. TEM images show (i) when the addition of GNRs is faster compared to that of TEOS, only a few GNRs are encapsulated by MS and the remaining GNRs aggregate and agglomerate around the free MS (Figure 3.1 c), (ii) when addition of GNRs is slower than that of TEOS, almost all the GNRs are found to have adhered on to the bulk MS surface (Figure 3.1 d) and (iii) when the addition speeds of both TEOS and GNRs are synchronized, a precise insertion of single GNR in to each MS particle becomes possible (Figures 3.1 e, 3.1

f and as depicted in Scheme 3.2 and 3.3. The following are the reasons; unsynchronized faster addition of GNRs disturbs the optimal seeding chances of GNRs there by leading to uncontrolled

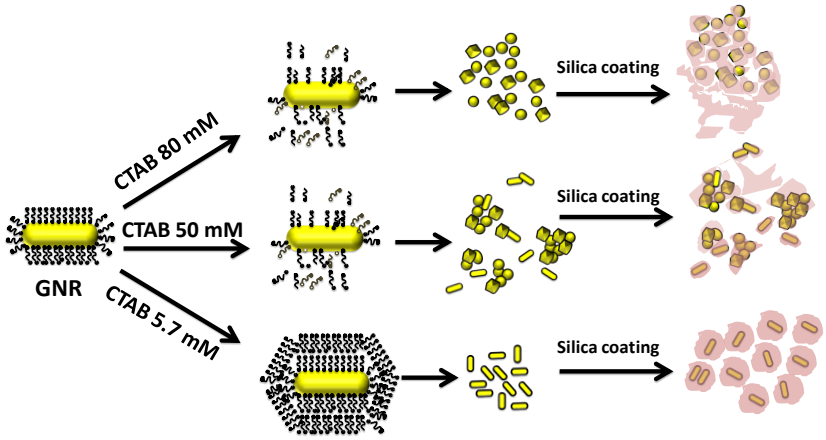

Scheme 3.2. *Effect of CTAB concentration on self assembly of surfactant which cause changes in the particle shape, size and their silica coating.*

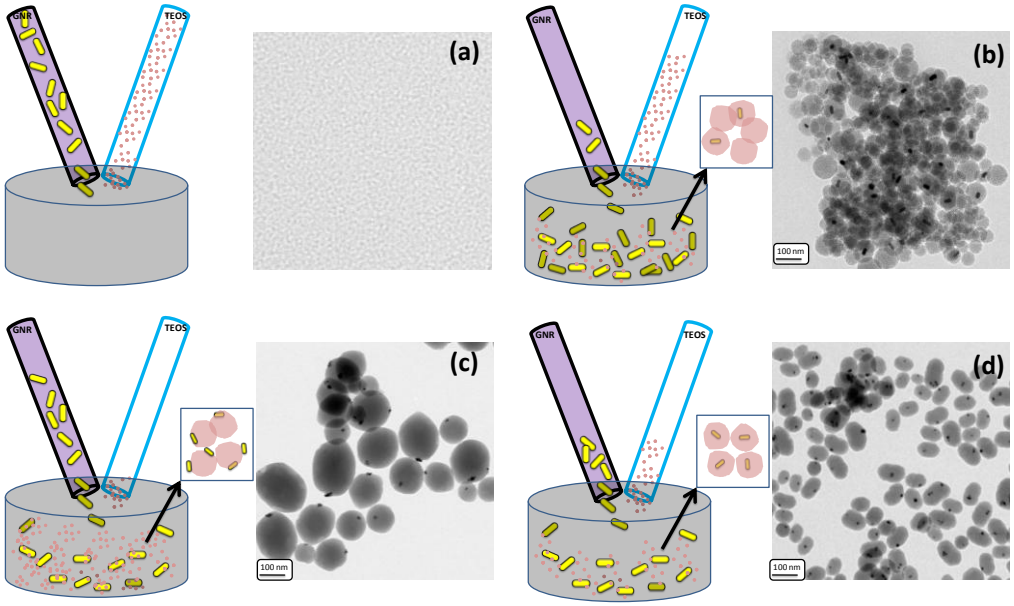

Scheme 3.3. *Addition mode of precursors and expected TEM images, (a) before addition, (b) GNR complete first than TEOS, (c) TEOS complete first than GNR and (d) TEOS and GNR complete at a time.*

condensation of TEOS. In contrast, its slower addition leads to their adhesion on the MS surface due to their delayed or failed seeding (Scheme 3.3). This significant understanding gives a better grip to control the GNR distribution among MS. Further rounds of optimization help in obtaining two kinds of GMS based nanohybrids for different therapeutic requirements as mentioned earlier: (i) 11 nm and (ii) 51 nm of silica shell thickness over the GNRs, labeled as GMS-MC and GMS-HC respectively (Figures 3.1 e and 3.1 f). Thick porous silica shell is ideally for exclusive photothermal therapy and cargo carrier hence a thin silica coating is good enough to fortify GNR and to retain its aspect ratio and not for cargo. Secondly, accomplishment of architectural features for enhanced synergistic performance of various components in the GMS nanohybrid is possible by retaining the AR of the plasmonic core, GNR. Further, attempts of MS coating over gold nano particles (size ~ 20-50 nm) using the recipe prove that control over layer thickness is irrespective of the shape and aspect ratio of the plasmonic core (Figure 3.2 a-d).

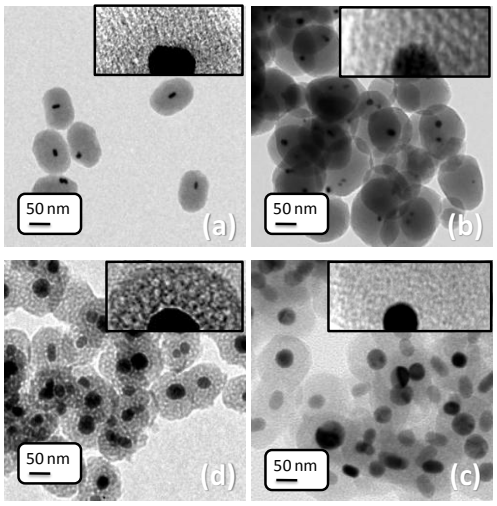

Figure 3.2. *TEM images of one-step direct deposition of silica over different shape of gold nanoparticles having different sizes (20-50 nm).*

3.4.1.1 Effect of CTAB and TEOS concentration

To increase the thickness of porous silica shell around the GNR is tricky and challenging. Several influencing parameters within the ranges reported on relevant literature cited in this chapter are covered in this study. CTAB concentration is the first parameter (Figure 3.3). It is observed that at high CTAB concentrations (between 50 and 80 mM), most GNRs lose their AR due to the equilibration between the CTAB that is bilayered around GNRs and that found in excess within the medium. Reshaping from rod to icosahedra/sphere promoting the aggregation of gold nanoparticles and the simultaneous formation of isolated void MS are also observed. At an optimal concentration of CTAB (5.7 mM), GNRs maintain the desired AR (Scheme 3.2) and adequate void MS spheres are observed. Thus, it may conclude that an optimal CTAB concentration of 5.7 mM helps both in maintaining the shape of GNRs and in the formation of thick porous silica shells (Figure 3.3 a-f and m). The optimization of the second parameter, TEOS concentration is carried out at a constant optimized concentration of CTAB (5.7 mM). It is expected that TEOS concentration primarily controls the silica layer thickness, the same is varied between 0.92 mM to 87.8 mM. Higher concentrations of TEOS (eg., at 87.8 mM shown in Figure 3.4 f) results in the formation of non-porous and fused silica whereas dispersed but heterogeneous mixture of MS is obtained at lower concentrations of TEOS (eg., 21.90 mM shown in Figure 3.4 d). It is interesting to observe that while the higher and lower boundaries of the concentration range of TEOS optimization seem to hamper the formation of nanohybrid with structural integrity, an optimal concentration, viz., 43.9 mM of TEOS at 5.7 mM CTAB (Figure 3.4) successfully favors it. Following literature analysis helped to

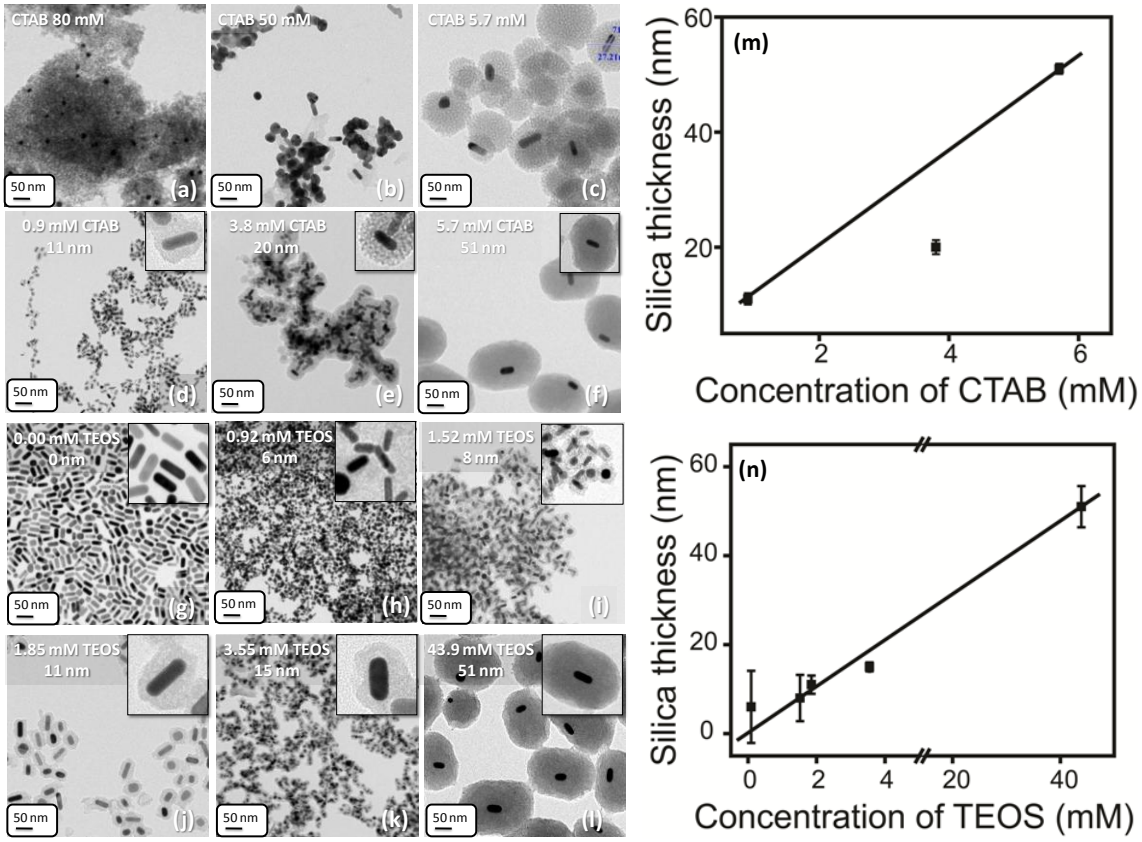

Figure 3.3. *TEM images showing effect of CTAB concentration (a) 80 mM, (b) 50 mM, (c) 5.7 mM (d) 0.9 mM (11 nm), (e) 3.8 mM (20 nm), (f) 5.7 mM (51 nm) on shape of GNRs, MS nanoparticles and silica thickness over GNRs. The effect of TEOS (g) no TEOS, only GNRs (h) 0.92 mM, (i) 1.52 mM, (j) 1.85 mM, (k) 3.55 mM and (l) 43.9 mM of TEOS concentrations for tuning silica thickness over GNR. Note that TEOS addition is in interval mode in general to all but it is in continuous mode for the case of (l). Plots for fine-tuning the silica shell thickness using various CTAB concentrations (m) and using various TEOS concentrations (n).*

achieve this control. Gorelikov and Matsuura's synthesis recipe for GMS (a single step coating of MS on GNRs with 1.5 mM CTAB at a TEOS concentration of 8 mM) has been considered as a standard recipe and followed later by many.[27] Several reports including Matsuura's have concluded that excess CTAB is unfavorable for obtaining an uniform coating of MS on GNRs.[12-14, 18-33] This was later contradicted. For instance, Dawei Chen

and coworkers have achieved uniform silica coated GNRs with ~ 32 nm silica shell thickness (surface area of 500 m^2/g) by using 200 mM CTAB concentration which is highest concentration reported so far[34,35] whereas, Chunying Chen and coworkers have reported 30 nm thick silica coated GNRs using 0.6 mM CTAB, the minimum concentration reported till date.[14] Thus the successful coating possibility under a large window of CTAB concentration with little differences in other conditions prompts that apart from the influence of CTAB concentration, role of other factors such as concentration of TEOS, temperature, pH of the reaction, addition mode of precursor and stirring speed also need better understanding.

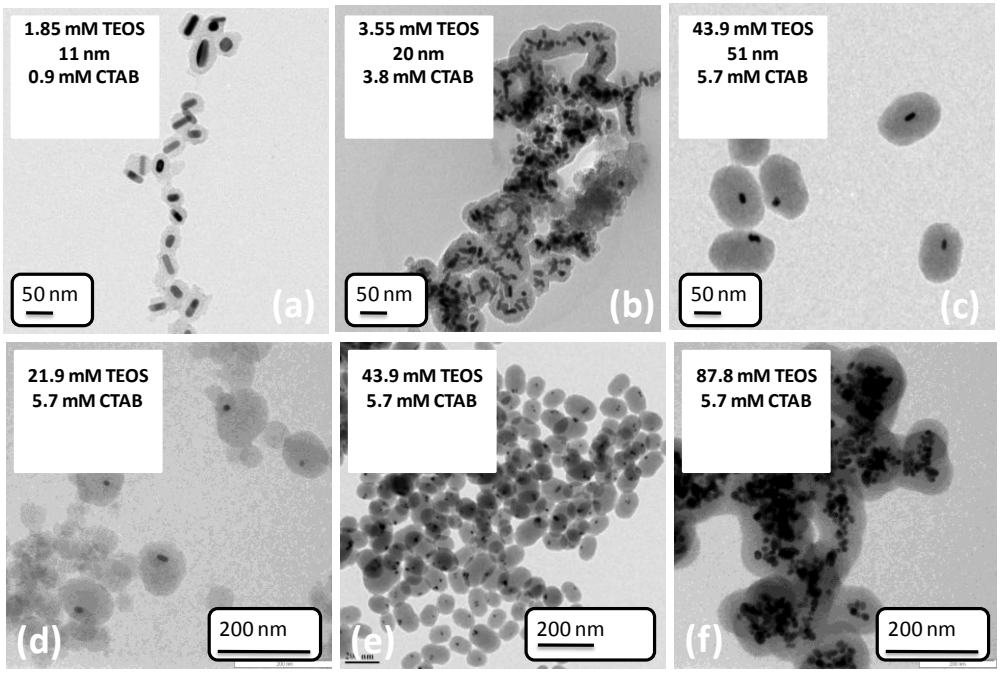

Figure 3.4. *TEM images of CTAB and TEOS combination effect on synthesis of GMS nanohybrid.*

For advanced photothermal therapy, thin silica is sufficient irrespective of its porosity as cargo handling is not a requirement. Instead, to retain the AR of GNRs at higher ablation

temperatures, fine tuning and control over the layer thickness is important. Various choices of parameters help us to achieve this control. Thinner silica layer with thicknesses from 6 to 15 nm are achieved at lower concentrations of TEOS added in few intervals between 0.92-3.55 mM (Figure 3.3 g-k and n). It is important to note that this is obtained without CTAB. Nanohybrid with large silica layer thickness of 20 and 51 nm (GMS-HC) are obtained as follows: 20 nm thickness with 3.55 mM (TEOS) and 3.8 mM (CTAB); 51 nm with 43.9 mM (TEOS) and 5.7 mM (CTAB) (Figure 3.4 b, c). It may be noted here that these thicker silica layers are obtained using CTAB and accordingly significant increase in porosity (upto 1100 m^2/g) are achieved (Figure 3.3 l). Another understanding of the tedious and tricky optimization process is that for the formation of a superior GMS nanohybrid as MFT agent not only the optimal concentrations of CTAB and TEOS but the controlled addition of the later with GNR suspension is also critical.

3.4.1.2 Effect of pH and temperature

In sol-gel chemistry, the rate of hydrolysis and condensation of silica precursor is intrinsically dependent on pH, temperature and the dynamics of reaction mixture logically, controlled rates should favor a slow and well-ordered coating of silica over GNRs. MCM-41 type of materials (without GNR core) are usually synthesized around pH 11 (or a pH>10).[6-10] In the present case, pH range between 10.2 to 10.8 is observed to yield in highly dispersed MS particles owing to optimal condensation rate (TEM images shown in Figures 3.5 a-d). Similarly, a lower temperature of 50 °C is observed to be ideal (Figure 3.5 d) unlike the higher temperatures of 70 to 90 °C usually reported for mesoporous silica synthesis.[10] Lowering it further resulted in the formation of fused silica (37°C as shown in Figure 3.5 c).

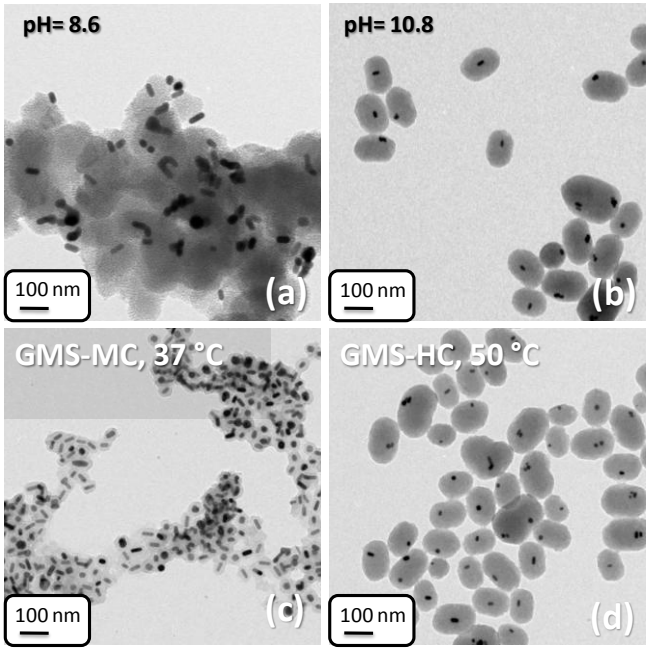

Figure 3.5. *TEM images of (a-b) effect of pH (c-d) effect of temperature.*

3.4.1.3 Effect of stirring speed and addition mode

Optimization under various stirring speeds viz., 100, 250, 300 and 400 rpm show that 250 rpm favors the best nanohybrid achieved during the present study (Figure 3.6 a-h). Due to collision theory at different stirring speed the types of nucleation are different. The stirring speeds, temperature and pH affect the rate of hydrolysis and condensation of silica precursor. Fast and separate small silica particles are formed at high stirring speed (400 rpm) due to the fast hydrolysis, condensation and large number of nucleation. Slow and fused silica nanoparticles are formed at low stirring speed (100 rpm) due to the slow hydrolysis, condensation and large nucleation for silica deposition. Silica deposition is perfect around the GNR at moderate (250 and 300 rpm) speed. The high stirring speed disturbed the micelle formation in reaction mixture and heavily GNR comes in aggregation form. TEM image (a) shows aggregation of GNRs with very thin coating of silica at high stirring speed (400 rpm), (d) shows again aggregation in GNRs and silica nanoparticles at

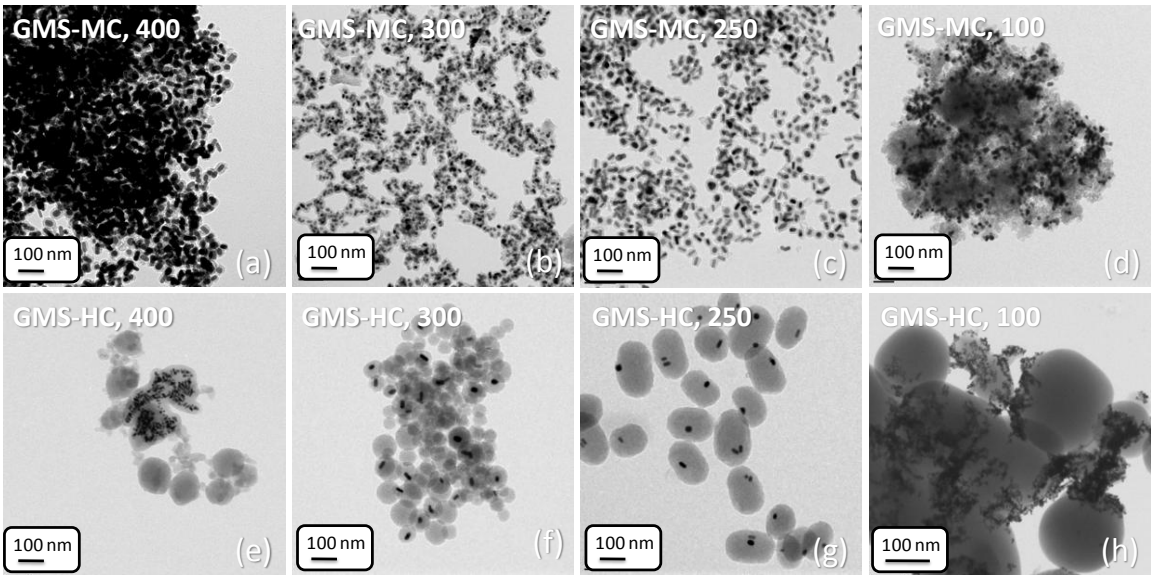

Figure 3.6. *TEM images of effect of stirring speed (a-d) of thin silica coated nanohybrid, GMS-MC and (e-h) of thick silica coated nanohybrid, GMS-HC.*

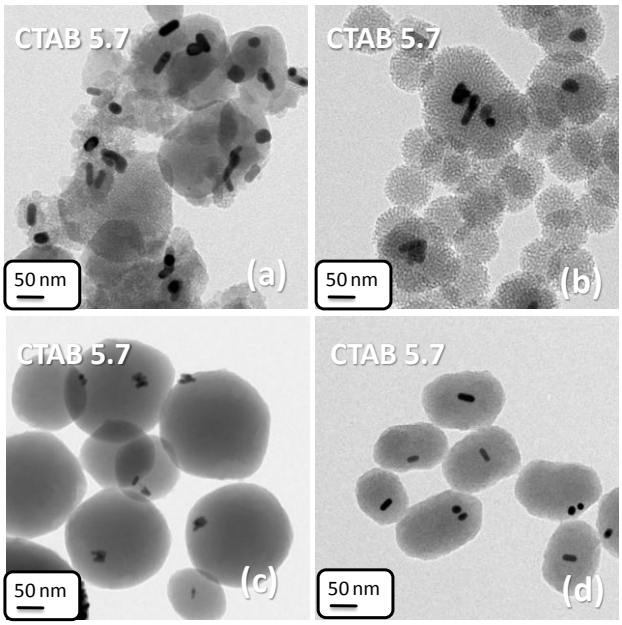

Figure 3.7. *TEM images of effect of addition mode of precursors.*

slow stirring speed (100 rpm). TEM images (b, c) show moderate stirring speed at 300 rpm and 250 rpm respectively. Due to moderate speed of reaction mixture the GNRs are effectively distributed with thin coated MS but in this case silica surface of particles are

partially fused to each other. TEM image (e) shows aggregation of GNRs with thick coating of silica at high stirring speed (400 rpm). TEM image (h) shows aggregation in GNRs and silica nanoparticles due to very slow stirring speed (100 rpm). TEM images (f, g) show controlled stirring speed at 250 rpm. The effective distribution control of GNRs in MS is accurately obtained by controlling some more reaction parameters like addition mode of GNR with silica precursor (Figure 3.7 a-d and Scheme 3). Due to single nucleation, moderate collision and dilution effect with respect to hydrolysis and condensation rate of silica precursor the hybrid formation is in controlled manner. To summarize, based on various optimizations during the study, we could evolve with a rapid and reproducible recipe for direct deposition of silica on GNR (GMS or GMS-HC) with a largest ever reported surface area and in turn with a highest ever reported cargo capacity. The highlight is that it is achieved in mere 2 h through a direct one shot addition of 43.9 mM TEOS with 5.7 mM CTAB at a pH of 10.8, temperature of 50 °C and stirring speed of 250 rpm.

3.4.1.4 Characterization of designed system

The structural design and performance of fabricated GMS nanohybrid is understood using various characterization techniques (Figure 3.8 a-i) and experiments. The effective distribution of GNRs in single MS shell and high surface area of designed nanohybrid are interesting for understanding the several capabilities of system.

3.4.1.4.1 Architectural understanding of designed nanohybrid

The homogenous distribution of mesoporous silica shell over GNRs is observed through TEM image showing ~ 100 nm particle size (Figure 3.1 f and 3.8 b). The components of GMS nanohybrid is confirmed by elemental mapping (green color for Si, red color for O

and bright yellow for Au) and EDAX analysis (Figure 3.8 c-f) which validates the framework of silica and presence of GNRs. TEM images of MS (MCM-41 type of mesoporous silica) and GMS show clear lattice fringes (calculated gaps are 3.7 and 3.3 nm, inset) which have almost similar fringes gap (Figure 3.8 g and h). Further, the roughness of GMS surface is confirmed by SEM image which clearly indicates the porous architecture of nanohybrid (Figure 3.8 i and inset).

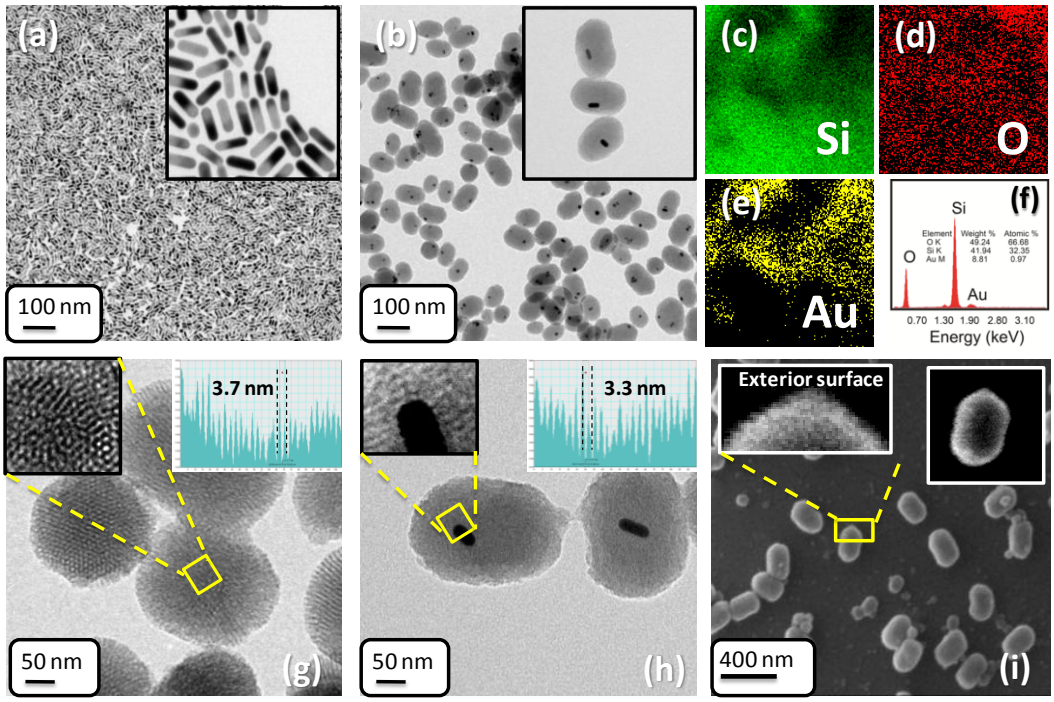

Figure 3.8. *TEM images of monodispersed (a) gold nanorods (GNRs), (b) GMS, (c-e) elemental mapping, (f) EDAX analysis of GMS nanohybrid (Au, Si, and O), (g, h) TEM images of MCM-41 mesoporous silica (MS) and GMS (fringe gaps calculated are 3.7 and 3.3 nm, insert) and (i) SEM image showing roughness of GMS surface.*

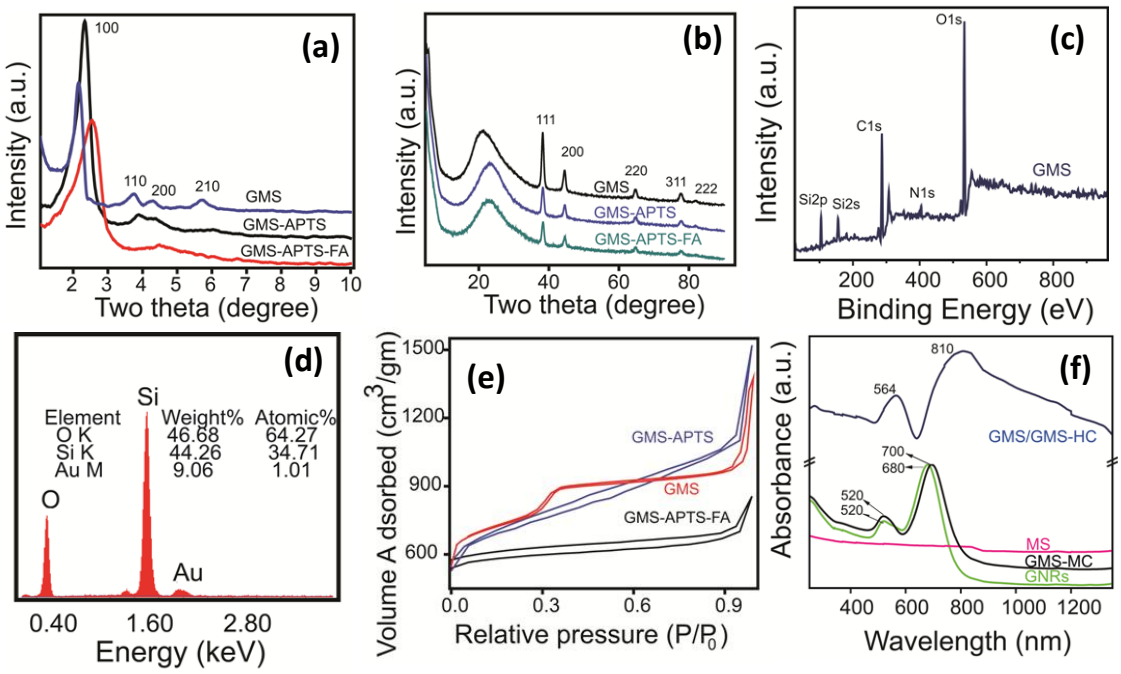

Figure 3.9. *(a) Low angle and (b) wide angle powder XRD patterns of GMS nanohybrid before and after surface functionalization with silane linker (APTS) and folic acid (FA), (c) wide scan XPS spectrum of GMS nanohybrid, (d) elemental analysis (SEM-EDAX) of surfactant free nanohybrid, (e) BET N_2 adsorption-desorption isotherms of nanohybrid before and after surface functionalization, (f) UV-vis-NIR absorbance spectra of MS, GNRs, GMS-MC and GMS-HC in aqueous solution.*

A low angle XRD pattern (Figure 3.9 a) confirms the mesoporous character and the 2D hexagonal pore packing of typical MS through its characteristics plans viz., *100, 110, 200* and *210* as observed at 2θ angles viz., 2.42, 4.02, 4.63 and 6.05 degrees respectively. Their corresponding d-values are 2.25, 1.24, 1.19 and 0.79. After exterior surface functionalization with silane linker (aminopropyle triethoxy silane, APTS, GMS-APTS) and folic acid (FA, GMS-APTS-FA also named as GMS-FA) a slight shift and reduction in diffraction planes are observed which attributes to functionalization of GMS. Wide angle XRD patterns (Figure 3.8 b) of GMS nanohybrid confirms the presence of GNR in MS through five diffraction planes (*111, 200, 220, 311, 222*) of GNRs that are seen at

diffraction angles (2θ) 38.2°, 44.3°, 64.6°, 77.6° and 81.6° respectively. Additional peak at 23° in the patterns is attributed to the presence amorphous silica (Figure 3.9 b).

The presence of GNRs in the deep core of silica shell is confirmed by XPS and EDX. The binding energy peaks as appear in the XPS spectrum, around 104, 152, 286, 404 and 533 eV are assigned to the electronic states of Si2p, Si2s, C1s, N1s, and O1s, respectively whereas binding energy peaks usually observed for $Au4f_{7/2}$, $Au4f_{5/2}$ and Br3p around 85, 89 and 190, respectively, are absent (Figure 3.9 c). On the other hand, SEM-EDX confirms the presence of elements such as Au, Si, and O elements. The absence of Au peaks in the surface sensitive XPS and its presence in the SEM-EDX, rather a bulk analysis technique, is a significant evidence of GNR is not on the surface but buried in the core of MS. Absence of peaks for N and Br in EDX spectrum and XPS confirms the efficient removal of CTAB (Figure 3.9 d). N_2 adsorption-desorption isotherm of GMS-HC (Figure 3.9 e) shows a typical type IV isotherm having a specific surface area 1100 m^2/g with a pore volume of 0.60 cm^3/g. The isotherm showing a clear capillary condensation at a relative pressure (P/P_0) of 0.1-0.4 corresponds to a pore size of ~ 3 nm, which corroborates with data obtained from TEM images. Two clear absorption bands viz., 520 nm (transverse) and 680 nm (longitudinal) are observed in the UV-Vis-NIR spectra of GNRs, GMS-HC and GMS-MC (Figure 3.9 f). GNRs in GMS-HC show a moderate red shift in the transverse band (564 nm) and longitudinal band (810 nm). GNRs in GMS-MC show a mild red shift (Figure 3.9 f). This effect can be ascribed to the refractive index (1.45) of the encapsulating silica shell of different thicknesses.[14, 18]

3.4.1.4.2 Exterior surface functionalization and pore sealing by FA targeting ligand

N_2 adsorption-desorption isotherms of GMS before and after surface functionalization with APTS and FA are shown in Figure 3.9 e. Before exterior surface functionalization, GMS displays a typical type IV isotherm (surface area 1100 m^2/g with ~3.2 nm pore diameter). A drastic reduction in BET surface area and pore volume (from 1100 to 81 m^2/g and 0.98 to 0.16 cm^3/g) and change in the shape of isotherm from type IV to I (after surface functionalization with FA) confirms the tight sealing of pores (Figure 3.9 e). To cross check the pore sealing of GMS, drug (doxorubicin, DOX an anticancer drug) loading test before and after surface functionalization with FA have been carried out (Figure 3.10). About 50 % drug loading efficiency is calculated before surface functionalization and after surface functionalization the loading efficiency is calculated ~ 2 % (DOX loading efficiencies are calculated using the linear equilibrium curve of drug and equations eq. 3.1 and 3.2).

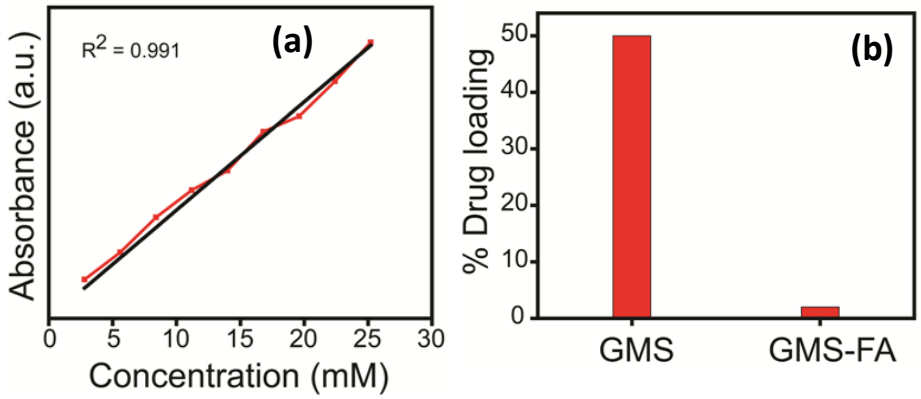

Figure 3.10. *(a) linear equilibrium curve of drug and (b) % drug loading efficiency of nanohybrid before and after surface functionalization with folic acid (GMS-APTS-FA/GMS-FA).*

Further, the surface functionalization is confirmed by FTIR spectra (Figure 3.11 a) and thermogravimetric (TG/DTA) analysis as shown in Figure 3.11 b and c. The observations of O-H stretching vibrations (3400 cm^{-1}), Si-O-Si stretching vibrations (796-1229 cm^{-1}) are characteristics of MS, peak at 1146 cm^{-1} due to Si-OCH_3 stretching and that at 1558 cm^{-1} corresponding to -NH_2 bending vibrations of silane linker confirm the attachment of APTS on to GMS. Vibrations as seen at 1700 $cm^{-1}$and 1603 cm^{-1} are assigned to C=O stretching and N-H bending of the CONH group. The IR bands between 1413 and 1507 cm^{-1} are due to stretching vibrations of the pteridine and p-amino benzoic acid rings of FA. In addition, thermogravimetric analysis of the GMS and GMS-APTS and GMS-APTS-FA (GMS-FA) are carried out in the temperature range of 0-900 °C, at a heating rate of 10 °C/min in nitrogen atmosphere. Two major weight losses in the temperature range of 150-280 °C (39.5 %) and 280-750 °C (25.8 %) are observed in TG curve of as synthesized GMS nanohybrid which may be due to the decomposition of CTAB surfactant. However, surfactant free GMS nanohybrid shows very little weight loss nearly 14.4 % that may be attributed to the moisture and indicates the removal of CTAB surfactant from the mesopores of nanohybrid. The TG curves of the GMS-APTS shows the weight loss in two stages. In the first stage, TG curve shows about 5-6 % weight loss between 50 and 150 °C that may be due to the removal of adsorbed water. Thermal decomposition of the organic components begins at temperature around 300 °C. The most important feature is the presence of an extremely intense exothermic peak centered at 305 °C and a less intense exothermic peak at 437 °C in the DTA curve, accompanied by a remarkable mass loss in the TG curve. From the TG curve, it is observed that near about 35 % weight loss occurred in the temperature range of 300-600 °C, which is assigned to the decomposition of

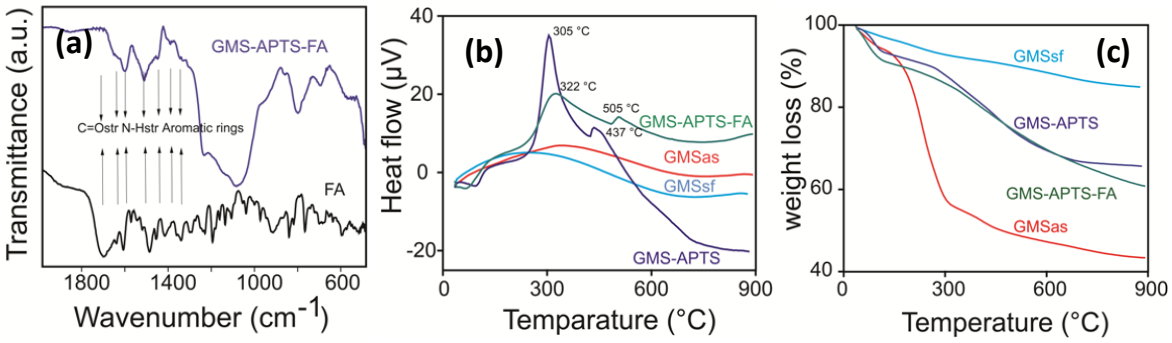

Figure 3.11. *(a) FTIR spectra of GMS-APTS-FA and FA, (b, C) DTA and TG curves of GMSas, GMSsf, GMS-APTS, GMS-APTS-FA.*

aminopropyl group functionalized with MS. The TG curves of GMS-APTS-FA have shown weight loss in three major stages. First weight loss in the temperature range of 50-108 °C, second in the temperature range of 150-350 °C and third weight loss in the temperature range of 350-850 °C. As observed at the end of the entire decomposition reaction, a total of 40-42 % weight losses occurred for folic acid anchored on the GMS through APTS. Further this observation is corroborated with DTA plots, which confirm the decomposition of folic acid. In DTA, an endothermic peak obtained around 108 °C that due to the loss of adsorbed water. Three exothermic peaks at around 140 °C, 322 °C and 505 °C that may be assigned for the decomposition of the various organic moieties of the folic acid.

3.4.1.4.3 Cargo capacity of nanohybrid

The cargo capacity (% loading and entrapment efficiency, Figure 3.12) of GMS is tested using doxorubicin hydrochloride (DOX), an anticancer drug and Rhodamine B (RhB) dye. The cargo capacities are calculated using equation 3.1 and the UV-Vis absorbance spectra. The tests reveal that GMS nanohybrid shows loading efficiencies of 57 % with DOX and 48 % with RhB.

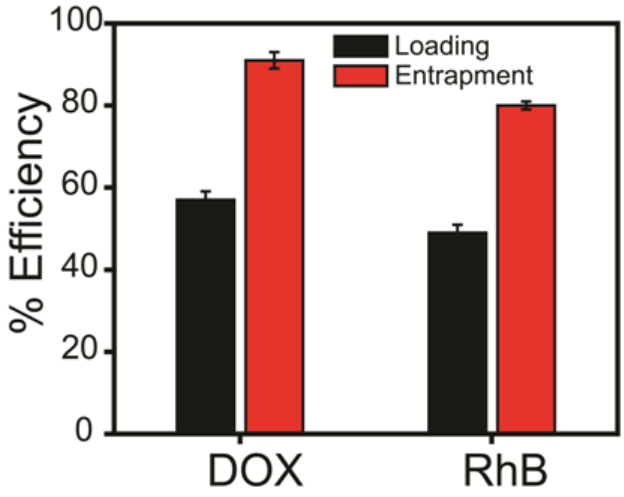

Figure 3.12. *% loading and entrapment efficiency of designed GMS nanohybrid.*

3.4.2 NIR responsive mesoporous nanohybrid for multimodal bio-imaging and targeted synergistic chemo-photothermal ablation for cancer cell lines

Today, chemotherapy and radiotherapy are the most commonly used treatments for cancer. Doses of these individual therapies are insignificant to eradicate the cancer cells. Therefore, GMS nanohybrid has been designed for multifunctional cancer theranostics (Scheme 3.4). In addition designed nanohybrid is used as a multimodal bio-imaging (X-ray CT and fluorescence) agent. Further, FA functionalized GMS nanohybrid shows highly selective targeting ability and quick synergistic combined chemo-photothermal ablation for breast cancer cell lines (MDA-MB-231 and MCF-7).

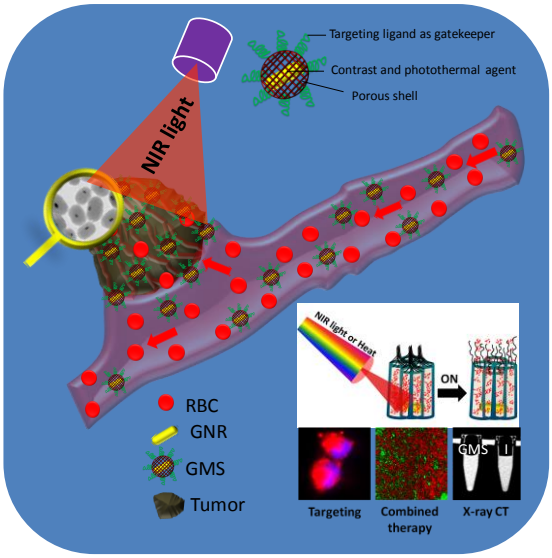

Scheme 3.4. *GMS nanohybrid shows targeted multimodal bio-imaging and cancer therapies.*

3.4.2.1 Photothermal and contrast performance

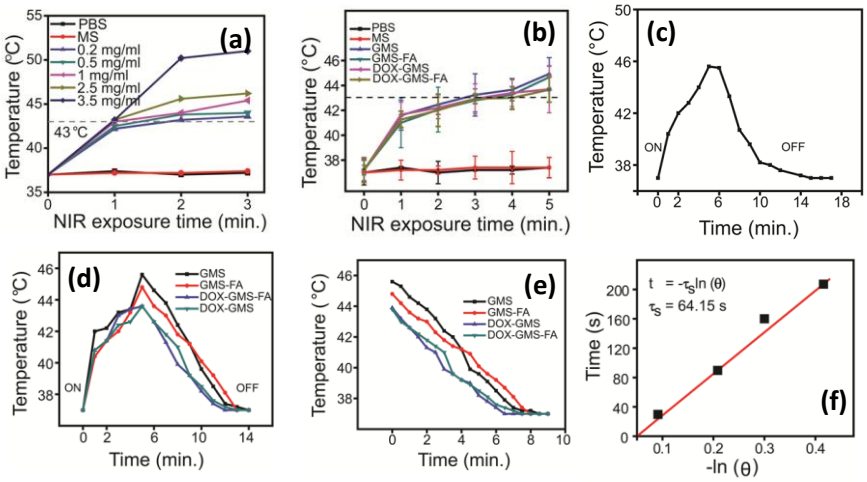

Figure 3.13. *Photothermal performance of GMS nanohybrid (a) temperature profile of GMS nanohybrid at different concentration as a function of irradiation time (3 min), (b) time dependent photothermal transduction behavior of GMS, GMA-FA, DOX-GMS, DOX-GMS-FA with PBS and MS as control using 0.2 mg/mL concentration of each, (c, d, e) time dependent steady-state temperature with "ON-OFF'' irradiation cycles, the laser is turned off after 5 min. irradiation of 808 NIR laser and (f) steady-state plot of cooling time versus negative logarithm of the temperature.*

Due to high atomic number (79), X-ray absorption coefficient and localized surface plasmon resonance (LSPR, 650-900 nm) [14] of gold nanorods (GNRs), the mesoporous silica coated gold nanorods (GMS) exhibit good photothermal and contrast ability.

To understand the photothermal performance of GMS nanohybrid, photothermal transduction experiments are carried out. The photothermal behavior of GMS nanohybrid at different concentrations (0.2-3.5 mg/mL) is evaluated by 3 min. continuous exposure of NIR radiation (wavelength = 800 ± 5 nm). The photothermal response constantly increases with the concentration of GMS, as observed through a constant raise in temperature (Figure 3.13 a). While the initial stabilized temperature is 37 °C, on NIR exposure for 3 min., the temperature increases to 44 °C for 0.2 mg/mL of (minimum) concentration and to 52 °C for a concentration of 3.5 mg/mL (maximum). Generally, yielding a temperature beyond 43 °C is considered as the on-set of photothermal therapy due to the denaturation of proteins, disruption of the cell membrane and ablation of tissue. Achieving this response with GMS in less than 3 min. especially at lower NIR power density of mere 0.5 W/cm^2 is fairly exceptional. This is further remarkable especially at a significantly low concentration of 0.2 mg/mL (Figure 3.13 b). The photothermal test of GMS nanohybrid (0.2 mg/mL) before and after drug loading and surface functionalization has been done, where time dependent temperature variation is recorded. Based on this transduction experiment, we understand that the designed nanohybrid shows hyperthermia temperature (43 °C) within 3 min. even after drug loading and surface functionalization which indicates that drug loading and surface functionalization does not affect the photothermal performance of nanohybrid (Figure 3.13 b).

To check the photothermal conversion efficiency of GMS, the time dependent steady-state temperature with "ON-OFF'' irradiation cycles by using 808 nm NIR laser (heating temperature ON and cooling temperature OFF, Figure 3.13 c) is recorded. Similarly, the "ON-OFF" laser irradiation is also checked for GMS nanohybrid before and after drug loading and surface functionalization. Based on above experiments, slow cooling rate (45.5 to 37 °C in 8 min.) than the heating rate (37 to 45.5 °C in 5 min.) is observed which indicates the good temperature holding capacity (8 min.) and photothermal conversion efficiency (~ 30 %) of nanohybrids (Figure 3.13 c-f and eq. 3.4, 3.5). Overall, after complete analysis of photothermal transduction experiment, photothermal performance and heating to cooling rate, GMS nanohybrid can be used as an excellent theranostics for cancer.

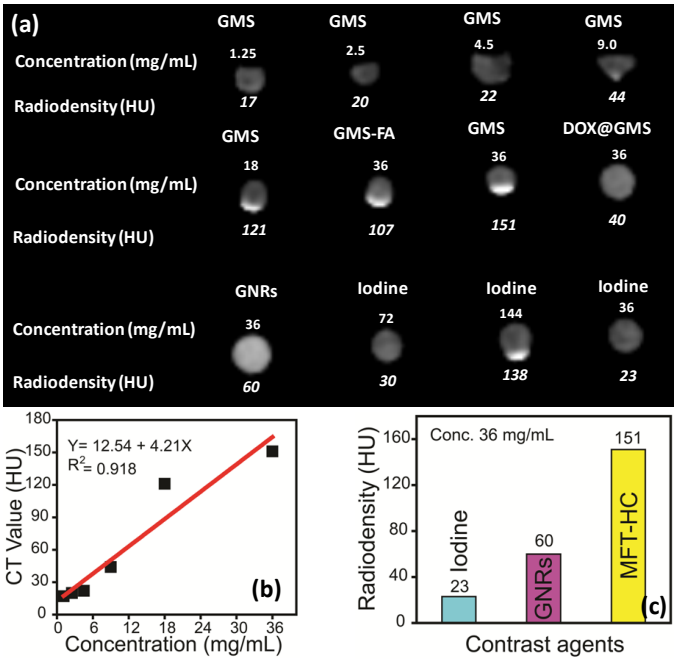

Figure 3.14. *(a) X-ray CT images with Hounsfield unit (HU) of Iodine, GMS nanohybrid at different concentrations and GNRs by using clinical Toshiba 64 slice CT scanner at 120 kV,50 mA, (b) linear correlation of Hounsfield unit (HU) and concentrations and (c) radiodensity comparison of designed GMS nanohybrid (MFT-HC) with GNRs and iodine.*

On the other hand, GMS also shows contrast ability (presence of GNRs) which can give 3D structure of tumor with high and deep resolution. The radiodensity (Hounsfield unit, HU value) of designed nanohybrid is measured by using RadiAnt DICOM Viewer. X-ray CT, a most commonly used diagnostic tool for high resolution deep 3D anatomic structure of tumor is used to study the contrast ability of GMS nanohybrid.[36-39] Figure 3.14 provides the correlation between the effective contrast ability of the GMS at different concentrations from 1.12 to 36 mg/mL. Results include the radiodensity in Hounsfield unit, (known as HU value) for GMS, GNRs and Iodine in aqueous media (Figure 3.14 a-c). As the concentration of nanohybrid increases, the CT signal intensity improves with a corresponding rise of contrast brightness. The HU values are measured by RadiAnt DICOM Viewer.[36] A representative linear correlation between concentration of GMS nanohybrid and the radiodensity (R^2 = 0.918) is shown in Figure 3.14 b. Due to high atomic number and density, gold shows higher contrast (19.32 g/cm^3) compared to that of Iodine (4.90 g/cm^3). The contrast distinction is further conspicuous at higher concentration viz., 36 mg/mL. While a radio density of 23 HU is recorded for a high iodine concentration, GMS recorded a brightness is 151 HU for the same concentration. This is attributed to the presence of GNRs in the cores of GMS whose X-ray attenuation is much stronger than that of iodine (Figure 3.14 c).

3.4.2.2 Stimuli responsive (pH, NIR light and temperature) drug release performance

Low molecular weight and high water soluble FA[40] plays dual role as pore covering agent that help to prevent the premature drug release and pores open during stimuli response (pH, NIR light and temperature) and as targeting ligand also (Figure 3.15 a-e). In details,

the time dependent (up to 24 h) drug leakage from GMS nanohybrid before and after surface decoration with FA (GMS-APTS-FA also named as GMS-FA) at physiological condition (7.4 pH and 37 °C) has been calculated ~ 16 % and ~ 3 % respectively. The negligible drug leakage from GMS-FA indicates the pore blocking nature of FA (due to л-л stacking, self assembly of pteridine and p-amino benzoic acid rings and H-bonding between two FA moieties) [41-44] helping in prevention of premature drug release. Further, the release kinetics is tested at various pH (2, 4, 5, 6 and 7.4) for a period of 24 h to understand the controlled drug release via. pore opening operation at various stages of intracellular uptake. When pH decreases from 7.4 to pH 6 then 5, the amount of drug release increases from 3 % to 50 %

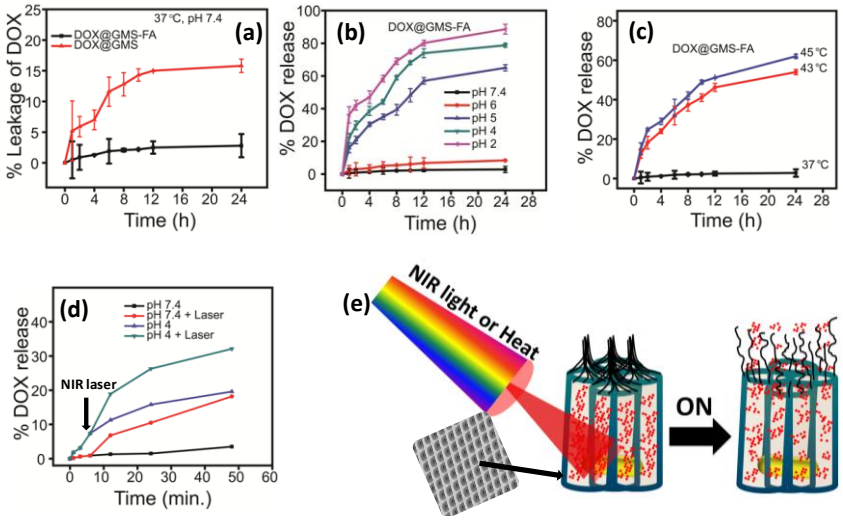

Figure 3.15. *Stimuli responsive triggered drug release and pore blocking and opening operation of FA on drug loaded GMS nanohybrid. (a) prevention of premature leakage of drug from DOX-GMS after surface decoration with FA, (b) pH, (c) temperature, (d) NIR responsive switching or pore opening operation of FA on DOX-GMS and its time dependent triggered drug release profiles and (e) schematic illustration of the evolution of molecular FA switches and gatekeeper mechanisms of FA on GMS nanohybrid.*

and 55 % respectively. Moreover, in the deep intercellular environment[28] at pH 4 and 2 the drug release is found to be ~ 78.6 % and ~ 89.7 % respectively. It is must to note that the amount of drug release is increased up to ~ 89.7 % from 3 % when nanovehicle travels from extracellular (pH 7.4) to deep intracellular environment (pH 2) which is due to the disturbance in self assembly, H-bonding of FA moieties and functional groups protonation of FA. Additionally, the release kinetics is also tested at various temperatures (37, 43 and 45 °C) for a period of 24 h to understand the controlled drug release through gatekeeper operation at various stages of photothermal conditions (hyperthermia, 43 °C and ablation, 45 °C). When the drug loaded GMS-FA nanohybrid introduced in physiological temperature (37 °C) the drug release is found to be negligible about 3 %. But in hyperthermia and ablation temperature the release increases to ~ 56.4 % and further ~ 60 % which is due to the disturbance in self assembly and H-bonding of FA moieties via external heating. Further, the NIR (800 nm for 5 min. exposure) triggered drug release kinetic study has been done at extracellular (pH 7.4) and intracellular (pH 4) conditions for a period of 50 min. Before NIR exposure on drug loaded nanohybrid or nanovehicle at pH 7.4, 3.8 % drug release is calculated which is further increased ~ 15 % after NIR exposure. When DOX loaded nanohybrid is introduced in intracellular (pH 4) condition, ~ 15 % drug release is calculated before NIR exposure, while ~ 33 % drug release is calculated after NIR exposure. The high amount of drug release in the short period of time indicates the successful operation of pore opening including both the factors: (a) internal heating and (b) acidic pH. Here in these conditions, the pore block/gatekeepers open due to the disturbance in self assembly (internal heating) and H-bonding (acidic pH) of FA moieties. From the

above studies, stimuli response of FA on exterior surface of nanohybrid for controlled drug release is understood successfully.

3.4.2.3 *In vitro* biocompatibility

In this chapter *in vitro* study (MTT assay) on normal cells (L929, NIH-3T3), red blood cells (RBCs) and cancer cells (HeLa cells, breast cancer cells MCF-7, MDA-MB-231 and 4T1) for biocompatibility and targeted synergistic therapy are reported. Cytotoxicity due to bare GMS, CTAB and functionalization of FA is understood by *in vitro* MTT assay on fibroblastic L929 normal cell-line using surfactant-free GMS (GMSsf), as-synthesized GMS (GMSas) and GMS-FA respectively (Figure 3.16 a). More than 90 % cell viability is observed with surfactant-free GMS and GMS-FA demonstrating their significant

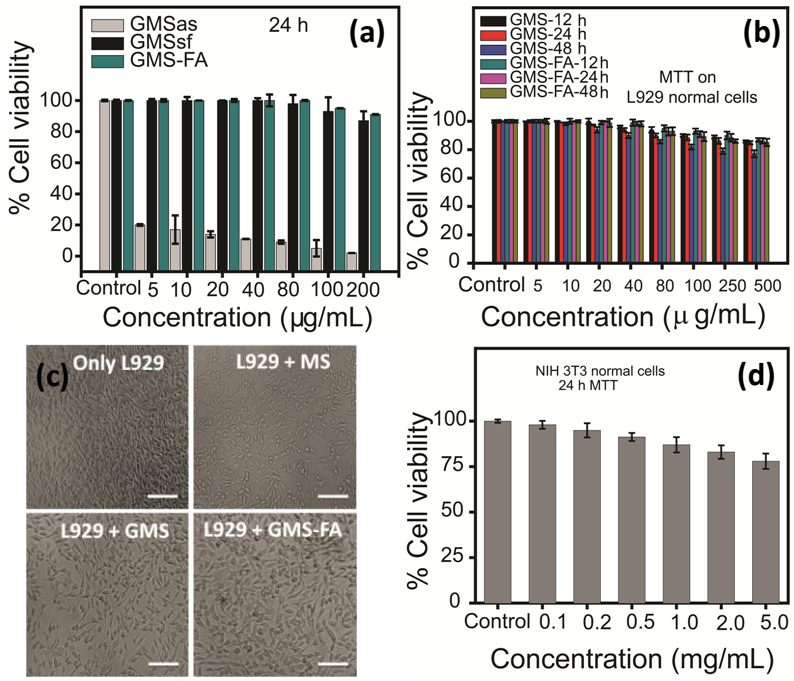

Figure 3.16. *Concentration dependent (a) MTT assay for as-synthesized GMS (GMSas), surfactant free (GMSsf) and GMS-FA on fibroblastic normal cell L929, (b) short and long term % cell viability of GMS and GMS-FA. (c) Bright field microscopy images of materials treated L929 normal fibroblastic cells and (b) % cell viability of GMS-FA on NIH-3T3 normal cells.*

biocompatibility. A drastic reduction in cell viability to ~ 20 % is observed with as-synthesized GMS. This is attributed to the presence of high concentrations of CTAB. It may be noted that the CTAB is completely removed later and the same is ensured by spectroscopy and through the significant increase in the cell viability as explained in the text earlier and as shown in Figure 3.16 a. To understand the function of GMS nanohybrid before and after surface functionalization for short and long term (12, 24 and 48 h) biocompatibility on normal fibroblastic cells (L929), concentration dependent (5-500 µg/mL) cytotoxicity studies has been done (Figure 3.16 b). More than 80 % cell viability is calculated for GMS (48 h, 500 µg/mL) whereas ~ 90 % viability is observed for GMS-FA due to high aqueous solubility and compatibility of folic acid. Figure 3.16 c shows nanohybrid treated L929 cells (bright field microscopic image). In addition, the designed nanohybrid shows good viability with NIH-3T3 normal cells also even at higher concentration (5 mg/mL, Figure 3.16 d). About 95 % cell viability is observed at minimum concentration (0.1 mg/mL), 85 % at 1 mg/mL concentration and more than 70 % viability is calculated at relatively high concentrations (5 mg/mL).

3.4.2.4 *In vitro* targeting ability and cancer theranostics understanding

Targeting performance of DOX loaded GMS-FA is carried out on various cancer cells viz., HeLa, MCF-7, MDA-MB-231 and 4T1 (Figure 3.17). A strong red fluorescence is observed in all the cases of DOX loaded nanohybrid on 4 h of incubation time with different cancer cells indicating the significant DOX release in the cellular interiors that clearly corroborates its targeting and delivering ability. Further, the time dependent targeting

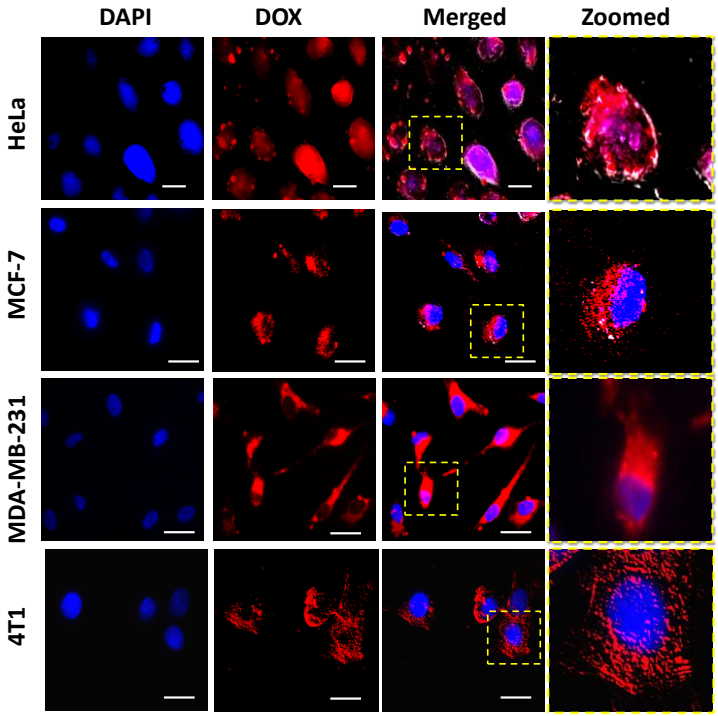

Figure 3.17. *In vitro targeting ability after 4 h incubation of DOX loaded GMS-FA on various cancer cell lines (HeLa, MCF-7, MDA-MB-231 and 4T1 cancer cells).*

ability (4, 12, 24 h and pre-saturated folate receptors on cell membrane, Figure 3.18) on both breast cancer cells (MCF-7 and MDA-MB-231) are understood. Fluorescence microscopic images show thick red patches (DOX) around the cell nucleus which increases with the incubation time (from 4 to 24 h) for both the cancer cells. The red patches (DOX) around the cell nucleus indicate the entry of DOX in the cell nuclei of both the cancer cells after 12 h of incubation time. It has been observed that more dark red patches in MCF-7 cells than the MDA-MB-231 cells which are due to fast cellular uptake through over expressed FR. Further, the targeting ability of DOX-GMS-FA is also confirmed with pre saturated FRs on cancer cell membrane by free FA on both cancer cells for 24 h (Figure

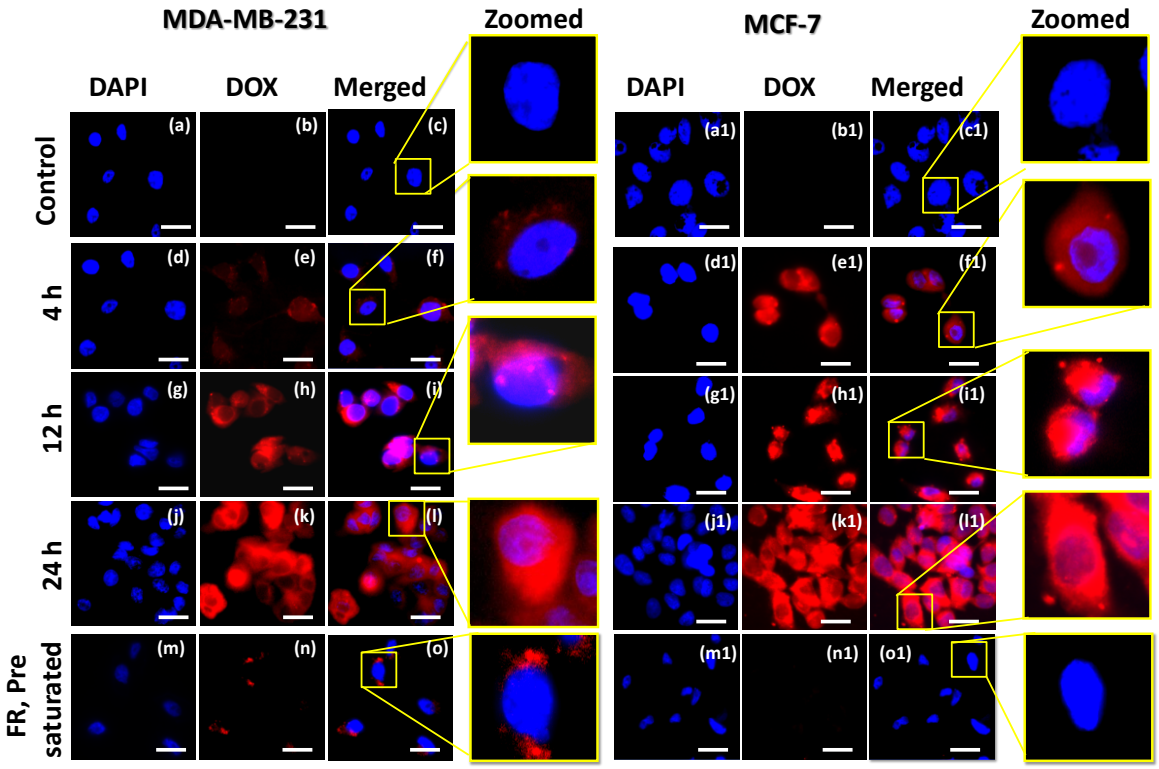

Figure 3.18. *Time dependent (4-24 h) in vitro targeting ability of DOX loaded GMS-FA on two different breast cancer cell lines (MDA-MB-231, a-l and MCF-7, a1-l1). Targeting ability after pre-saturation of folate receptors on both the cancer cell membrane (m-o and m1-o1).*

3.18 m-o and m1-o1). Further, multifunctional theranostics performance of nanohybrid (with and without drug loading and surface functionalization) is understood for cancer cell lines (MDA-MB-231 and MCF-7). Herein, we have observed that only NIR laser, GMS nanohybrid and NIR exposed GMS nanohybrid before DOX loading and FA functionalization does not affect the cell death for both MDA-MB-231 and MCF-7 breast cancer cells (cell viability is calculated ~ 98 %). In case of targeted photothermal therapy (treatment with GMS-FA), cell viabilities are calculated 15 % for MCF-7 and 25 % for MDA-MB-231 while more than 95 % cell viability is calculated before NIR treatment for both cancer cell lines, respectively (Figure 3.19 a-c). In the above study, the cell death is

observed due to photothermal activity (produced heat after NIR exposure) of GMS-FA nanohybrid under NIR light exposure.

Further, following groups of treatment for individual targeted chemotherapy, photothermal therapy and synergistic combined chemo-photothermal therapy are made (Figure 3.19); Group-1: only breast cancer cells with and without NIR light (800 nm) exposure for 5 min., Group-2: GMS and DOX-GMS treated cancer cells with and without 5 min. NIR exposure, Group-3: GMS-FA and DOX-GMS-FA treated cancer cells with and without 5 min. NIR exposure and Group-4 both cancer cells are pre-treated with free FA which saturates the folate receptors (FR) on the cell membrane. Now, FR saturated cells are treated with GMS-FA and DOX-GMS-FA, respectively. In the above studies, each set of treatment is tested through MTT assay (Figure 3.19 b and c) and following cell viability is calculated. For both cancer cells the viability is calculated 100 % before and after NIR treatment which indicates that NIR does not affect the cells (control). GMS shows 100 % viability and DOX-GMS shows more than 90 % cell viability before and

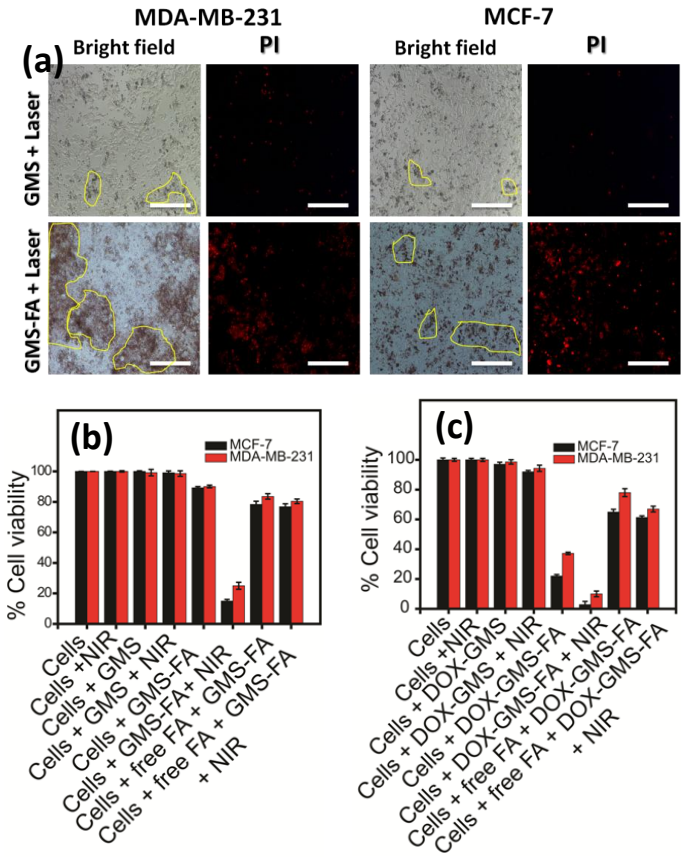

Figure 3.19. *Therapeutic efficiency of designed nanohybrid (a) dead cells can be seen in fluorescence microscopy images of breast cancer cells, laser spot (yellow circles) and cell death (red, PI staining) scale bar is 150 μm. (c, d) % cell viability of both breast cancer cells (MCF-7 and MDA-MB-231) treated with GMS-FA, DOX- GMS-FA and pre saturation of FR receptors on cell membrane by free FA with and without NIR light exposure.*

after NIR exposure (control). When both cancer cell lines are treated with DOX loaded GMS-FA the cell viability is calculated 22 % for MCF-7 and 37.2 % for MDA-MB-231 cells before NIR exposure which indicates the chemotherapeutic effect on both cancer cell lines. Further, in case of NIR light exposure, cancer cell lines treated with DOX loaded GMS-FA, the cell viability is calculated ~ 2.8 % for MCF-7 and 10 % for MDA-MB-231 cells which is due to the effect of drug and heat produced by nanohybrid under NIR exposure. The variation in cell death or viability of both breast cancer cell lines indicates

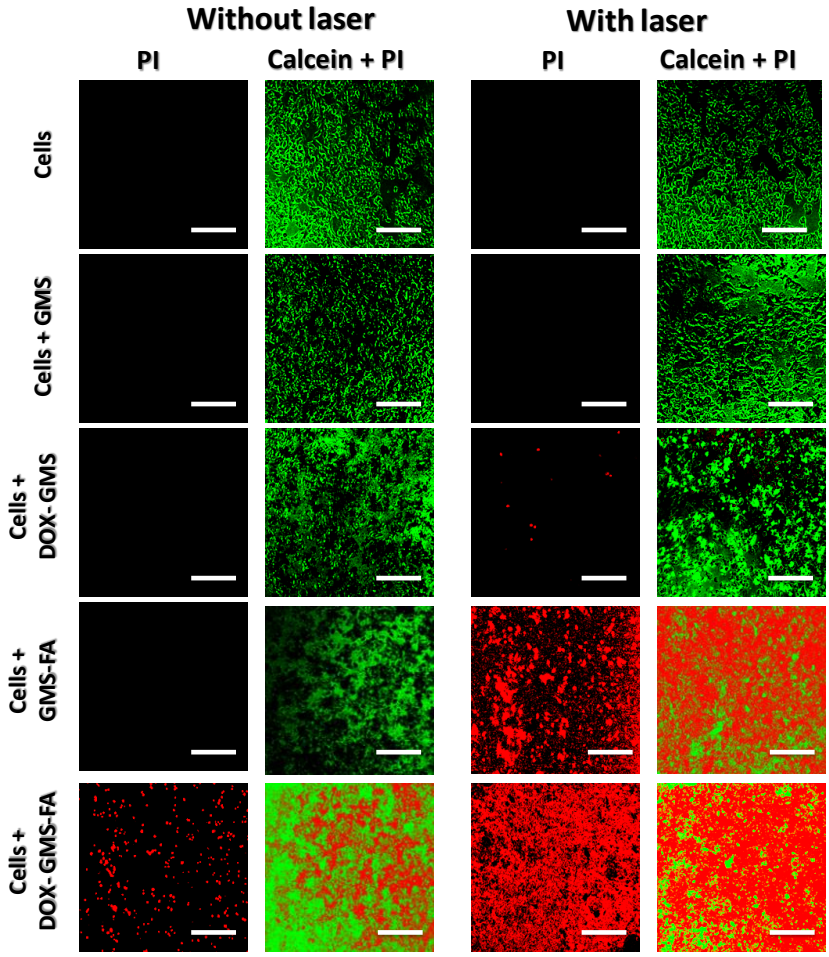

Figure 3.20. *In vitro therapeutic efficiency of designed nanohybrid. Dead and live breast cancer cells (MCF-7) after individual therapy (chemo, photothermal therapy) and synergistic combined chemo-photothermal therapy can be seen through fluorescence microscopy images after staining with two different dyes (Calcin AM green, for live cells and PI red, for dead cells).*

that the MCF-7 may have more FR on their cell membrane compared to MDA-MB-231 cells. Moreover, to reconfirm the targeting ability and synergistic chemo-photothermal therapy on both cancer cells, the FR on both cells membrane are pre saturated with free FA and then these cells are treated with GMS-FA and DOX-GMS-FA before and after NIR treatment. Here, 78 % and 76 % cell viability for MCF-7 before and after NIR exposure are calculated while 83 % and 80 % cell viability are calculated for MDA-MB-231 before

and after NIR exposure. In case of DOX loaded nanohybrid (DOX-GMS-FA) 65 % and 61 % cell viability are calculated for MCF-7 cells whereas 78 % and 72 % cell viability is calculated for MDA-MB-231 cancer cell lines. The above cell viabilities indicate that both cancer cells are successfully pre saturated with free FA which prevents the cellular uptake of GMS-FA. The pre saturation of FR by free FA on both cancer cells are also confirmed by fluorescence imaging (Figure 3.18). The poor fluorescence of DOX is observed as compared to unsaturated cells when DOX-GMS-FA is treated with both cancer cell lines. Figure 3.19 a, fluorescence microscopic images (bright field image and propidium iodide, PI staining) show the laser spot (yellow circles) in the both breast cancer cell lines. Further, to observe the dead and live cells (MCF-7, Figure 3.20) after individual therapy (chemo, photothermal therapy) and synergistic combined chemo-photothermal therapy the cancer cells are stained with two different dyes (Calcin AM green, for live cells and PI red, for dead cells). We have observed high PI staining in the set of DOX-GMS-FA treated MCF-7 cancer cells after NIR exposure (combined chemo-photothermal therapy, Figure 3.20). Overall, the combined chemo-photothermal therapy is more effective than the individual ones (chemo and photothermal therapy).

3.4.2.5 Hemolysis study

Further, to understand the functional influence of nanohybrid on RBCs the hemolytic activity (Figure 3.21) has been investigated.[45-48] In this study, the concentration range (50-1500 µg/mL) of GMS nanohybrids are used. In detail, 0.8 mL of nanohybrids in PBS from desired concentrations are mixed with 0.2 mL of isolated RBCs and further incubated for a period of 12 h at room temperature (RT). Similarly, the positive and negative controls are prepared by mixing 0.8 mL of DI water and PBS respectively, to RBCs.[45, 47] Hemolytic

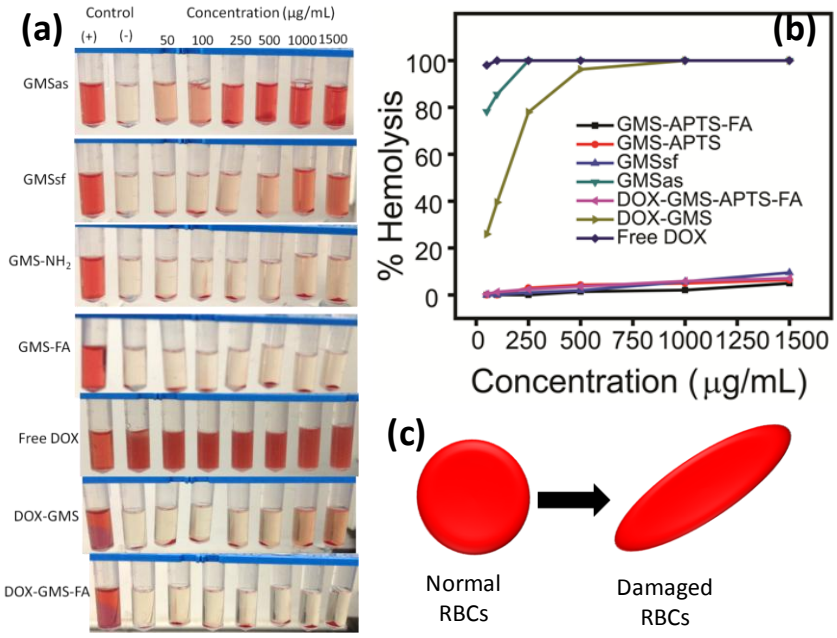

Figure 3.21. *Hemolysis study (a) digital photographs and (b) % Hemolysis of RBCs incubated GMS based nanohybrids at different concentrations ranging from 50 to 1500 µg/mL for 12 h. The presence of red hemoglobin in the supernatant indicates damaged RBCs. DI water and PBS are used as positive and negative control, respectively. (c) Schematic represents the damage of RBCs during hemolysis.*

activity of nanohybrids are calculated by UV-Vis absorption of hemoglobin at 540 nm, which is released in to the solution from hemolyzed RBCs (eq. 3.7). The nonporous GMS nanohybrid shows highest hemolysis (78 % at 50 µg/mL and 100 % at 1500 µg/mL) which is due to high electrostatic interaction between negatively charged GMS surface (OH groups) and positively charged choline group of RBCs and also the presence of CTAB surfactant.[45] On the other hand, mesoporous GMS nanohybrid also shows hemolytic activity (1 % at 50 µg/mL and 6 % at 1500 µg/mL). Surface functionalized GMS (silane linker and folic acid) shows negligible hemolytic activity which is calculated to be ~ 2 % and 1 % after silane and FA functionalization. In the end of hemolysis experiment, precipitated RBCs can be seen in digital photographs which are given in Figure 3.21 a. In

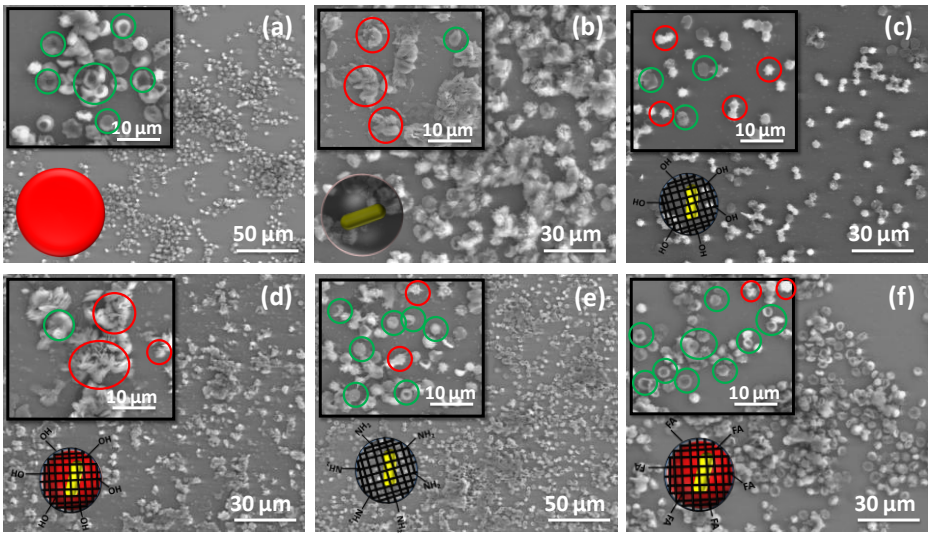

Figure 3.22. *SEM images of RBCs treated materials. (a) only RBCs as control, (b) RBCs treated as synthesis GMS, (c) RBCs treated with porous GMS nanohybrid, (d) RBCs treated with drug loaded GMS (DOX-GMS), (e) RBCs treated with amine functionalized GMS and (f) RBCs treated with drug loaded FA functionalized GMS (DOX-GMS-FA).*

addition, the same experiment has also been done with drug loaded GMS, GMS-FA and free drug (DOX). Negligible hemolysis (1 %) is calculated for DOX-GMS-FA even at high concentration (1500 µg/mL) which is due to the blocking of DOX in GMS pores and high biocompatibility of FA. Further, about 20 % (50 µg/mL) to ~ 100 % (1500 µg/mL, Figure 3.21 b) hemolysis are calculated for DOX-GMS which are due to the DOX released from GMS pores. To check the adsorption of hemoglobin (absorbance at 540 nm) on the surface of nanohybrids, nanohybrids are incubated with the RBCs overnight. The visibility of red color indicates the released hemoglobin from damaged RBCs (Figure 3.21 c) which is clearly seen in positive control (DI water), nonporous and porous GMS nanohybrids, free DOX and DOX-GMS. The colorless supernatant in all concentrations are observed for the surface functionalized GMS nanohybrid (amine and FA functionalized GMS). The clear damage and morphological changes of RBCs can be seen in SEM images (Figure 3.22 a-f)

of RBCs treated with GMS nanohybrid before and after drug loading and surface functionalization. In Figure 3.22 SEM images, (a) only healthy RBCs (in green circles) as a control (without nanohybrid treatment), (b) shows RBCs treated with as synthesized GMS where damaged cells can be seen in red circles which is due to CTAB surfactant and silanol groups, (c) RBCs treated with surfactant free nanohybrid the minimum damaged cells (red circle) and healthy ones (green circle) can be seen, which is due to the only silanol groups, (d) RBCs treated with drug loaded GMS nanohybrid where clumps of damaged cells can be seen in red circles which is due to the released drug and silanol groups, (e) RBCs treated with amine functionalized GMS where maximum healthy cells are observed which is due biocompatible amine moiety on GMS nanohybrid and (f) RBCs treated with FA functionalized GMS where maximum healthy cells are also seen which is due biocompatible FA moiety on GMS nanohybrid. The electrostatic binding between silanol groups (negatively charged) of GMS nanohybrid and phosphatidyl choline (zwittionic) group of RBC membrane is the main region for deformation/hemolysis of RBCs. Here, the masking of silanol groups of GMS nanohybrid is preventing hemolysis.

3.4.3 Nanohybrid as a safe contrast agent for *in vivo* tumor diagnosis

Biocompatibility and high radiodensity of nanosized contrast agents are necessity for tumor imaging. Various gold and silica based nanohybrids are studied for biomedical imaging. Their systematic course for tumor diagnosis, organs safety, contrast ability and smooth excretion are less understood so far. Here in this chapter, we report a minimal single dose administration of newly designed safe contrast agent viz., mesoporous silica coated gold nanorods (GMS nanohybrid, Scheme 3.5) for localized 4T1 tumor diagnosis and specific bio-distribution.

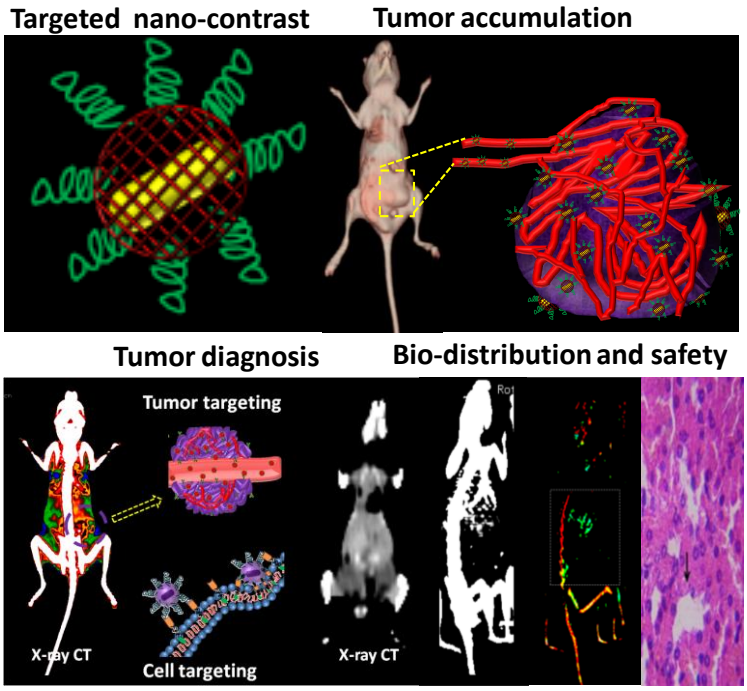

Scheme 3.5. *Schematic shows the targeted tumor diagnosis, bio-distribution and safety of designed nanohybrid for mice model.*

Another objective of this work is to understand the specific tumor diagnosis, bio-distribution and *in vivo* toxicity of designed GMS nanohybrid. Prior to *in vivo* study several aspects of nanohybrid such as biocompatibility, contrast and targeting ability have been understood which are discussed earlier. Contrast linearity between Hounsfield units (HU) and concentration is observed at clinical voltage of CT scanner (120 kVp). The presence of encapsulated GNRs brings about 7 times higher (HU = 151) contrast as compared to the iodinated contrast[2] (HU = 23, today's contrast agent, Figure 3.14).

3.4.3.1 *In vivo* tumor diagnosis by targeted contrast agent

To check the tumor accumulation and targeting ability of FA functionalized nanohybrid, a minimum and single dose (10 mg/kg body weight) of nanohybrid as a targeted contrast agent is subcutaneously injected in 4T1 tumor bearing female Balb/c mice (Figure 3.23 a-e) and CT scans are taken at 1 and 24 h respectively (see Figure 3.23 b-d). Specific breast

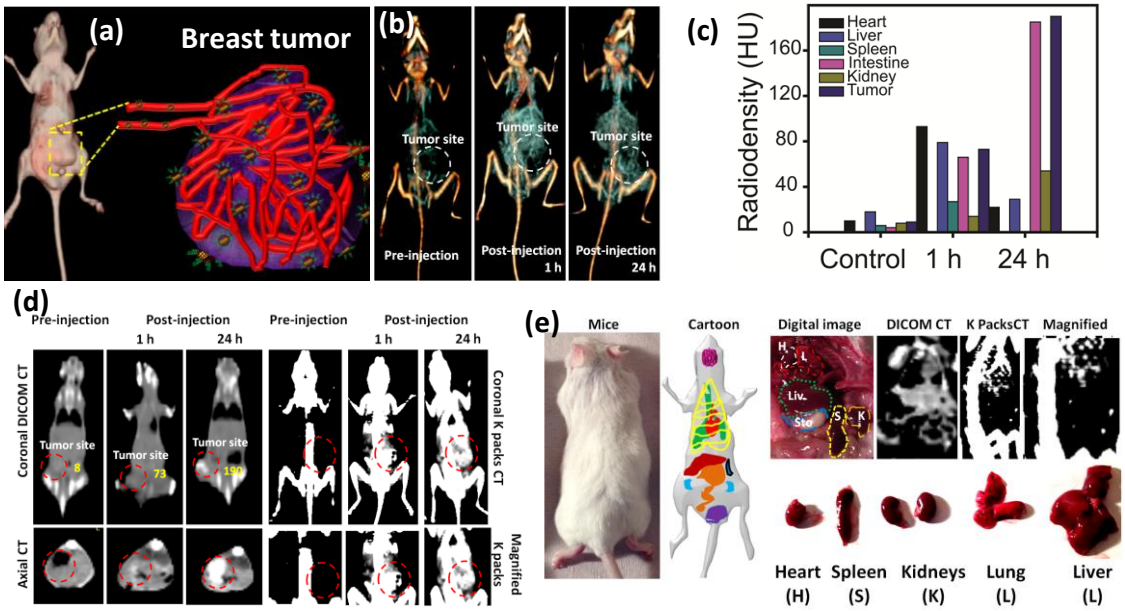

Figure 3.23. *(a) Specific tumor accumulation of targeted GNMS-FA nanohybrid in breast tumor and tumor location in mice body, (b) tumor location in mice body at various time point (1 and 24 h) through CT scans after nanohybrid injection with compared to pre-injected mice, (c) radiodensity observation at tumor site and in major organs (heart, liver, spleen, intestine, kidney) at multiple time points in post-injected mice which is compared to pre-injected mice as a control, (e) coronal and axial images through DICOM viewer and K packs show the time dependent tumor location in mice body with enhanced radiodensity and brightness at tumor site and (e) bio-distribution of nanohybrid in major organs of Balb/c mice, organs is seen in digital photographs and contrast in major organs is seen through X-ray CT images.*

tumor location is observed through coronal and axial CT slices of mice body with high radiodensity in heart (HU = 52), liver (HU = 68) and spleen (HU = 43) within an hour post-injection (radiodensity of tumor spot is HU = 73, Figure 23 b-d) of nanohybrid. Further, the radiodensity decreases gradually from heart (HU = 4), liver (HU = 28) and spleen (HU = 7) and is seen to increase in the intestine (HU = 180) and tumor site (HU = 190, Figure 3.23 c, d) with higher brightness and contrast after a passage of 24 h post-injection. However, tumor spot is difficult to identify in pre-injected mice as understood

from CT images. Moreover, contrast observations are present for a 24 h time period (after nanohybrid injection through subcutaneous) at the tumor site location with enhanced radiodensity (HU= 190) and brightness indicating the higher accumulation of nanohybrid in tumor through specific receptor-ligand strong binding.

3.4.3.2 Bio-distribution and *in vivo* toxicity of targeted contrast agent

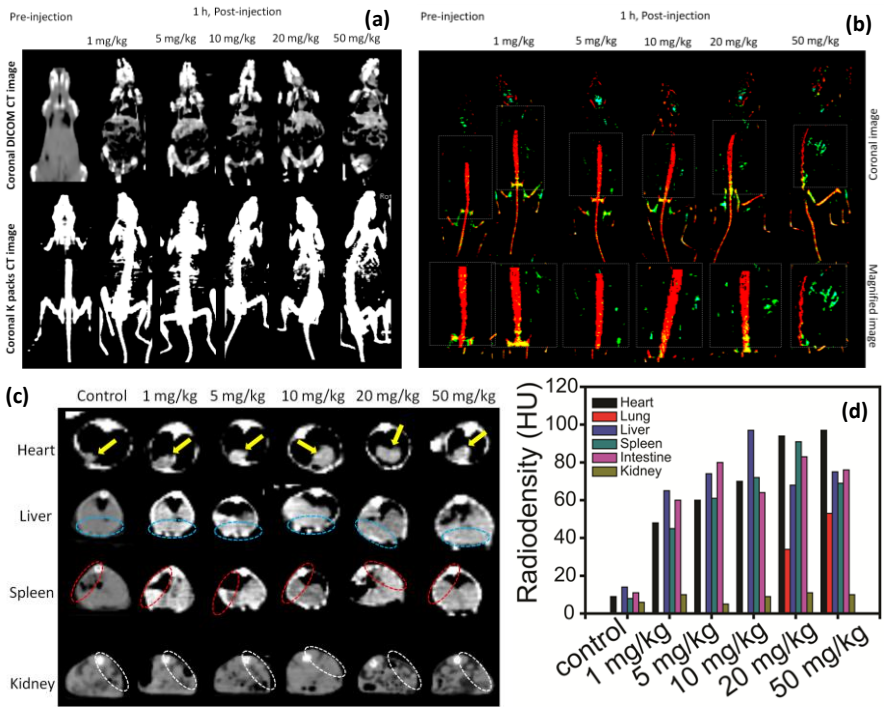

Figure 3.24. *(a and b, imaging from same group of mice using different software) Dose dependent (1-50 mg/kg body weight) in vivo contrast ability and bio-distribution of nanohybrid in major organs of through CT scans, nanohybrid injected mice with compared to pre-injected mice (DICOM CT and K packs CT images), (c) axial CT images of dose dependent contrast/radiodensity observation of nanohybrid in major organs (heart, liver, spleen and kidney) in post-injected mice which is compared to pre-injected mice as a control and (d) quantitative analysis of radiodensity observation in major organs (heart, lung, liver, spleen, intestine and kidney).*

To evaluate the bio-distribution and *in vivo* toxicity, PBS dispersed nanohybrid at various doses (1 to 50 mg/kg body weight) is subcutaneously injected into female Balb/c mice and distribution traced through X-ray CT imaging. Within an hour of post-injection, a clear and high contrast with respect to dose augmentation is observed in the heart, liver, spleen and intes-tine (due to reticuloendothelial system, RES and phagocytic cells in RES)[49] compared to pre-injected mice (the qualitative and quantitative understanding of radiodensity or brightness in major organs are shown in Figure 3.24 a-d). Interestingly, the contrast is not observed in kidney. The quick response (1 h) of contrast and its long circulation time (24 h) in animal body indicates the high dispersion, smooth and easy blood pool circulation of nanohybrid. Overall, the presence of contrast in intestine gives a conception about excretion of nanohybrid from lower abdomen organs like intestine. Similar type excretion of various MS nanoparticles is reported in previous *in vivo* studies demonstrating the biocompatibility of nanoparticles.[50-53] The renal clearance of MS nanoparticles is still under debate which may damage the glomerulus of kidney as per earlier reports.[52]

To understand the renal clearance and *in vivo* toxicity of designed GMS nanohybrid, we have carried out detailed *in vivo* studies. In details, four groups (3 mice/group) of animals (1) first group of pre-injected mice as a control and (2) remaining three groups at various time point post-injected mice as a treatment are considered for this. All groups of Balb/c mice are observed at various time intervals (1 h, 24 h and 14 days) to determine any harmful and side effect or injury in major organs (heart, lung, liver, spleen and kidney). Controlled (pre-injected) and treated (post-injected) mice groups show similar body weight, health without injurious symptoms in normal behavior during planned

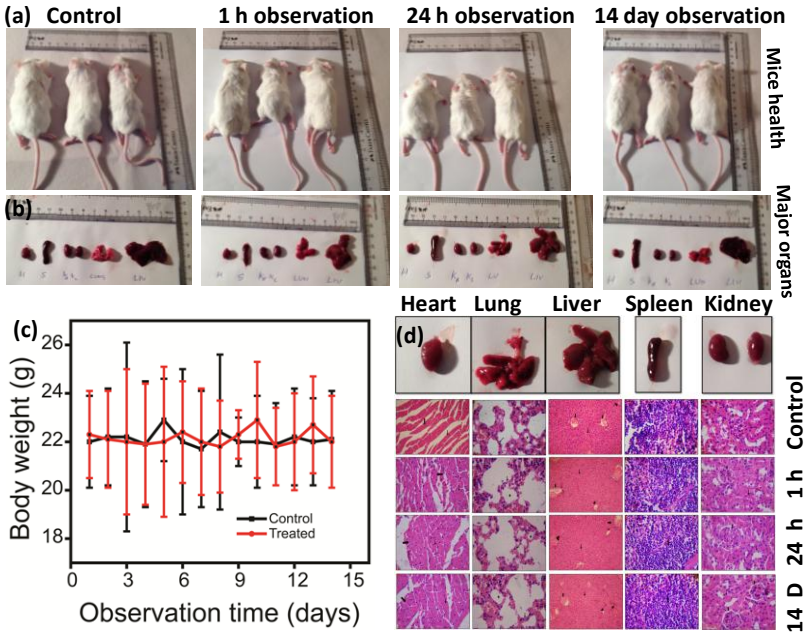

Figure 3.25. *(a) Health observation of mice at various time points (digital photographs, 1 h, 24 h and 14th day of treatment), (b) digital photographs of collected major organs (heart, spleen, kidney, lung and liver), (c) body weight analysis of all treated group of mice with compared to without treated mice as control and (d) histological examination through H&E analysis for the collected major organs with compared to control once.*

observation (Figure 3.25 a, b, c). The *in vivo* toxicity of designed nanohybrid is determined through histological examinations. Animals from an individual group (control and treated) are sacrificed at 1 h, 24 h and on 14th day time point of planned study and major organs are collected. Hematoxylin and eosin (H&E) are used for histological examination for the collected organs. The analysis reveals that, myofibre and muscle bundle in heart are with-out any injures in the treated group (1 h, 24 h and 14th day) and is comparable with controlled ones. Similarly, portal triad, hepatocyte and central vein in liver are also normal in both the groups at all studied times. In addition, glomerulus and tubules of kidney are observed without any types of histological changes and tissue injures even after 14 days of treatment and found similar to control which is due to smooth clearance and good

biocompatibility of designed nanohybrid (shown in Figure 3.25 d). In previous reports, abnormality in glomerulus after subcutaneous injection of various nanoparticles is noted[46], [47] whereas no acute injuries or toxicity in glomerulus is observed throughout the current study.

3.5 Conclusion

In summary, we have developed a simple, one pot and a rapid (2 h) recipe for synthesizing NIR active GMS nanohybrid. The ease of a direct silica deposition over GNRs is demonstrated to produce GMS nanohybrid with superior advantages viz., (a) consistent distribution of GNRs inside highly monodispersed (particle size ~ 100±10 nm) MS, (b) highest ever reported surface area of 1100 m^2/g, (c) largest ever reported cargo capacity (57 % for DOX), (d) superior and quicker photothermal response (<2 min) at relatively lower NIR power density (at 0.5 W/cm^2), (e) good biocompatibility (>90 % cell viability) and (f) higher radio density (HU 151) compared to that of the widely practiced iodine (HU 23). *In vitro* studies including synergistic targeted chemo-photothermal therapy on several cancer cell lines demonstrate its outstanding multifunctional design and performance. In addition, the designed nanohybrid have following enhanced features such as (a) high product yield (~ 1 g/batch), (b) high photothermal efficiency (30 %, 43 °C in 3 min.), (c) short irradiation time and low power density (5 min. and 0.5 W/cm^2) of NIR laser, (d) dual nature folic acid as gatekeeper and targeting ligand. Further, GMS nanohybrid shows long term biocompatibility (normal L929 cells and RBCs), successful targeting ability for breast cancer cells/tumor by single, minimal dose (10 mg/kg body weight), smooth circulation (24 h) of designed material, good biocompatibility with organs and healthy glomerulus of kidney indicates the successful renal clearance of nanohybrid.

3.6 References

(1) Allen, T. M.; Cullis, P. R. *Science* 2004, **303**, 1818.

(2) Nicolas, J.; Mura, S.; Brambilla, D.; Mackiewicz, N.; Couvreur, P. *Chem. Soc. Rev.* 2013, **42**, 1147.

(3) Vallet-Regi, M.; Ramila, A.; del Real, R. P.; Perez-Pariente, *J. Chem. Mater.* 2001, **13**, 308.

(4) Slowing, I.; Trewyn, B.G.; Lin, V.S. J. Am. Chem. Soc. 2006, 128, 14792-14793.

(5) Naomi J. Halas *ACS Nano* 2008, **2**, 179.

(6) Cauda, V.; Engelke, H.; Sauer, A.; Arcizet, D.; Brauchle, C.;¨Radler, J.; Bein, T. *Nano Lett.* 2010, **10**, 2484.

(7) Hrvoje L; Mark W. G.; *Chem. Rev.* 2013, **113**, 1641.

(8) Lee, J. E.; Lee, N.; Kim, T.; Kim, J.; Hyeon, T. *Acc. Chem. Res.* 2011, **44**, 893.

(9) Piao, Y.; Burns, A.; Kim, J.; Wiesner, U.; Hyeon, T. *Adv. Funct. Mater.* 2008, **18**, 3745.

(10) Singh, N.; Karambelkar, A.; Gu, L.; Lin, K.; Miller, J. S. ; Chen, C. S.; Sailor M. J.; Bhatia, S. N. *J. Am. Chem. Soc.* 2011, **133**, 19582.

(11) Argyo, C.; Weiss, V.; Bräuchle, C.; Bein, T. *Chem. Mater.* 2014, **26**, 435.

(12) Yang, X.; Liu, X.; Liu, Z.; Pu, F.; Ren J.; Qu, X. *Adv. Mater.* 2012, **24**, 2890.

(13) Chang, Y. T.; Liao, P. Y.; Sheu, H. S.; Tseng, Y. J.; Cheng, F. Y.; Yeh, C. S. *Adv. Mater.* 2012, **24**, 3309.

(14) Zhang, Z.; Wang, L.; Wang, J.; Jiang, X.; Li, X.; Hu, Z.; Ji, Y.; Wu, X.; Chen, C. *Adv. Mater.* 2012, **24**, 1418.

(15) Murphy, C. J.; Gole, A. M.; Stone, J. W.; Sisco, P. N.; Alkilany, A. M.; Goldsmith, E. C.; Baxter, S. C. *Acc. Chem. Res.* 2008, **41**, 1721.

(16) Cong, H.; Toftegaard, R.; Arnbjerg, J.; Ogilby, P. *Langmuir* 2010, **26**, 4188.

(17) Liu, W.; Zhu, Z.; Deng, K.; Li, Z.; Zhou, Y.; Qiu, H.; Gao, Y.; Che, S.; Tang, Z. *J. Am. Chem. Soc.* 2013, **135**, 9659.

(18) Shen, S.; Tang, H.; Zhang, X.; Ren, J.; Pang, Z.; Wang, D.; Gao, H.; Qian, Y.; Jiang, X.; Yang, W. *Biomaterials* 2013, **34**, 3150.

(19) Huang, X.; El-Sayed, I.H.; Qian, W.; El-Sayed, M. A. *J. Am. Chem. Soc.* 2006, **128**,

2115.

(20) Huff, T.B.; Tong, L.; Zhao, Y.; Hansen, M.N.; Cheng, J.X.; Wei, A. *Nanomedicine* 2007, **2**, 125.

(21) Popovtzer, R.; Agrawal, A.; Kotov, N. A.; Popovtzer, A.; Balter, J.; Carey, T. E.; Kopelman, R. *Nano Lett.* 2008, **8**, 4593.

(22) Alkilany, A. M.; Nagaria, P. K.; Hexel, C. R.; Shaw, T. J.; Murphy, C. J.; Wyatt, M. D. *Small* 2009, **5**, 701.

(23)Yun-Sheng C.; Wolfgang F.; Seungsoo K.; Pieter K.; Kim-berly H.; Stanislav E. *Nano Lett.* 2011, **11**, 348.

(24) Tang, H.; Shen, S.; Guo, J.; Chang, B.; Jiang, X.; Yang, W. *J. Mater. Chem.* 2012, **22**, 16095.

(25) Huang, P.; Bao, L.; Zhang, C.; Lin, J.; Luo, T.; Yang, D.; He, M.; Li, Z.; Gao, G.; Gao, B.; Fu, S.; Cui, D. *Biomaterials* 2011, **32**, 9796.

(26) Abadeer, N. S.; Brennan, M. R.; Wilson, W. L.; Murphy, C. J. *ACS Nano* 2014, **8**, 8392.

(27) Gorlikove, I.; Matsuura, N. *Nano Lett.* 2008, **8**, 369.

(28) Wu, C.; Xu, Q. *Langmuir* 2009, **25**, 9491.

(29) Li, Y.; Wen, T.; Zhao, R.; Liu, X.; Ji, T.; Wang, H.; Shi, X.; Shi, J.; Wei, J.; Zhao, Y.; Wu, X.; Nie, G. *ACS Nano* 2014, **8**, 11529.

(30) Wu W. C.; Tracy, J. B. *Chem. Mater.* 2015, **27**, 2888.

(31) Zhang, T.; Diang, Z.; Lin, H.; Cui, L.; Yang, C.; Li, X.; Niu, H.; An, N.; Tong, R.; Qu, F. *Eur. J. Inorg. Chem.* 2015, **13**, 2277.

(32) Wang, F.; Cheng, S.; Bao, Z.; Wang, J. *Angew. Chem., Int. Ed.* 2013, **52**, 10344.

(33) Li, H.; Tan, L. L.; Jia, P.; Li, Q. L.; Sun, Y. L.; Zhang, J.; Ning, Y. Q.; Yu, J.; Yang, Y. W. *Chem. Sci.* 2014, **5**, 2804.

(34) Liu, Y; Xu, M; Chen, Q; Guan, G; Hu, W; Zhao, X; Qiao, M; Hu, H; Liang, Y; Zhu, H; Chen, D. *Int J Nanomedicine* 2015, **10**, 4747.

(35) Huang, C. C.; Huang, C. H; Kuo, I. T; Chau, L. K; Yang, T. S. *Colloids Surf A Physicochem Eng.* 2012, **409**, 61.

(36) Swierczewska, M.; Lee, S.; Chen, X. *Mol. Imaging* 2011, **10**, 3.

(37) Dewey, W. C. *Int. J. Hyperthermia* 2009, **25**, 3.

(38) Pastoriza-Santos, I.; Pe´rez-Juste, J.; Liz-Marza´n, L. M. *Chem. Mat.* 2006, **18**, 2465.

(39) Swarup K. M.; Sivaramapanicker S.; James J.; Manjing L.; Tingchao H.; Yan T.; Handong S.; Sidney W. K. Y.; Yanli Z. *Adv. Mater.* 2014, **26**, 5633.

(40) Prasad, R; Aiyer, S; Chauhan, D. S; Srivastava, R; Selvaraj, K, *Nanoscale*, 2016, **8**, 4537.

(41) Liang, L; Subirade, M. *J. Phys. Chem. B* 2010, **114**, 6707.

(42) Yu,X; Fan, H; Wang, L; Jin, Z. *Angew. Chem. Int. Ed.* 2014, **53**, 12600.

(43) Ciuchi,F; Nicola,G.D; Franz,H; Gottarelli, G; Marisni,P; Bassi,M.G.P; Spada,G.P. *J. Am. Chem. Soc.*, 1994, **116**, 7065.

(44) Atluri,R; Iqbal,M.N; Bacsik, Z; Hedin,N; Villaescusa,L.A; Garcia-Bennett,A.E. *Langmuir* 2013, **29**, 12003.

(45) Lin,Y.S; Haynes,C.L. *J. Am. Chem. Soc*. 2010, **132**, 4834.

(46) Roggers, R.A; Joglekar, M; Valenstein, J.S; Trewyn,B.G. *ACS Appl. Mater. Interfaces* 2014, **6**, 1675.

(47) Yildirim, A; Ozgur,E; Bayindir,M. *J. Mater. Chem. B*, 2013, **1**, 1909.

(48) Lin,Y.S; Abadeer, N; Hurley, K.R; Haynes, C.L. *J. Am. Chem. Soc.* 2011, **133**, 20444.

(49) Kumar, R.; Roy, I.; Ohulchanskky, T. Y.; Vathy, L. A.; Bergey, E. J.; Sajjad, M.; Prasad, P. N. *ACS Nano* 2010, **4**, 699.

(50) Fu, C.; Liu, T.; Li, L.; Liu, H.; Chen, D.; Tang, F. *Biomaterials* 2013, **34**, 2565.

(51) Souris, J. S.; Lee, C. H.; Cheng, S. H.; Chen, C. T.; Yang, C. S.; Ho, J. A.; Mou, C. Y.; Lo, L. W. *Biomaterials* 2010, **31**, 5564.

(52) Feng, C.; Hao, H.; Yin, Z.; Hector, F. V.; Sixiang, S.; Glen, S. K.; Charles, P. T.; Todd, E. B.; Weibo, C. *ACS Nano* 2013, **7**, 9027.

(53) Feng, C.; Hao, H.; Shreya, G.; Stephen, A. G.; Hakan, O.; Emily, B. E.; Sixiang, S.; Charles, P. T.; Robert, J. N.; Weibo, C. *ACS Nano* 2015, **9**, 3926.

(54) Xi, C.; Wang, Z.; Zhou, J.; Fu, X.; Liang, J.; Qiu, Y.; Huang, Z. *Int J Nanomedicine* 2015, **10**, 1.

(55) Osama Mohamed, M S.; Rehab, M H. *Int J Nanomedicine* 2014, **9**, 1505.

Chapter IV

Bioresponsive fluorescent nano-gated mesoporous nanohybrid for cancer theranostics

Mesoporous silica nanoparticles (MSNPs) have been discussed for their drug delivery applications due to their high surface area, cargo capacity and biocompatibility in earlier chapters. Recently, MSNPs have declared as safe material for human trials by US FDA. Accordingly, engineering the exterior porous surface of these nanoparticles with nano-gates for preventing premature drug release and controlled drug delivery is a current demand for therapeutics. Further, designing bioresponsive fluorescent nano-gated mesoporous nanocarriers for controlled and efficient intracellular drug release for cancer therapy is a major thrust area in nanomedicine. Simultaneously, fluorescent graphene/carbon quantum dots (GQDs/CQDs), have also been discussed as possible alternates for their imaging application to overcome more toxic and relatively less efficient predecessors. However, they are less known as gate keepers for drug release control. This chapter addresses the dual functionality (imaging and gate keeping) with good control on preventing the premature release and exceptional bio-imaging of cancer cells. During the course of this work, design of a multifunctional (gatekeeper, imaging agent and targeted drug delivery) bioresponsive fluorescent carbon nano-gated mesoporous silica nanohybrid for cancer theranostics is understood and addressed.

The work presented in this chapter is published, Nanoscale, 2016,**8**, 4537

4.1 Introduction

Several aspects of the present introduction have been discussed in the Introduction Chapter. However, for the sake of continuity and accountability of the present Chapter, some aspects presented earlier are recollected here. A major challenge is to design bioresponsive[1-4] multifunctional drug delivery system[5, 6] comprising of various function-specific components to synergistically promote improved site specific chemotherapy[7-9] and thereby reducing the side effects. In recent years, mesoporous silica (MS)[9-11] nanoparticles are seen as promising candidates for drug delivery systems due to advantages viz., large surface area, ordered uniform pores, high pore volume and surfaces (both exterior and interior) that are easily functionable with biomolecules and targeting ligands thereby enhancing the biocompatibility too.[10-18] A nanodot of this material has recently been approved by United States Food and Drug Administration (FDA)[19] as safe material for human trials to be tested as first investigational new drug (IND) application for molecular biomedical imaging.[7,8,19-21]

A series of mesoporous silica nanoparticles (MSNPs) have been synthesized for various applications including drug delivery, gene delivery apart from other generic applications viz., catalysis, CO_2 capture, etc.[11-16, 22-27] The architectural control and surface functionalization of MSNPs have brought new possibilities for targeted drug delivery and bio-imaging.[18, 26-33] So far, various MSNPs based drug delivery systems with organic (supramolecules) [26, 28, 31] and inorganic gatekeepers (metal nanoparticles) [30] have been developed for the prevention of premature drug release and controlled drug delivery. Sir Stoddart and Prof. Zink earlier conceptualized stimuli responsive gatekeepers by using supramolecular nanovalves on MS nanoparticles[23, 26, 28, 34] and in general, nanocarrier

systems that respond to either extracellular or intracellular stimuli such as light[23], temperature[23, 28], pH[9], [28, 34] and enzyme.[28, 30] Among these individual stimuli, pH and redox-responsive release mechanisms have been recognized as effective ones for controlled drug release at target sites.[23, 26, 34]

A contemporary thrust area is to explore stable, efficient and safe nanolight agents for biomedical imaging and integrating them in to such multifunctional systems.[29, 35-38] Many fluorescent organic dyes and quantum dots (QDs) have been independently attempted for bioimaging.[38-40] However, due to several strong demerits, they are far from *in vivo* applications.[39, 40] To mention a few, semiconductor and metal QDs owing to poor photostability, photo-blinking and poor biocompatibility.[41, 42] Recently, carbon and graphene quantum dots, a new class of fluorescent materials, have attracted many researchers for their exploitation in bio-sensing and bio-imaging.[35-36] As compared to other quantum dots and organic dyes, carbon quantum dots (CQDs) are superior in properties such as good luminescence, photostability, water solubility and biocompatibility making them suitable for biomedical applications.[37-42] Many methods have been proposed to prepare CQDs which are classified into “Top-down” and “Bottom-up” approaches and their modification can be achieved by synthesis processes.[43-53] For example, Ajayan and coworkers have reported different fluorescent graphene QDs with blue, green and yellow fluorescence.[54] Despite many achievements, understanding their other possible functions and the feasibility to be included in a multifunctional system are yet to be realised. They remain as major challenges in biomedical research due to complexities in synthetic fabricating steps and yet maintaining their performances.

Upsurge concerns over issues such as toxicity and bio-compatibility are often obvious in case of using several functional components. However, integrating them in to a single system, strongly suppresses them. For instance, apart from its role in bioimaging, a fluorescent material may also perform a role of gate keeping. This chapter presents the successful design where mesoporous silica nanoparticles (MSNPs), used as nanocarriers for anticancer drug, are capped with CQDs that play dual roles viz., (i) fluorescent agent for site-specific bioimaging and (ii) efficient gatekeepers to prevent the premature drug release facilitating targeted delivery. In specific, for the first time the present work in this chapter demonstrates a remarkable bioresponsive gatekeeping ability of CQDs.

In recent literature, very few reports on MSNPs capped with CQDs are available. Qu and coworkers have attempted to cap MSNPs with CQDs, however, with a significant premature release of anticancer drug, doxorubicin (DOX).[33] This issue has been later addressed to a larger extent by Fu and coworkers using graphene quantum dots (GQDs) to cap MSNPs.[34] These scanty reports published in this respect rather suggest the huge scope of further explorations in terms of issues viz., improving the pore sealing to further reduce premature drug release, reducing the number of synthesis steps involved, etc. The disparity between pore diameter and size of quantum dots used for capping may result in loosely sealed pores which may be attributed to the premature drug release. In addition, while these articles mainly report pH based response, the significance of elevated glutathione (GSH) concentration, an evident characteristic factor of cancer cells from normal ones has never been exploited in gate keeping by using CQDs. This chapter reports a successful design of bioresponsive GQDs/CQDs capped MSNPs based targeted nanocarrier for

bioimaging of cancer cells and controlled intracellular delivery of DOX when subjected to a mimicked cancer cell environment.

4.2 Experimental Section

4.2.1 Materials

Millipore/Milli-Q water (MPW) is used in all experiments and to prepare all buffer solutions. N-cetyltrimethylammonium bromides (CTAB), tetraethylorthosilicate (TEOS), dimethylsulphoxide (DMSO), sodium hydroxide (NaOH), sulphuric acid (98.08 % H_2SO_4) and nitric acid (70 % HNO_3) are purchased from Merck limited, Mumbai, India. Graphite powder, 1-ethyl-3-(3-dimethylaminopropyl) carbodiimide (EDC), N-hydroxysuccinimide (NHS), folic acid (FA), citric acid, cystamine dihydrochloride, glutathione and 3-(4, 5-dimethylthiazol-2-yl)-2, 5-diphenyltetrazolium bromide (MTT) are purchased from Sigma-Aldrich Pvt. Ltd., USA. Sodium carbonate (Na_2CO_3, 99.9 %) is purchased from Fischer Scientific limited Mumbai, India. Dulbecco's modified Eagle's medium (DMEM), fetal bovine serum (FBS), phosphate-buffered saline (PBS), antibiotic-antimycotic solution are procured from HiMedia Laboratories Pvt. Ltd., India. Quantum dots are obtained from graphene oxide and sugarcane carbon powder.

4.2.2 Characterization techniques

The size synthesized graphene/carbon quantum dots (GQDs/CQDs) are systematically characterized with various physicochemical techniques. The size and morphology of nanostructures are examined by transmission electron microscopy (TEM FEI Tecnai T-20) operating at 200 kV. Samples for TEM are prepared by evaporating a droplet of sample onto 200 mesh carbon coated copper grid. Optical properties of CQDs, MS-CQDs NPs (Carbon quantum dots capped mesoporous silica nanoparticles), MS-CQDs-FA NPs (Folic

acid conjugated carbon quantum dots capped mesoporous silica nanoparticles) are characterized by UV/visible/NIR (Jasco V570) and photoluminescence (Scinco, Korea) spectrophotometer using standard quartz cuvette having a path length of 1 cm . A Zetasizer ZS 90 apparatus utilizing 633 nm red laser (at 90° angle) from Malvern instruments is used for DLS measurements. A minimum of three readings are collected using freshly prepared samples in PBS, saline and SBF solutions. Powder XRD (PXRD) patterns of nanostructures are recorded using a PANalytical X'pert pro dual goniometer diffractometer. The data are collected with a step size of 0.008° and scan rate of 0.5° min^{-1} by using Cu Kα (λ = 1.54 Å) radiation source. Fourier transform infrared (FT-IR) spectra are recorded by using Perkin-Elmer FT-IR spectrum GX instrument. KBr crystals are used as the matrix for preparing samples. The N_2 adsorption-desorption isotherms are recorded using Quantachrome Quadra Win Instrument. The specific surface area is calculated using the Multiple point Brunauer-Emmett-Teller (BET) theory. Pore volume is estimated at a relative pressure of P/P_o = 0.99. Barrett-Joyner-Halenda (BJH) analyses are used to calculate the surface area, pore size and pore volume. Digital photographs are captured in UV cabinet. AFM images are obtained from atomic force microscope (PSIA XE- 100) on tapping mode. The samples for AFM measurements are prepared by drop casting on clean silicon wafers surface after ultrasonic treatment (Equitron ultrasonic cleaner). Bio-imaging and intracellular localization of drug and carrier is performed with the help of fluorescence microscope. The fluorescence microscopic images are taken by Carl Zeiss inverted fluorescence microscope model AXIO OBSERVER.ZI using DAPI (350-430 nm blue), Alexa (488-520 green) and rhodamine (480-580 nm red) filters.

4.2.3 Synthesis of mesoporous silica (MS) nanoparticles

Mesoporous silica nanoparticles (MSNPs) are synthesized according to previously reported procedure with some modifications.[9, 10] In brief; 1 g of N-cetyltrimethylammonium bromide (CTAB) is dissolved in 480 mL of water 3.5 mL of 2 M NaOH aqueous solution is added to the CTAB solution followed by adjusting the solution temperature to 80 °C. 5 mL of Tetraehtylorthosilicate (TEOS) is added drop wise to the surfactant solution under vigorous stirring. The mixture is stirred for 2 h to give a white precipitate. The product is collected via centrifugation (10,000 rpm for 20 min.). Thereafter, it is thoroughly washed with water and methanol. Further, placed under high vacuum at 70 °C for 24 h to remove the remaining solvent from the pores of MSNPs. To remove the surfactant template CTAB, 1 g of the synthesized MSNPs is refluxed with 1 mL of 11.2 M HCL in 100 mL of methanol at 65 °C for 12 h. The resulting material is filtered and thoroughly washed with water and methanol then placed under high vacuum for 24 h at 70 °C temperature.

4.2.4 Synthesis of green fluorescent graphene/carbon quantum dots (GQDs/CQDs)

In a round bottom flask, 100 mg of graphene oxide powder[39] is mixed with 15 mL of concentrated H_2SO_4 and the mixture is left to bath sonicate for 2 h at room temperature. Thereafter, mixture is added into a concentrated solution of H_2SO_4 and HNO_3 prepared at volume ratio of 15:10 and stirred for 24 h at 100 °C. After completion of reaction (24 h), 200 mL water is added and its pH is adjusted to 7 with the help of Na_2CO_3 and NaOH. Reaction solution is left to slowly stir in ice bath for 3 h to remove the salts in the form of precipitation. After that, product is dialyzed using dialysis bag (molecular weight cut-off 2000 Da) for 2 days.

4.2.5 Synthesis and functionalization of green fluorescent CQDs

In a round bottom flask, 100 mg of carbon powder from natural source (carbon powder formed by burning in tube furnace) is mixed with 15 mL of concentrated H_2SO_4 and the mixture is left to bath sonicate for 2 h at room temperature. Thereafter, mixture is added into a concentrated solution of H_2SO_4 and HNO_3 prepared at volume ratio of 15:10 and stirred for 24 h at room temperature. After completion of reaction (24 h), 200 mL water is added and its pH is adjusted to 7 with the help of Na_2CO_3 and NaOH. Reaction solution is left to slowly stir in ice bath for 3 h to remove the salts in the form of precipitation. To introduce carboxyl groups on the surface of CQDs, 10 mg/mL of citric acid and 10 mL of CQDs solution are mixed under stirring and subsequently left for 6 h at room temperature. After that, product is dialyzed using dialysis bag (molecular weight cut-off 2000 Da) for 2 days. The resulting solution is checked for fluorescence by passing UV light in UV cabinet. To functionalize the surface of CQDs with amine group, cystamine dihydrochloride is used. Carboxyl group of CQDs is activated by 1-ethyl-3-(3-dimethylaminopropyl) carbodiimide (EDC) and N-hydroxysuccinimide (NHS) for 24 h. Thereafter, 5 mL of activated CQDs is mixed with 10 mg of cystamine dihydrochloride dispersed in 10 mL of water. Mixture of CQDs and cystamine dihydrochloride is left to vigorous stirring for 12 h at room temperature and subsequent product cystamine conjugated CQDs (CQDs-Cyst) is purified by dialysis.

4.2.6 Synthesis of folic acid conjugated CQDs-Cyst (CQDs-Cyst-FA)

The surface functionalization of CQDs-Cyst with folic acid is carried out stepwise. To activate carboxyl group, 60 mg of 1-ethyl-3-(3-dimethylaminopropyl) carbodiimide and 50 mg of N-hydroxysuccinimide are added in 200 mg of folic acid dissolved in 20 mL of

water. After 12 h, 15 mL solution of CQDs-NH_2 (CQDs-Cyst) having conc. of 2 mg/mL is added to the activated folic acid solution and allowed to react at room temperature for 24 h. The activation of folic acid and anchoring on amine functionalized CQDs reactions should be protected from light.

4.2.7 Silica surface decoration with green CQDs and CQDs-FA (MS-CQDs- FA)

Synthesized MSNPs are dried in oven at 120 °C for 12 h. 0.50 g of dried MSNPs are mixed with 5 mL aqueous solution of cystamine functionalized CQDs and left to stir for 24 h at room temperature. CQDs capped mesoporous silica nanoparticles (MS-CQDs NPs) is pelleted down at 5000 rpm for 10 min. Thereafter, thoroughly washed with water and dried under high vacuum at 60 °C for 24 h. The same method is used to synthesize folic acid functionalized CQDs capped mesoporous silica nanoparticles (MS-CQDs-FA).

4.2.8 Drug loading and release studies

Loading efficiency of MSNPs and MS-CQDs-FA NPs are tested with the help of anticancer drug doxorubicin (DOX). DOX is dissolved at conc. of 1 mg/mL in PBS buffer (pH 7.4). 15 mg of surfactant free MSNPs and MS-CQDs-FA NPs are dispersed separately in 5 mL of drug solution. The MSNPs and MS-CQDs-FA nanoparticles are left to stir at room temperature for 24 h. Thereafter, dispersion is centrifuged to collect the drug loaded MSNPs and MS-CQDs-FA NPs. In order to remove drug on the exterior surface of MSNPs and MS-CQDs-FA NPs, they are thoroughly washed with water. The amount of drug loaded into MSNPs and MS-CQDs-FA NPs are calculated by subtracting the amount of drug in the supernatant from the total amount of drug used. For drug release study, 1.0 mL of DOX loaded MS-CQDs-FA NPs are transferred into a dialysis bag (molecular weight cut-off 12 KD). The bag is subsequently placed in 100 mL of various pH buffer (7.4, 6, 5,

4 and 4 with 10 mM GSH) solutions andleft to stir at 37 ℃. At different time intervals, 1 mL solution is collected and replaced with 1 mL of fresh PBS solution to keep volume constant. The amount of DOX in the release medium is measured by UV-Vis spectroscopy at the wavelength of 480 nm.

4.2.9 Detachment of CQDs from silica surface

To detach CQDs from pores of MS-CQDs-FA NPs. 200 mg of MS-CQDs-FA NPs are added in 100 mL of 10 mM glutathione (GSH) solution of pH 4 and kept for vigorous stirring. After 2 h, product is collected by centrifuging at 10,000 rpm for 20 min. Thereafter, it is thoroughly washed with water, methanol and dried under high vacuum at 70 °C for 12 h to yield the CQDs detached MSNPs.

4.3 Applications

4.3.1 Cell culture and *in vitro* biocompatibility study

To understand the biocompatibility and therapeutic efficiency of nanohybrid, normal NIH-3T3 cells and HeLa cancer cells are cultured in Dulbecco's Modified Eagle's Medium (DMEM Gibco, Carlsbad, CA, USA) supplemented with 10% Fetal Bovine serum and penicillin/ streptomycin, under 5% CO_2 atmosphere at 37 °C.

In vitro cytotoxicity studies are performed over NIH-3T3 cells using 24 h MTT assay. Cells are seeded at density of ~ 10^4 cells per well of 96-well plate. After overnight incubation at 5 % CO_2 and 37 °C, 100 µl of different concentration (10-80 µg/mL) of MSNPs, CQDs, MS-CQDs, MS-CQDs-FA and MS-CQDs-FA after DOX release nanoparticles dispersed in media are added into wells. Following 24 h incubation wells are washed off with PBS and 20 µl of MTT dye is added. Formazan crystals formed after 4 h are dissolved by 200 µL of DMSO. Optical absorbance is recorded at 570 nm and 690 nm

using microplate reader (Tecan Infinite 200 PRO). Percentage cell viability is calculated in reference to untreated cells (negative control).

4.3.2 Targeting ability and tracking of green fluorescent CQDs

To check the cell targeting performance, we have chosen folic acid (FA) as a targeting ligand and HeLa cells are treated with folic acid functionalized MS-CQD. Before this study the HeLa cells seeded in 96 well plate at density of 2×10^4 cells/well and incubated overnight in incubator maintained at 5 % CO_2 and 37 °C. Next day, wells are washed off with PBS and 100 µl of 40 µg/mL of MS-CQDs-FA NPs are added. After 2 h, wells are washed off with PBS twice to remove unbound particles. Thereafter, 4 % paraformaldehyde solution is added to the cells and after 10 min of incubation nuclei are stained with 4, 6-diamidino-2-phenylindole (DAPI). Cover slip is then mounted over a drop of 70 % glycerol on glass slide to fix the phase of the cell. Images are captured using fluorescence microscope (Axio Observer Z1, Carl Zeiss). To evaluate the green fluorescence performance of CQDs, HeLa cells are treated with 40 µg/mL concentration folic acid functionalized MS-CQDs for different incubation time (2, 4 and 6 h).

4.3.3 Intracellular localization of DOX using fluorescence microscope

To check localization and distribution of DOX inside cancer cell, HeLa cells are treated with DOX-MS-CQDs and DOX-MS-CQDs-FA for incubation time 2 h and 18 h. Before this study the HeLa cells are grown in Dulbecco's Modified Eagle's Medium (DMEM Gibco, Carlsbad, CA, USA) at the density of 2×10^4 cells/well in 96 well plates and incubated for 24 h. After being rinsed with PBS, the cells are incubated with 40 µg/mL concentration of DOX-MS-CQDs and DOX-MS-CQDs-FA 2 h and 18 h. After incubation for a required interval of time, HeLa cells are washed with PBS twice to get rid of all the

unbound particles. Then for each, 4% paraformaldehyde solution is added to the cells and incubated for 10 min and nuclei are stained with 4, 6-diamidino-2-phenylindole (DAPI). The cover slip is then mounted on a drop of 70 % glycerol on glass slide to fix the phase of the cell. The fluorescence images are taken using fluorescence microscope (Axio observer. Z1).

4.3.4 *In vitro* targeted therapeutic study

To understand the therapeutic efficiency of nanohybrid, *in vitro* chemo therapy is tested on HeLa cancer cell lines. Cancer cells are seeded onto 96 well plates with a density of 2×10^4 cells/well and incubated for 24 h in 5 % CO_2 atmosphere at 37 ºC. After being rinsed with PBS, the cells are incubated with 100 µg/mL of MS, MS-CQDs, DOX-MS-CQDs and DOX loaded FA attached nanohybrid for 24 h. After incubation the cells are washed with PBS three times to get rid of all the unbound particles. Cell viability is determined by the addition of MTT (20 µL, 1 mg/mL dye in sterile PBS). The plate is incubated for an additional 4 h at 37 °C and 5% CO_2, allowing viable cells to convert the blue solution into pink dye. Formazan crystals are dissolved by adding 100 µL DMSO to each well. Optical absorbance is recorded at 570 nm using microplate reader (Tecan Infinite 200 PRO). Percentage cell viabilities are calculated in reference to untreated cells (control).

4.4 Results and Discussion

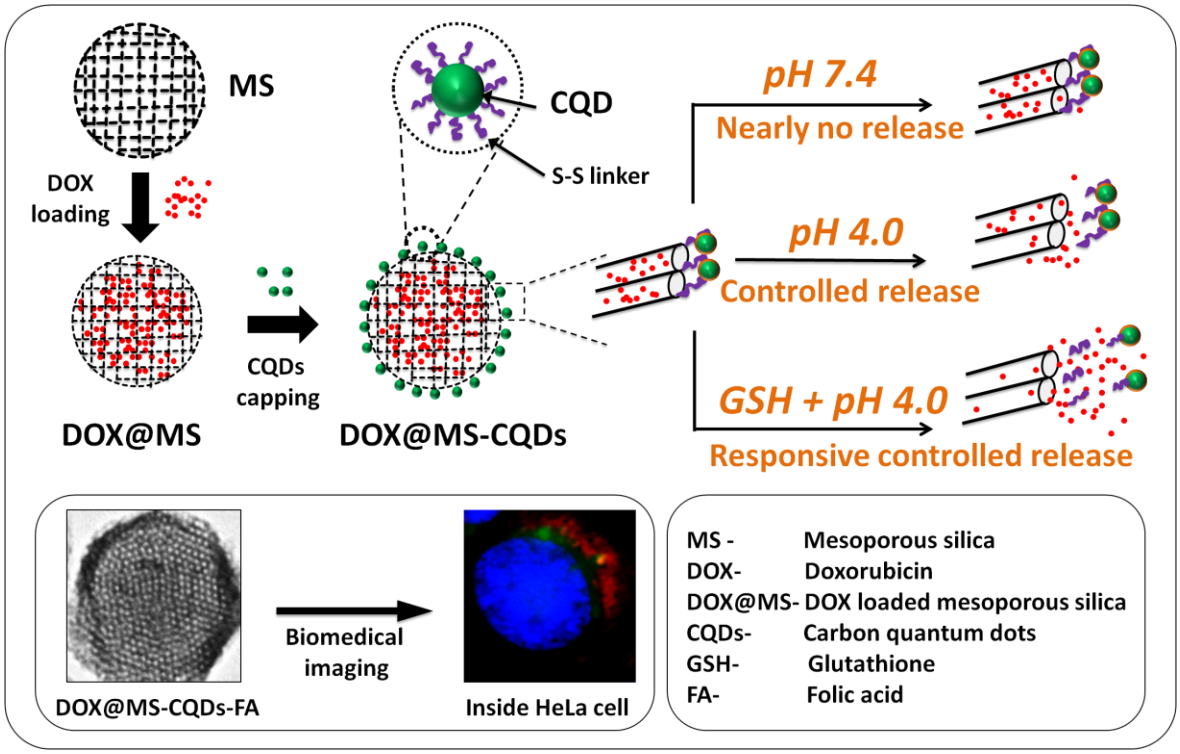

Scheme 4.1. *Schematic showing bioresponsive dual functional CQDs capped MS.*

The main objective of this work is to design the bioresponsive nanohybrid for multifunctional cancer theranostics (Scheme 4.1). To check the feasibility of fabricating such a systems using inexpensive CQDs synthesized through simple synthesis route from natural sources and yet achieving the performances compared to that of the relatively expensive GQDs. Fluorescent quantum dots (GQDs/CQDs) are obtained from graphene oxide from Graphite and natural source, sugarcane waste. The synthesized GQDs and CQDs have particle size ~ 6 nm and ~ 5 nm respectively along with thickness of ~ 1.5 nm and 1 nm, respectively (from the AFM images obtained in tapping mode, Figure 4.1). The

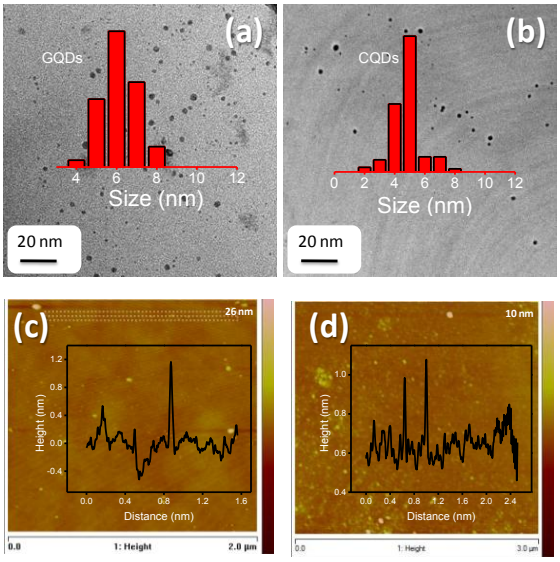

Figure 4.1. *TEM images of (a) graphene quantum dots (GQDs), (b) carbon quantum dots with their particle size histograms, AFM images of (c) GQDs and (d) CQDs with their height profiles.*

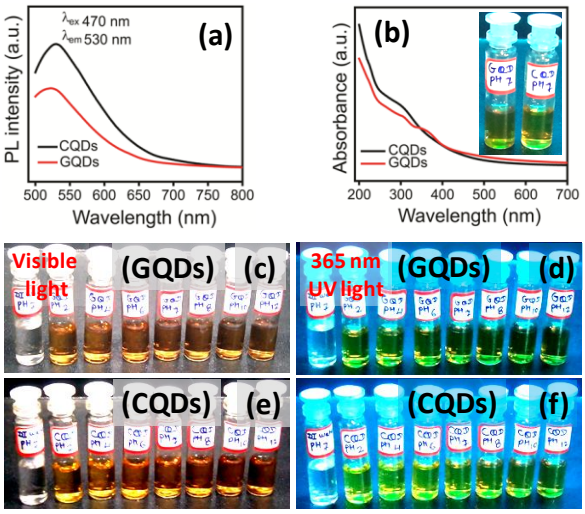

Figure 4.2. *(a) PL spectra, (b) absorption spectra of GQDs and CQDs, digital photographs (c-f) of GQDs and CQDs at different pH in aqueous media.*

green fluorescent nature of both QDs is confirmed by photoluminescence (PL) spectra showing emission ~ 530 nm with 470 nm excitation wavelength. Digital photographs of QDs indicate their green fluorescent nature and their better dispersion ability in aqueous media (Figure 4.2). The extensive characterization carried out on both QDs proves that there is almost no difference between them in terms of their optical properties. Hence, the green fluorescent CQDs are employed as bioresponsive gatekeepers in the present work to assess their ability to prevent the premature release of DOX and also to be as efficient marker for bio-imaging of human cancer cells. Notably, these CQDs are synthesized at ambient conditions unlike reported in the literature and this synthesis route from natural sources is reported here for the first time. A brief description of the functional design of the proposed system is discussed in this chapter (Scheme 4.1). Green fluorescent CQDs are capped onto the openings of the DOX loaded pores of MSNPs by using GSH sensitive

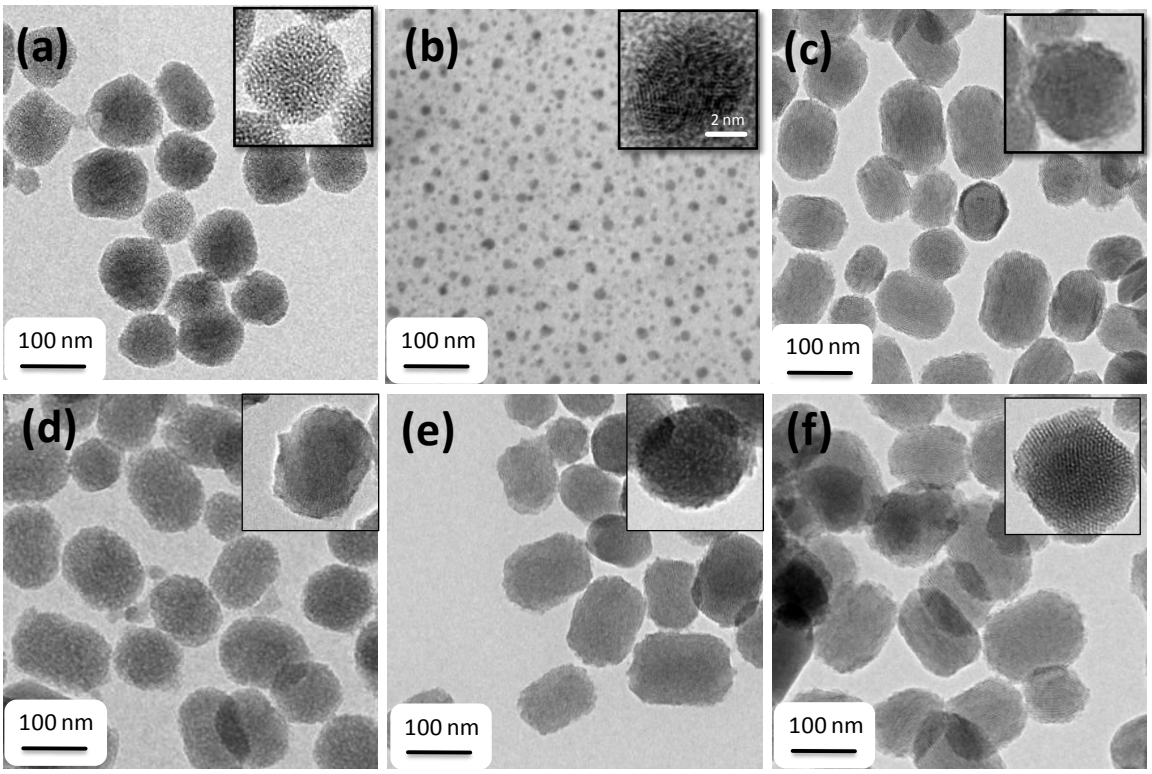

***Figure 4.3**. TEM images of (a) mesoporous silica (MS), (b) CQDs, (c) CQDs capped MS, (d) folic acid attached CQDs capped MS, (e) before CQDs detached MS and (f) after CQDs detached MS, inset single particle of each.*

disulphide bonds[28] (MS-CQDs). MS-CQDs nanoparticles on exposure to a cancer mimicked intracellular environment, release of drug is expected as the cystamine disulphide bonds are cleaved in response to the excess glutathione concentrations (2-20 mM).[55-57] Intracellular glutathione concentrations of normal cells are generally lesser by an order compared to that of cancer cells.[58-61] At extracellular conditions in physiological pH (7.4), the amine functionalized green fluorescent CQDs are tightly attached onto the MSNPs by electrostatic interactions thus sealing the pores and preventing the premature release of DOX. However, in acidic pH the protonation causes electrostatic disturbance and thus loosening of the CQDs caps from the MSNP pore openings leading to release of

DOX. In general, the amount of drug release depends upon the nature of release medium.[56, 59, 62] A successful bioresponse is indicated by further release of DOX on exposure to a release medium of pH 4 along with elevated concentrations of GSH. This is due to rapid cleavage of disulphide bonds and weakening of electrostatic interactions on MSNPs surface due to protonation in acidic pH respectively.

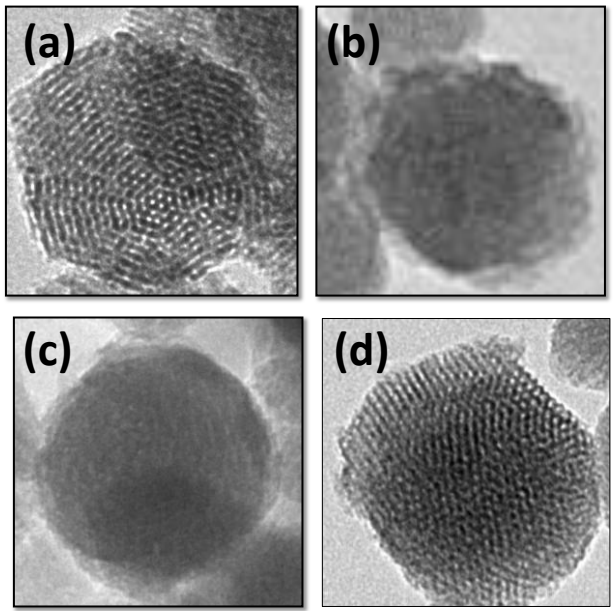

***Figure 4.4**. Single particle TEM images of (a) mesoporous silica, MS, (b) CQDs capped MS, (c) folic acid functionalized CQDs capped MS and (d) after CQDs detachment from MS surface (crop images of single particle).*

MS nanoparticles are synthesized according to a reported method with some modifications[9, 10] and pores are capped by green fluorescent CQDs. 1-ethyl-3-(3-dimethylaminopropyl) carbodiimide (EDC) and N-hydroxysuccinimide (NHS) are used to activate the carboxylic groups present on green fluorescent CQDs. The treatment of these activated CQDs with disulphide bond containing cystamine (Cyst) resulted into cystamine functionalized CQDs (CQDs-Cyst) which is further attached onto the surface of mesoporous silica via electrostatic interactions giving green fluorescence CQDs capped

MSNPs. Highly dispersed spherical MSNPs covered by CQDs with sizes of ~ 100 nm and ~ 5-6 nm respectively are observed from the TEM images (Figure 4.3 a-f). It is also evident (from the AFM image of CQDs obtained in tapping mode) that the thickness of the majority of dots is approximately 1 nm which corresponds to a single-layered dispersion of CQDs (Figure 4.1). The presence of ordered hexagonal arrays of mesopores in MSNPs and MS-CQDs are further confirmed by TEM images and XRD patterns. The MSNPs show clear lattice fringes which are diminished to an extent upon capping with CQDs (Figure 4.3 a, c) and reappear in the images of MSNPs taken after the detachment of CQDs (Figure 4.3 e, f). The lattice fringes of MSNPs are seen from TEM images (Figure 4.3 and 4.4).

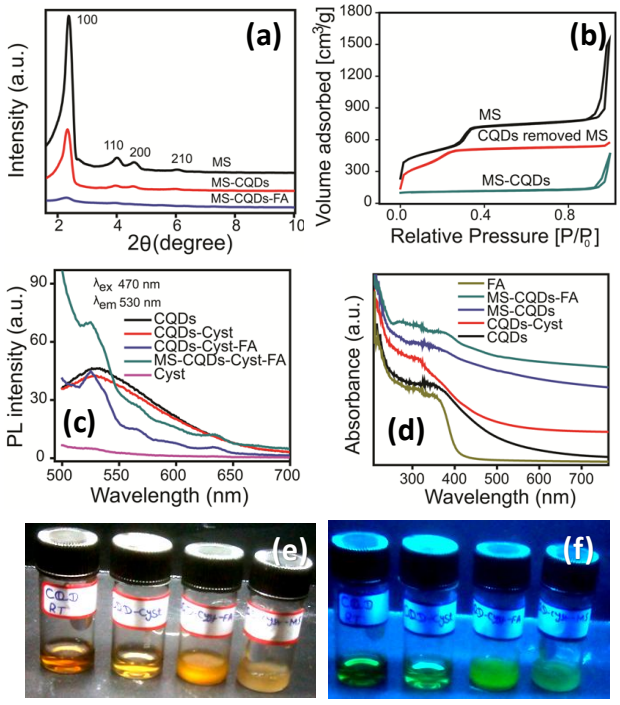

***Figure 4.5**. (a) PXRD patterns of MS, MS-CQDs and MS-CQDs-FA, (b) BET isotherms of MS, MS-CQDs and CQDs detached MS, (c) PL spectra of CQDs, Cystamine functionalized CQDs (CQDs-Cyst), folic acid functionalized CQDs-Cyst (CQDs-Cyst-FA), CQDs-Cyst-FA capped MS and Cystamine (Cyst) and (d) absorption spectra of CQDs and CQDs capped MS with digital photographs (e and f) of CQDs, CQDs-Cyst, CQDs-Cyst-FA and MS-CQDs-Cyst-FA.*

Low angle powder X-ray diffraction (LAPXRD) pattern is used to determine the mesophase structures of MSNPs, MS-CQDs and MS-CQDs-FA nanoparticles (Figure 4.5 a and Table 4.1). Four characteristic reflections for the diffraction planes (*100, 110, 200, 210*) of mesoporous silica (MCM-41) are observed at respective diffraction angles (2θ) 2.3°, 4.0°, 4.5° and 6.2° indicating the existence of highly ordered 2D hexagonal array of mesopores.[9, 10] Slight shift in diffraction planes and reduction of respective peak intensities are observed in case of MS-CQDs which are attributed to functionalization and subsequent pore capping. The disappearance of diffraction planes (*110, 200, 210*) on further attachment of folic acid (FA) to MS-CQDs nanoparticles is consistent with the literature.[9, 32] From combined TEM and XRD analysis it is concluded that surface functionalization of MS and its pore capping with CQDs have no destructive impact on the mesoporous structure. Nitrogen adsorption-desorption isotherms of MS nanoparticles, MS-CQDs and MS after CQDs detached are shown in Figure 4.5 b. It is evident that MSNPs follows a typical IV isotherm having surface area 1058 m^2/g with ~ 3 nm pore diameter. A drastic reduction in BET surface area (from 1058 to 154 m^2/g, Table 4.2) a change in the shape of the isotherm from type IV to type I (after CQDs capping) and a drop in pore volume (from 0.9 to 0.2 cm^3/g) are observed when MS pores are capped with CQDs thus confirming their tight sealing. Detachment of CQDs from sealed pores under acidic pH along with elevated concentrations of GSH (10 mM), is evident from the significant increase in the surface area (from 154 to 785 m^2/g) and in pore volume (from 0.2 to 0.5 cm^3/g). This further confirms the pore sealing is effective. This highly effective pore sealing is attributed to the ideal size match between that of the MS pores (~ 3 nm) and CQDs (~ 5 nm) unlike trials attempted earlier in literature. UV source in cabinet is used for preliminary screening of fluorescence

	Diffraction planes			
Sample name	***100***	***110***	***200***	***210***
MS	(2θ) 2.3°	(2θ) 4.0°	(2θ) 4.5°	(2θ) 6.2°
MS-CQDs	(2θ) 2.3°	(2θ) 4.1°	(2θ) 4.5°	Disappear
MS-CQDs-FA	(2θ) 2.4°	Disappear	Disappear	Disappear

Table 4.1*. Powder XRD observations.*

Sample name	Surface area m^2/g	Pore volume cm^3/g
MS	1058	0.90
MS-CQDs	154	0.23
CQDs removed MS	785	0.5

Table 4.2*. Summary of BET analysis.*

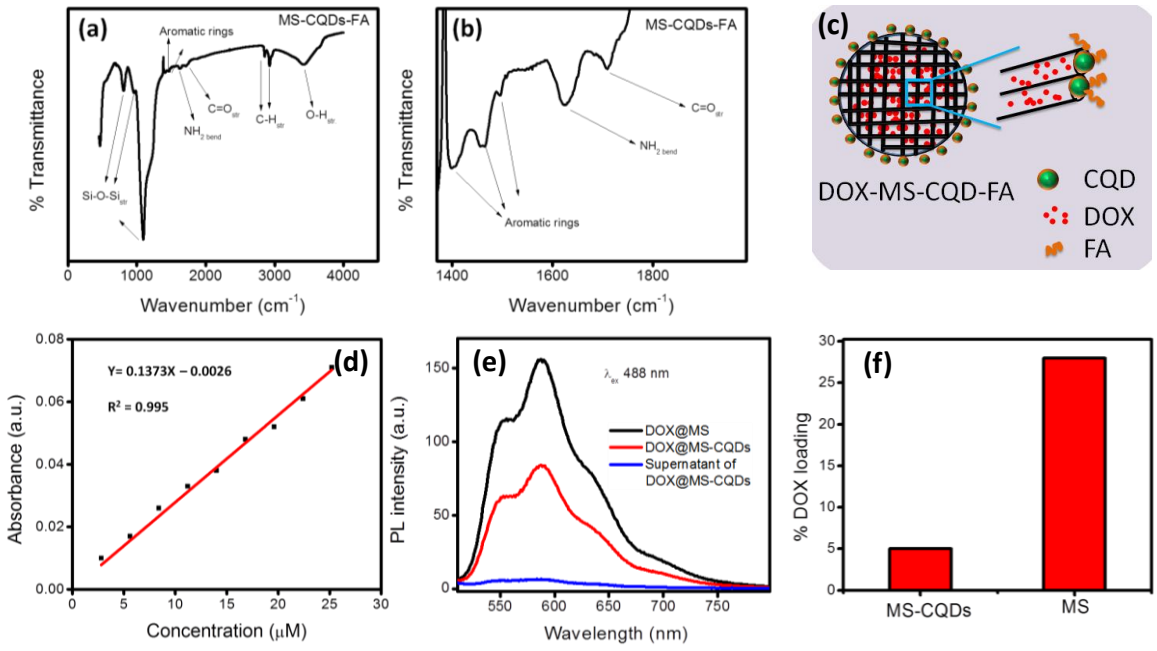

Figure 4.6*. (a) FTIR spectrum of MS-CQDs-FA, (b) zoomed spectrum of MS-CQDs-FA, (c) cartoon of DOX loaded MS-CQDs-FA, (d) linear equilibrium curve of drug, (e) photoluminescence (PL) spectra for drug loading measurement and (f) % DOX loading efficiency of MS-CQDs and MS.*

$$\% \text{ loading} = \frac{\text{Mass of drug in MSCQDs}}{\text{Mass of drug-Mass of drug loaded MSCQDs}} \times 100 \qquad \text{(eq. 4.1)}$$

$$\% \text{ Entrapment} = \frac{\text{Mass of drug in MSCQDs}}{\text{Initial mass of drug}} \times 100 \qquad \text{(eq. 4.2)}$$

behavior of CQDs, MS-CQDs and MS-CQDs-FA (Figure 4.5 c, e and f). The green fluorescent nature of CQDs, CQDs-Cyst, CQDs-Cyst-FA and MS-CQDs-FA is confirmed by photoluminescence (PL) spectra showing emissions at 530 nm with 470 nm excitation wavelength (Figure 4.5 c), thus making them promising substrate for *in vitro* and *in vivo* bio-imaging. In the absorption spectra of CQDs, CQDs-Cyst, CQDs-Cyst-FA and MS-

CQDs-FA (Figure 4.5 d), the peaks centered at λ_{max} 220 nm and 340 nm correspond to π-π* transition of the C=C band and n-π* transition of C=O band respectively. In addition to the above peaks, folic acid functionalized MS-CQDs show absorption peaks at 290 and 360 nm which are significant peaks of FA thus, confirming the successful attachment of FA with green fluorescent CQDs. Additionally, the O-H stretching vibrations (3426 cm^{-1}) and the C=O stretching vibrations (1697 cm^{-1}) in FT-IR spectra confirm carboxyl groups on CQDs. Peak at 1620 cm^{-1} corresponding to -NH_2 bending vibrations of the cystamine moiety reveals successful functionalization of cystamine on CQDs. Peaks at 2824 and 2933 cm^{-1} corresponding to -C-H stretching vibrations. The IR bands between 800-1180 cm^{-1} correspond to Si-O-Si stretching whereas the bands between 1413-1507 cm^{-1} indicate stretching vibrations of the aromatic rings of folic acid moieties (Figure 4.6 a, b and cartoon in 4.6 c). Further, the efficacy of pore sealing is checked once again with doxorubicin (DOX) loading tests carried out on MS and MS-CQDs (the efficiencies are calculated by linear equilibrium curve of drug and equations (eq.4.1 and eq.4.2) for drug loading amount and efficiency; Figure 4.6 d). MS shows 28 % loading efficiency before pore sealing and the loading efficiency decreased to ~ 5 % (believed to be mostly on external surface) for MS-CQDs where the pores are sealed with CQDs (Figure 4.6 e) corroborating the BET data. To check if the process of sealing with CQDs results in any loss of DOX, the samples before and after the process are tested with UV-Vis and also PL and the loss is calculated to be meager (~3 %) (Figure 4.6 f, eq. 4.1 and eq. 4.2). Nanoparticles of designed system are well dispersed and stable (Figure 4.7). The stability is confirmed by testing these particles as dispersed in various media such as simulated

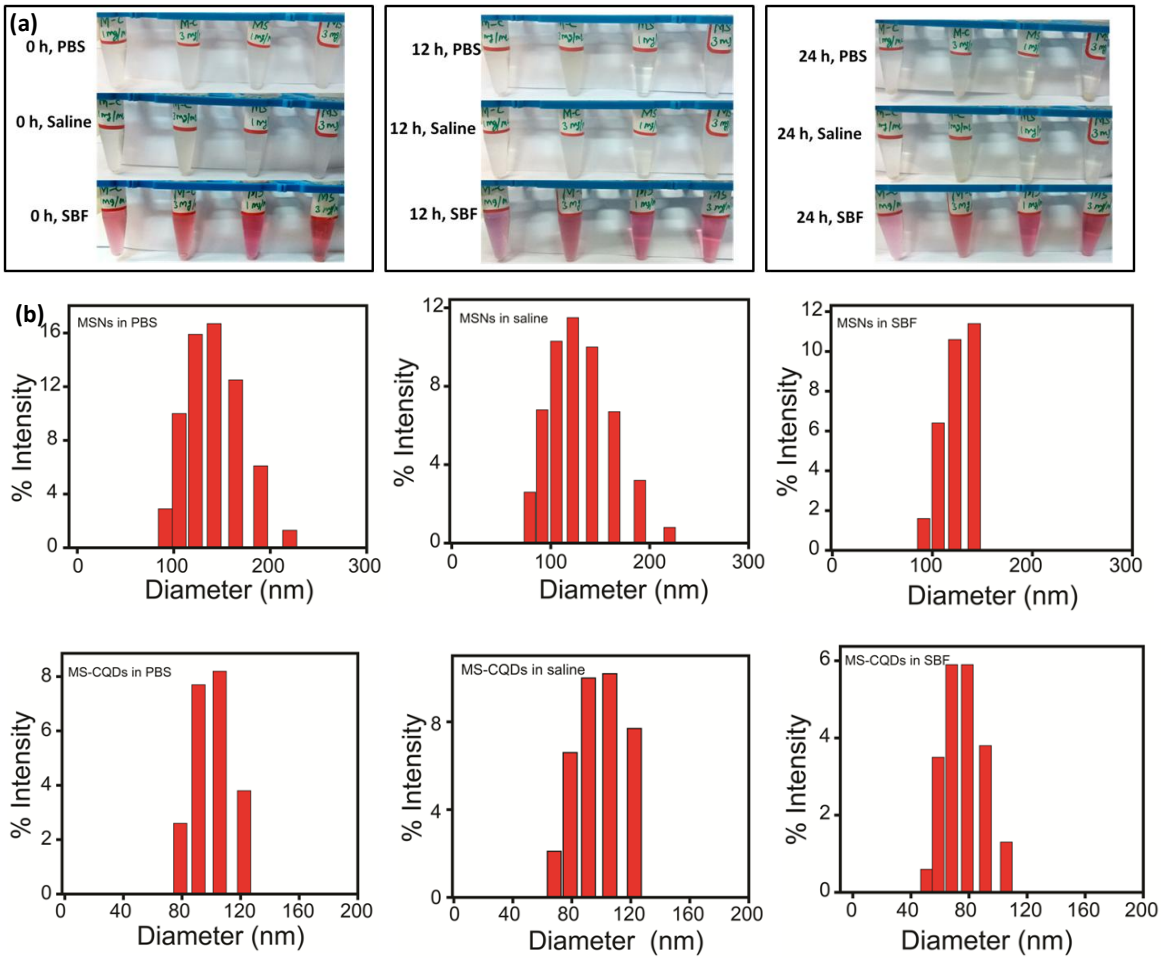

Figure 4.7*. (a) Digital photographs and (b) dynamic light scattering (DLS) analysis of MSNs and CQDs capped MSNs dispersed in PBS, saline and SBF solutions.*

body fluid (SBF), phosphate buffered saline (PBS) and saline for a period of 24 h using dynamic light scattering (DLS) measurement (Figure 4.7 a, digital photographs and Figure 4.7 b, average particle size from DLS). MTT assay with NIH-3T3 normal cell-line is used for *in vitro* cytotoxicity studies of CQDs, MS, MS-CQDs, MS-CQDs-FA and MS-CQDs-FA after DOX release prior to their bio-medical applications (Figure 4.8 a). More than 90 % cell viability is observed even at concentrations upto 80 µg/mL of CQDs, MS, MS-CQDs, folic acid functionalized MS-CQDs (MS-CQDs-FA). A cell viability of 73 % has

been observed for the sample MS-CQD-FA after DOX release and the meager reduction of viability is attributed to the loss of biocompatibility due to the removal of surface functionalized species such as CQDs, FA etc., during the release of DOX. To prove the redox-responsive gatekeeper behavior of CQDs on the MS surface, anticancer drug DOX is chosen for loading and release kinetics (eq. 4.1-4.3).

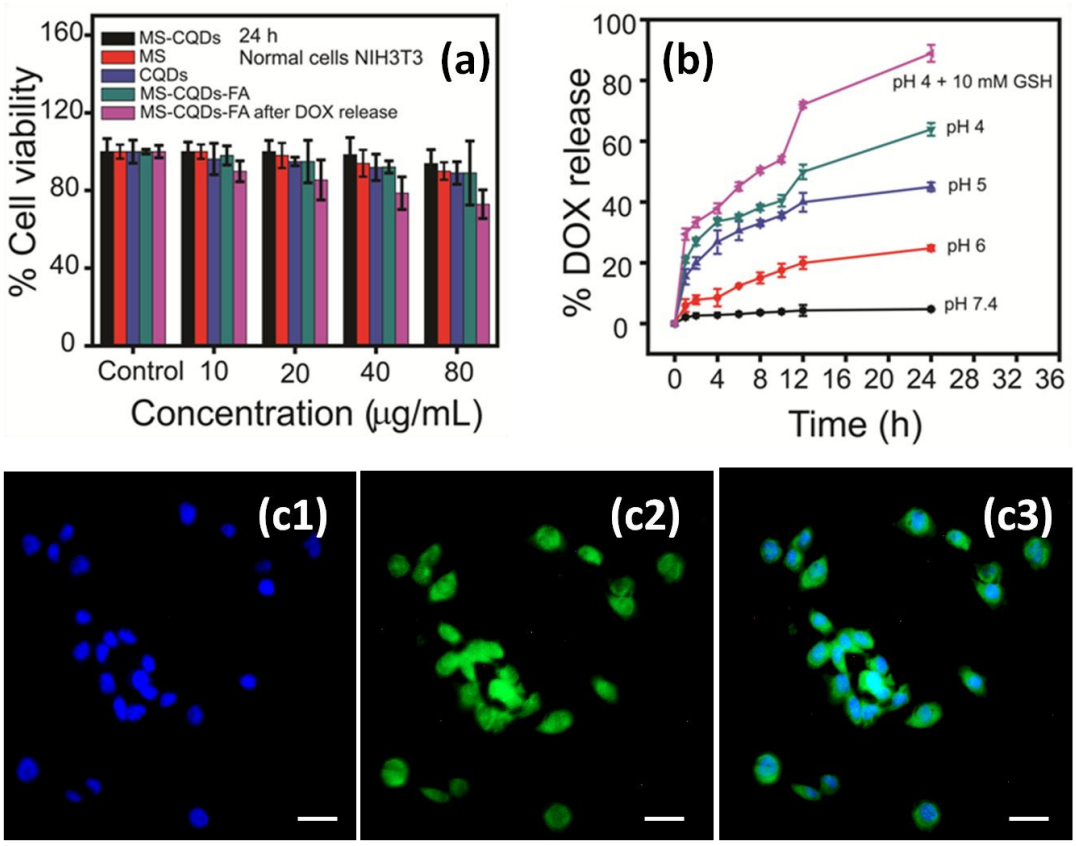

Figure 4.8*. (a) % Cell viability by MTT assay of CQDs, MS, MS-CQDs, MS-CQDs-FA and MS-CQDs-FA after DOX release with NIH-3T3 normal cell, (b) time dependent drug release profiles at different release media and targeting ability of MS-CQDs-FA on HeLa cells through fluorescence microscopy images, (c1) DAPI stained nucleus in blue, (c2) presence of CQDs inside the cell emitting green fluorescence and (c3) merged fluorescence, scale bar is 40 µm.*

$$\% \text{ Release } = \frac{\text{Mass of drug at time}}{\text{Initial mass of drug}} \qquad (\text{eq. } 4.3)$$

Though literature reports pH 7.4 and 4 to mimic the extracellular and deep intra cellular late endosomal environments in general[62-64] release kinetics are tested for a period of 24 h at various pH as 7.4, 6, 5 and 4 to get a deeper insight about the drug release capabilities at various stages of intracellular uptake. In addition to just pH 4 that along with 10 mM GSH to mimic deep intracellular and late endosomal conditions especially where the excess concentration of GSH can trigger the disulphide bond cleavage based drug release is also tested. Figure 4.8 b clearly shows the drug release kinetics at various conditions. An insignificant 4.3 % of release at neutral pH shows the best possible sealing of the pores and the effective control on premature drug release at extracellular and normal physiological conditions. However, as the material enters into the cell where the pH lowers around 6 to 5 the release goes up steadily to 24.8 % and 45 % respectively. For a deep intracellular environment where the pH goes down to 4, the release is about 63.9 %. A late endosomal condition as mimicked by a reduced pH of 4 along with 10 mM GSH almost doubles (88.9 %) the raise in the release of DOX at pH4 without GSH. It is also to be noted that the distinct GSH based triggering of drug release is more pronounced after 12 h. Though, the disulphide bond cleavage based mechanism is reported in literature with other systems. [55, 57-59] This clear demonstration of the bio-responsiveness of a judicious design with green CQDs is in this way, a first ever report to the best of our knowledge. To evaluate the bio-imaging and targeting ability of fluorescent payload nanomaterials, HeLa cells are cultured in physiological conditions and incubated with 40 μg/ mL of MS-CQDs-FA, DOX loaded

MS-CQDs and DOX loaded MS-CQDs-FA. The green fluorescence by MS-CQDs-FA after 2 h incubation with HeLa cells considerably gives primary indication of targeting ability (Figure 4.8 c1-3). Further, the visibility of green fluorescence increase with

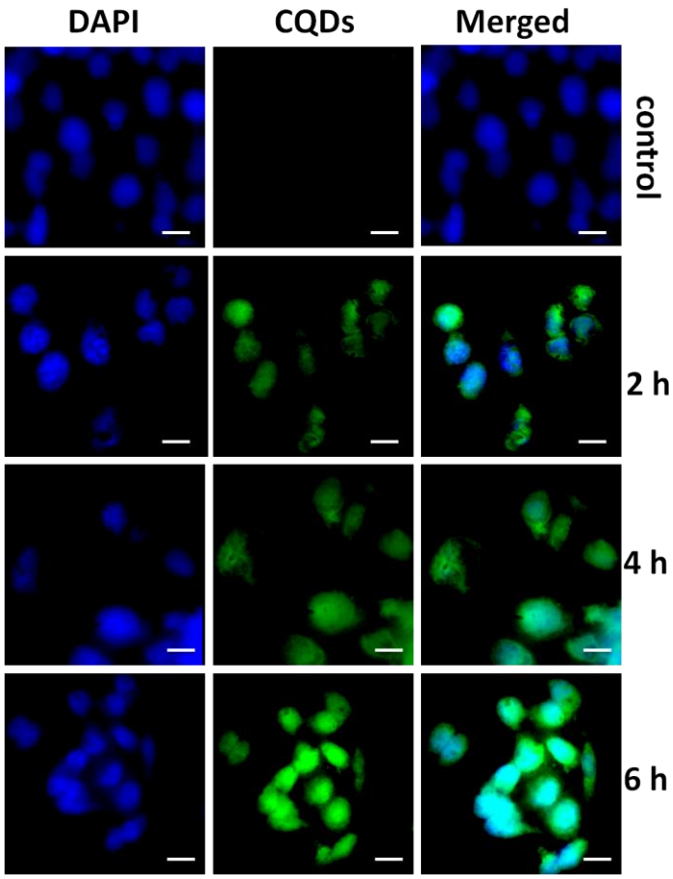

***Figure 4.9**. Distribution and visibility of detached green fluorescent CQDs from MS-CQDs-FA in HeLa cells through dual responsive cleavage (pH and GSH), fluorescence microscopy images with different incubation time, DAPI stained nucleus in blue, detached CQDs in cell interior with green fluorescence and merged fluorescence. All images are with 20 µm scale bar.*

incubation time (2, 4 and 6 h, Figure 4.9) of MS-CQDs-FA with HeLa cells when compared to control (without MS-CQDs-FA nanoparticles) confirming their efficient bio-imaging ability and thus strengthens their candidature as cell markers. Moreover, the enhanced visibility of green fluorescence after 6 h attributes superior intracellular delivery.

Further to understand the effectiveness of targeting and successive delivery of DOX, the fluorescence microscopy images of incubated (2 h) HeLa cells are collected for blue (DAPI), green (CQDs) and red (DOX) (Figure 4.10). Images shown in Figure 4.10 (a1-f1), explain the

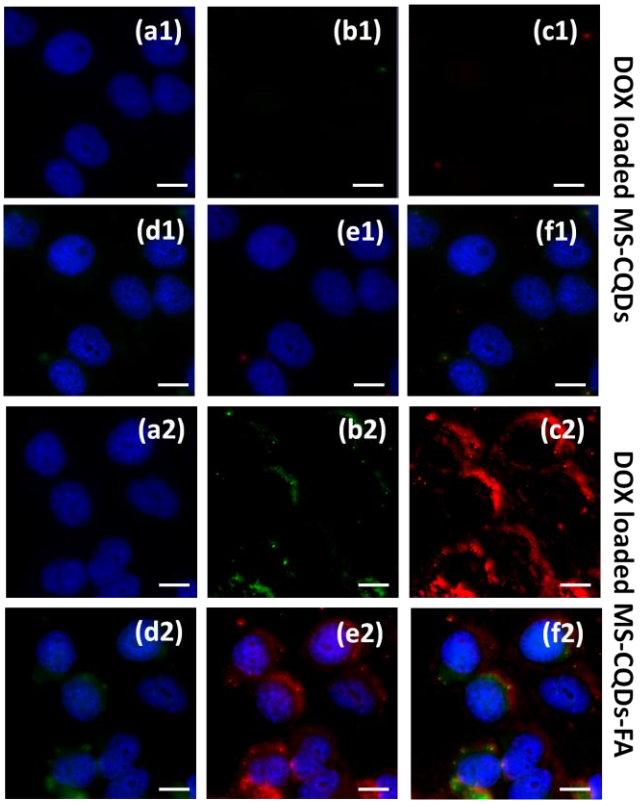

***Figure 4.10**. Cell uptake and distribution of DOX in HeLa cells when cells are incubated with 40 µg/ mL of DOX loaded MS-CQDs (a1-f1) and MS-CQDs-FA (a2-f2) for 2 h. Due to targeting, Intra cellular localization of DOX loaded MS-CQDs-FA was fast compared to DOX @MS-CQDs. Fluorescence microscopy imaging of treated cells, DAPI stained nucleus (blue a1,a2), CQDs (green b1, b2), DOX (red c1,c2), merged fluorescence of blue and green (d1, d2), merged fluorescence of blue and red (e1, e2) and merged fluorescence of blue, green and red (f1, f2). All images are with 10 µm scale bar.*

intracellular uptake of DOX in HeLa cells in the absence of targeting ligand (FA), while images in Figure 4.10 (a2-f2) explain the enhanced intracellular uptake due to the presence of functional FA ligand. The increase in green and red florescence in the second set of

images (a2-f2) clearly indicates the effective targeting due to functional ligand, FA and successive intracellular delivery of DOX. In addition, to understand the extent of intracellular uptake at extended incubation periods, additional experiments are carried out

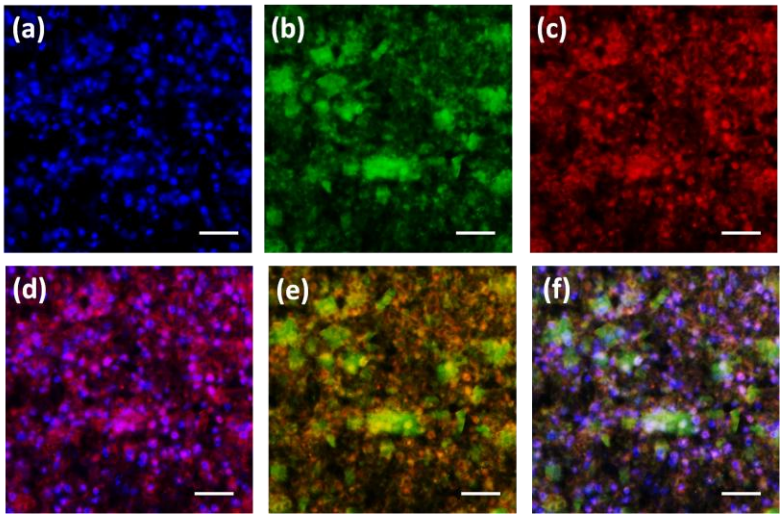

Figure 4.11. *Cell uptake and distribution of DOX in HeLa cells when cells are incubated with 40 µg/ mL of DOX@MS-CQDs-FA for 18 h. Fluorescence microscopy imaging of treated cells, DAPI stained nucleus (blue, a), CQDs (green, b), DOX (red, c), merged fluorescence of blue and red (d), merged fluorescence of green and red (e) and merged fluorescence of blue, green and red (f). Images are with 100 µm scale bar.*

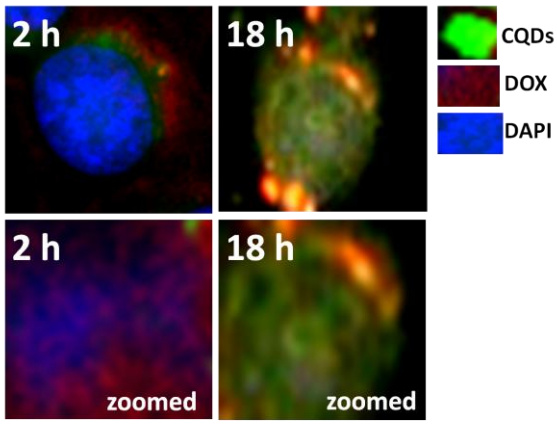

Figure 4.12. *Intracellular localization of DOX-MS-CQDs-FA in HeLa cell by using fluorescence microscope.*

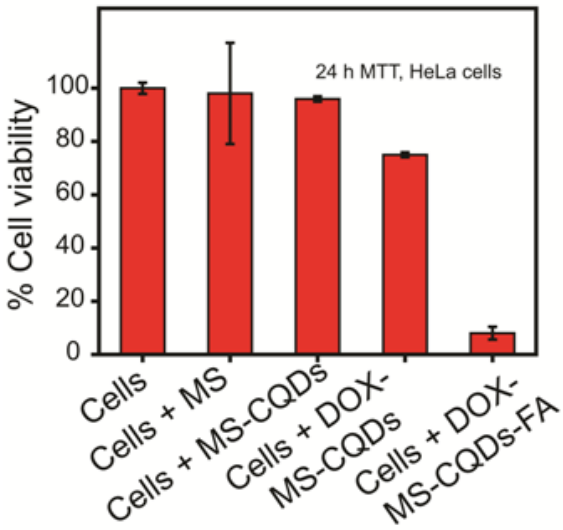

***Figure 4.13**. Targeted chemotherapeutic efficiency (% Cell viability by MTT assay) of designed nanohybrid on HeLa cancer cells. 100 µg/mL concentration of each.*

$$\% \text{ Cell viability} = \frac{\text{OD (treated)-OD (blank)}}{\text{OD (negative control) –OD (blank)}} \times 100 \qquad \text{(eq. 4.4)}$$

for a period of up to 18 h with DOX-MS-CQD-FA on HeLa cancer cell lines. Fluorescence images clearly show that as the incubation time increases, the intracellular delivery of DOX and its entry in to the cell nuclei are constantly increasing (Figure 4.11 and 4.12 for better comparison). The bio-responsive chemotherapeutic efficiency of drug loaded nanohybrid is performed on HeLa cancer cells. More than 90 % cell death is observed for folic acid functionalized DOX-MS-CQDs which is a significant therapeutic response of nanohybrid (Figure 4.13 and eq. 4.4). In the case of DOX-MS-CQDs (without folic acid) about 75 % cell viability is calculated. Approximately 95 % cell viability is calculated for MS and MS-CQDs treated cancer cells. The drug release curve and fluorescence imaging experiments significantly indicate no leakage of drug (DOX) which is desirable in order to

reduce side effects of anticancer drugs on normal cells. Therefore, present nano-carrier clearly demonstrates the prevention of premature leakage. Further, the fluorescence studies showing the presence of drug inside the cells can be attributed to the successful intracellular release of drug by nano-carrier. The targeted release further suggests that disulphide bonds are bio-responsive as observed in release kinetics data (Figure 4.8 b) and that their cleavage leads to pore opening followed by the release of DOX inside the cancer cells.

4.5 Conclusion

In summary, we have designed a novel bioresponsive dual functional green fluorescent CQDs functionalized mesoporous silica nanoparticles based nano-theranostic agent. The design ensures (1) targeted bio-imaging, (2) prevention of premature drug release and (3) bio-responsive drug release. Bioresponsive gate keeping ability of CQDs has been reported for the first time. Inexpensive and ambient synthesis of CQDs from sugarcane waste and their fitness for exploitation in bioresponsive theranostics have been demonstrated successfully for the first time. DOX loaded nano-carrier releases the drug on exposure to the mimicked intracellular cancerous environment i.e., acidic pH and elevated levels of glutathione (GSH). The fluorescence and release kinetics studies show that the green fluorescent CQDs improve bio-imaging effectively preventing the premature release of drug and bioresponsive.

4.6 References

1. Wang, J.; Wang, C. F.; Chen, S., *Angew. Chem. Int. Ed*., 2012, **51**, 9297.

2. Lim, S. Y.; Shen, W.; Gao, Z., *Chem. Soc. Rev.*, 2015, **44**, 362.

3. Alberti, S.; Soler-Illia, G. J. A. A.; Azzaroni, O., *Chem. Commun*., 2015, **51**, 6050.

4. Lorenzo, C. A.; Concheiro, A., *Chem. Commun*., 2014, **50**, 7743.

5. Zhang, Y.; Zhao, Y.; Yermukhambetova, A.; Bakenov, Z.; Chen, P., *J. Mater. Chem. A*, 2013, **1**, 295.

6. Peer, D.; Karp, J. M.; Hong, S.; Farokhzad, O. C.; Margalit, R.; Langer, R., *nat. nanotechnol*, 2007, **2**, 751.

7. Tang, L.; Cheng, J., *Nano Today*, 2013, **8**, 290.

8. Mai, W. X.; Meng, H., *Integr. Biol*., 2013, **5**, 19.

9. Slowing, I.; Trewyn, B. G.; Lin, V. S., *J. Am. Chem. Soc.*, 2006, **128**, 14792.

10. Zhao, Y. L.; Li, Z.; Kabehie, S.; Botros, Y. Y.; Stoddart, J. F.; Zink, J. I., *J. Am. Chem. Soc*., 2006, **132**, 13016.

11. Li, Z.; Barnes, J. C.; Bosoy, A.; Stoddart, J. F.; Zink, J. I., *Chem. Soc. Rev*., 2012, **41**, 2590.

12. Melloa, M. R.; Phanonb, D.; Silveira, G. Q.; Llewellyn, P. L.; Ronconi, C. M., *Micropor. Mesopor. Mat.*, 2011, **143**, 174.

13. Kushwaha, O. S.; Avadhani, C. V.; Singh, R. P., *Carbohyd Polym*, 2015, **123**, 164.

14. Vivero-Escoto, J. L.; Slowing, I. I.; Trewyn, B. G.; Lin, V. S.-Y., *Small*, 2010, **6**, 1952.

15. Coti, K. K.; Belowich, M. E.; Liong, M.; Ambrogio, M. W.; Lau, Y. A.; Khatib, H. A.; Zink, J. I.; Khashab, N. M.; Stoddart, J. F., *Nanoscale*, 2009, **1**, 16.

16. Vallet-Regı, M.; Balas, F.; Arcos, D., *Angew. Chem. Int. Ed.*, 2007, **46**, 7548.

17. Manzano, M.; Vallet-Regi, M., *J. Mater. Chem.*, 2010, **20**, 5593.

18. Singh, N.; Karambelkar, A.; Gu, L.; Lin, K.; Miller, J. S.; Chen, C. S.; Sailor, M. J.; Bhatia, S. N., *J. Am. Chem. Soc*., 2011, **133**, 19582.

19. Lee, J. E.; Lee, N.; Kim, T.; Kim, J.; Hyeon, T., *Acc. Chem. Res*., 2011, **44**, 893.

20. Piao, Y.; Burns, A.; Kim, J.; Wiesner, U.; Hyeon, T., *Adv. Funct. Mater*., 2008, **18**, 3745.

21. Rosenholm, J. M.; Mamaeva, V.; Sahlgren, C.; Lindén, M., *Nanomedicine*, 2012, **7**,

111.

22. Niedermayer, S.; Weiss, V.; Herrmann, A.; Schmidt, A.; Datz, S.; Muller, K.; Wagner, E.; Bein, T.; Brauchle, C., *Nanoscale*, 2015, **7**, 7953.

23. Meng, H.; Xue, M.; Xia, T.; Zhao, Y.; Tamanoi, F.; Stoddart, J. F.; Zink, J. I.; Nel, A. E., *J. Am. Chem. Soc.*, 2010, **132**, 12690.

24. Argyo, C.; Weiss, V.; Bräuchle, C.; Bein, T., *Chem. Mater.*, 2014, **26**, 435.

25. Mackowiak, S.; Schmidt, A.; Weiss, V.; Argyo, C.; Schirnding, C. V.; Bein, T.; Bräuchle, C., *Nano Lett*., 2013, **13**, 2576.

26. Fernando, I. R.; Ferris, D. P.; Frasconi, M. ; Malin, D.; Strekalova, E.; Yilmaz, M. D.; Ambrogio, M. W.; Algaradah, M. M.; Hong, M. P.; Chen, X.; Nassar, M. S.; Botros, Y. Y.; Cryns, V. L.; Stoddart, J. F., *Nanoscale*, 2015,**7**, 7178.

27. Mal, N. K.; Fujiwara, M.; Tanaka, Y.; Taguchi, T.; Matsukata, M., *Chem. Mater*., 2003, **15**, 3385.

28. Ambrogio, M. W.; Pecorelli, T. A.; Patel, K.; Khashab, N. M.; Trabolsi, A.; Khatib, H. A.; Botros, Y. Y.; Zink, J. I.; Stoddarrt, J. F., *Org. Lett*., 2010, **12**, 3304.

29. Song, N.; Yang, Y. W., *Chem. Soc. Rev*., 2015, **44**, 3474.

30. Giri, S.; Trewyn, B. G.; Stellmaker, M. P.; Lin, V. S., *Angew. Chem. Int. Ed*., 2005, **117**, 5166.

31. Li, H.; Tan, L. L.; Jia, P.; Li, Q. L.; Sun, Y. L.; Zhang, J.; Ning, Y. Q.; Yu, J.; Yang, Y. W., *Chem. Sci*., 2014, **5**, 2804.

32. Chen, T.; Yu, H.; Yang, N.; Wang, M.; Dinga, C.; Fu, J., *J. Mater. Chem. B*, 2014, **2**, 4979.

33. Zhou, L.; Li, Z. H.; Liu, Z.; Ren, J. S.; Qu, X. G., *Langmuir*, 2013, **29**, 6396.

34. Li, Z.; Barnes, J. C.; Bosoy, A.; Stoddart, J. F.; Zink, J. I., *Chem. Soc. Rev*., 2012, **41**, 2590.

35. Mewada, A.; Pandey, S.; Shinde, S.; Mishra, N.; Oza, G.; Thakur, M.; Sharon, M., *Mater. Sci. Eng. C*, 2013, **33**, 2914.

36. Baker, S. N.; Baker, G. A., *Angew. Chem. Int. Ed.*, 2010, **49**, 6726.

37. Shen, J. H.; Zhu, Y. H.; Yang, X. L.; Li, C. Z., *Chem. Commun*., 2012, **48**, 3686.

38 Lim, S. Y.; Shen, W.; Gao, Z., *Chem. Soc. Rev*., 2015, **44**, 362.

39. Shen, J.; Zhu, Y.; Yang, X.; Li, C., *Chem. Commun*., 2012, **48**, 3686.

40. Genger, U. R.; Grabolle, M.; Jaricot, S. C.; Nitschke, R.; Nann, T., *Nat. Methods*, 2008, **5**, 763.

41. Liu, J.; Cao, L.; LeCroy, G. E.; Wang, P.; Meziani, M. J.; Dong, Y.; Liu, Y.; Luo, P. G.; Sun, Y. P., *ACS Appl. Mater. Interfaces*, 2015, **7**, 19439.

42. Dong, Y.; Zhou, N.; Lin, X.; Lin, J.; Chi, Y.; Chen, G., *Chem. Mater*., 2010, **22**, 5895.

43. Xu, X. Y.; Ray, R.; Gu, Y. L.; Ploehn, H. J.; Gearheart, L.; Raker, K.; Scrivens, W. A., *J. Am. Chem. Soc*., 2004, **126**, 12736.

44. Mewada, A.; Pandey, S.; Thakur, M.; Sharon, M.; Jadhav, D.; Sharon, M., *J. Mater. Chem. B*, 2014, **2**, 698.

45. Zhu, S. J.; Zhang, J. H.; Qiao, C. Y.; Tang, S. J.; Li, Y. F.; Yuan, W. J.; Li, B.; Tian, L.; Liu, F.; Hu, R.; Gao, H. N.; Wei, H. T.; Zhang, H.; Sun, H. C.; Yang, B., *Chem. Commun*., 2011, **47**, 6858.

46. Zhao, J.; Chen, G. F.; Zhua, L.; Li, G. X., *Electrochem. Commun*., 2011, **13**, 31.

47. Cao, L.; Wang, X.; Meziani, M. J.; Lu, F.; Wang, H.; Luo, P. G.; Lin, Y.; Harruff, B. A.; Veca, L. M.; Murray, D.; Xie, S. Y.; Sun, Y. P., *J. Am. Chem. Soc*., 2007, **129**, 11318.

48. Selvi, B. R.; Jagadeesan, D.; Suma, B. S.; Nagashankar, G.; Arif, M.; Balasubramanyam, K.; Eswaramoorthy, M.; Kundu, T. K., *Nano Lett*., 2008, **8**, 3182.

49. Zhao, Q. L.; Zhang, Z. L.; Huang, B. H.; Peng, J.; Zhang, M.; Pang, D. W., *Chem. Commun*., 2008, **5**, 116.

50. Liu, H.; Ye, T.; Mao, C., *Angew. Chem. Int. Ed*., 2007, **46**, 6473.

51. Li, Y.; Hu, Y.; Zhao, Y.; Shi, G. Q.; Deng, L. E.; Hou, Y. B.; Qu, L. T., *Adv. Mater.*, 2011, 23, 776.

52. Shen, J. H.; Zhu, Y. H.; Chen, C.; Yang, X. L.; Li, C. Z., *Chem. Commun*., 2011, **47**, 2580.

53. Liu, R.; Wu, D.; Feng, X.; Müllen, K., *J. Am. Chem. Soc*., 2011, **133**, 15221.

54. Peng, J.; Gao, W.; Gupta, B. K.; Liu, Z.; Aburto, R. R.; Ge, L.; Song, L.; Alemany, L. B.; Zhan, X.; Gao, G.; Vithayathil, S. A.; Kaipparettu, B. A.; Marti, A. A.; Hayashi, T.; Zhu, J. J.; Ajayan, P. M., *Nano Lett.*, 2012, **12**, 844.

55. Takae, S.; Miyata, K.; Oba, M.; Ishii, T.; Nishiyama, N.; Itaka, K.; Yamasaki, Y.; Koyama, H.; Kataoka, K., *J. Am. Chem. Soc*., 2008, **130**, 6001.

56. Kim, H.; Kim, S.; Park, C.; Lee, H.; Park, H. J.; Kim, C., *Adv. Mater*., 2010, **22**, 4280.

57. Li, Y. L.; Zhu, L.; Liu, Z.; Cheng, R.; Meng, F.; Cui, J. H.; Ji, S. J.; Zhong, Z., *Angew. Chem. Int. Ed.*, 2009, **48**, 9914.

58. Saito, G.; Swanson, J. A.; Lee, K. D., *Adv. Drug Deliv. Rev*., 2003, **55**, 199.

59. Zhao, Q.; Geng, H.; Wang, Y.; Gao, Y.; Huang, J.; Wang, Y.; Zhang, J.; Wang, S., *ACS Appl. Mater. Interfaces*, 2014, **6**, 20290.

60. Zhou, J.; Hao, N.; Zoyza, T. D.; Yan, M.; Ramström, O., *Chem. Commun*., 2015, **51**, 9833.

61. Lee, M. H.; Yang, Z.; Lim, C. W.; Lee, Y. H.; Dongbang, S.; Kang, C.; Kim, J. S., *Chem. Rev*., 2013, **113**, 5071.

62. Chen, M.; He, X.; Wang, K.; He, D.; Yang, S.; Qiu, P.; Chen, S., *J. Mater. Chem. B*, 2014, **2**, 428.

63. Zhao, Y. L.; Li, Z.; Kabehie, S.; Botros, Y. Y.; Stoddart, J. F.; Zink, J. I., *J. Am. Chem. Soc*., 2010, **132**, 13016.

64. Meng, H.; Xue, M.; Xia, T.; Zhao, Y. L.; Tamanoi, F.; Stoddart, J. F.; Zink, J. I.; Nel, A. E., *J. Am. Chem. Soc*., 2010, **132**, 12.

Chapter V

Biodegradable Near-IR responsive graphene oxide nanoflakes-liposome nano-composite as a multifunctional cancer theranostics

Several compositions of organic/inorganic systems with unique physicochemical properties, high therapeutics efficiency, multimodal imaging ability are reported and explored for medical applications. However, aspects of biocompatibility and degradability are major concerns. To address them, several soft materials such as liposome doxorubicin and paclitaxel polymeric micelles, etc. have been proposed for cancer treatment on account of their biocompatibility, aqueous solubility, and high drug loading capacity. Alongside, various morphologies of carbon based nanohybrids such as carbon nanodots, nanotubes, graphene oxide, graphene lipid composites etc. are being explored in medical applications such as sensing, drug delivery, gene delivery, tissue engineering etc. Major drawbacks with applications of soft and carbon based materials are their poor stability, lack of NIR emission for deep tissue imaging and photothermal ability. Here in this chapter, a novel design of biodegradable NIR responsive graphene oxide nanoflakes-liposome nano-composite for multifunctional cancer theranostics is discussed. The biocompatibility, stability, multifunctional cancer theranostics ability, stimuli responsive drug delivery, specific targeting ability for cancer cells/tumor, NIR responsive photothermal therapy and combined chemo-photothermal therapy for breast cancer cell lines studies demonstrated it to be a potentially clinically relevant material.

A part of the work presented in this chapter is communicated for publication.

5.1 Introduction

Integrating biodegradable imaging and therapeutic modalities into a single nanohybrid system can offer specific diagnosis and treatment for cancer theranostics.[1-7] It is understood that these theranostics[5] modalities are sturdily dependent on the architecture, compositions, nanoscopic morphologies, surface chemistry and physicochemical properties of nanohybrid.[8-13] Due to their aqueous solubility, high drug loading capacity, biocompatibility several soft materials such as lipid self assemblies, liposomes, polymeric nanoparticles, micelles etc. are widely studied for biomedical applications.[14-20] While, various formulations of above mentioned soft nanoparticles[18] are reported for cancer theranostics, the poor stability in extracellular environment before reaching the target site is their disadvantage.[16, 18-20] To improve the strengthen of biocompatible liposomal nanoparticles, several inorganic and polymeric coating or covering materials such as silica, calcium phosphate, metal oxides, peptides, various polymeric chains etc. have been reported.[37-40] However, their poor degradation, slow excretion, low dispersion and non specific distribution are still major concerns.

Various types of carbon based nanohybrids carbon/graphene quantum dots (CQDs/GQDs)[21], carbon nanotubes, graphene oxide (GO), reduced graphene oxide composites etc.)[22] are also parallely explored for biomedical applications such as sensing, drug delivery, gene delivery, tissue engineering etc.[22-25] Graphene oxide (GO)[22] and its various formulations have stood out as promising materials in biomedical applications including the anticancer drug delivery, photothermal therapy (PTT), photodynamic therapy (PDT), bio-sensing etc.[26-34] However, low photothermal conversion efficiency is observed for hydrophilic GO sheets due to the existence of structural defects.[29, 32] This is addressed

by graphene oxide nanoflakes (GOF)[35] whose unique optical properties make them attractive agents for NIR responsive diagnosis and therapy. Using these GOFs there is a potential to combine diagnostics and therapeutics in a single system for theranostics.[30, 36] Hence, GOF coating over liposome can solve the issues mentioned earlier. Integration of soft materials like liposomes and GO based nanoformulation in a single system is a new approach in the direction for multifunctional cancer theranostics.

A first simple design of GOF-liposomal composite nanoparticles at ambient conditions and their good theranostics efficacy has been addressed in the present chapter. The design of nano-composite ensures (a) uniform coating of GOF over liposome, (b) uniform distribution and (c) specific architectural features that enhance their synergistic multifunctional ability. In addition, the designed system shows good aqueous solubility, biocompatibility, red emissive and NIR responsive photothermal property, specific bio-distribution, localized tumor diagnosis using single dose of nano-composite with its successful combined chemo-photothermal therapy.

5.2 Experimental Section

5.2.1 Materials

L-alpha-dipalmitoylphosphatidylcholine, DPPC is ordered from Lipoid (Switzerland), Graphite powder, 1-ethyl-3-(3-dimethylaminopropyl) carbodiimide (EDC), N-hydroxysuccinimide (NHS), folic acid (FA), cystamine dihydrochloride, citric acid and 3-(4, 5-dimethylthiazol-2-yl)-2, 5-diphenyltetrazolium bromide (MTT) are purchased from Sigma-Aldrich Pvt. Ltd., USA. Sulphuric acid (98.08 % H_2SO_4), nitric acid (70 % HNO_3) and Dimethylsulphoxide (DMSO, 95 %) are purchased from Merck limited, Mumbai, India. Sodium carbonate (Na_2CO_3, 99.9 %) and sodium hydroxide (NaOH, 98 %) are

purchased from Fischer Scientific limited Mumbai, India. Dulbecco's modified Eagle's medium (DMEM), fetal bovine serum (FBS), phosphate-buffered saline (PBS), antibiotic-antimycotic solution and anticancer drug doxorubicin hydrochloride (DOX.HCl) are procured from HiMedia Laboratories Pvt. Ltd., India. Milli-Q grade water ((Milli-Q or Millipore) > 18.2 MΩ cm) is used for all experiments. All glasswares are rinsed with double distilled water before using them for synthesis and applications.

5.2.2 Characterization techniques

The size and morphology of nanostructures are examined by transmission electron microscopy (TEM FEI Tecnai T-20) operating at 200 kV and scanning electron microscopy (SEM system FEI, Model Quanta 200 3D). Samples for TEM are prepared by evaporating a droplet of sample onto 200 mesh carbon coated copper grid. Elemental analysis is done by energy-dispersive X-ray analysis (EDAX) and measurements are performed on TEM system. Atomic force microscopy (AFM) images are obtained from atomic force microscope (PSIA XE- 100) on tapping mode. The samples for AFM measurements are prepared by drop casting on clean silicon wafers surface after ultrasonic treatment (Equitron ultrasonic cleaner). Optical properties of nano-composite are characterized by UV/visible/NIR (Jasco V570), photoluminescence (Scinco) spectrophotometer using standard quartz cuvette having a path length of 1 cm and IVIS spectrum imaging system (IVIS spectrum Xenogen). Fourier transform infrared (FT-IR) spectra are recorded by using Perkin-Elmer FT-IR spectrum GX instrument. KBr crystals are used as the matrix for preparing samples. Raman spectra are collected using a Lab RAM HR 800 (Horiba scientific) using laser excitation wavelength of 532 nm excitation (1.7 mW power) with a 50X objective at room temperature. Digital photographs are

captured in UV cabinet. Bio-imaging and intracellular localization of drug and carrier is performed with the help of fluorescence microscope. The fluorescence microscopic images are taken by Carl Zeiss inverted fluorescence microscope model AXIO OBSERVER.ZI using DAPI (350-430 nm blue) and rhodamine (480-580 nm red) filters. All photothermal transduction experiments and photothermal performance of composite nanoparticles have been done by using 808 ± 5 nm continuous wave NIR laser source with tunable power density 0.5 to 2.0 W (SDL-808-LM-1000T).

5.2.3 Synthesis of red emissive and NIR responsive graphene oxide nanoflakes (GOF)

In a round bottom flask, 300 mg of graphene oxide is added into concentrated solution of H_2SO_4 and HNO_3 (volume ratio of 30:10) and further stirred for 12 h at 37 °C (room temperature). After completion of reaction (12 h), 400 mL Milli-Q/MPW is added and its pH is adjusted to 7 by adding Na_2CO_3 and NaOH. Reaction solution is left to slowly stir in an ice bath for 3 h to remove the salts in the form of precipitation. After that, product is dialyzed using dialysis bag (molecular weight cut-off 2000 Da) for 2 days.

5.2.4 Preparation of small unilamellar vesicles (Liposomes)

For liposome preparation, a suitable amount (100 mg) of L-alpha-dipalmitoylphosphatidylcholine, DPPC (phase transition temperature = 41 °C), is dissolved in chloroform (6 mL). After complete removal of the chloroform (at 41 °C under reduced pressure), 10 mL of PBS (PBS, 150 mM, pH 7.4) is added to phospholipid film sample in order to obtain a 10 mg/mL lipid suspension in the form of large multilamellar vesicles during film hydration process. The suspended multilamellar vesicles are then extruded

above the transition temperature (41 °C) of the lipids using polycarbonate membranes (mean size diameter: 400, 200 and finally 100 nm, Nucleopore).

5.2.5 Fabrication of biodegradable red emissive and NIR responsive graphene oxide liposome nano-composite (GOF-Lipo)

To design a biodegradable nano-composite, 100 mg of DPPC (phase transition temperature = 41 °C), is dissolved in 6 mL chloroform. After complete removal of the chloroform (at 41 °C under reduced pressure), 10 mL of PBS containing 2 mg of red fluorescent GOF (PBS, 150 mM, pH 7.4) is added to phospholipid film sample in order to obtain the large multilamellar vesicles during film hydration process. The suspended multilamellar vesicles are then extruded above the transition temperature (41 °C) of the lipids using an extruder with polycarbonate membranes (mean size diameter: 400, 200 and finally 100 nm, Nucleopore). To load the anticancer drug, 1 mg/mL concentration of DOX is prepared in PBS buffer (pH 7.4). Further, above procedure is followed for drug loading experiment and 0.5 mg doxorubicin drug is used for filling hydrophilic cavity of liposome. The mass of drug loaded into nano-composite is calculated by subtracting the mass of drug in the supernatant from the total mass of drug in initial solution as mentioned in following equations (eq. 5.1 and 5.2). The amount of drug adsorbed is analyzed with UV-vis spectrophotometer.

$$\% \text{ loading} = \frac{\text{Mass of drug in nano-composite}}{\text{Mass of drug-Mass of drug loaded nano-composite}} \times 100 \qquad \text{(eq. 5.1)}$$

$$\% \text{ Entrapment} = \frac{\text{Mass of drug in nano-composite}}{\text{Initial mass of drug}} \text{ x } 100 \qquad \text{(eq. 5.2)}$$

5.2.6 Surface functionalization of nano-comosite with targeting ligand

The surface functionalization of designed system is carried out by two steps. In the first step, functional groups of GOF are activated by EDC/NHS agents and then further ligated with cystamine. In the second step, folic acid (FA) is anchored on the amine functionalized nano-composite. Folic acid (180 mg) is also activated by 1-Ethyl-3-(3-dimethylaminopropyl) carbodiimide (EDC, 56 mg) and N-hydroxysuccinimide (NHS, 46 mg) in 16 ml of Milli-Q/MPW for 12 h at room temperature. The aqueous solution of amine functionalized GOF-liposome composite (GOF-Lipo, 10 mL) is mixed with activated folic acid and reacted for a time period of 12 h. After completion of the reaction, the mixture is dialyzed using dialysis bag (molecular weight cut-off 2000 Da) for overnight.

5.2.7 Stimuli responsive (pH, temperature and NIR light mediated) drug release kinetics

To check the stimuli responsive drug release kinetics, 1 mL of DOX loaded GOF-liposome nano-composite dialysis bag is immersed into 100 mL of PBS with various pH values (viz., 2, 4, 5 and 7.4). In the same way the temperature is varied to be 37, 43 and 48 °C, respectively at physiological pH. A 808 nm NIR light exposure for 5 minutes is also tested for triggered drug delivery. At different time intervals, 2 mL solution is collected and replaced with same volume of fresh PBS solution to keep the volume constant. The amount

of DOX in the release medium is measured by UV-Vis spectroscopy at 480 nm wavelength and following equation.

$$\% \text{ Release } = \frac{\text{Mass of drug at time}}{\text{Initial mass of drug}} \qquad (\text{eq. } 5.3)$$

5.2.8 Photothermal efficacy of designed nano-composite

The photothermal performance of GOF-liposome nano-composite is examined at various concentrations (0.2-2.5 mg/mL, pH 7.4). Aliquots (200 µL) are deposited into 96 well plate. The initial temperature is stabilized at 37 °C in water bath. Wells are exposed with an 808 ± 5 nm continuous wave NIR laser source (SDL-808-LM-1000T) with a tunable power density (0.5-2.0 W) for 5 min. Further, time dependent photothermal response (temperature) has been recorded.

5.2.9 NIR fluorescence measurement

To check the red emissive ability of designed system, the NIR fluorescence is observed using IVIS imaging system (IVIS spectrum Xenogen) at 500 nm wavelength of excitation light. The fluorescence is observed at various concentrations of designed nano-composite in aqueous solutions.

5.2.10 Disintegration study

Various conditions (temperature, NIR light, pH and combination of NIR light and pH) have been used to check the degradation of designed GOF-Lipo composite (200 µg/mL). The degradation of composite is understood by microscopic analysis.

5.3 Applications

5.3.1 Cell culture and *in vitro* biocompatibility study

To evaluate the biocompatibility and therapeutic study of nano-composite and its components, L929 fibroblastic normal cells, breast cancer cell lines (MDA-MB-231 and 4T1) are cultured in DMEM media supplemented with 10% FBS, 1 % penicillin and 1 % streptomycin, under 5 % CO_2 atmosphere at 37 ºC. To check the biocompatibility of GOF, liposome, GOF-liposome (GOF-Lipo) and folic acid functionalized GOF-liposome nanocomposite (GOF-Lipo-FA), L929 normal cells are seeded at density of 1×10^4 cells per well in 96 well plates and incubated for 24 h in 5 % CO_2 atmosphere at 37 ºC. After 24 h incubation, 200 µl of different concentration (25-2000 µg/mL dispersed in media) of GOF, liposome, GOF-Lipo and GOF-Lipo-FA nanoparticles are added into wells. Following 24 h incubation wells are washed off with PBS and 20 µl of MTT dye is added. Formazan crystals formed after 4 h are dissolved by 200 µL of DMSO. Optical absorbance is recorded at 570 nm and 690 nm using microplate reader (Tecan Infinite 200 PRO). Percentage cell viability is calculated in reference to untreated cells (control).

5.3.2 Blood collection, handling and hemolysis assay

5 mL of blood is taken from healthy mice (ethylenediaminetetraacetic acid stabilized blood). To remove plasma, the collected blood is centrifuged at 3000 rpm for 5 min. (three times) and the remaining red blood cells (RBCs) are washed with PBS. For hemolysis assay, 2 mL of healthy RBCs is diluted to 50 mL with PBS. 0.2 mL of isolated RBCs is mixed with each set of different concentration range (50-1500 µg/mL) of GOF, liposome, GOF-Lipo, GOF-Lipo-FA and DOX-GOF-Lipo-FA. 0.8 mL volume of nano-composite from each concentration is mixed with 0.2 mL of isolated RBCs and further incubated for a

period of 12 h at room temperature (RT). Similarly, the positive and negative controls are prepared by mixing 0.8 mL of water and PBS with RBCs. These mixtures are centrifuged at 3000 rpm for 5 min. and supernatant is collected into a cuvette. Hemolytic activity of composite is calculated from UV-Vis absorption of hemoglobin at 540 nm, which is released in to the solution from hemolyzed RBCs. The percent hemolysis of RBCs is calculated using the following equation:

$$\% \text{ Hemolysis} = \frac{\text{Sample absorbance-Negative control absorbance}}{\text{Positive control absorbance-Negative control absorbance}} \times 100 \quad \text{(eq. 5.4)}$$

5.3.3 Animals models and tumor growth

All procedures involving mice and experimental protocols are approved by Institutional Animal Ethical Committee (IAEC) of National Centre for Cell Science, Pune, India (NCCS, Pune). 6-8 weeks old female Balb/c mice are used for current study. PBS suspended 1×10^4 4T1 breast cancer cells are injected subcutaneously into the flank of Balb/c mice and tumor growth evaluated.

5.3.4 *In vitro* targeting ability and intracellular localization of nano-composite

The time dependent targeting ability of designed composite is understood on 4T1 breast cancer cells. To check the targeting ability of designed system, 4T1 cancer cells are seeded into 96 well plates with a density of 1×10^4 cells/well and incubated for 24 h in 5 % CO_2 atmosphere at 37 ºC. After being rinsed with PBS, the cells are incubated with 200 µg/mL of GOF-Lipo-FA (100 µl) for 4 h. Further, to understand the intracellular localization of GOF-Lipo-FA, the incubation time is increased up to 24 h. After incubation

the cells are washed with PBS for three times to remove all unbound particles. Then 4 % paraformaldehyde solution is added to the cells and incubated for 10 min and nuclei are stained with 4, 6-diamidino-2-phenylindole (DAPI, 1 µg/mL in PBS). At the end of the incubation period, the staining solution is removed by washing with PBS once. The cover slip is then mounted on a drop of 70 % glycerol on glass slide to fix the phase of the cell. The fluorescence images are taken using fluorescence microscope (Axio observer. Z1).

5.3.5 *In vitro* targeted therapeutic studies

To understand the therapeutic efficiency of designed nano-composite, *in vitro* therapies and combined chemo-photothermal therapy are tested on 4T1 and MDA-MB-231 breast cancer cell lines. Cancer cells are seeded into 96 well plates with a density of 2×10^4 cells/well and incubated for 24 h in 5 % CO_2 atmosphere at 37 ºC. After being rinsed with PBS, the cells are incubated with 200 µg/mL of GOF-Lipo before and after DOX loading and FA functionalization for 4 h. After incubation the cells are washed with PBS three times to get rid of all unbound particles. *in vitro* therapy test is divided in following groups: (i) only cancer cells (Group 1) (ii) NIR light exposed cells (Group 2), (iii) Only GOF-Lipo treated cells, (iv) cells are treated with GOF-Lipo under NIR exposure, (v) Cells treated with GOF-Lipo-FA, (vi) GOF-Lipo-FA incubated with breast cancer cells under continuous 808 nm NIR exposure for 5 minutes (vii and viii) cancer cells treated with DOX loaded GOF-Lipo before and after NIR exposure, respectively, (ix) Cells treated DOX-GOF-Lipo-FA before laser treatment and (x) Cells treated DOX-GOF-Lipo-FA under NIR light exposure of 5 minutes for combined chemo-photothermal therapy. In addition, the combined chemo-photothermal therapy at various concentrations of nanocomposite (25-1000 µg/mL) is carried out on breast cancer 4T1 cells.

Cell viability is determined by addition of MTT dye (20 µL, 1 mg/mL dye in sterile PBS). The plate is incubated for an additional 4 h at 37 °C and 5 % CO_2, allowing viable cells to convert the blue solution into pink dye. Formazan crystals are dissolved by adding 100 µL DMSO to each well. Optical absorbance is recorded at 570 nm using microplate reader (Tecan Infinite 200 PRO). Percentage cell viabilities are calculated in reference to untreated cells (control). Further, treated groups of 4T1 cancer cells are stained with propidium iodide (PI) dye to visualize the dead cells through fluorescence microscope.

$$\% \text{ Cell viability} = \frac{\text{OD (treated)-OD (blank)}}{\text{OD (negative control)-OD (blank)}} \times 100 \qquad \text{(eq. 5.5)}$$

5.3.6 GOF-Lipo as a targeted imaging agent for *in vivo* tumor diagnosis

IVIS imaging system (IVIS spectrum Xenogen for NIR fluorescence) at 500 nm of excitation is used to understand the specific targeting and imaging ability of nano-composite. For *in vivo* tumor diagnosis, a minimum single dose (10 mg/kg) of GOF-Lipo-FA contrast agent is intravenously injected in 4T1 tumor bearing female Balb/c mice. Post-injection, the *in vivo* NIR fluorescence images at various time points (starting from 0.25 h to 24 h) are captured from anaesthetized mice and are compared with those of pre- injected mice. The bio-distribution of imaging agent in major organs (heart, lung, liver, spleen, intestine and kidney) and tumor site are understood using IVIS system.

5.3.7 *In vivo* photothermal performance and targeted therapy

808 nm NIR laser source is used to understand the photothermal efficiency of GOF-Lipo-FA injected mice (a minimum single dose, 10 mg/kg). The temperature on tumor site and

out of tumor area is recorded using digital thermometer at various time points under NIR exposure. The results are compared with those of pre-injected mice.

For the *in vivo* therapeutics studies, the designed nano-composite is injected in following groups (4 mice in each group) of tumor bearing balb/c mice (20 g body weight): (1) only tumor bearing mice, (2) for chemotherapy, DOX loaded GOF-Lipo-FA injected (single dose) tumor bearing mice, (3) for combined chemo-photothermal therapy, DOX loaded GOF-Lipo-FA is injected in tumor bearing mice and these mice are exposed with 808 nm NIR light for 5 min. The treatment of individual group is repeated after 2 days time interval using same conditions as mentioned earlier. Temperature changes in tumor region under laser irradiation are recorded by using IR thermometer for different groups. Tumor growth is monitored the following 21 days, and mice are sacrificed at 21st days of planned treatment and tumors are slice up. These tumors are weighed to evaluate the therapeutic efficacy of different groups. In addition, the tumor regression is also understood by bioluminescence (using luciferin) study of treated mice that is compared with pre-injected mice.

5.4 Results and Discussion

5.4.1 Simple design and characterizations of biodegradable NIR responsive nanotheranostics

GOF-Lipo nano-composite is obtained through a simple procedure at ambient conditions as discussed earlier. Firstly, the red emissive graphene oxide nanoflakes (GOF) are prepared from large sheets of graphene oxide (GO, with ~ 1.0 nm thickness (from the AFM images obtained in tapping mode) via chemical cutting process (Figure 5.1 TEM and AFM images with height profile). Further, these GOF are decorated on

lipid bilayer during film hydration which prevents the destabilization of lipid self assembly and produces stable liposomes after extrusion (see Scheme 5.1). GOF-Lipo nano-composite is characterized through various techniques. The synthesized GOF have

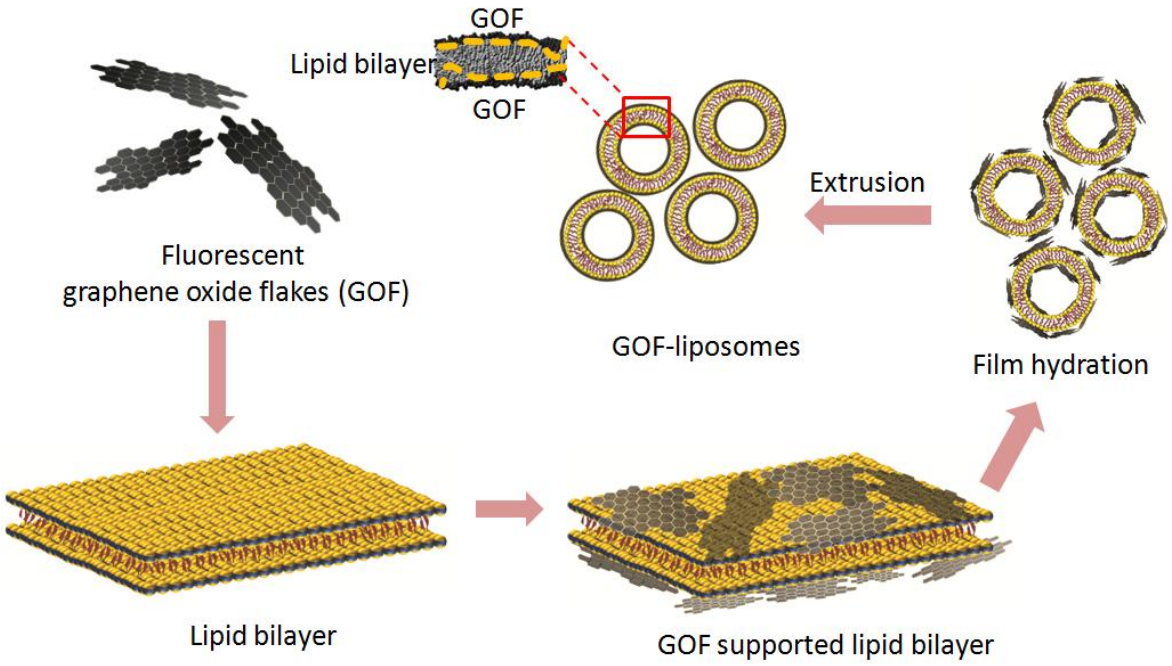

Scheme 5.1. *Schematic showing the simple design of GOF-Liposomes (GOF-Lipo).*

a monodispersed particle size of ~ 20 nm (Figure 5.1 and 5.2 a) with thickness of ~ 1.5 nm (from the AFM images obtained in tapping mode, Figure 5.1). Further, the obtained GOF (Figure 5.2 a) are decorated/supported on lipid bilayer self assembly and then extruded to get the GOF-Lipo nano-composite. The designed composite is also monodispersed with an average particle size of ~200 nm and uniform thickness of GOF over liposome (TEM images Figure 5.2 b). The stability of GOF-Lipo is checked in physiological condition which shows the maintained morphology of designed composite even after 1

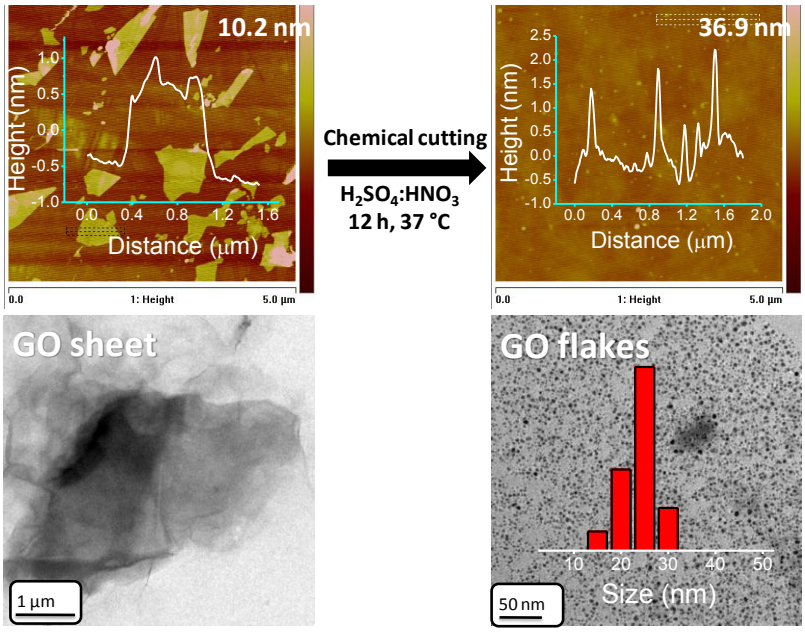

Figure 5.1. *AFM images of synthesized graphene oxide sheets (GO) and graphene oxide flakes (GOF) with their height profiles. TEM images of GO and GOF with its particle size histogram.*

month (TEM images and histogram in Figure 5.2 c). The spherical morphology of GOF-Lipo is confirmed through microscopic characterization (see TEM and SEM images in Figure 5.2 b-d). The maintained spherical morphology of GOF-Lipo is due to the support of graphene oxide flakes on lipid bilayer surfaces (exterior and interior) as seen in Scheme 5.1 and Figure 5.2 b TEM images.). The particle size histograms are shown in Figure 5.2 e and f. Elemental mapping (Figure 5.2 g, h) and EDAX analysis (Figure 5.2 i) of GOF supported liposome indicates the presence of N, O, P, C elements.

Figure 5.3 shows the optical properties of GOF and GOF-Lipo. Absorption spectra (Figure 5.3 a) shows a absorption peak at 240 nm which is assigned to the π-π * transition of C=C in sp^2 aromatic domains. Peak

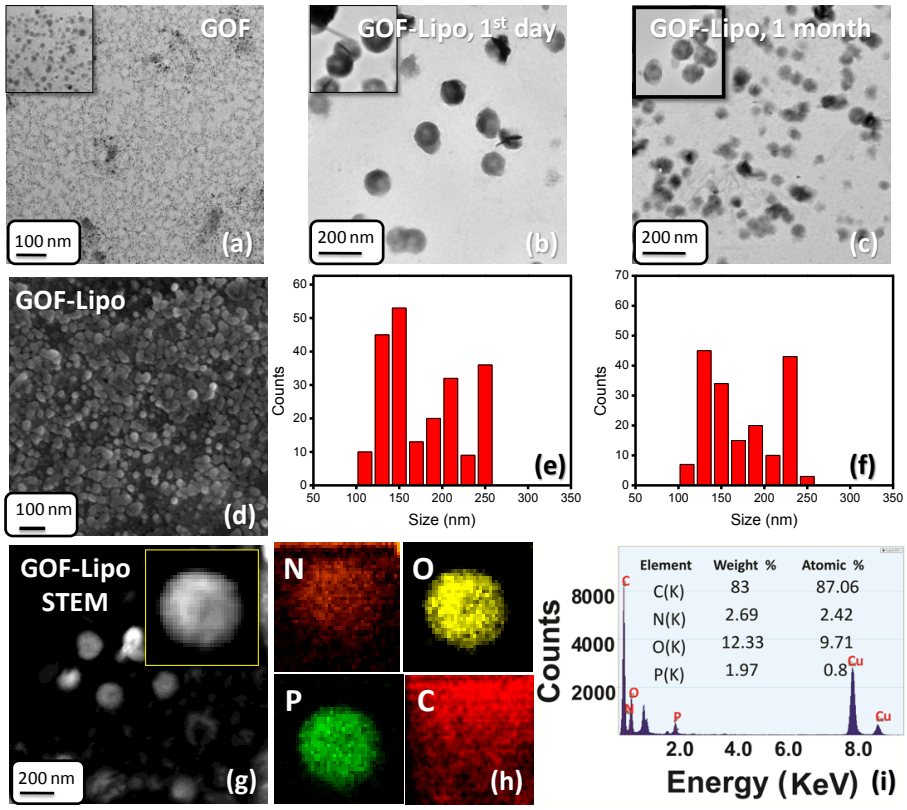

Figure 5.2. *TEM images (a-c) of graphene oxide flakes (GOF), designed GOF-Lipo nano-composite at 1st day and after 1 month. SEM image shows spherical morphology (d), Figure e and f show particle size distribution histograms. Elemental mapping and energy-dispersive X-ray analysis (EDAX) elemental analysis of GOF-Lipo (g-i).*

at 300 nm is assigned to the n-π * transition of C=O bonds. The broad absorption between 600 to 900 nm represents the NIR absorption of GOF and GOF-Lipo composite. Thus, the composite is NIR active. Red fluorescent nature of GOF and GOF-Lipo nano-composite is confirmed by photoluminescence (PL, Figure 5.3 b) spectra showing a deep-red emission between 690-870 nm with 500 nm excitation wavelength.

The Raman spectra of GOF and GOF-Lipo show clear G-band (~ 1585 cm^{-1}) and D-band (~ 1350 cm^{-1}) corresponding to the plane of sp^2 carbons and sp^3 hybridised carbons, respectively (Figure 5.3 c). In addition, the red emissive nature of nano-composite is

confirmed via. fluorescence microscopic characterizations (Figure 5.3 d-h bright field and fluorescence images) and using *in vivo* imaging system (IVIS[34] at 500 nm excitation, Figure 5.3 i). Dispersive studies show that the particles of GOF-Lipo composite are well dispersed and stable in various media such as phosphate buffered saline (PBS), saline and simulated body fluid (SBF) for a period of 24 h (digital photographs, Figure 5.3 j). The transiency in all dispersion media is observed from digital photographs in dispersion test that indicates the good dispersion ability of GOF-Lipo composite.

The above results demonstrate the potential of GOF to be employed as NIR responsive multifunctional agent while stabilizing the liposome. Significantly, these GOF and GOF-Lipo nanoparticles are synthesized at ambient conditions for the first time in the literature.

5.4.2 Optimization and stimuli responsive disintegration of nanotheranostics

The concentration of GOF is a critical parameter to obtain perfectly spherical GOF-Lipo nano-composites. Figure 5.4 a-d shows the effect of GOF concentration on nano-composite morphology and architecture (TEM images). From TEM images it is clear that lower concentration of GOF (0.5 and 1 mg, Figure 5.4 a and b) is not enough to cover the liposome. Here the pre-matured nano-composite disintegrates during TEM imaging due to direct electron exposure and poor support of GOF over liposome. At a higher GOF concentration (3 mg) is disturbing the lipid self assembly and free GOF particles are seen in excess with destructed liposome formation. Moderate concentration of GOF (2 mg) leads to perfectly maintained size and shape of GOF-Lipo composite with each liposome fully covered by GOF (Figure 5.4 c). Thus, 2 mg of GOF is an optimal concentration for GOF-Lipo design.

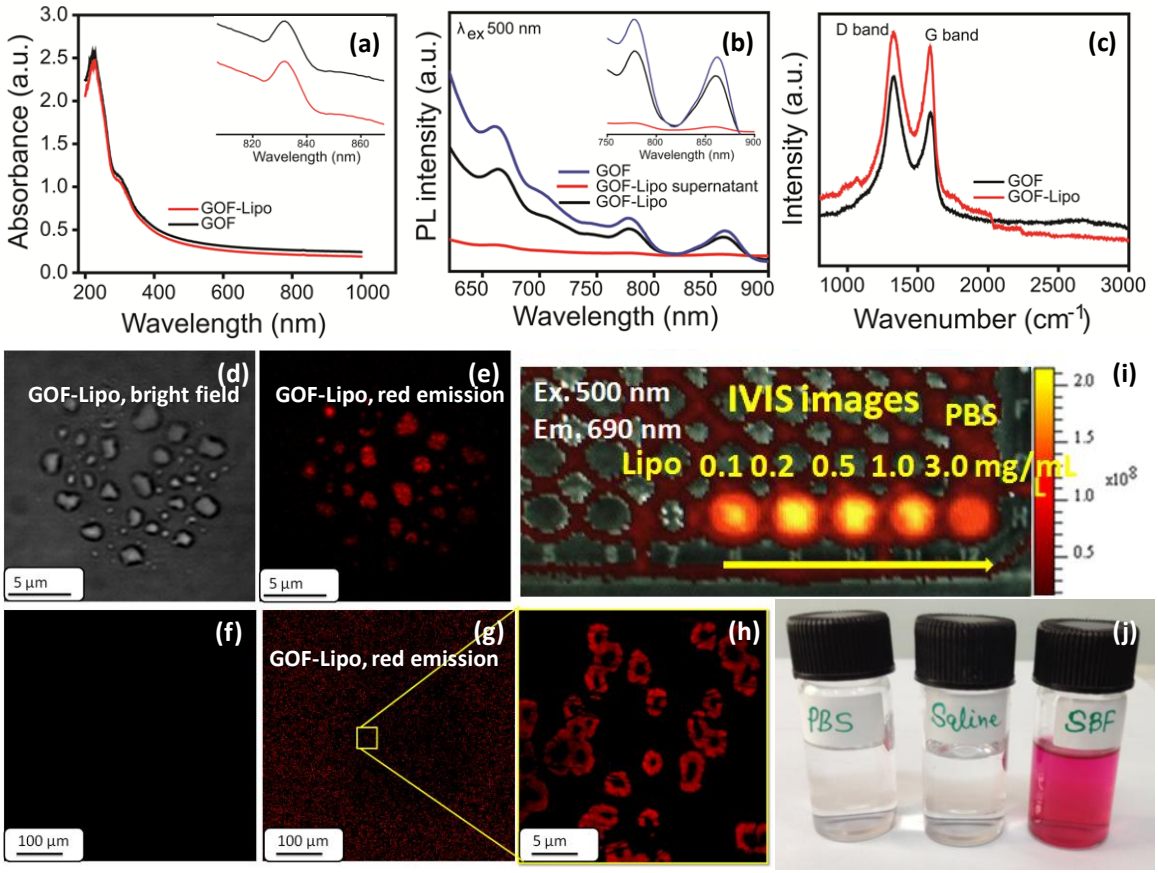

Figure 5.3. *(a) Absorption spectra, (b) photoluminescence, (c) RAMAN spectra of graphene oxide flakes (GOF) and designed GOF-Lipo nano-composite. Fluorescence microscopic images (d-h) and (i) IVIS image show red emissive nature of designed nano-composite and (j) dispersion ability of GOF-Lipo in various media such as phosphate buffered saline (PBS), saline and simulated body fluid (SBF) for a period of 24 h.*

Stimuli responsive disintegration or degradation of GOF-Lipo nano-composite (200 µg/mL) has been studied at using various conditions (viz., temperature, NIR light, pH and combination of NIR light and pH, Figure 5.5). The microscopic image of designed nano-composite shows maintained spherical morphology at physiological condition (37 °C, pH 7.4, Figure 5.5 a). In case of NIR light exposure, disintegrated GOF-Lipo nanoparticles are observed due to produced photothermal heat by GOF (Figure 5.5 b). In addition,

destabilization/ disintegration of these nano-composites in acidic environment (pH 4.0, cancer cell interior condition) are noticed due to induced disturbances within electrostatic interactions (protonation) between liposome and GOF (Figure 5.5 c). Similarly, disintegrated GOF-Lipo nanoparticles are observed under the combined conditions of NIR light exposure and a pH 4.0 (Figure 5.5 d).

The liposomal nanoparticles maintain spherical morphology beyond its glass transition (~ 41 °C) and hyperthermia temperature (43 °C) due to the successful covering of GOF over liposome particles (Figure 5.5 e, f). At ablation temperatures of 47°C, GOF-Lipo nano-composites collapse and do not maintain their spherical morphology as seen in Figure 5.5 g.

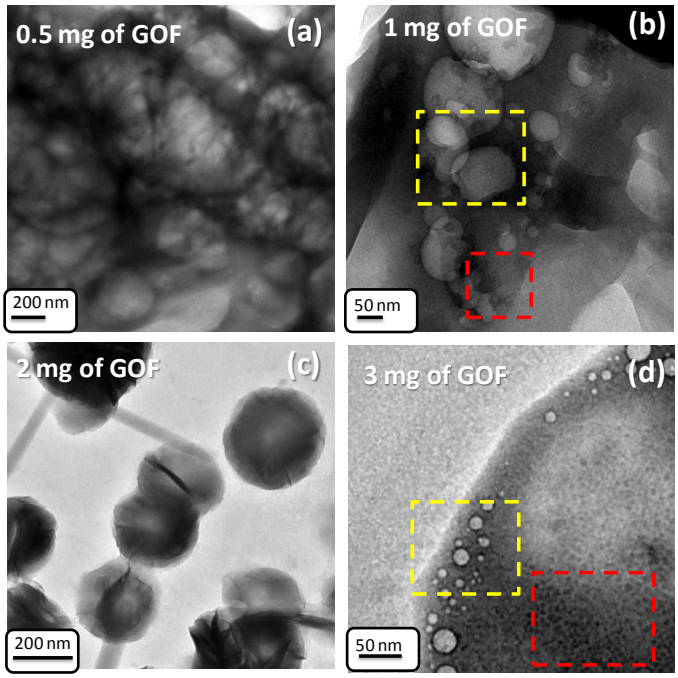

Figure 5.4. *The effect of GOF concentration on morphology of GOF-Lipo and their TEM images (a) 0.5 mg of GOF, (b) 1 mg of GOF, composites with poor morphological control (yellow box) and free GOF (red box), (c) 2 mg of GOF with perfect spheres of GOF-Lipo and (d) 3 mg of GOF with excess free GOF (red box)and GOF-Lipo spheres (yellow box).*

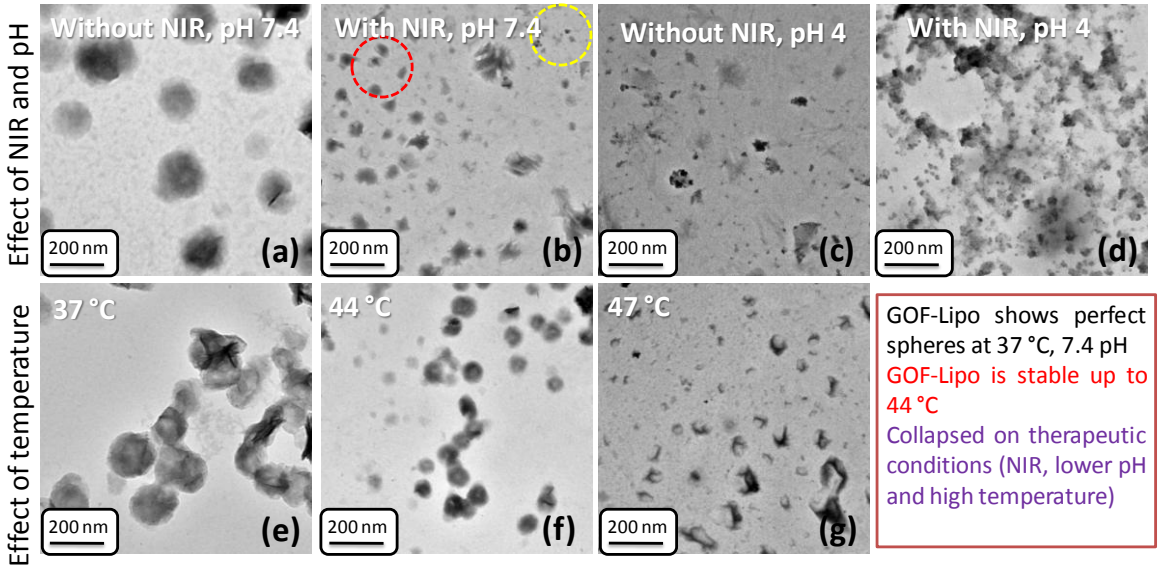

Figure 5.5. *Disintegration study of GOF-Lipo in various conditions (a, b) effect of NIR light, free GOF are seen in yellow circle and destabilized nano-composites are in red circle, (c, d) effect of NIR light and pH and (e-g) effect of temperature on morphological changes of designed GOF-Lipo nano-composite.*

5.4.3 Exterior surface functionalization with folic acid (FA) as targeting ligand

The surface functionalization with folic acid (FA) is examined by FTIR spectroscopy (Figure 5.6). The observations of O-H stretching vibrations (3415 cm^{-1}) and P-O and -O-CH_3 stretching peaks between 900-1026 cm^{-1} confirm the presence of lipid molecules. Vibrations at 1690 $cm^{-1}$and 1610 cm^{-1} are assigned to C=O stretching and N-H bending of the CONH group on GOF. The -N-H bending reveals successful functionalization of cystamine on GOF. The IR bands between 1420-1515 cm^{-1} are due to stretching vibrations of the pteridine and p-amino benzoic acid rings of FA. Peaks at 2819 and 2889 cm^{-1} corresponding to -C-H stretching vibrations.

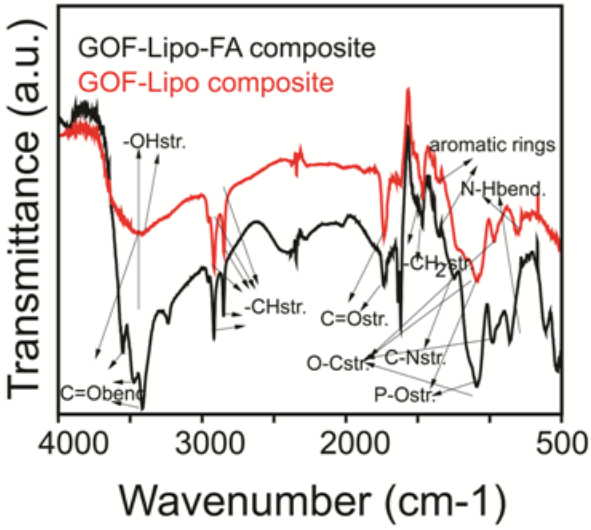

Figure 5.6. *FTIR spectra of GOF-Lipo nano-composite before and after FA functionalization.*

5.4.4 NIR responsive multifunctional theranostics performance of designed system

5.4.4.1 Photothermal performance of GOF-Lipo nano-composite

Time dependent photothermal performance of nano-composite is evaluated at various concentrations of nano-composite (0.2 to 2.5 mg/mL) using 808 nm NIR laser source with tunable power density (0.5 to 2.0 W). In all these cases, initial temperature is stabilized at 37 °C. Figure 5.7 a shows the temperature response at lower power of NIR light (0.5 W) using various concentration of nano-composite (0.2 to 2.5 mg/mL). The hyperthermia temperature (43 °C) at 0.2 mg/mL concentration is noticed in 5 minutes of 0.5 W NIR irradiation. About 46 °C temperature at 2.5 mg/mL concentration is recorded using same power of NIR laser. With the 1 W of NIR light exposure, the maximum temperature viz., 54 °C at 2.5 mg/mL concentration is observed in 5 minutes. The hyperthermia temperature within 4 minute is recorded at lower concentration (0.2 mg/mL) of composite using above mentioned power of NIR (Figure 5.7 b).

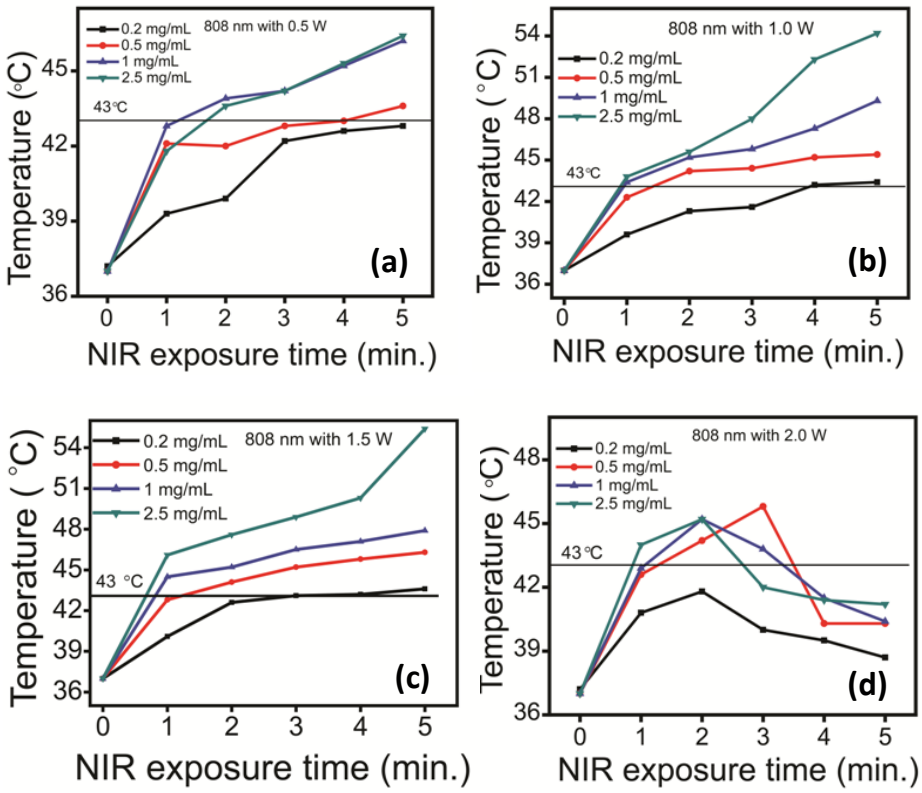

Figure 5.7. *Time dependent photothermal performance of GOF-Lipo at various concentration using 808 nm NIR laser source with tunable power density (0.5-2.0 W).*

The quick response in hyperthermia temperature (43 °C) is observed within 3 minute of 1.5 W NIR at lower concentration of nano-composite (0.2 mg/mL, Figure 5.7 c). More than 54 °C temperature is recorded at maximum concentration (2.5 mg/mL) of designed nano-composite in 5 minute of 1.5 W NIR irradiation. Thus, the quick response in hyperthermia temperature and temperature linearity are recorded with respect to tunable power density (0.5 to 1.5 W) of NIR laser source. The temperature linearity indicates about good absorption and light to heat conversion efficiency of designed nano-composite. Thus, GOF can be considered as a good photo thermal agent for photothermal therapy and stabilizing agent for liposome.

On the other hand, the 2 minute of high power exposure viz., 2 W is resulted about 45 °C temperature at maximum concentration (2.5 mg/mL) of nano-composite (Figure 5.7 d). The drastic reduction in temperature from 45 to 41 °C is observed in the above transduction experiment that may be due to high collision effect and disintegration of GOF-Lipo nano-composite. Hence, the high power (2 W) of NIR source is not favorable to the designed composite for further theranostics applications.

5.4.4.2 Studies of stimuli responsive (pH, NIR light and temperature) drug release performance

A 24 hour time dependent drug release response is studied for stimuli conditions (pH, NIR light and temperature, Figure 5.8 a-c). First, we discuss the drug release response as a function of temperature. The ability of GOF support over liposome in preventing premature drug release as a function of temperature is understood via drug leakage kinetic studies and compared with parental liposome's performance. A negligible drug release (~ 2.5 %) is observed at physiological condition (7.4 pH and 37 °C) from parental liposome. Further, about 20 % of release is observed at a hyperthermia temperature of 43 °C from the same. At a photothermal ablation temperature of 48 °C about 100% release is observed from liposomes due to its destabilization and denaturation (Figure 5.8 a). In case of GOF covered liposome (GOF-Lipo), a negligible drug release of ~ 3 % is observed in physiological (7.4 pH and 37 °C) and hyperthermia (43 °C) conditions. Further, more than 90 % drug release is noticed at the photothermal ablation temperature of 48 °C, indicating the disintegration of GOF-Lipo nano-composite.

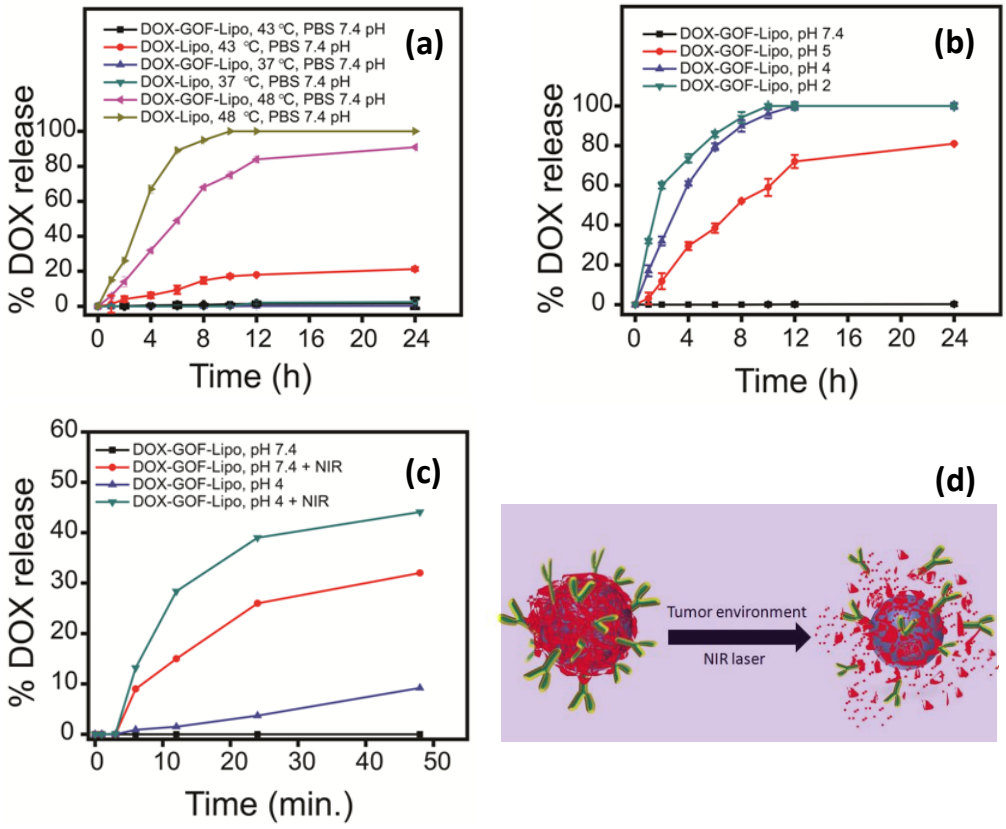

Figure 5.8. *Time dependent drug release performance (a) effect of temperature, (b) effect of pH, (c) NIR light mediated triggered drug release kinetics and (d) shows the disintegration of designed system in cancer mimicked environment and triggered drug release from system.*

Next, release kinetics of nano-composite is studied at various pH of 2, 4, 5 and 7.4, respectively (Figure 5.8 b). When the pH is decreases from 7.4 to 5, the amount of drug release increases from 3 % to ~80 %. About 100 % drug release is observed for pH values of 2 and 4 (these values correspond to late endosome conditions) within 12 h of kinetics due to the disintegration of nano-composite.

The role of NIR light (800 nm for 5 min. exposure) on release kinetics is also tested at various conditions. The drug release response from nano-composite is evaluated at pH 7.4 and pH 4 before and after NIR exposure. At a pH of 7.4, about 3 % of drug release is noted

before NIR exposure which increases to ~ 30 % after NIR exposure. This is once again attributed to the disintegration of designed GOF-Lipo nano-composite due to generated heat on NIR exposure. At a pH 4, a drug release of ~ 8 % is seen before the NIR exposure, while, more than 40 % drug release is calculated after NIR exposure. The marginally higher release at pH4 as compared to pH 7.4 can be attributed higher disintegration of GOF-lipo composite on the combined effect of NIR and acidic pH (see Figure 5.8 c).

5.4.4.3 *In vitro* biocompatibility

The biocompatibility and cancer therapuitic studies of nano-composite are carried out on normal cells (L929), red blood cells (RBCs) and breast cancer cells (MDA-MB-231 and 4T1) using *in vitro* 24 h MTT assay. The cytotoxicity of GOF, liposome (Lipo), GOF-Lipo and FA functionalized GOF-Lipo (GOF-Lipo-FA), respectively are checked on fibroblastic L929 normal cell line (Figure 5.9 a). More than 90 % cell viability of GOF, Lipo, GOF-Lipo and GOF-Lipo-FA are obtained even at higher concentration (2000 µg/mL) demonstrating their significant biocompatibility.

Next, the therapuitic efficiencies viz., chemo, photothermal and combined chemo-photothermal therapy of designed nano-composite (200 µg/mL concentration) are examined on breast cancer cell lines (MDA-MB-231 and 4T1). About 10 % cell viability of MDA-MB-231 cells is observed for drug loaded GOF-Lipo-FA before NIR light exposure. After NIR exposure ~ 3 % viability is calculated for the same due to the combined effect of drug and NIR light (Figure 5.9 b). Similarly, ~ 25 % and ~5% of cell viabilities are calculated for 4T1 breast cancer cells before NIR and after exposure, respectively (Figure 5.9 c).

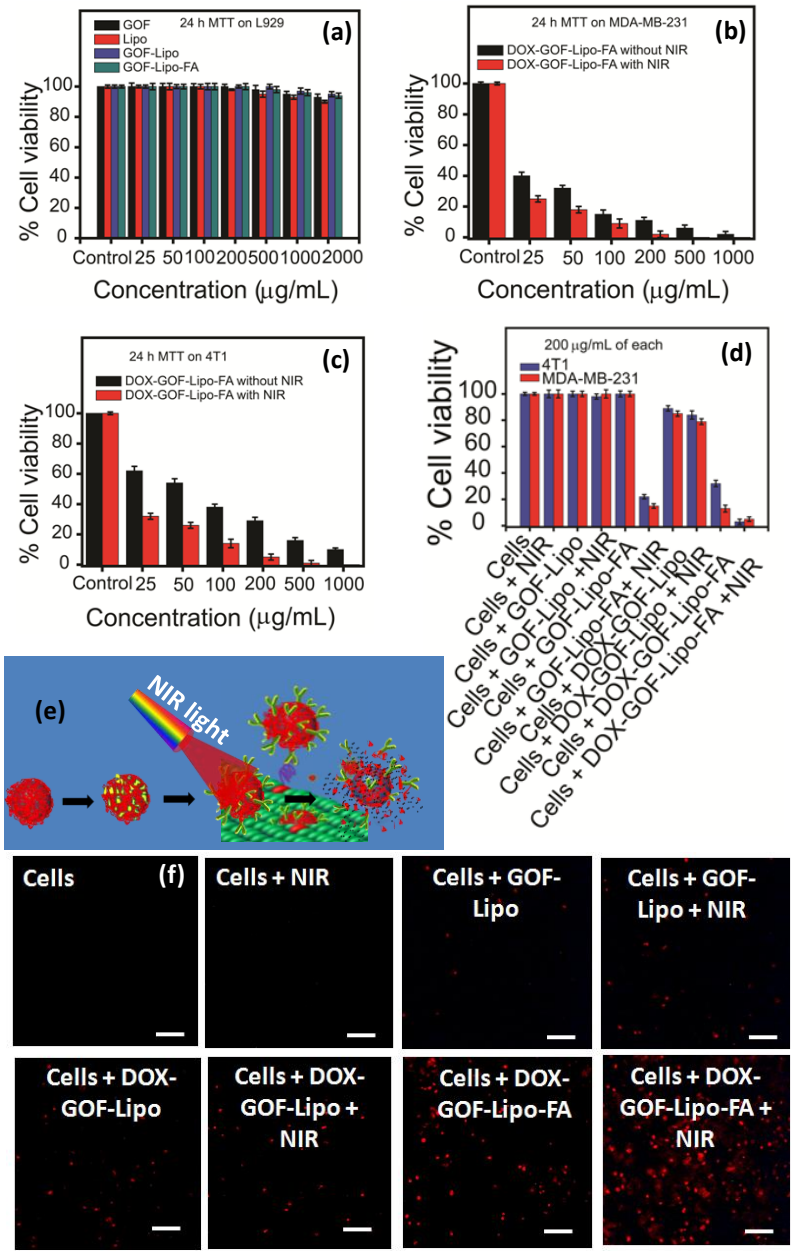

Figure 5.9. *Concentration dependent (a) % cell viability of GOF, liposome (Lipo), GOF-Lipo and FA attached GOF-Lipo on L929 normal cells, (b, c) therapeutics efficiency of drug loaded GOF-Lipo-FA on breast cancer cells (MDA-MB-321 and 4T1), (d) therapeutics performance of various formulations of GOF-Lipo nano-composite by 24 h MTT assay, (e) cartoon shows the disintegration of GOF-Lipo-FA and triggered drug release under NIR exposure in cancer mimicked environment and (f) dead cells (red, PI staining) can be seen in fluorescence microscopy images, scale bar is 150 μm.*

In order to discuss the observations from individual targeted chemotherapy and photothermal therapy and combined chemo-photothermal therapy on both the cancel cell lines (viz., MDA-MB-231 and 4T1), the following groups are made (Figure 5.9 d); Group-1: Untreated breast cancer cells before and after 5 minutes of a NIR exposure of 808 nm, Group-2: GOF-Lipo treated cancer cells before and after NIR exposure, Group-3: GOF-Lipo-FA treated cancer cells before and after NIR exposure, Group-4: Cancer cells treated with drug loaded GOF-Lipo before and after NIR exposure, and Group-5: Cancer cells treated with drug loaded GOF-Lipo-FA before and after NIR exposure.

The MTT assay is used for above set of treatment and the cell viability calculations are reported below. Untreated cancer cells (Group 1) demonstrate a viability of 100 % before and after NIR treatment. Thus NIR does not affect the cell death in untreated cancer cells. GOF-Lipo treated cells (Group 2) show 100 % viability before and after NIR exposure. The cells treated with FA functionalized GOF-Lipo nano-composite (Group 3) do not show any kind of cell death (~100% cell viability) before NIR exposure. On the other hand, ~ 20 % cell viability of 4T1 cells and ~ 18 % viability for MDA-MB-231 are observed on NIR exposure. Thus, the cancer cells respond to the photothermal effect of FA functionalized GOF-Lipo.

More than 80 % cell viabilities are observed when cells are treated with drug loaded GOF-Lipo nano-composite (Group 4). This value is same before and after NIR treatment due to non specific targeting ability of nano-composite. However, ~ 38 % cell viability of 4T1 and 18 % viability of MDA-MB-231 are calculated for DOX loaded GOF-Lipo-FA nano-composite (Group 5) before NIR irradiation due to targeted chemotherapeutic effect on cancer cell lines. After NIR exposure, only 3-5 % cell viabilities of both cancer cell lines

(4T1 and MDA-MB-231) are observed due to the combined effect of drug and NIR light (chemo-photothermal therapy) as shown in Figure 5.9 d.

Figure 5.9 e, demonstrates the targeted therapeutics and disintegration of nano-composite in cancer mimicked environment under NIR exposure. The dead cells visualization from the treatment of each of the above groups, after PI staining, is seen in Figure 5.9 f. Overall, it is seen that the combined chemo-photothermal therapy is more effective than the individual chemo or photothermal therapy.

5.4.4.4 *In vitro* targeting ability

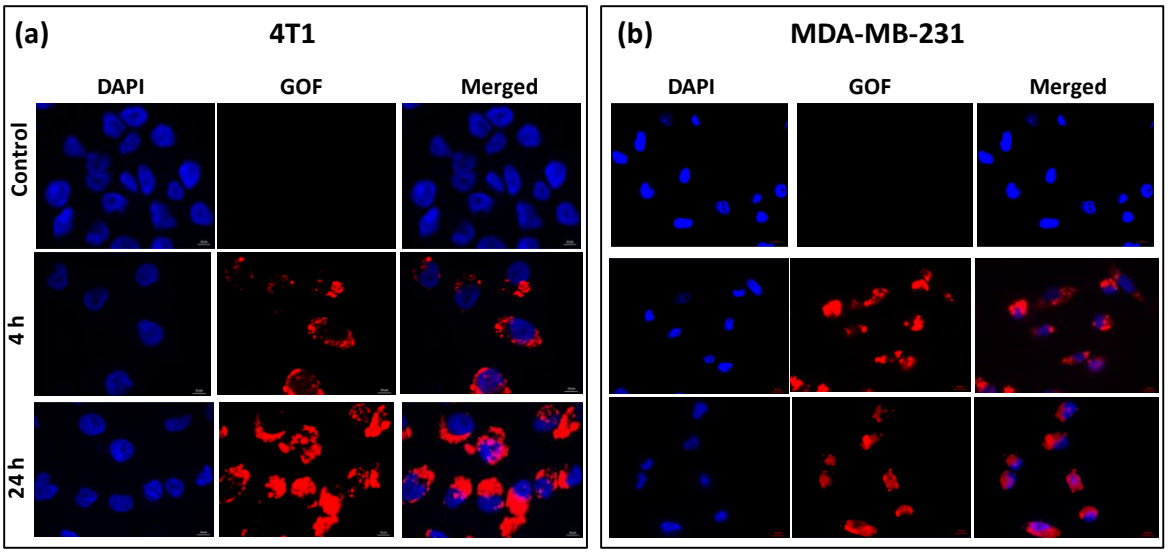

Figure 5.10. *Time dependent (4 and 24 h) in vitro targeting ability of GOF-Lipo-FA on 4T1 and MDA-MB-231 breast cancer cells.*

Targeting performance of synthesized nano-composite (GOF-Lipo-FA) is examined onMDA-MB-231 and 4T1 breast cancer cell lines. Figure 5.10 shows a strong red fluorescence in the interior of both cancer cells after 4 h of incubation time that is indicative of significant targeting ability of the GOF-Lipo-FA composite. Further, thick red

patches (due to GOF) around the cell nucleus are observed with increasing the incubation time of 4 to 24 h, that is indicative of the nucleus targeting ability of the nano-composite (see Figures 5.10 a and b). From this study, it has been understood that the GOF-Lipo-FA nano-composite shows dual targeting ability (cell cytoplasm and nucleus).

5.4.5 Hemolysis study

Prior to in vivo study, it is important to understand the hemolytic activity of designed nano-composite. The functional groups of and theranostic system influence the rapture of RBCs and that is evaluated for the present nano-composite. The hemolysis assay is carried out as a function of nano-composite concentration of 50-1500 µg/mL (Figure 5.11 a-c). For the above concentrations, 0.8 mL of fabricated composite in PBS is mixed with 0.2 mL of isolated RBCs and incubated for a period of 12 h at room temperature (RT).

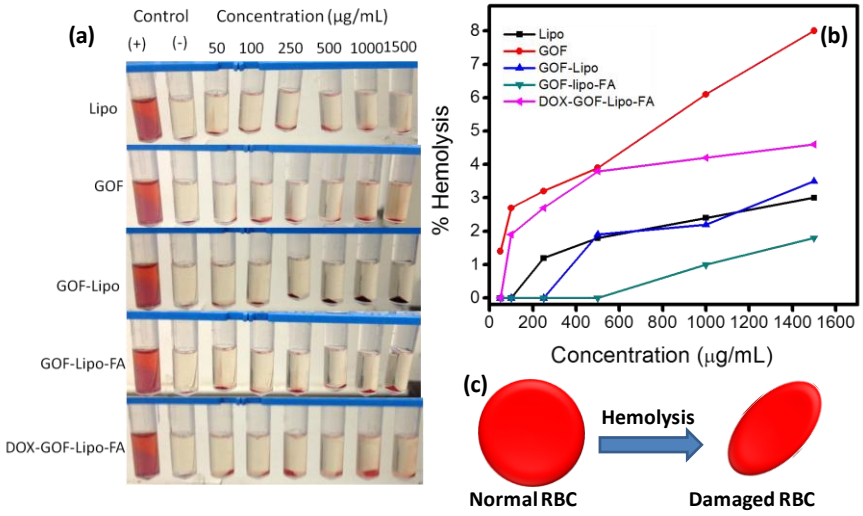

Figure 5.11. *Hemolysis study (a) digital photographs and (b) % Hemolysis of RBCs incubated GOF-Lipo based nano-composites at different concentrations ranging from 50 to 1500 µg/mL for 12 h. The presence of red hemoglobin in the supernatant indicates damaged RBCs. DI water and PBS is used as positive and negative control, respectively. (c) Schematic represents the damaged RBCs during hemolysis.*

The positive and negative controls are prepared by mixing 0.8 mL of DI water and PBS respectively, to RBCs. Hemolytic activity of various formulations of nano-composites is calculated by UV-Vis absorption spectroscopy (see eq. 5.4). The fluorescent GOF shows ~ 8 % damage of RBCs (hemolysis at 1500 µg/mL concentration). The damage of RBC's occurs due to electrostatic interaction between the negatively charged GOF surface (OH groups) and positively charged choline groups of RBCs. On the other hand, bare liposome (Lipo), GOF-Lipo composite and FA attached GOF-Lipo composite show negligible hemolytic activity (1-3 % only) even at maximum concentration (1500 µg/mL). Drug loaded GOF-Lipo-FA (DOX-GOF-Lipo-FA) also shows insignificant hemolysis (about 4 %). The negligible hemolytic activity of indicates the good biocompatibility of designed nano-composite. At the end of hemolysis experiment, precipitated RBCs can be seen in digital photographs (Figure 5.11 a). The interaction between functional groups of GOF and phosphatidyl choline (zwittionic) group of RBC membrane is the significant factor for hemolysis of RBCs.

5.4.6 GOF-Lipo as a NIR responsive theranostics agent

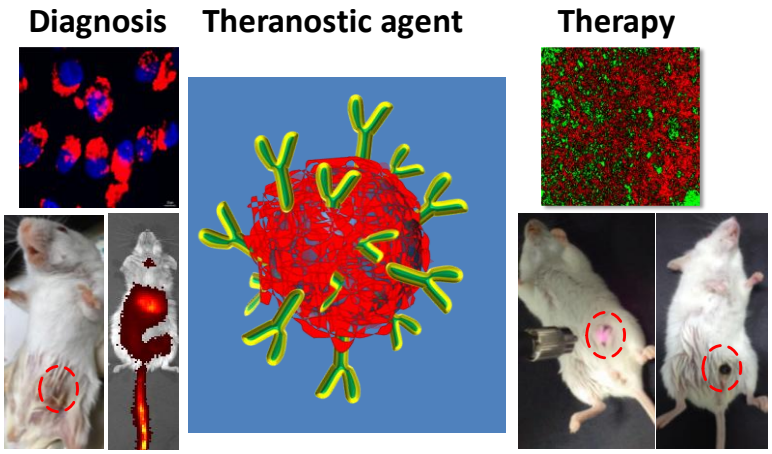

Figure 5.12. *Multifunctional theranostics performance of GOF-Lipo-FA. Targeted tumor diagnosis and NIR light mediated targeted therapy.*

Prior to *in vivo* study several aspects of designed theranostics system such as biocompatibility, photothermal performance, NIR red emissive nature and *in vitro* targeted cancer therapies have been evaluated.

5.4.6.1 *In vivo* tumor diagnosis and bio-distribution of targeted contrast agent

To check the tumor accumulation and targeting ability of FA functionalized GOF-Lipo, a minimum and single dose (10 mg/kg body weight, Figure 5.13 a-g) of nano-composite (GOF-Lipo-FA) is injected through tail vein intravenous (IV) in 4T1 tumor bearing female Balb/c mice. *In vivo* fluorescence of contrast injected mice is observed at various time points viz., 15 minutes, 1, 6 and 24 h (IVIS images in Figure 5.13 a-e). Bio-distribution of red emissive nano-composite in major organs (heart, liver, lung and spleen) and breast tumor are observed after 1 h post-injection. The fluorescence intensity decreases gradually from major organs (heart, liver, lung and spleen) and is seen in the intestine and tumor site with higher intensity after a passage of 24 h post-injection (Figure 5.13 e and f).

The tumor spot is difficult to identify in pre-injected mice (Figure 5.13 a). After 24 h post-injection of nanohybrid the observation of fluorescence from tumor site indicating the higher accumulation of nano-composite in tumor through specific receptor-ligand binding. Additionally, the fluorescence is also observed in lower abdomen organs like kidney and intestine that can indicate the clearance of designed nano-composite from mice body (Figure 5.13 f).

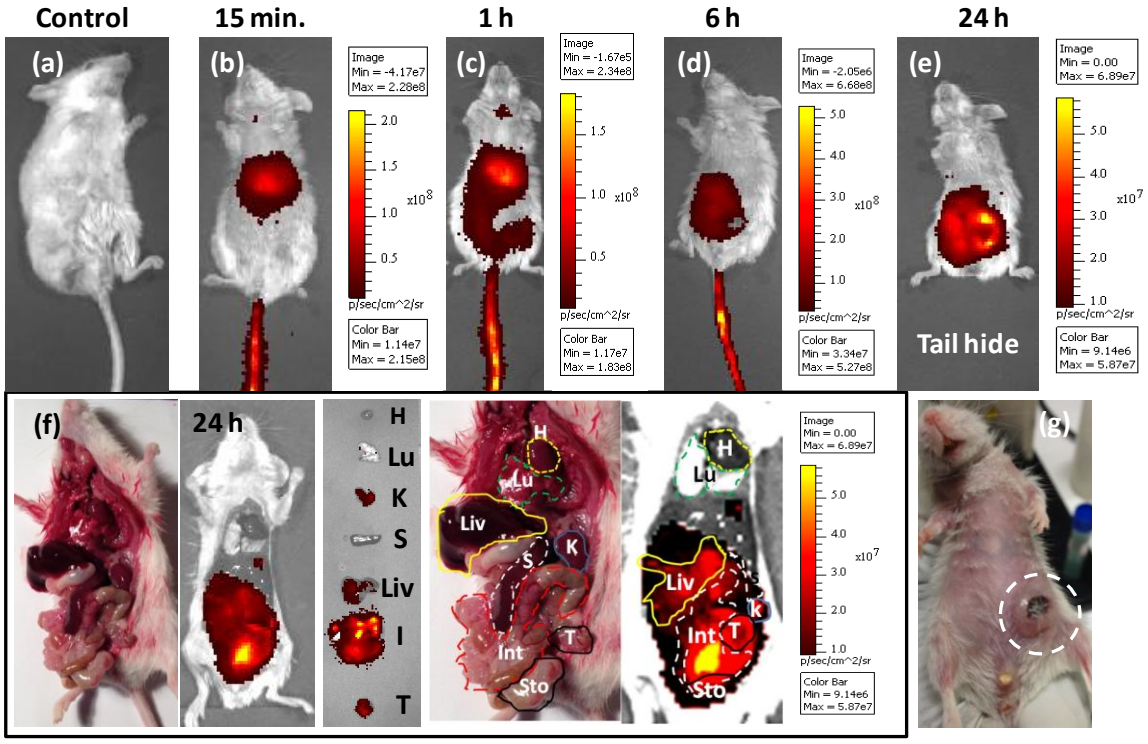

Figure 5.13. *(a-e) Time dependent targeting ability of intravenous (IV) injected FA functionalized GOF-Lipo contrast agent for 4T1 tumor using single dose (10 mg/kg body weight) and their respective in vivo NIR fluorescence images, (f) shows NIR fluorescence in the intestine and tumor site with higher intensity after a passage of 24 h post-injection and (g) 4T1 tumor bearing female Balb/c mice.*

5.4.6.2 *In vivo* photothermal performance of designed nano-composite

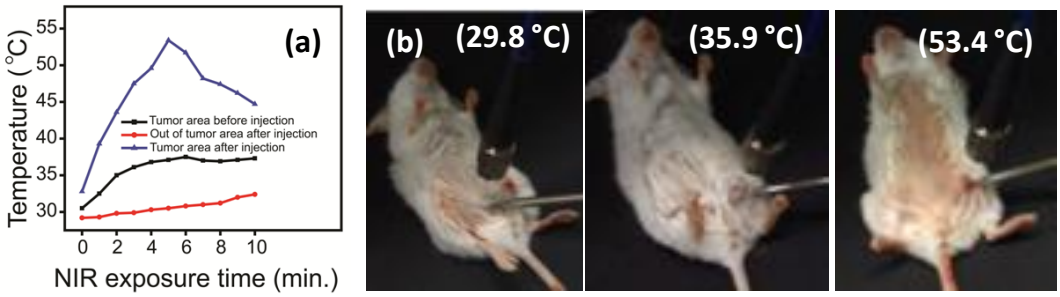

Figure 5.14. *(a) In vivo photothermal performance of post injected GOF-Lipo-FA nano-composite in 4T1 tumor bearing female Balb/c mice and (b) digital photographs are taken during photothermal experiment. 29.8 °C temperature is observed from out of tumor area of post-injected mice, 35.9 °C temperature is recorded from tumor area of pre-injected mice and 53.4 °C temperature is recorded from tumor area of post-injected tumor bearing mice.*

I*n vivo* photothermal performance of fabricated GOF-Lipo-FA composite is examined in post-injected tumor bearing mice and compared with pre-injected mice. A minimum and single dose (10 mg/kg body weight, Figure 5.14) of nano-composite (GOF-Lipo-FA) as NIR active photothermal agent is injected in 4T1 tumor bearing female Balb/c mice and temperature variations are recorded at various time points (0-10 minutes). Negligible thermal response (35.9 °C) on tumor site is observed in pre-injected tumor bearing mice and photothermal ablation temperature (53.4 °C during 5 min. of 808 nm NIR exposure) on same site is recorded after post-injection of nano-composite. On the other hand, 29.8 °C temperature is recorded from out of tumor area in post-injected mice whereas the recorded 53.4 °C temperature from tumor site indicate the high accumulation of FA functionalized GOF-Lipo nano-composite through folate receptor-folic acid specific binding.

Continuous temperature down from 53.4 to ~ 45 °C is observed after 5 minutes of NIR irradiation (between 5-10 minutes observations during NIR exposure) that can indicate the disintegration of designed nano-composite.

5.4.6.3 *In vivo* tumor location and multifunctional therapeutics performance of designed nano-composite

To evaluate the *in vivo* multifunctional therapeutics efficiency of designed nano-composite, the following groups (4 mice in each group) of tumor bearing mice are made; Group 1 is pre-injected tumor bearing mice, post-injection of DOX loaded GOF-Lipo-FA (single dose of 10 mg/kg body weight) in tumor bearing mice as a chemotherapy Group 2 and Group 3 is made for combined chemo-photothermal therapy (chemo-PTT) using same dose of DOX loaded GOF-Lipo-FA nano-composite under 808 nm NIR light for 5 minutes (Figure 5.16 a). Treatment of individual group is repeated after 2 days time interval using single dose of nano-composite. Successful tumor regression is seen after combined chemo-photothermal therapy due to the significant effect of anticancer drug and photothermal response of nano-composite (Figure 5.16 b). The tumor regression or shrinking during chemo-PTT is further corroborated by *ex vivo* NIR fluorescence and *in vivo* bio-luminescence (Figure 5.16 c and d).

Before treatment the NIR fluorescence is observed from *ex vivo* image of tumor due to the high accumulation of nano-composite. Tumor of treated mice group does not show fluorescence indicating the disintegration and detachment of composite from tumor. In addition, the successful tumor shrinking is corroborated from *in vivo* bio-luminescence. From the bio-luminescence images, the poor intensity of 4T1 cells are observed after chemo and combined chemo-PTT therapy compared to control (before treatment, Figure

5.16 d). The tumor volume measurements are taken on the each therapeutic day and further followed for 21 days. The ablated tumor site is clearly seen from digital photographs of female Ballb/c mice after combined therapy treatment (Figure 5.17 a, b). The complete control on tumor growth (tumor volume in mm) is seen after first treatment of combined chemo-photothermal therapy (chemo-PTT) and chemotherapy compared to control (without treatment) group (Figure 5.17 c).

All groups of mice are sacrificed at 21st days of planned treatment and tumors are sliced up. These tumors are weighed to evaluate the therapeutic efficacy of the different groups (Figure 5.17 d, e). The tumor weight is gradually decreased after treatment with chemo therapy and combined chemo-photothermal therapy compared to control once that is due to the effect of anti cancer drug DOX and photothermal effect of injected nano-composite. The reduced tumor weight is observed from about 0.38 g to 0.08 g (Figure 5.17 d), similarly the reduction in tumor volume from 300 mm to 25 mm is observed that is due to the effect of combined targeted therapy. The successful tumor elimination with black spot is observed after combined therapy due to high photothermal effect of injected nano-composite.

It has been understood that the designed nano-composite shows its promising and targeted multifunctional cancer theranostics performance for *in vitro* as well as *in vivo* application.

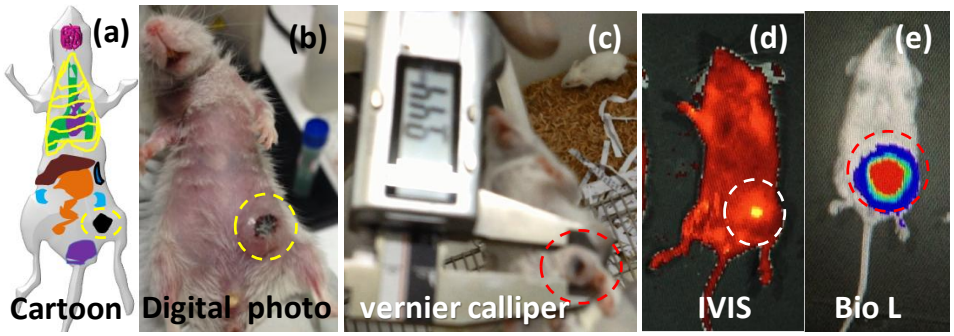

Figure 5.15. *Tumor location in mice body through various techniques before start the treatment (a) cartoon of tumor bearing mice, (b) digital photograph of tumor bearing mice, (c-e) tumor location via vernier caliper, in vivo NIR fluorescence (IVIS) and bio-luminescence.*

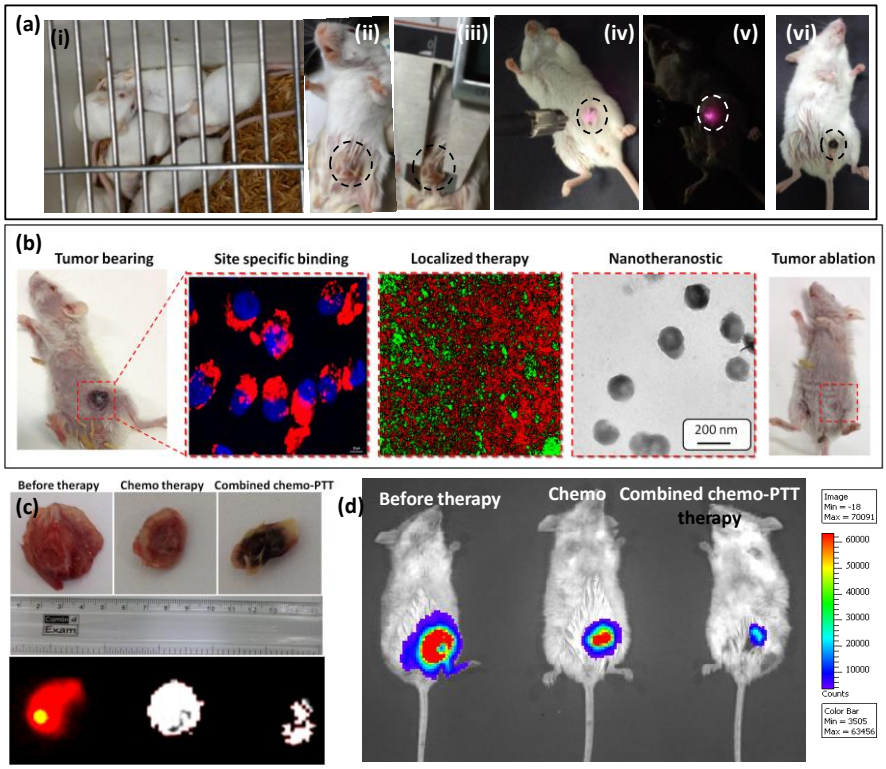

Figure 5.16. *(a) Digital photographs of tumor bearing Balb/c female mice during combined chemo-photothermal (chemo-PTT) therapy with localized therapy area in circle, (b) the effect of combined therapy on tumor regression and microscopic images of designed nano-composite, (c) digital photograph and ex vivo NIR fluorescence image of tumor before and after chemo, combined chemo-PTT therapy and (d) in vivo bio-luminescence before and after chemo therapy and combined chemo- PTT.*

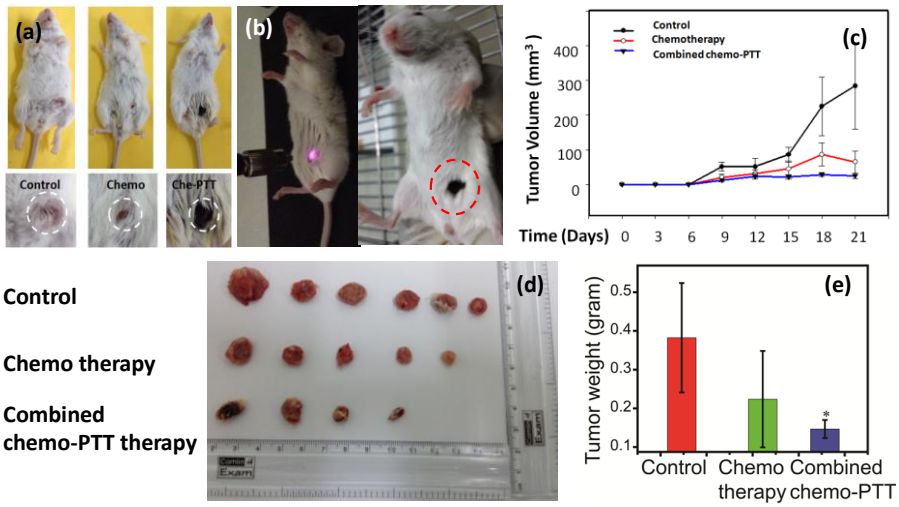

Figure 5.17. *(a, b) Digital photographs of tumor bearing Balb/c female mice during treatment (chemotherapy, combined chemo-PTT under NIR exposure) and their treated area in circle, (c) the effect of chemo and combined chemo-PTT therapy on tumor volume, (d) digital photograph of collected tumor after therapeutics course and compared with control group and (e) tumor weight measurement before and after chemo therapy and combined chemo- PTT.*

5.5 Conclusion

In summary, we have designed a biodegradable NIR responsive multifunctional GOF-Lipo nano-composite for cancer theranostics. The fabricated system has been obtained at ambient conditions. Monodispersed NIR responsive and red emissive GO nanoflakes with about 25 nm in size are obtained from GO sheets at ambient condition. Further, the successful covering of NIR responsive and red emissive GOF over liposome is clearly seen from microscopic images (TEM images) and further corroborated with photoluminescence. The designed nano-composite shows following advantages viz., (a) uniform covering of GOF over liposome and spherical morphology (particle size ~ 200 nm), (b) good dispersion ability in various media and stability in physiological condition, (c) quick photothermal response at tunable NIR power density (0.5-2.0 W of 808 nm NIR laser

source), (d) collapsed or disintegrate on therapy and its degradation in cancer mimicked environment, (e) good biocompatibility (> 95 % cell viability) and (f) red emissive in nature. *In vitro* as well as *in vivo* studies including combined targeted chemo-photothermal therapy on cancer cell lines demonstrate its outstanding multifunctional design and performance. In addition, the designed system shows good performance for triggered drug delivery and dual targeting ability (cytoplasm and nucleus). Moreover, enhanced *in vivo* photothermal efficiency (54.3 °C in 5 min. of NIR exposure) is observed. Nano-composite shows quicker site specific tumor targeting (in 1 h) for long time (24 h) and tumor regression (~ 300 to ~ 25 mm) is observed within 2 weeks course of treatment. Further, smooth blood circulation, specific bio-distribution, localized tumor diagnosis, strong tumor binding (24 h) and successful tumor ablation by designed nano-composite is understood. Finally, based on multifunctional cancer theranostics ability of GOF-Lipo system, it is concluded that the fabricated nano-composite can consider as a clinical relevant material for further application.

5.6 References

(1) Nicolas, J.; Mura, S.; Brambilla, D.; Mackiewicz, N.; Couvreur, P. *Chem. Soc. Rev.* 2013, **42**, 1147.

(2) Slowing, I.; Trewyn, B.G.; Lin, V.S. J. Am. Chem. Soc. 2006, 128, 14792-14793.

(3) Cauda, V.; Engelke, H.; Sauer, A.; Arcizet, D.; Brauchle, C.;¨Radler, J.; Bein, T. *Nano Lett.* 2010, **10**, 2484.

(4) Hrvoje L; Mark W. G.; *Chem. Rev.* 2013, **113**, 1641.

(5) Lee, J. E.; Lee, N.; Kim, T.; Kim, J.; Hyeon, T. *Acc. Chem. Res.* 2011, **44**, 893.

(6) Piao, Y.; Burns, A.; Kim, J.; Wiesner, U.; Hyeon, T. *Adv. Funct. Mater.* 2008, **18**, 3745.

(7) Singh, N.; Karambelkar, A.; Gu, L.; Lin, K.; Miller, J. S. ; Chen, C. S.; Sailor M. J.;

Bhatia, S. N. *J. Am. Chem. Soc.* 2011, **133**, 19582.

(8) Li, Y.; Shi, J. *Adv. Mater*. 2014, **20**, 3176.

(9) Taylor-Pashow, K. M. L.; Della Rocca, J.; Huxford, R. C.; Lin, W. *Chem. Commun*., 2010, **46**, 5832.

(10) Lu, F.; Wu, S.H.; Hung, Y.; Mou, C. Y.; *Small*, 2009, **12**, 1408.

(11) Napierska, D.; Thomassen, L. C.; Rabolli, V.; Lison, D.; Gonzalez, L.; Kirsch-Volders, M.; Martens, J. A.; Hoet, P. H.; *Small*, 2009, **7**, 846.

(12) Huang, X.; Li, L.; Liu, T.; Hao, N.; Liu, H.; Chen, D.; Tang, F., *ACS nano*, 2011, **7**, 5390-5399.

(13) Albanese, A.; Tang, P. S.; Chan, W. C.; *Annual review of biomedical engineering*, 2012, **14**, 1.

(14) Iha, R. K.; Wooley, K. L.; Nystrom, A. M.; Burke, D. J.; Kade, M. J.; Hawker, C. J. *Chem. Rev.*, 2009, **109**, 5620.

(15) Jesorka, A.; Orwar, O. *Annu. Rev. Anal. Chem.*, 2008, **1**, 801.

(16) Iwasaki, Y.; Ishihara, K. *Analytical and bioanalytical chemistry*, 2005, **381**, 534.

(17) Barenholz, Y.C. *J. Control. Release*, 2012, **160**, 117.

(18) Lian, T.; Ho, R. J. *J. Pharm. Sci.*, 2001, **90**, 667.

(19) Cheng, R.; Meng, F.; Deng, C.; Klok, H. A.; Zhong, Z. *Biomaterials*, 2013, **34**, 3647.

(20) Dahlman, J. E.; Barnes, C.; Khan, O. F.; Thiriot, A.; Jhunjunwala, S.; Shaw, T. E.; Xing, Y.; Sager, H. B.; Sahay, G.; Speciner, L.; Bader, A. *Nat. Nanotechnol*., 2014, **9**, 648.

(21) Goenka, S.; Sant, V.; Sant, S. *J. Control. Release*, 2014, **173**, 75.

(22) Yang, K.; Feng, L.; Liu, Z. *Adv. Drug Deliv. Rev*. 2016, **105**, 228.

(23) Hsieh, C. J.; Chen, Y. C.; Hsieh, P. Y.; Liu, S. R.; Wu, S. P.; Hsieh, Y. Z.; Hsu, H. Y. *ACS Appl. Mater. Interfaces*, 2015, **7**, 11467.

(24) Rong, J.; Ge, M.; Fang, X.; Zhou, C. *Nano Lett.*, 2013, **14**, 473.

(25) Bo, Z.; Shuai, X.; Mao, S.; Yang, H.; Qian, J.; Chen, J.; Yan, J.; Cen, K. *Sci. Rep.*, 2014, **4**, 4684.

(26) Feng, L.; Wu, L.; Qu, X. *Adv. Mater.* 2013, **25**, 168.

(27) Yang, K.; Feng, L.; Shi, X.; Liu, Z. *Chem. Soc. Rev.*, 2013, **42**, 530.

(28) Yang, K.; Wan, J.; Zhang, S.; Tian, B.; Zhang, Y.; Liu, Z. *Biomaterials*, 2012, **33**, 2206.

(29) Yang, K.; Zhang, S.; Zhang, G.; Sun, X.; Lee, S. T.; Liu, Z. *Nano Lett.*, 2010, **10**, 3318.

(30) Orecchioni, M.; Cabizza, R.; Bianco, A.; Delogu, L. G. *Theranostics*, 2015, **5**, 710.

(31) Rong, P.; Yang, K.; Srivastan, A.; Kiesewetter, D. O.; Yue, X.; Wang, F.; Nie, L.; Bhirde, A.; Wang, Z.; Liu, Z.; Niu, G. *Theranostics*, 2014, **4**, 229.

(32) Sahu, A.; Choi, W. I.; Lee, J. H.; Tae, G. *Biomaterials*, 2013, **34**, 6239.

(33) Chong, Y.; Ma, Y.; Shen, H.; Tu, X.; Zhou, X.; Xu, J.; Dai, J.; Fan, S.; Zhang, Z. *Biomaterials*, 2014, **35**, 5041.

(34) Ge, J.; Lan, M.; Zhou, B.; Liu, W.; Guo, L.; Wang, H.; Jia, Q.; Niu, G.; Huang, X.; Zhou, H.; Meng, X. *Nat. Commun.*, 2014, 5.

(35) Khan, M. S.; Abdelhamid, H. N.; Wu, H. F. *Colloids Surf B Biointerfaces*, 2015, **127**, 281.

(36) Lim, E. K.; Kim, T.; Paik, S.; Haam, S.; Huh, Y. M.; Lee, K. *Chem. Rev.*, 2014, **115**, 327.

(37) Rengan, A. K.; Bukhari, A. B.; Pradhan, A.; Malhotra, R.; Banerjee, R.; Srivastava, R.; De, A. *Nano Lett*, 2015, **15**, 842.

(38) Beloglazova, N. V.; Goryacheva, O. A.; Speranskaya, E. S.; Aubert, T.; Shmelin, P. S.; Kurbangaleev, V. R.; Goryacheva, I. Y.; De Saeger, S. Talanta, 2015, **134**, 120.

(39) Li, J.; Chen, Y. C.; Tseng, Y. C.; Mozumdar, S.; Huang, L.; *J. Control. Release*, 2010, **142**, 416.

(40) Li, C.; Zhang, Y.; Su, T.; Feng, L.; Long, Y.; Chen, Z. *Int J Nanomedicine*, 2012, **7**, 5995.

Chapter VI

Conclusion and future perspective

This chapter summarizes various salient findings and understandings as outcomes of the research work carried during the period of the degree program. Various material and nano hybrid materials with different objectives were designed, synthesized and studied for various applications in biomedicine and biomedical imaging. These are presented under four different chapters in this thesis. Understandings experienced during their synthesis, characterizations and applications tests are provided in each chapters. This being the last one to summarize their conclusions along with future scope of this research area.

6.1 Conclusion

Chapter 1 of the thesis provides a comprehensive review of literatures available in the area of nanotheranostics, It covers various topics including general material science in nanomedicine, the newly emerging concept namely nanothernostics. It provides details of atypical structural and functional features of an ideal theranostics system, and the need for their synergistic multifunctional performance in specific applications. While the individual components and their best performance are explained with respect to available literature, their integration in to a nanocarrier system is discusses with the probabilities with demerits. Various functional options for bioimaging and cargo carrying abilities are introduced. Stimuli response controlled cargo delivery is a uniquely novel concept picking

up a major attention in this field. Various stimuli responsive nano-gated delivery concepts are introduced with example cases. At the end of the chapter, a comprehensive opinion about the current state of this area of research is discussed with clear objectives and scope of thesis. This introduction is appropriately supported with a decent collection of relevant literature available till date.

Chapter 2 deals with a serious issue. Gold nanorods are though known for their excellent contrasting ability and SPR for efficient photothermal therapy, the presence of CTAB on their surface as stabilizing agent fixed them to be yet are unsafe material to be approved and used as CTAB is proved to exhibit strong cytotoxicity. However, careful replacement of CTAB by other less toxic but more stabilizing molecules are perceived as a possible solution to this through all earlier reports partial success to achieve this as loss of GNR aspect ratio and their aggregations were inevitable. This chapter provides a solution to this with good sustenance of AR. Further this cytotoxicity removal has also been proved by enhanced biocompatibility. Many others studies shows that the lipid capped GNRs are showing good targeting abilities and good contrasting abilities with high photothermal properties.

The surface modified GNRs are obtained with good control in aspect ratio and optical property without losing silver ions from its surface. The simple recipe produces monodispersed nanorods with maintained aspect ratio. The surface modification of GNRs with lipid bilayer is understood using microscopic and spectroscopic techniques (TEM, STEM, EDAX, UV-Vis absorbance and FTIR). The designed nanorods show good biocompatibility (> 95 % cell viability), dispersion ability in various solvents, superior and quicker photothermal response (<2 min) at 1 W NIR power density and (f) higher radio

density (HU 60) compared to that of the widely practiced iodine (HU 23) contrast agent. *In vitro* plasmonic photothermal therapy on cancer cell lines demonstrate its outstanding multifunctional design and performance. Further, the fabricated lipid modified nanorods show successful *in vivo* tumor diagnostic ability by using single and minimal dose (10 mg/kg body weight).

Thus, the newly designed lipid modified GNRs as a contrast agent has a potential to replace the existing iodinated contrast agent due to its good biocompatibility, high atomic number, brightness and radiodensity. As these nanorods are sensitive to NIR light they are ideal for photothermal therapy. To make them suitable as a cargo carrier a control coating of gold nanorods surface with chemically inert materials such as mesoporous silica coating is employed here to overcome several hurdle to convert them into multifunctional theranostics agents.

To enhance the cargo capacity and to maintain the aspect ratio of GNRs, mesoporous silica (MS) is directly deposited over them and discussed in Chapter 3. The tunable silica thickness deposition is obtained via a simple, one pot and a rapid (2 h) recipe at near ambient conditions. The designed nanohybrid shows superior advantages viz., (a) effective distribution of GNRs inside highly monodispersed (particle size ~ 100±10 nm) MS nanoparticles, (b) highest ever reported surface area of 1100 m^2/g, (c) largest ever reported cargo capacity (57 % for DOX), (d) superior and quicker photothermal response (<2 min) at relatively lower NIR power density (at 0.5 W), (e) good biocompatibility (>90 % cell viability) and (f) higher radio density (HU 151) compared to that of the widely practiced iodine (HU 23). *In vitro* synergistic targeted chemo-photothermal therapy on various cancer cell lines demonstrate its outstanding multifunctional design.

The designed nanohybrid also shows enhanced features such as (a) high product yield (~ 1 g/batch) and (b) dual nature folic acid as gatekeeper and targeting ligand. Further, the fabricated nanohybrid shows successful targeting ability for breast cancer cells/tumor by single, minimal dose (10 mg/kg body weight).

The controlled pore opening on mesoporous cargo carrier with nano sized gates are required to prevent the premature drug release and stimuli responsive pore opening in cancer mimicked environment is observed. In Chapter 4, multi-stimuli sensitive (GSH and pH) bioresponsive fluorescent nano-gates are decorated on the exterior of mesoporous silica. The designed system ensures (a) targeted bio-imaging, (b) prevention of premature drug release and (c) bio-responsive drug release performance. Bioresponsive gate keeping ability of fluorescent carbon/graphene quantum dots (CQDs/GQDs) has also been reported for the first time. Inexpensive and ambient synthesis of quantum dots from sugarcane waste and their fitness for exploitation in bioresponsive theranostics have been demonstrated successfully in this chapter. Drug loaded nanohybrid releases the drug molecules on exposure to the mimicked intracellular cancerous environment i.e., acidic pH and elevated levels of glutathione (GSH). The fluorescence and release kinetics studies show that the green fluorescent CQDs improve bio-imaging effectively preventing the premature release of drug and bioresponsive.

The biodegradation of above discussed gold, silica and their nanohybrids is a major concern for nanomedicine. Thus, the new design of biodegradable multifunctional nanohybrid for cancer theranostics applications is becoming a prime objective for nanomedicine. The new design of biodegradable NIR responsive multifunctional GOF-liposome nano-composite is discussed in Chapter 5. The fabricated system has been

obtained at ambient conditions. The monodispersed NIR responsive and red emissive GO nanoflakes with about 25 nm in size are obtained from GO sheets. The successful covering of GOF over liposome is clearly seen from microscopic images (TEM images) and the NIR emissive nature is corroborated with photoluminescence spectroscopy. The designed nano-composite shows following advantages viz., (a) uniform covering of GOF over liposome and spherical morphology (particle size ~ 200 nm), (b) good dispersion ability in various media and stability in physiological condition, (c) quick photothermal response at tunable NIR power density (0.5-2.0 W of 808 nm NIR laser source), (d) collapsed or disintegrate on therapy and in cancer mimicked environment, (e) good biocompatibility (> 95 % cell viability) and (f) red emissive in nature for deep tissue penetration.

In vitro as well as *in vivo* studies including combined targeted chemo-photothermal therapy on cancer cell lines demonstrate its outstanding multifunctional design and performance. In addition, the designed system shows triggered drug delivery and dual targeting ability (cytoplasm and nucleus). The good *in vivo* photothermal efficiency (54.3 °C in 5 min. of NIR exposure) of nano-composite is observed. The nano-composite shows higher accumulation in tumor and specific tumor targeting (in 1 h) for long time (24 h). The regression (~ 300 to ~ 25 mm) of breast tumor is observed within 2 weeks course of NIR light mediated treatment. The multifunctional cancer theranostics ability of GOF-Lipo composite indicate about it significant impact for clinical relevant material in nanomedicine.

6.2 Future Perspective

In this thesis we have mentioned our several efforts to understand the design of multifunctional nanohybrids for cancer diagnosis and therapeutic applications. So far,

iodinated contrast agents are commonly used imaging probe for diagnosis but these contrasts shows several allergic issues, nephrotoxicity, rapid clearance (less than 10 min.), non specific bio-distribution, lack of surface functionalization etc. However, these contrast agents requires permanent replacement with good biocompatible contrast agents. To overcome this issue various shapes of gold nanoparticles are heavily used as a contrast agent for diagnosis and their good biocompatibility is recognized recently. Due to specific optical property, good contrast ability (brightness and radiodensity) these gold nanoparticles can be applicable for human trials in near future.

On other side, mesoporous silica (MS) has been considered as a safe material for drug delivery due to its high surface area, high cargo capacity, easy to surface functionalization, good biocompatibility etc. The MS based carrier system can deliver the diagnostics and therapeutics agents at the targeted site which can solve the problem for specific distribution of several drug molecules and specific tumor diagnosis. Due to good biocompatibility of silica, few silica based nano sized hybrids are in clinical applications. Thus the chances of MS can be approved for human trials because of its high cargo capacity, biocompatibility. In addition, several formulations of soft materials are in clinical trials (liposomal nanohybrids with drug encapsulations) but these systems are far from their multifunctional performance. Near-infra red (NIR) light responsive photodynamic therapy is known for clinical applications. However, biodegradation, red emissive nature, NIR responsive, multifunctional ability of nano sized hybrids materials can be consider for new demand for clinical practice. A new design of red emissive and NIR responsive multifunctional nano sized system for cancer theranostics applications have been discussed in this thesis. The designed system is further biodegradable in nature under therapeutics command. Thus, the

designed nano-composite can be consider as clinical relevant material for further Food and Drug Administration (FDA) approval and its clinical applications.

Finally, the impact of nanotechnology on cancer diagnosis and therapies has been understood from this thesis work. The designed each nanohybrid/composite system has advanced concept for new developments in nanomedicine and shows their capability for solving the various issues of oncology.

List of publications

- **Rajendra, P.**; Sandhya, A.; Deepak, S. C.; Rohit, S.; Selvaraj, K., Bioresponsive carbon nano-gated multifunctional mesoporous silica for cancer theranostics, *Nanoscale*, **2016**, 8, 4537-4546.
- **Rajendra, P.;** Selvaraj, K., Rapid scalable direct deposition of ordered mesoporous silica over gold nanorods for cancer theranostics, submitted to *Chem. Mater.* 2017.
- **Rajendra, P.;** Sachin, B. A.; Deepak, S. C.; Rohit, S.; Selvaraj, K., Biocompatible plasmonic nanohybrid as a safe contrast agent for *in vivo* tumor diagnosis via X-ray computed tomography, *ACSNANO*, 2017, under revision.
- Deepak, S. C.[#]; **Rajendra, P.[#];** Rohit, S.[*]; Selvaraj, K.[*], Dual therapeutic disintegrable GNR-liposome nanohybrid for plasmonic photothermal cancer theragnostic, submitted to *Bioconjugate Chem.* 2017 ([#]these authors contributed equally to the work and [*]corresponding authors).
- **Rajendra P.;** Deepak, S. C.; Piyush K.; Rohit, S.; Selvaraj, K., Multifunctional inorganic nanohybrid for targeted photothermal therapy, photothermal ablation and cell imaging, *to be communicated*.
- **Rajendra, P.;** Amit, K. Y; Mhadeov, G.; Deepak, S. C.; Gopal, K.; Rohit, S.; Selvaraj, K., Biodegradable NIR responsive red emissive GOF-liposome nano-composite as a targeted multifunctional cancer theranostics, *to be communicated*.

- **Rajendra P.;** Krati J.; Selvaraj, K., Synthesis and surface modification of mesoporous silica, *under preparation.*

List of patents

- **Rajendra, P.;** Selvaraj, K.; Krishan, K.; Meghana, O., Enhanced multifunctional mesoporous nanodrug carrier for targeted and triggered delivery and photothermal therapy (Application No. 306/DEL/2015).
- **Rajendra, P.;** Selvaraj, K.; A Novel biodegradable theranostics nano-composite and use thereof (INV-2016-0095, 12/09/2016).